Surface Modification and Scan Imaging of Upconverting Nanoparticles

DISSERTATION ZUR ERLANGUNG DES DOKTORGRADES DER
NATURWISSENSCHAFTEN (DR. RER. NAT.) DER FAKULTÄT
CHEMIE UND PHARMAZIE DER UNIVERSITÄT REGENSBURG

vorgelegt von

Andreas Sedlmeier

aus Regensburg

im Jahr 2015

Diese Doktorarbeit entstand in der Zeit von November 2011 bis Dezember 2015 am Institut für Analytische Chemie, Chemo- und Biosensorik an der Universität Regensburg.

Die Arbeit wurde durchgeführt bei Prof. Dr. Otto S. Wolfbeis und Prof. Dr. Antje J. Bäumner unter Anleitung von PD Dr. Hans-Heiner Gorris.

Promotionsgesuch eingereicht: Dezember 2015

Kolloquiumstermin: 29.01.2016

Prüfungsausschuss:

Vorsitzender: Prof. Dr. Frank-Michael Matysik

Erstgutachter: Prof. Dr. Antje J. Bäumner

Zweitgutachter: PD Dr. Hans-Heiner Gorris

Drittprüfer: Prof. Dr. Achim Göpferich

Acknowledgment

Table of Content

1. Introduction

The detection of (bio)molecules in *in vitro* or *in vivo* is a key issue in various fields of bioanalysis. In addition to the qualitative evidence of these targets, i.e. their presence in the biological system, their quantification is at least equally important. Changes in the (bio)molecule concentration for example can indicate responses of a cell to extracellular stimuli interacting with cell receptors. The detection system for a low concentration of the (bio)molecule has to be highly sensitive to the target but also highly selective to avoid false positive results by chemically or structurally similar compounds.

Both high sensitivity and selectivity can be achieved by using techniques that are based on optical phenomena. Especially fluorescence methods are among the most important detection systems in this regard since they are also versatile, non-invasive, and enable a high spatial resolution.[1] However, most (bio)molecules that are of high interest in research as well as in clinical studies rarely show intrinsic fluorescence. Therefore, a variety of luminescent labels is available that can be linked to the target with high selectivity, partially even directly in biological samples without the need for sample purification. Organic fluorophores are commonly used for this purpose, since these small molecules can easily be modified by conventional reactions to show the required binding functionality without any changes in their optical properties. A drawback of these labels is their susceptibility to photobleaching which hampers their use in long-term studies. Another class of labels is based on inorganic materials on the nanometer scale. The optical characteristics of nanosized semiconductor materials, so called quantum dots, only rely on the material employed and the nanoparticle size. They show no photobleaching[2, 3], have a higher emission intensity signal, allow an optimization of both the synthesis and the surface modification, and enable the simultaneous introduction of various functionalities and properties into one nanoparticle. Consequently, these fluorescent labels are more suitable for bioanalysis than organic fluorophores. Most quantum dot materials, such as CdS or CdSe, however, display a high (cyto)toxicity due to the heavy metal cadmium rendering them unsuitable for any bioanalytical application[3, 4].

Nanoparticles made of upconverting materials (UCNPs), in contrast, are not only photostable and basically nontoxic, but also enable a shift of the excitation wavelength from the ultraviolet or visible range to the near infrared domain. This change in irradiation light allows studies with drastically reduced photodamage and autofluorescence of biological species. The underlying Anti-Stokes process "upconversion" describes one way to convert low-energy photons (NIR) by sequential absorption into a photon with a shorter wavelength (mostly VIS). This phenomenon, investigated thoroughly by Auzel[5] in the 1960s, occurs with a high efficiency also in nanosized inorganic materials doped with lanthanide ions such as ytterbium, erbium, and/or thulium. The optical characteristics of

the resulting upconversion emission can be divided in two classes according to their dependence on the nanoparticle size. While several parameters such as number, wavelength, and peak width of the emissions are unaffected by the reduction of the upconverting material, other properties like the emission intensity are strongly affected by the altered surface-to-volume ratio owing to enhanced quenching effects.

However, since most syntheses for monodisperse and bright UCNPs rely on hydrophobic size-controlling and surface-capping agents such as oleic acid, the resulting nanoparticles have hydrophobic surfaces unsuitable for any kind of bioanalytical applications. Therefore, surface engineering is indispensable in order to benefit from the advantageous chemical and optical characteristics of UCNPs. Several methods that were originally developed for other nanoparticle types like quantum dots[6] and silica nanoparticles[7, 8] are applicable for these modifications. However, this surface engineering process has to be adjusted to account for the differences in the surface chemistry of the UCNPs compared to the original targets of these functionalization techniques. Methods based on non-covalent interactions such as ligand exchange or covalent binding such as the growth of a silica shell and a potential silanization creates a hydrophilic UCNP surface and consequently renders these nanoparticles dispersible in aqueous systems. The use of Click chemistry, more precisely the Huisgen cycloaddition of an azide and an alkyne[9, 10], enables a potential direct reaction of the nanoparticle surface with a suitable compound both *in vitro* and *in vivo*, since this reaction as well as both functionalities are bioorthogonal[11]. As a result, both functionalities as well as their coupling reaction neither interfere with any biochemical reactions nor are affected by (bio)chemical species. Additionally, both functional groups are exchangeable against each other enabling a flexible optimization of the Click reaction.

Although these modified UCNPs can be used as labels in different bioanalytical applications, they are prone to several detrimental effects. Changes, for example in the composition of the nanoparticle surroundings, can lead to enhanced aggregation tendencies, a loss or alteration of the surface functionalities, or accumulation of the nanoparticles, especially in *in vivo* studies. Therefore, the creation of a biomimetic surface by using virus capsids is an approach of great interest to obtain stable nanostructures, so-called virus-like nanoparticles (VLPs)[12, 13]. They combine the extremely high long-term stability, biocompatibility[12, 14, 15] as well as long blood circulation durations of the virus capsids with the unique optical characteristics of UCNPs. The synthesis of these VLPs can be performed according to three different approaches.[12] Firstly, the nucleation and growth of the nanoparticle inside the assembled virus capsid via an introduction of the starting materials; secondly, the attachment of the nanoparticle material to protein parts that later form the inner surface of the

virus capsid; thirdly, the use of a surface-engineered nanoparticle to act as the new nucleation grain to initiate the capsid self-assembly after the removal of the viral RNA[16, 17].

The use of UCNPs as luminescent labels is also hindered by the lack of measurement instruments with a NIR excitation source to detect the upconversion emission in biological systems. Since UCNPs have only recently become commercially available, upconversion devices usually are self-made in most research laboratories. Therefore, the manufacturing and optimization efforts of such devices have to be intensified to enable a more commercial usability of UCNPs. Especially imaging applications with UCNP labels currently rely more on more sophisticated methods such as luminescence microscopy[18-21] or on self-made instruments, especially for whole animal imaging[22-24]. The transfer of scanning measurements of any kind of specimen from these instruments to a commercially available upconversion reader will greatly enhance the rapidity and accuracy of the scan, but foremost the comparability of results from different research groups which is necessary for a standardization of UCNP labels.

The aim of this thesis was on the one hand the creation of virus-like particles (VLPs) with surface-modified UCNPs as the nucleation grains. A variety of modifications, relying either on covalent or non-covalent interactions, were investigated regarding their stability in aqueous systems and thereby their aggregation tendency, any changes in the nanoparticle diameter after the modification, and the strength of the resulting surface charge. As-modified UCNPs with a negative surface charge were decisive for the assembly of virus-like particles (VLP). The concept of Click chemistry, more precisely the copper(I)-catalyzed Huisgen cycloaddition, was also applied on very small UCNPs in order to create a versatile functionalization platform on the nanoparticle surface. This modal functionalization system was suitable for subsequent reactions to generate a negative nanoparticle surface by different functionalities.

On the other hand, this work was focused on adapting and optimizing an upconversion microtiter plate reader for scanning UCNPs in (bio)imaging applications. UCNPs doped with ytterbium and either erbium or thulium were utilized for the instrument optimization as well as for the scanning real sample. The effect of several parameters such as the collecting time, scan point distance and the choice of filters were studied in order to optimize the scanning process. The lateral resolution, the limit of detection, and the signal-to-noise ratio were the most crucial optimization indicators during this process. The optimized scanning mode was applied to real samples by the readout of agarose gel electrophoresis and lateral flow assays. Furthermore, the increase of the UCNP emission by surface plasmon resonance by a gold surface was investigated.

2. Background

2.1 Upconversion

2.1.1 Mechanisms of Upconversion

Upconversion (UC), as described for the first time in the 1960s[5], belongs to the Anti-Stokes processes and describes one way to convert low-energy photons into a photon of higher energy with the others being simultaneous two-photon absorption (STPA) and second harmonic generation (SHG). Similar to other nonlinear optical processes, the upconversion luminescence intensity substantially depends on the power density of the excitation source.[5, 25, 26] However, there are several photophysical features that clearly differentiate upconversion from other processes such as STPA and SHG and render it much more favorably for bioanalytical applications. Firstly, only discrete, metastable and long-lived energy levels are occupied during the excitation process without the need of virtual levels necessary for STPA and SHG (Figure 2.1). Secondly, the absorption of the two excitation photons has to occur simultaneously with almost no possible delay of the second photon both for the STPA and SHG process owing to these distinction of the energy level, whereas UC relies on the sequential absorption of at least two excitation photons with a longer possible delay between the different absorption processes.
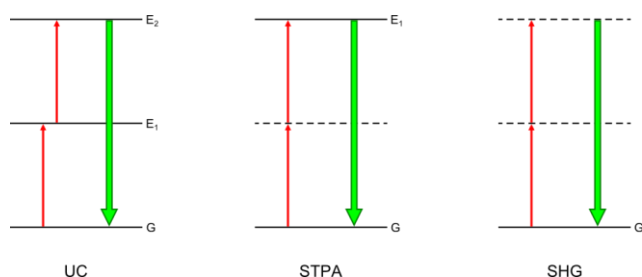
Figure 2.1 Schematic illustration of the two-photon processes "upconversion" (UC), "simultaneous two-photon absorption" (STPA) and "second harmonic generation" (SHG). Solid lines: ground state (G), discrete energy levels ($E_{1/2}$); dashed lines: virtual energy levels; red arrows: absorption; green arrows: emission. The shifted arrangement of the red arrows for UC indicates the sequential photon absorption, while the on-the-line arrangement for STPA and SHG indicates the simultaneous absorption.

Thirdly, the quantum efficiency (η) of the three processes differs significantly, provided the same excitation density is used. While the efficiency for STPA ($\eta = 10^{-13}$) and SHG ($\eta = 10^{-11}$) are quite low, UC ($\eta = 10^{-5}$ - 10^{-3}) shows an efficiency several magnitudes higher depending on the upconversion mechanism. The high influence of the considered upconverting material on the quantum efficiency has to be taken into account for a conclusive comparison as well.[27]

As implied previously, the upconversion process can be ascribed to three mechanisms: excited state absorption (ESA), energy transfer upconversion (ETU), and photon avalanche (PA). After the temporary storage in transition energy levels the accumulated energy of the excitation photons is combined during all three mechanisms to stimulate the emission of higher-energy light, mostly in the visible range.

ESA is the only mechanism taking place in a single ion and thus is independent of the ion concentration (Figure 2.2a). After the absorption of one photon of matching energy to promote the electron from the ground state G to the metastable energy level E_1, a second photon excites the electron to the final energy level E_2. Finally, the emission of a higher-energy photon occurs by an E_2-G transition of the electron.[5, 26, 28]

The ETU mechanism can be derived from the ESA by including a second ion in the excitation mechanism. The precise excitation process can occur according to different excitation sequences and two of them will be described in the following. The first possibility includes the excitation of one electron of each ion to the intermediate energy level E_1 (Figure 2.2b). A subsequent energy transfer from ion 1 (energy donor) to ion 2 (energy acceptor) promotes the electron of the energy acceptor to the emitting energy level E_2, while the electron of the energy donor returns to the ground state G. Again, the transition of the electron from E_2 to G leads to the emission of a higher-energy photon. In the second excitation sequence one ion completely takes over the role as the energy donor while the other one solely acts as the energy acceptor (Figure 2.2c). In two sequential runs the energy donor (ion 2) absorbs a photon, transfers the energy to the second ion (ion 1) and its electron returns to the ground state and thus promotes the electron of the energy acceptor to energy level E_2 resulting in the emission of a higher-energy photon.[5, 26, 28]
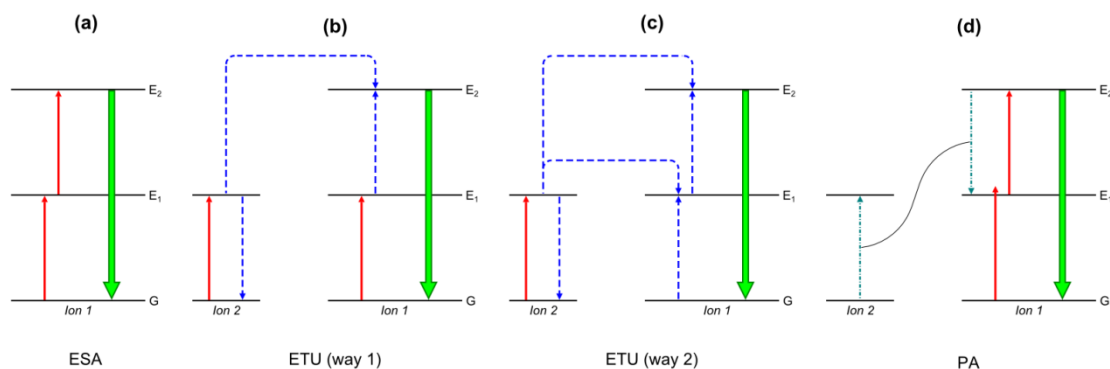
Figure 2.2 Schematic illustration of the different mechanisms mainly contributing to the upconversion process: (a) excited state absorption (ESA), (b/c) energy transfer upconversion (ETU, way 1/2), (d) photon avalanche. Solid red arrows: absorption; dashed blue arrows: energy transfer; dash-dotted teal arrows: cross relaxation; solid green arrows: emission.

The third mechanism PA also employs two ions during the excitation process but a specific threshold of the excitation intensity has to be passed for this mechanism to occur. The first step during the excitation succession is a non-resonant transition of an electron of the ion 1 from G to E_1 followed by a resonant excitation to E_2 (Figure 2.2d). A cross relaxation between this excited ion and a neighboring ion leads to the transition E_2-E_1 in ion 1 and the transition G-E_1 in ion 2. The absorption of an excitation photon can promote both ions to the E_2 level starting the cross relaxation/absorption cycle anew. This "avalanche" process results in an exponential increase of the population of the E_2 energy level and thus enables a strong UC emission after the E_2-G transition of each ion.[5, 26, 28]

The percentage of the overall upconversion emission of each mechanism differs strongly due to their substantially varying upconversion emission efficiency, i.e. quantum efficiency. The energy transfer upconversion (ETU) results in a nearly simultaneous emission after the excitation process without temporal delay which is independent of the intensity of excitation source. In contrast, the emission takes several seconds to occur after excitation for the photon avalanche (PA) process provided a sufficiently high excitation density is given.[5, 28] Although the ESA process features a lower efficiency by a factor of 100 compared to the ETU mechanism, it is still several magnitudes more efficient than other two-photon processes.[27]

2.1.2   Design of Upconverting Materials

The development of upconverting materials requires a sophisticated and thorough tuning of the inorganic material, the so-called host material, the doped ions, and the dopant concentration to obtain a strong upconversion luminescence. While the host material sets the spatial properties of the dopants and the probability of non-radiative processes, the dopant type and its concentration defines the wavelengths of the upconversion emission and the efficiency of the upconversion process, respectively. Especially the number of different dopants strongly influences the upconversion phenomenon, since for an efficient ETU mechanism[5] two ions are necessary, optimally with differing photophysical properties.

Requirements for the host material with declining priority are a high chemical stability to avoid degradation, low phonon energy to avoid non-radiative relaxation of the excited states of the dopants, and low crystal symmetry to enhance transition probabilities during the upconversion process. Various inorganic crystals including oxides[29-38], oxysulfides[39], oxyfluorides[40-42], phosphates[43], and halides[44-50] are usable to create upconverting materials and meet these characteristics differently. Oxides and phosphates show a high stability in most chemically demanding systems but have high phonon energies of above 500 cm^{-1} and above 1000 cm^{-1},

respectively.[28, 29, 51] Oxysulfides show a strong proneness to acidic conditions. The class of fluoride materials bears a special position compared to the heavier halides. While a very low phonon energy (approx. 300 cm^{-1})[51] is typical for all halides, only fluorides are chemically stable[28, 29] and are therefore the materials of choice for most research applications. The importance of the last crucial characteristic mentioned above, the extent of crystal symmetry, can significantly be seen when investigating the two modifications of the fluoride NaYF$_4$, one of the most commonly used host materials so far[52-54]. While the cubic modification (α-NaYF$_4$) creates a dopant environment with a high symmetry, the crystal structure around the various doped ions differs from each other in a host material with the hexagonal modification (β-NaYF$_4$). These differences in the dopant environment strongly influence the transition probability. Its extent increases with rising system asymmetry for specific transitions[26] that are parity forbidden in highly symmetric systems according to the Laporte rule. Consequently, β-NaYF$_4$ has a higher upconversion efficiency by one order of magnitude than α-NaYF$_4$.[55-57]

The central role of lanthanide ions as the dopants of choice for upconverting materials can be attributed to several of their unique and intrinsic characteristics. All lanthanides in nature can occur as trivalent ions (Ln^{3+}). The strongly similar ion radius of these ions to other cations like Na$^+$ and Y^{3+} allows the formation of host materials with less point defects due to doping.[28, 29] Therefore, host materials consisting of these ions with lanthanide doping lead to an enhanced upconversion process compared to other inorganic crystals and thus doped NaYF$_4$ features the highest upconversion efficiency known. Trivalent lanthanide ions with the electronic configuration [Xe] 4f^n (n= 0-14) also show only a weak electron-phonon interaction since the electrons in the completely occupied 5s and 5p orbitals (i.e. 5s^2 5p^6) efficiently shield off the 4f-electrons from the chemical environment.[28, 58] Although the electron transitions between two f-orbitals, i.e. f-f transitions, are parity forbidden according to the Laporte rule, the use of host lattices with a high asymmetry renders these transitions partially allowed and thus increases their probability, as mentioned above.[26] These two electronic characteristics of lanthanide ions result in narrow and sharp f-f transition bands and a long lifetime of the excited states. A prerequisite for lanthanide ions to show upconversion is the presence of more than one excited energy level given the underlying mechanisms ESA, ETU, and PA (Figure 2.2). Almost all lanthanides meet these conditions more than satisfactory with the only exceptions being lanthanum (La^{3+}), cerium (Ce^{3+}), ytterbium (Yb^{3+}), and lutetium (Lu^{3+})[28, 59] and thus can act as activators, i.e. as emitting ions during the upconversion process. The lanthanides erbium (Er^{3+}), holmium (Ho^{3+}), and thulium (Tm^{3+}), in particular, are popular activators. Their ladder-like configuration of the 4f energy levels perfectly enables an efficient upconversion process by photon absorption and energy transfers under single wavelength excitation.[59]

Upconverting materials can be created by singly doping the host material with one of these emitting lanthanides. The resulting upconversion process, however, nearly exclusively relies on the quite inefficient ESA mechanism (Figure 2.2a) and these activators also feature low absorption cross sections. Consequently, only a low upconversion luminescence can be observed for these upconverting materials. A raise of the dopant concentration leads to a higher likelihood of occurrence of the ETU mechanism due to a decrease in the ion distance[21, 60] and may enable an envisaged intensity increase of this emission. The impending quenching effect by cross relaxation between two excited ions at higher dopant concentrations[21, 60-62] yet certainly limits the advantageous effect of this option. Therefore, the level of doping with erbium/holmium or thulium should not exceed 3% and 0.5%, respectively, of the overall lanthanide concentration in the material.[28, 29, 60, 62] This disadvantageous phenomenon clearly diminishes the usefulness of just one dopant to obtain an efficient and thus bright upconverting material.

The co-doping with another lanthanide, a so-called sensitizer, can greatly enhance the upconversion efficiency. These additional dopants ideally feature a significantly larger absorption cross section than the activators whose cross section is generally low[28, 63]. The lanthanide ion ytterbium (Yb^{3+}) with only one excited state may not be of use for upconversion as an activator but this lack of any emitting energy levels predestines it as a highly effective sensitizer. Additional to its high absorption cross section[64, 65] the energy gap between its two energy levels $^2F_{7/2}$ and $^2F_{5/2}$ perfectly matches the excitation photon energy (λ = 980nm) as well as the energy necessary to promote electrons of the activators Er^{3+} and Tm^{3+} to their respective emitting energy level.[52, 65, 66] This condition allows a highly efficient energy transfer to these activators and thus greatly strengthens the probability of the ETU process. In contrast to the activators, the concentration of the sensitizers can be chosen significantly higher, around 15-25% of the overall lanthanide concentration in the material.[28, 60] The resulting upconversion luminescence is by far stronger compared to materials doped with only an activator due to the much higher efficiencies of the ETU and PA process. According to these unique characteristics the doping with both ytterbium (Yb^{3+}) and erbium (Er^{3+}) or thulium (Tm^{3+}) leads to the most efficient upconverting materials known so far. The proposed upconversion process for $NaYF_4$ doped with ytterbium (Yb^{3+}) and erbium (Er^{3+}) or thulium (Tm^{3+}) is given in Figure 2.3.

The upconversion process with erbium as the activator results in emissions in the green and red spectral range. The transitions $^2H_{11/2}$ - $^4I_{15/2}$, $^4S_{3/2}$ - $^4I_{15/2}$, and $^4F_{9/2}$ - $^4I_{15/2}$, are two photon processes and are responsible for the green emissions at 520 nm or 540 nm and the red emission at 655 nm.[67-74] Thulium-doping leads to an upconversion luminescence located at 450 nm, 475 nm, 646 nm, 696 nm, and 800 nm. The blue emissions corresponding to the $^1D_2$ - $^3F_4$ and the $^1G_4$ - $^3H_6$ transitions are based on a 4- and 3-photon process. The emissions in the red and near infrared range rely almost

exclusively on 2-photon processes and are assigned to the $^3F_2$ - $^3H_6$, $^3F_3$ - $^3H_6$, $^3H_4$ - $^3H_6$ transitions, respectively.[28, 29, 67, 68, 74, 75] An exception is the $^1G_4$ - $^3F_4$ transition also resulting in an emission at 646 nm but relies on a 3-photon process.[68, 74-76] The magnitude of luminescence at the different wavelengths strongly differs with the near infrared emission at 800 nm being the strongest and the red emissions at 646 nm and 696 nm being the weakest.[61, 74, 75, 77, 78]
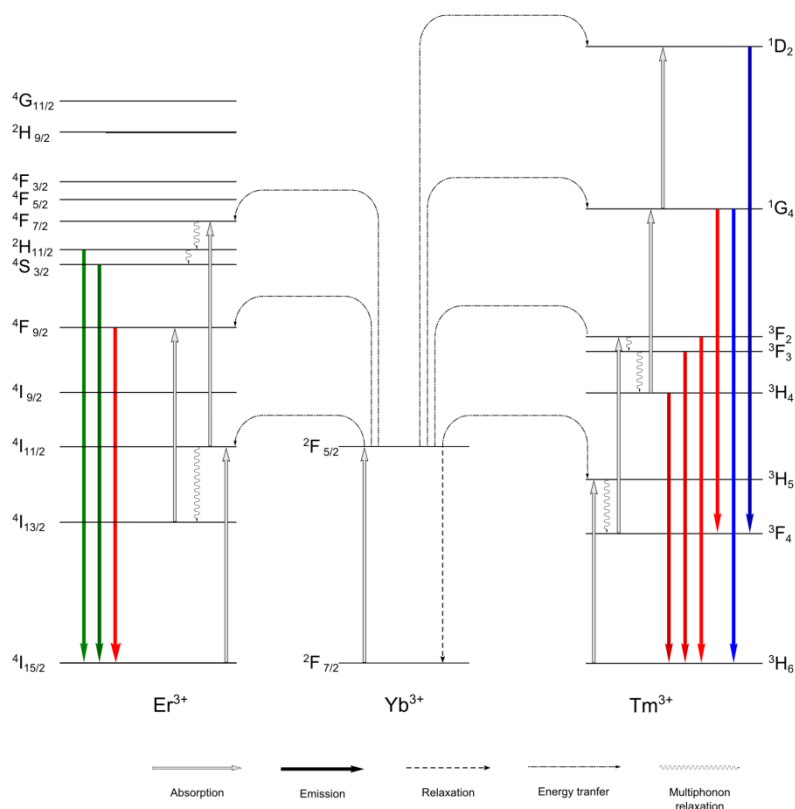
Figure 2.3 Upconversion process with ytterbium as the sensitizer and erbium (left) and thulium (right) as the activators.

2.1.3 Upconversion in the Nanometer Scale

For three decades after the first studies, the practical application of upconversion was limited to the use of the bulk material in form of films, glasses or fibers. Its use was a main focus of research especially in regard of optical devices including solid-state lasers[46, 68], lighting sources[68, 79], and temperature sensors[30, 48]. Thereafter, finally a growing research effort for the development of efficient synthesis routes emerged to obtain upconverting materials in the micro- or nanometer range. Coprecipitation[76, 80, 81], thermal decomposition[82], solvothermal synthesis[83-85], and sol-gel processing[86] yield upconverting nanoparticles (UCNPs). The nanoparticle characteristics including size, monodispersity, shape, surface functionality, or phase modification strongly depend on the type of synthesis and its conditions. UCNPs with a hydrophilic surface, a prerequisite for bioanalytical applications, are obtainable directly during synthesis routes performed in aqueous media such as

hydrothermal synthesis[75, 87-90] or sol-gel processes[38, 86] but these nanoparticles lack a narrow size distribution and a sufficient long term stability in dispersion. Therefore, the synthesis routes such as high-temperature coprecipitation[91-93] and thermal decomposition[82, 94-97] carried out in high-boiling organic solvents like octadecene are favored, since they yield monodisperse and highly stable UCNPs. The necessary control of the nanoparticle nucleation and growth during these synthesis routes is preferentially performed by the use of oleic acid which at the same time acts as capping agent on the surface to stabilize the nanoparticles in dispersion. Other potential agents are trioctylphosphine[98], trioctylphosphine oxide[95], N-(2-hydroxyethyl)ethylenediamine[45, 99, 100], or oleyl amine[101] but they play only a marginal role. Since all these favorable synthesis techniques result in a hydrophobic UCNP surface, subsequent modification steps to create a hydrophilic surface are indispensable for bioanalysis. A short overview on the most common technique is given in chapter 2.2.

Furthermore, UCNPs are the only choice to use upconversion luminescence as a detection signal in (bio)analysis, since an efficient interaction with biological targets with a high selectivity and sensitivity is only feasible on the nanoscale, the same size dimension as most biomolecules. However, as the size of the upconverting material is reduced, surface-related effects are amplified due to an increasing surface-to-volume ratio. Most of these effects lead to a decrease of the upconversion emission intensity owing to an enhanced probability of non-radiative relaxation. Energy migration via lanthanide ions from the nanoparticle center to the surface[56, 71], point defects of the crystal structure of the host material at the surface created by lanthanide doping[102-104], or the high vibrational states of surface-bound molecules matching the phonon states of the host material[103-105] can be considered as reasons or promoters of this detrimental impact on the upconversion luminescence. Especially water with its two O-H bonds show high vibrational states and thus has a stronger quenching effect than organic compounds being either solvent or capping molecules.[106-109]

There are some preventive measures against this quenching including the growth of an pure host material shell, a so called inert shell, on the UCNP surface[105, 106, 110, 111] or the use of bulky or branched surface ligands[112]. While the first approach increases the distance between the doped lanthanide ions and capping molecules or disrupts the energy transfer to the surface[56, 71, 107, 113], the second option entails an improved shielding of the actual UCNP surface from solvent molecules, especially water in aqueous systems. The increase of the UCNP diameter is one of the most apparent options to improve the brightness. However, its benefit for bioanalysis is limited despite the consequent reduced impact of quenching effects on the detected luminescence signal. Especially smaller UCNPs are favorable as labels for bioanalytical applications since they exert only a very low influence on cellular structures. The cellular uptake mechanism such as endocytotic or paracellular

uptake also strongly depends on the particle size.[114-116] Consequently, a compromise between the brightness and the (bio)applicability of UCNPs has to be found.

In the last years the influence of nanomaterials on the environment and especially on the health of living organisms, the so called cytotoxicity, became more and more an object of interest both for researchers as well as for the general public.[117] The prominent example asbestos was a promising material for many different areas of application but showed a high cytotoxicity and carcinogenicity due to the presence of micron-sized fibers in the material that are easily released into the air by different processes.[118-120] Therefore, the determination of the cytotoxicity of UCNPs as a new nanomaterial is crucial for bioanalytical applications. Various investigation methods are applied including viability tests of cells[121-126] or small organisms[127] or *in vivo* investigation of the nanoparticle biodistribution[22, 123-125, 127, 128].

2.1.4 Luminescence Enhancement by Surface Plasmon Resonance

The enhancement of the upconversion luminescence is a key topic of research for the optimization of the synthesis and design of upconverting materials. However, nanosized dimensions and a high hydrophilicity of these materials are required, particularly in bioanalytical fields. These necessary nanoparticle characteristics lead to enhanced surface-related effects like quenching which strongly reduces the achievable brightness, as described earlier. In addition to the coating with a shell made of host material, either undoped or doped[129], other materials proved to be useful to both provide a good shielding of the nanoparticle surface from quenchers and to strengthen the emission intensity. The plasmonic enhancement of the upconversion luminescence by noble metals is a method whose usage for bioanalysis just recently became the focus of enforced studies. Surface plasmon resonance describes the coherent oscillation of valence electrons of a metal induced by light.[4, 117, 130-132] This phenomenon has been extensively employed as an analytical measurement signal in the past, especially with the noble metal gold, both in the form of surface layers or nanoparticles.[9, 133-136] The enhancement of luminescence by this phenomenon is well known for different organic fluorophores[137-141] and quantum dots[142, 143] if the metal surface is in close proximity to these luminescent species with the right spatial distance. This rise in intensity can be attributed to an increased radiative rate of the emission or a strengthening of the excitation intensity. These effects can also occur simultaneously and thus combine their impact on the upconversion luminescence.[26]

Recent studies showed that this effect also has a beneficial impact on the upconversion luminescence of UCNPs. There are three major structural designs used during these investigations (Figure 2.4) to take advantage of this enhancement[26]: (a) the deposition of UCNPs on a gold or silver

surface[31, 144, 145]; (b) the attachment of metal nanoparticles on the UCNP surface either by electrostatic interactions[146-152] or by their direct synthesis on the UCNP surface[126, 146, 153, 154]; (c) the design of a nanoparticle structure with a UCNP/metal core, a metal/UCNP outer shell, and a spacing layer of silica[155-159].

(a)   (b)   (c)
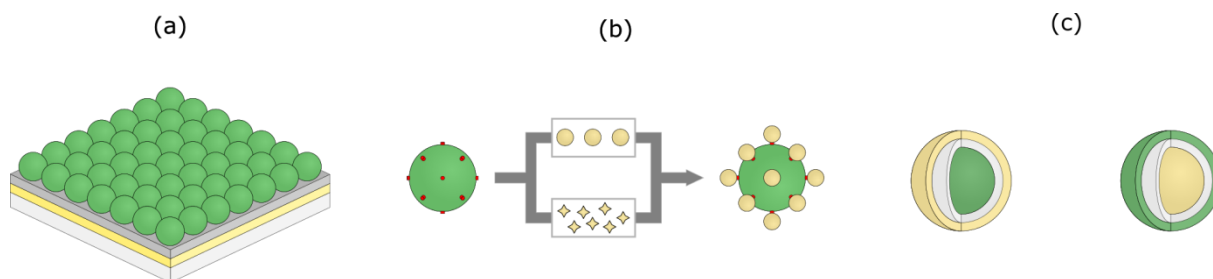
Figure 2.4 Structural designs for plasmon enhancement: (a) deposition of UCNPs on a gold surface with a spacer layer, (b) attachment (top) or direct synthesis (bottom) of gold nanoparticles on the UCNP surface mediated by gold-specific binding sites, (c) coating of an UCNP (left) or gold nanoparticle (right) with a spacer shell on the surface and a second shell made of gold or UCNP material.

All these options lead to an increase of the upconversion luminescence, partially by extremely high factors, but a thorough and efficient optimization of the design is indispensable for such results. While the enhancement obtainable by (a) and (c) depends first and foremost on the optimal distance between metal and UCNP, a precise tuning of the gold nanoparticle surface or the synthesis parameters for (b) is crucial for a successful attachment. All these factors place high demands on the synthesis reproducibility and accuracy of the different structural designs.

In contrast to these enhancement studies, there is also evidence that the surface plasmon resonance may lead to a decrease of the overall upconversion emission.[26, 146, 155, 160] This phenomenon can be reduced to either a resonance energy transfer from the upconverting material to the noble metal or absorption of the upconversion emission by the noble metal.[26, 161] The determination of the quantum yield can indicate if an enhancement or a quenching of the upconversion luminescence is prevalent and may be informative of the nature of the associated causes mentioned before. There are well established methods for fluorophores and quantum dots to obtain this information. However, an unambiguous cause assignment is complicated for UCNPs due to the non-linearity of the upconversion process and thus its dependency on the excitation density.[26, 161] Nevertheless, it is unquestioned that a direct contact or a too close proximity of UCNP and metal strongly promotes luminescence quenching by SPR which again reinforce the necessity of an optimized structure design including a suiting spacer component.

2.1.5   Advantages of Upconverting Nanoparticles for Bioanalysis

Nowadays, organic fluorophores and quantum dots are well established and common luminescent tools for bioanalytical applications. Despite their vast use as probes, labels, or sensor parts they have quite a few intrinsic characteristics which are adverse to their applicability in biological systems. The photophysical and material-related nature of UCNPs addresses several of these drawbacks and thus either eliminates or at least weakens their impact on any potential application. The first advantage of UCNPs in this regard is at the same time one of the most fundamental and representative aspects of the upconversion process: the use of near infrared light as the excitation source. While fluorophores and quantum dots need high-energy UV/VIS irradiation to show luminescence, UCNPs emit visible light upon the absorption of NIR photons, mostly with a wavelength of 980 nm.

The near infrared spectral range between 750 nm and 1000 nm is often referred to as the "optical window"[18, 73, 77, 78, 102, 162-165] whose limit definition can vary about 100 nm. Photons of these wavelengths show only low interaction with biological systems in contrast to UV photons[166] entailing the following benefits of NIR light for bioanalytical applications. Biological species, above all biomolecules such as proteins or oligonucleotides, show no fluorescence under NIR excitation preventing the occurrence of autofluorescence[5, 167-169] which is one of the major problems of the use of UV light in bioanalysis. This virtually zero background fluorescence allows studies with higher signal-to-noise ratio and thus improves the sensitivity and/or resolution of the respective application.[22, 95] Also hardly any photodamage against biological samples by NIR excitation is detectable due to its low energy content. Local thermal damaging, however, may occur due to heating effects[170, 171]. A shift of the excitation wavelength from 980 nm to 800 nm realizable by an additional doping with the sensitizer neodymium (Nd^{3+}) can partly avoid this effect owing to a lower absorption coefficient of water at this wavelength[171, 172]. Furthermore, the penetration depth of NIR light is by far greater than for UV- or visible light ranging from a millimeter to several centimeters[173-176] instead of a few millimeters at most[166, 177, 178] and thus enables the excitation of labels or probes even in subjacent tissue layers[179].

However, since the emission bands of UCNPs are primarily located in the visible range, i.e. outside the "optical window", absorption and scattering phenomena caused by biological species also start to influence the detectability of the luminescence emission signal.[180] An exception is the emission of thulium-doped materials at 800 nm which falls in the optical window and thus can be detected with a relatively high sensitivity.[49, 106, 162] Moreover, there is a significant advantage of the upconversion mechanism regarding the NIR excitation source usable compared to other Anti-Stokes processes. Techniques relying on two-photon absorption, for example, need quite sophisticated and high-cost

excitation sources with very high power density (10^6-10^9 W cm^{-1}) that are predominantly utilized in a pulsed mode to avoid sample damages.[28, 87] In contrast, the use of simple and inexpensive continuous-wave laser diodes as the excitation source with a comparatively low power output density (1-10^3 W cm^{-1}) is both sufficient to induce upconversion and benign for most biological samples.[28, 68, 87, 106, 179]

Luminescent technologies aiming at a long term detection of the target require probes or labels that are compatible with sustained or brief but frequent irradiation intervals and give a continuous signal during excitation. Common organic fluorophores are susceptible to photobleaching, i.e. molecular damages due to intense or prolonged excitation.[20, 181-186] Although quantum dots hardly photobleach over time[3, 28, 187-191], they show an intermittent emission behavior during excitation, so called "blinking"[4, 133, 192, 193], with a dwell time in the dark state of up to several seconds[2, 3]. In contrast, the upconversion emission remains stable without any indication of "blinking".[168, 194, 195] It is also unaffected by NIR irradiation over a longer period of time[23, 168, 171, 194-200] since the luminescence originates from 4f atomic orbitals instead of molecular orbitals[121, 151, 196]. Therefore, UCNPs surpass both organic fluorophores and quantum dots as luminescent labels or probes in long-term studies.[26, 91, 198, 201]

The emission bands of UCNPs, more precisely their respective wavelength, their width and their number, also result in several features favorable for bioanalytical applications. The emission wavelengths remain unaffected by any changes in UCNP diameter[202], whereas the absorption and emission spectra of quantum dots are strongly size dependent[6, 83, 203-205]. The emission bands with a width of approximately 10 nm[206, 207] are extremely sharp and are also well separated from the excitation peak owing to a large Anti-Stokes shift[79, 177]. In contrast, the broad emission bands of organic fluorophores have only a quite small Stokes shift[76]. The most striking characteristic of the upconversion emission spectra, however, is the presence of more than one emission band which enables the use of UCNPs in several important applications. Firstly, the assignment of a specific luminescent code to a sample, also called encoding, allows its direct identification for example in high throughput screening or combinatorial chemistry, especially important in the submicron domain where a purely spatial sample differentiation is impossible.[175, 182, 208, 209] Secondly, a ratiometric measurement exploits the presence of an unaltered upconversion emission as an intrinsic reference to take drifts and fluctuations of the signal into account and to cancel out their influence on the evaluation.[163, 179, 208, 210, 211] Thirdly, multiplexing, i.e. the simultaneous detection of several targets in one system[26, 105], can be realized with UCNPs, since the emission wavelengths of nanoparticles with different dopings are spectrally well separated and thus allow an unambiguous detection signal differentiation.[83, 91, 212-219]

As has been mentioned earlier, a low cytotoxicity and thus a high biocompatibility are decisive for the use of luminescent nanomaterials in bioanalysis. Beside its many favorable characteristics, one of the major disadvantages of quantum dots is their harmful effect on biological systems. The most popular material for the quantum dot synthesis, CdSe, is highly susceptible to (photo)oxidation initiated by either air or UV irradiation necessary for excitation.[3, 4, 204, 220, 221] The heavy metal ion Cd^{2+} released by this process has been found to be extremely cytotoxic[204, 220-222]. Although this release can be reduced by the growth of a shell made of a material either less susceptible to (photo)oxidation like ZnS or CdS[3, 220, 221, 223] or inert like silica[224], long-term studies are indispensable to prove a potential improved biocompatibility and thus applicability in bioanalysis[2, 192, 204]. In contrast, most host materials of UCNPs have a low cytotoxicity as has been shown for ligand-free UCNPs made of Y_2O_3 [79]. However, since hardly any UCNPs without any surface ligands or shells are used in bioanalytical applications, the surface composition is most decisive in this regard provided no detachment or degradation of the surface occurs during application. The range of investigated surface functionalities includes among others small molecules such as citrate[123], polymers such as polyacrylic acid (PAA)[57, 125, 225], polyethylenimine (PEI)[178], or polyethylene glycol (PEG)[166], biomolecules such as folic acid[199] or oligonucleotides[126], and additional shells such as pure or silanized silica[121, 128, 183, 184, 226]. All these studies give evidence of a low cytotoxicity independent of the surface rendering UCNPs suitable for bioanalytical applications.

2.2   Surface Modifications of Upconverting Nanoparticles

The hydrophobic character of UCNPs originating from the reaction conditions during most favored syntheses is one of the major challenges that have to be overcome for UCNPs being usable as labels or probes in bioanalysis. Additionally, any surface changes should not affect the desired high monodispersity and long-term dispersion stability obtained after a research-intensive and time-consuming process of synthesis variations and optimizations. Therefore, modification methods have to be found that yield modified nanoparticles void of any aggregation tendencies. The countless publications and the magnitude of excellent reviews[53, 91, 169, 182, 207, 226-228] about the surface modification and functionalization of UCNPs from different point of views clearly shows the elevated efforts of research groups in this aspect of UCNP studies. Therefore, only a short insight in a few modification options that were used during this thesis is given in this chapter.

2.2.1 Silica Coating

Silica is one of the most popular materials in nanoscience to create nanoparticles[7, 8, 229-237] or an additional shell on a foreign nanoparticle surface including quantum dots[6, 224, 238], metal oxide nanoparticles[181, 239-243], noble metal nanoparticles[131, 132, 244, 245], or UCNPs[128, 165, 183, 184, 246]. This favoring of silica in nanosciences, especially in regard to surface coating with an adequate layer thickness, can be attributed to its high chemical inertness[6, 229, 241, 243], hydrophilicity[235, 236], and the increase of the nanoparticle dispersibility in aqueous systems[8, 78, 80, 128, 165]. The high transparency[247] of silica, a premise for its use as a modification material of luminescent compounds, is particularly pronounced in the NIR region enabling an unaltered excitation of silica-coated UCNPs by light at 980 nm or similar wavelengths[51, 248]. Additionally, the upconversion emission in the visible range is only slightly affected by the coating due to scattering[249]. The high biocompatibility[165, 184, 229, 250], non-toxicity[231, 239, 250], and potential prevention of non-specific binding[78] of biological species justifies the popular use of silica in diverse biological applications as a coating material. Another more application-related advantage of silica is its potential functionalization with a well established and versatile process, the so called "silanization", which will be described in chapter 2.2.2.

There are a great number of methods to cover nanoparticles with a silica shell that are primarily based either on the Stöber process or the microemulsion technique. Although the Stöber process was one of the first synthesis routes for pure silica nanoparticles[7], its applicability can be extended by respective modifications to also grow a silica shell on a hydrophilic nanoparticle surface.[10, 51, 80, 251] However, since most synthesis routes for UCNPs nowadays yield nanoparticles with a hydrophobic surface, the microemulsion technique (Figure 2.5) clearly is more important in research and application than the Stöber process for the growth of a silica shell on the UCNP surface.
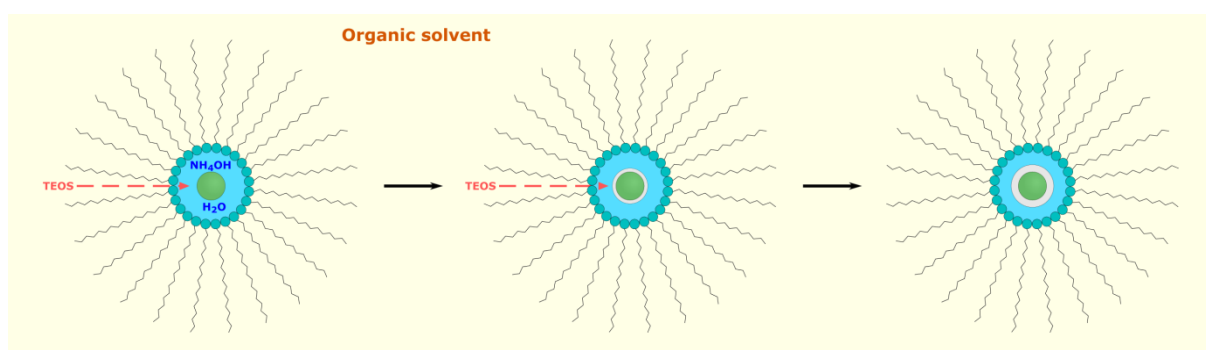
Figure 2.5 Scheme of the microemulsion process in three steps: (1) the formation of reversed micelles in an organic solvent by the detergent encompassing an aqueous ammonia solution, (2) Diffusion of TEOS molecules into the micelles and their hydrolysis initiating the growth of a silica shell, (3) growth of the silica shell by further TEOS hydrolysis until complete consumption.

The central element of this technique is a reversed micelle formed by a detergent in an organic solvent, e.g. cyclohexane. An added tetraalkyl silicate like tetraethyl orthosilicate (TEOS) is hydrolyzed by an aqueous ammonia solution inside of these nanoreactors and forms the silica shell on the UCNP surface by polycondensation. The original hydrophobic surface ligands remain in the organic solvent. The amount of detergent defines the micelle size which should be just slightly larger than the nanoparticle to ensure an inclusion of only a single UCNP in the reversed micelle.[247] Additionally, the thickness of the resulting silica shell can be adjusted by the amount of the tetraalkyl silicate added[56, 244, 252]. This parameter is especially important for distance-dependent phenomena and their use in (bio)analytical applications. A relatively thin layer, for example, is required to ensure an efficient luminescence resonance energy transfer (LRET) from a UCNP to surface-bound dyes[78].

Although a coating of UCNPs by a silica shell introduces a variety of advantageous characteristics, it may also be responsible for enhanced aggregation of the modified UCNPs. As mentioned before, the micelle size sets the number of UCNPs encapsulated in its cavity and thus multicore encapsulation by silica may occur if the detergent concentration is inadequately low resulting in larger or non-spherical micelles.[240, 247, 253] This incorporation of more than one UCNP in a silica shell leads to a higher polydispersity of the nanoparticle dispersion[254] which counteracts the optimization efforts for synthesis routes yielding highly monodisperse UCNPs. Additionally, dispersions of silica-coated UCNPs can show an increased aggregation tendency due to the large surface area and hydrodynamic radius of the modified nanoparticles.[8, 166] The choice of the dispersant composition strongly influences this tendency and an optimization is crucial for the respective silica-coated nanoparticle with a special focus on pH and ionic strength of the dispersant.[69, 255] An easier and more favorable way to reduce aggregation of the silica-coated UCNPs in dispersion is a functionalization of the silica shell by silanization.

2.2.2 Silanization

For many bioanalytical applications, UCNPs have to be equipped with functionalities allowing a directed labeling, also called targeting, or a selective recognition of the respective analyte. Biomolecules like oligonucleotides, proteins, or antibodies are capable to meet these functions and can be easily attached to a silica surface by physical adsorption. However, a higher control over number and orientation of bound biomolecules is desired for most applications. Covalent binding processes provide a good regulation of the final number of biomolecules by preset binding sites and a high accessibility of the biomolecule's active site. Furthermore, covalently bound functionalities cannot detach from the nanoparticle surface during application. Consequently, a high control over the biomolecule attachment can be exerted by these processes. The silanol groups are not accessible

for the direct binding of biomolecules by common linkage reactions and thus a modification with suitable functional groups by silanization is indispensible for the use of silica-coated UCNPs in bioanalysis. This functionalization can be performed either subsequently or simultaneously to the silica shell growth. During the silanization process the alkoxy groups of a silane with the desired functionality are hydrolyzed and condensate to the silanols on the silica surface.

Amine and carboxylic functionalities are among the most popular binding sites for the attachment of biomolecules due to their great number in biomolecules and the well-established and understood activation with N-hydroxysuccinimide (NHS) and 1-ethyl-3-(3-dimethylaminopropyl) carbodiimide (EDC).[20, 248, 256] The positive charge of amines present at physiological pH leads to strong aggregation due to the strong electrostatic attraction of amines with the partly negatively charged silanol groups of the silica shell. A conversion into carboxylic acids via anhydrides[218] or the simultaneous silanization with longer-chained or bulkier silanes with negative or neutral head groups[8] are two options to minimize this attraction. In contrast, UCNPs functionalized with carboxylic acids are well stabilized in dispersion by electrostatic repulsion due to the intrinsically negative charge of these groups at physiological pH.

Although the abundant presence of amines and carboxylic acids in biological systems can be favorable for a magnitude of bioanalytical methods, their selective labeling *in vitro* or *in vivo* becomes extremely complicated or even impracticable. Functionalities with a high bioorthogonality prove to be convenient substitutes. They enable a binding process which does not interfere or interact with biological processes or species[11] and can still be simply performed with a high selectivity. The bioorthogonal organic azides and terminal alkynes, the components of the copper(I)-catalyzed Huisgen cycloaddition[257-259], can easily be brought onto a surface of silica-coated UCNPs by silanization and are highly selective binding sites for (bio)molecules carrying the complementary functionality.

A way to alter the optical properties of UCNPs takes advantage of the simple and reliable silanization process by binding fluorophores to the silica surface.[183] A radiative or non-radiative energy transfer from the UCNP to the bound fluorophore under NIR irradiation[92] enables the tuning of the UCNP emission and thus the creation of nanolamps with an emission spectra customized for the respective application. In contrast, the additional excitation of the fluorophore with the respective UV/VIS light provides a downconversion emission usable as an additional detection signal for multimodal readout. Furthermore, this emission can also act as a signal substitute for the upconversion emission. This surrogate detection signal is especially necessary if no instruments with a NIR excitation source for UCNPs are available and applications, for example the imaging electrophoresis gels[260], are thus strongly complicated or even impossible.

2.2.3 Ligand Exchange

In contrast to the growth of a silica shell, a ligand exchange relies completely on non-covalent intermolecular interactions between the UCNP surface and hydrophilic molecules, similar to the interaction of the size-controlling and surface-capping agents during synthesis such as oleic acid. Both the original and new surface ligands with their negative moieties take advantage of the intrinsic positive surface charge of UCNPs originating from the doped trivalent lanthanide ions. The arising electrostatic interactions are by far stronger than other intermolecular interactions. According to this beneficial but not mandatory characteristic, hydrophilic species are favorably used for ligand exchange that show at least one negatively charged functionality under the exchange conditions, mostly acidic molecules or polymers. While this so called headgroup coordinates to the UCNP surface, the second functionality present in the new ligand defines the hydrophilicity of the UCNP, their dispersibility in the respective solvent, and their interaction with their chemical or biological surroundings. Consequently, citrate[58, 123, 194, 261] and polyacrylic acid (PAA)[56, 112, 125, 146, 262-266] are among the most favored surface ligands suitable to create hydrophilic UCNP surfaces by ligand exchange, but also other carboxylic acids[124, 225, 267, 268] or derivatives of polyethylene glycol[101, 106, 107] are objects of research in this regard.

A desired complete replacement of all hydrophobic by hydrophilic ligands requires the optimization of various process parameters including temperature, ligand concentration, and solvent composition. While elevated temperatures aligned with the thermal stability of the new ligand and the addition of the hydrophilic ligand in excess is sufficient for an optimization regarding the first two parameters, the solvent composition has to be chosen carefully. Additional to a high dispersibility or solubility of the hydrophobic UCNPs and the hydrophilic ligand, respectively, the attachment/detachment equilibrium of the hydrophobic and hydrophilic ligand, i.e. the dynamic solubility in this solvent system, should favor a complete exchange.[267] Furthermore, some ligand characteristics can be exploited to force a completion of the ligand exchange process. Differences in the coordination ability of the ligand functionalities have a strong impact on the exchange efficiency. The exemplary functionality pair carboxylic acid/amine shows a higher coordination strength of the acid to the nanoparticle surface compared to the amine. Also the number of coordinating groups is decisive resulting in a preference of multidentate over monodentate ligands.[267]

The treatment of hydrophobic UCNPs with $NOBF_4$ in dimethylformamide (DMF) presents a type of ligand exchange that features a high dispersion stability of UCNPs over extended periods of time, simple performance, and high process versatility regarding the final surface functionality.[269] The original nanoparticle dispersion is simply mixed with a solution of $NOBF_4$ in DMF leading to a

replacement of the hydrophobic surface ligands by BF_4^- anions and thus to a phase transfer. The resulting "naked" UCNPs are stabilized by these anions with the assistance of DMF molecules with a long-term stability of several years.[269] UCNPs with the desired hydrophobic or hydrophilic surface functionality can be derived from this stable dispersion by again simply mixing the nanoparticle dispersion with a solution of the respective surface ligand in a solvent immiscible with DMF. Both ligand exchange processes can be performed at room temperature with a procedure duration of only a few minutes.[269] The simplicity and briefness of this process clearly proves the favorability of the $NOBF_4$ method compared to other ligand exchange techniques needing strongly elevated temperatures[58, 106, 112, 125, 267], performance times between a few hours and several days[107, 191, 255, 270], and in some cases even a protective atmosphere[56, 162, 266].

2.3 Click Chemistry

2.3.1 Concept of Click Chemistry & Click Reactions

The term "click chemistry", firstly defined by Sharpless et al in 2001, describes a concept imitating nature that uses modular and selective building blocks to develop larger molecular structures.[271] The chemical reactions forming the necessary heteroatom bonds have to meet several criteria to be suitable for the "click chemistry" concept and thus can be termed "click reaction". Modularity, wide scope, high stereospecificity are expected as well as high yields of the resulting product without any offensive byproducts. The reaction process must feature a simple implementation, ideally without a susceptibility to water or air, readily available starting materials and reagents, no or at least benign solvents (e.g. water), and finally a facile product work-up and purification by non-chromatographic methods, for example distillation or crystallization.[271-274]

Most "click reactions" known at present rely on carbon-heteroatom bonding during their process demonstrated in the following examples. Suitable cycloadditions of unsaturated components include 1,3-dipolar types such as the Huisgen cycloaddition[271, 272] or hetero-Diels-Alder reactions[271, 272, 275]. Furthermore, nucleophilic substitution, especially in form of ring-opening reactions of strained heterocycles such as epoxides or aziridines[271, 272], or non-aldol carbonyl reactions like the formation of urea, thiourea, aromatic heterocycles[271, 272, 276] can be ascribed to the "click chemistry" concept. Finally, the addition to carbon-carbon multiple bonds can be used for example in form of epoxidation[271, 272], dihydroxylation[271, 272], aziridination[271, 272, 277], or nitrosyl and sulfenyl halide additions[271, 272].

Additional to a "click chemistry" assignment some of these examples can also be called "bioorthogonal reactions" rendering them favorable for bioanalysis, especially for *in vitro* and *in vivo* applications. According to the concept of "bioorthogonal chemistry"[278] these reactions neither interact nor interfere with biological processes and show fast kinetics, especially under physiological conditions, to ensure a sufficient product formation even with low reactant concentrations. Additionally, the participating functionalities should form a stable covalent bond, be nontoxic and inert in regard to the multitude of functional groups in biological systems such as water, reductants, nucleophils or other moieties of biomolecules.[11, 278] Especially small functionalities are of great interest, since they can be easily introduced in biological systems as "chemical reporters" to form the bioorthogonal binding sites in (bio)molecules. However, this artificial modification should be free of any structural perturbation to avoid detrimental impacts on the natural bioactivity of the molecule.[11, 278]

Organic azides and terminal alkynes as reactive groups clearly meet the conditions set by the "bioorthogonal chemistry" concept. Their corresponding reaction, the copper(I)-catalyzed Huisgen cycloaddition, is the classic example of the "click chemistry" concept explaining the synonymous use of the term "click reaction" for this specific reaction type[274]. This simultaneous suitability for both demanding concepts highlights this reaction type as a convenient method for a variety of bioanalytical applications.

2.3.2 Huisgen Cycloaddition

The family of 1,3-dipolar cycloadditions was firstly described in detail by Huisgen[257] in the 1960s and includes a wide variety of potential functionalities. Organic azides and terminal alkynes are among the most prominent functionalities that undergo a 1,3-dipolar cycloaddition which is also called Huisgen cycloaddition due to his clarification of the mechanism involved and it is shown in Figure 2.6.
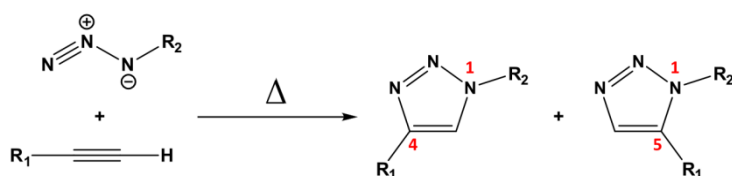
Figure 2.6 Huisgen cycloaddition of organic azides and terminal alkynes.

However, the necessary elevated temperature, long reaction times and low regioselectivity[259, 279, 280], apparent in the obtained 1:1 mixture of 1,4-disubstituted and 1,5-disubstituted 1,2,3-triazoles, prohibit the assignment of the native Huisgen cycloaddition to either the "Click chemistry" or the "bioorthogonal chemistry" concept. The independent discoveries of Sharpless et al[259] and

Meldal et al[258] showed that a catalysis of the cycloaddition by copper(I) ions drastically changes the reaction characteristics for the better. This copper-catalyzed azide-alkyne cycloaddition (CuAAC) features a reaction performance at room temperature[258, 259], a reaction acceleration[281, 282] by a factor of 10^7-10^8 enabling a reaction performance in a few hours, and high regioselectivity for the 1,4-disubstituted triazole[258, 259, 272, 274, 280, 282]. Additional to these characteristics rendering the CuAAC a "bioorthogonal reaction"[278], the high yield, the wide scope, the magnitude of usable solvents, and the simple work-up and purification process clearly demonstrates the high suitability of the reaction for the "Click chemistry" concept.[259, 281, 282]

The mechanistic aspect of the CuAAC process has been studied thoroughly.[259, 282] According to Sharpless et al[259] the stepwise process is clearly favored compared to a concerted 1,3-dipolar cycloaddition. Therefore, this mechanism will be explained by means of a schematic illustration of the catalytic cycle, given in Figure 2.7.
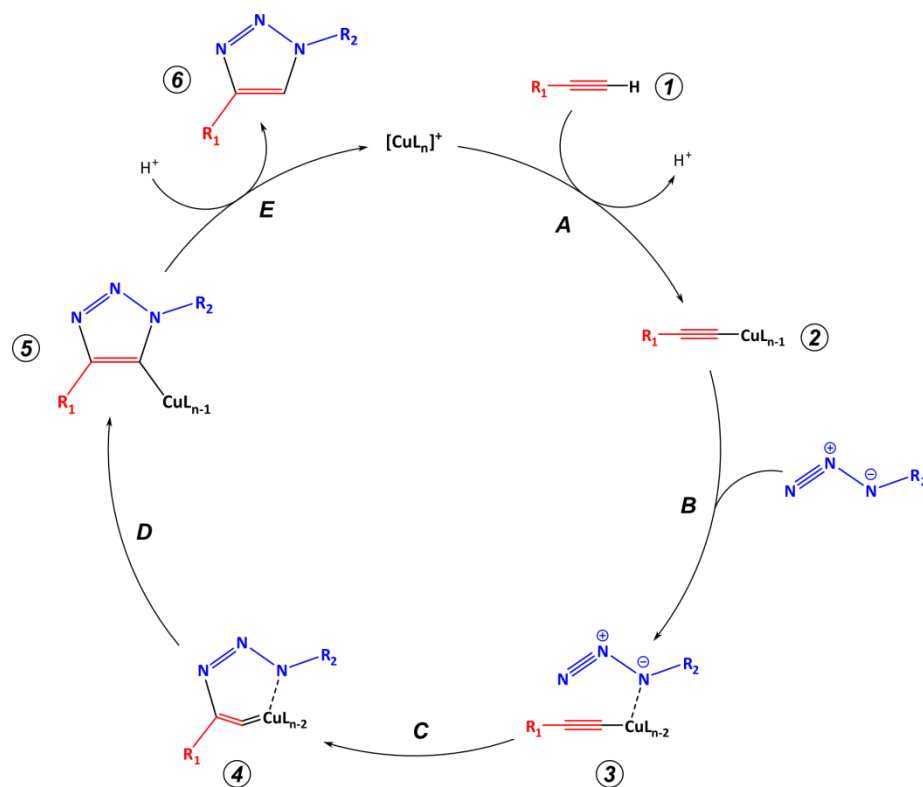
Figure 2.7 Stepwise mechanism of the copper-catalyzed azide-alkyne cycloaddition (CuAAC)[259]; the different mechanism steps and intermediates are indicated by letters or numbers; for a better recognizability the azide and alkyne functionalities are depicted in blue and red, respectively.

The formation of an acetylene π-complex by the Cu(I) species strongly decreases the pk_a of the C-H group[282] of the acetylene. This initiates the first step (**A**), the deprotonation of the terminal acetylene ①, to form the acetylide ②. Subsequently, a ligand exchange (**B**) occurs between one ligand of the Cu(I) complex and the organic azide whose nitrogen proximal to the carbon coordinates

to the Cu(I) ion resulting in species ③. Hereafter, a Cu(III)-containing metallacycle ④ is formed by the attack of the C-2 of the former acetylide by the distal nitrogen of the azide (**C**). The following ring contraction (**D**) results in the triazolyle derivate ⑤ which is converted in the final triazole product ⑥ by a proton transfer (**E**) and the Cu(I) complex is regenerated for a new catalytic cycle.

The catalyzing effect of Cu(I) ions can be utilized by either an addition of a Cu(I) salt like CuI or an *in situ* generation via the reduction of Cu(II) ions by a reducing agent. Especially the combined use of $CuSO_4$ as the Cu(II) ion source and ascorbic acid/sodium ascorbate as the reducing agent clearly is favorable compared to Cu(I) salts due to lower costs, higher purity, and no solvent limitations.[259, 282] However, the use of ascorbic acid still holds some problems, since the formed dehydroascorbate and other reduction byproducts readily react with biological moieties. The reaction with the side chains of the amino acids lysine and arginine, for example, enhances the aggregation tendency of the protein due to a covalent modification.[283-285]

The azide and alkyne functionalities themselves show a high metabolic stability, more precisely an inertness towards common biological functionalities[273, 278, 280, 286-288], observable in the lack of any side reactions[259]. There is also no need for protecting groups for these functional groups during other binding processes and protecting groups for common biological functionalities are unaffected during the CuAAC reaction.[10, 258, 274, 289] Despite the applicability limitation to terminal alkynes[258] the CuAAC is one of the few reactions considered both a "bioorthogonal reaction" and a "click reaction". However, the introduction of the Cu(I) catalyst also gives rise to new problems, both during the CuAAC process itself and for its applicability in biological systems. Firstly, Cu(I) ions are prone to oxidation by atmospheric oxygen[258, 282, 283, 290] and therefore a stabilization of Cu(I) by suiting ligands[283, 291-294] is advisable to ensure an unaffected catalytic activity. This approach can even be beneficial for the reaction kinetics by reaction acceleration provided an appropriate optimized ligand is used.[291, 294-296] Secondly, the high cytotoxicity of copper[273, 287, 297] completely precludes the use of the CuAAC in any living organisms such as living cells[286, 298, 299], bacteria[298] or animals[299] from the start. Again, a complexation of the Cu(I) ion can minimize this undesired impact on the *in vivo* applicability but also the replacement by other metals can counteract this restriction.[281, 289, 290, 296, 300] A Ru(II)-based complex, for example, greatly catalyzes the Huisgen cycloaddition generating exclusively the 1,5-disubstituted 1,2,3-triazole[279] but requires again elevated temperatures rendering this alternative useless for biological applications. A complete metal-free version of the CuAAC utilizes strained alkynes[273, 286, 287, 298, 299, 301] such as cyclooctyne. Their acceleration effect originates from deformation of the bond angle of the acetylene in these compounds.[302] An optimization of the cyclic alkyne, e.g. by fluorination, allows to achieve a reactivity similar to the

CuAAC process.[287, 288, 297, 299]. Furthermore, a sequential modification process can be envisioned by using copper-free and copper-catalyzed cycloadditions[288].

The high efficiency and simplicity strongly highlights the use of the CuAAC to create a highly flexible and versatile platform on the surface of UCNPs enabling an easy and modulate attachment of a wide variety of different (bio)molecules. Therefore, focuses of this thesis included also the feasibility to introduce azides or terminal alkynes by silanization on silica-coated UCNPs and the efficiency of a subsequent coupling reaction via the CuAAC of these as-modified nanoparticles.

2.4   Virus-Like Particles

2.4.1 Viruses

Viruses are omnipresent in nature occurring in bacteria, fungi, plants, and animals[303-308] and represent the second largest share of biomass on earth, only surpassed by prokaryotes[303, 308, 309]. A classification of the vast and still growing number of viruses can be based on the host organism, virus morphology, replication method, or genome organization[303, 310-312] and leads to more than 90 families[12]. Their basic blueprint always includes a protein cage, the virus capsid, and a nucleic acid core.[12, 313] Additional to this simple components the viral structure can also feature a lipid bilayer which envelopes the capsid and originates from the host[12, 303] or a multi-piece protein tail system which are predominantly present in eukaryotic viruses and bacteriophages, respectively. The viral genetic information can be stored in single- or double-stranded (ss and ds) RNA or DNA. The respective nucleic acid strand can be either linear or circular and may be split into several smaller parts instead of a complete single strand.[303, 314] These oligonucleotides can be either of positive(+) or negative(-) sense.[303] A direct translation into viral proteins is realizable if the strand is of positive-sense. In contrast, a prior conversion into the translatable positive-sense by a polymerase is required when a negative-sense is present. The number of proteins encoded by the genome can range from a few to several hundred different species[303] Among these proteins the class of capsomers are given the task to form the virus capsid by self-assembly of a defined number of proteins[12, 313, 315]. This capsid provided with specific functionalities by the capsomers is responsible for genome protection, host recognition, cell attachment and entering, viral gene release, and formation and externalization of virions, the mature form of the virus[303, 313, 314]. The possible symmetry of these protein cages includes icosahedral, helical, or more complex and it is ultimately defined by the genetic material contained owing to the dependence of the decisive factors such as capsomer composition and dimension of the nucleic acid on it.[12, 316, 317] Furthermore, this symmetry

together with the respective capsomers dictate the outer appearance of capsid leading to a quasi-spherical (icosahedral) or a rod-shaped (helical) characteristic, for example.[12]

The brome mosaic virus (BMV) belonging to the Bromovirus genus, family Bromoviridae is the first plant virus with a split ssRNA whose genetic information was decoded.[318-321] Four positive(+) strands constitute the genome and store the blueprint for replication-related capsid proteins.[14, 317, 321] The icosahedral capsid with the symmetry-defining triangulation number T = 3[322, 323] consists of 180 capsomers with a protein mass of 20 kDa.[14, 323-325] The hexameric and pentameric substructures of the icosahedron are built by the self-assembly of preliminary formed capsomer dimers.[14, 317, 323] The resulting quasi-spherical virus capsid has an overall diameter of approximately 28 nm with an inner cavity of 18 nm (Figure 2.8).[317, 321-323]
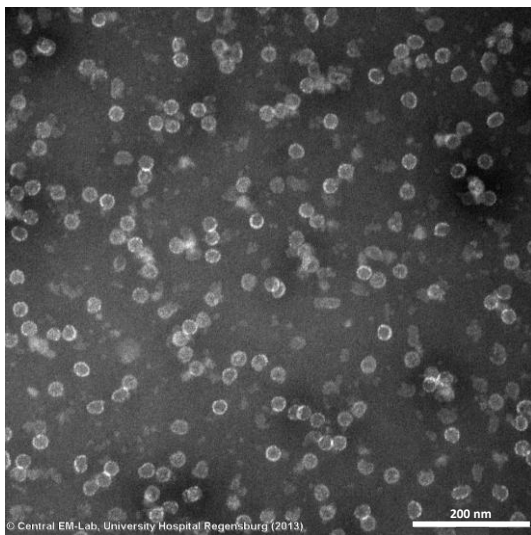
Figure 2.8 TEM image of brome mosaic virus (BMV) in their native form (100,000x magnification, scale bar: 200 nm).

The self-assembly process is initiated by electrostatic interaction of the RNA with the positively charged basic amino acid residues of the capsomers forming the cavity interface[14]. The subsequent formation and stabilization of the resulting capsid is driven by weak interactions of capsomers with each other[14, 313, 324] and the nonspecific interaction between the RNA and the capsomers[317, 326]. A swelling and thereby a permeability of the capsid can be induced by pH changes as for all viruses that finally leads to a breaking of the capsid. While the capsid remains closed and stable around pH 5 and a moderate ionic strength of the solvent, it swells during a pH increase to 7 with a potential stabilization by Mg^{2+} ions until finally the capsid breaks after passing the threshold of pH = 7.5 and an ionic strength of 0.5 M.[317] However, the broken capsid can easily be reassembled by a reduction of the pH and ionic strength provided the unaffected RNA or a suiting substituent is present.[317, 324, 327]

2.4.2 Definition of Virus-Like Particles

Viruses or more precisely their capsids were brought into the spotlight of research as a potential platform for a multitude of applications thanks to their intrinsic properties. The consequential preparation of so-called virus-like particles (VLP) addresses different capsid parts for the process including the cavity, the inner or the outer surface. Generally, these nanostructures can be described as virus capsids devoid of its genome with a potential replacement by non-genomic material. Consequently, they take advantage of the many outstanding features of capsids mentioned above for practical applications without any restrictions implied by the genome such as recombinogenic mechanisms.[12, 309, 314] In the following some of the most striking advantages of the virus capsid are outlined in respect to their usefulness for an application as VLPs.

The generation of monodisperse and uniformly sized nanostructures with high reproducibility and symmetry is one of the greatest challenges in nanoparticle synthesis but is already intrinsically established in the capsid with no need for optimization.[13, 309, 315, 328-333] The capsid represents a biocompatible and flexible surface that shows excellent formability as a response to external influences.[12-14, 309] While its closed form efficiently protects its cargo from any adverse effects caused by the outer media[13], changes in pH lead to a permeability of the protein cage and allows a material exchange between the interior and the exterior of the virus, the so-called "gating"[12, 17, 309, 334]. This mechanism is crucial for the use of capsids as nanoreactors or as transportation vehicles, since it enables a loading with materials like the starting material for nanoparticle synthesis, therapeutic molecules, or imaging agents and a selective release at the envisioned destination.[13, 17, 309, 335] The involved swelling of the virus capsid, however, may lead to changed capsid symmetry or appearance, i.e. a hysteresis is possible.[336, 337]

Furthermore, multivalent binding sites that originally have the task to specifically recognize the host cell surface or to avoid immune response of the host are intrinsically installed on the inner and outer surface of the capsid with the same chemical environment. Their identical reactivity facilitates a significant enhanced interaction with the target compared to monovalent systems.[309, 317, 338-341] The exterior binding sites ensure a potential targeting mechanism and accessibility for modifications, partially crucial for refined target recognition. In contrast, the inner functionalities can be used as specific access points for the covalent cargo attachment or as initiators of a crystallization process, more precisely the generation of a nanoparticle inside the capsid.[12, 13, 15, 17, 342-344]

The capsomers providing both the inner and outer functionalities are less prone to denaturation or proteolytic cleavage compared to other proteins.[328] Their inducible dis- and reassembly[13, 327, 345] with a high reproducibility, mostly at neutral pH and high ionic strength[346], enables an efficient

encapsulation of both genomic and non-genomic material such as polymers or nanoparticles. In addition, the possible assembly of empty capsids, for example at lower pH and ionic strength[346], allows the creation of nanoreactors or transportation vehicles.[17, 309, 347] Since the amino acid sequence of the capsomers is encoded in the viral genome, selective engineering of the capsid can be achieved by the established methods such as mutagenesis.[12, 15, 309, 314, 348, 349] In this way, introducing new functionalities like polypeptides or changes in the capsid architecture, e.g. tubes or planar sheets instead of icosahedrons, can be realized as a part of a "tailoring" of the capsid characteristics optimized for the respective (bio)application.[14, 314-316, 324] Going one step further, even artificial virus capsids can be engineered showing most of the native viral characteristics but allow an even more directed and sophisticated optimization of the protein cage for the respective application.[350, 351]

These beneficial characteristics, either intrinsic or introduced by genome engineering, allowed the creation of virus-like particles (VLPs) from a variety of different virus capsids that feature the same physicochemical properties as the respective native virus.[313, 328, 338, 352-355] Especially capsids of RNA viruses excel as the biological component for the VLP generation due to two reasons. Firstly, their self-assembly is thermodynamically well understood. Secondly, the electrostatic interaction of the positively charged inner capsid interface with the negative charge of the core is predominantly non-specific which allows a certain leeway in terms of the choice of the encapsulated cargo.[12, 317, 356] Also the structural flexibility of a RNA virus capsid entails a significant adaptability to the size of the non-genomic material by changes in the triangulation number defining symmetry and the number of capsomers comprising the capsid.[315, 357] However, there are also some obstacles regarding the VLP applicability for different (bio)applications that have to be overcome for an unrestricted use. Some virus capsids need at least a part of the original nucleic acid strand as a starting point to accelerate the reassembly or to initiate the process at all.[358, 359] Also the anticipated response of the immune system towards the virus-related surface of the VLP and a potential arising toxicity has to be taken into account, especially for *in vivo* applications.[309, 360]

2.4.3   Synthesis Routes for Virus-Like Particles

Two concepts distinguished themselves during research for VLP synthesis: (1) the direct generation of non-genomic material inside the capsid cavity acting as a nanoreactor, (2) the self-assembly of the capsid around the non-genomic material. Since each of them relies on a separate phenomenon, they can be considered as complementary methods.[12, 309]

The uniform cavity inside a capsid with its high degree of functionalities arranged regularly on the inner interface offers the perfect environment for syntheses in a confined space and thus can be

defined as "nanoreactors" (Figure 2.9). The processes applicable are inspired by nature's "biomineralization"[12, 17, 361] and provide a way to generate an artificial core inside the capsid under biocompatible conditions without the need of necessarily breaking it.

The required starting material is introduced into the cavity either by enclosing the respective molecules during the capsid formation[360] or by harnessing the "gating" mechanism of the virus capsid initiated by a pH increase and the entailed swelling of the protein cage[17]. While the form of the nanoreactor is set by the overall symmetry of the virus capsid, the growth of the non-genomic material by mineralization inside proceeds until the constraints of the cavity interface are reached. As a result, the choice of an icosahedral or a helical protein cage leads to the generation of a quasi-spherical[16, 17, 361-363] or rod-shaped[309, 364-370] nanostructure, commonly known as a nanoparticle and a nanowire, respectively.
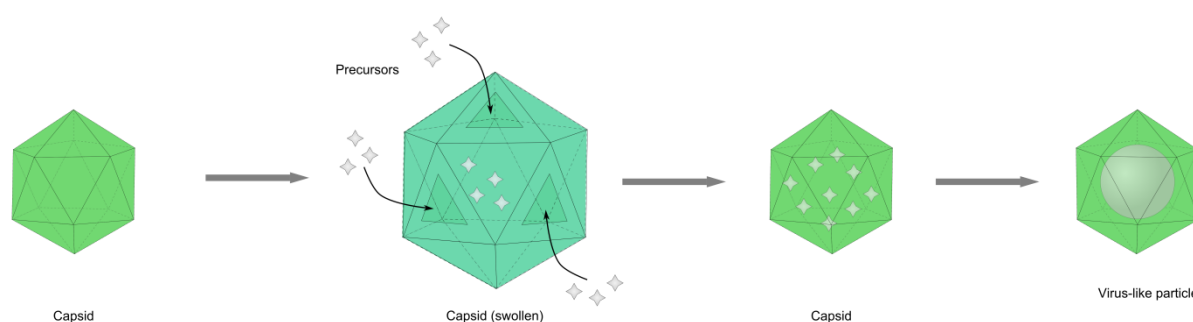
Figure 2.9 VLP synthesis via the "nanoreactor" route including (1) swelling of the virus capsid, (2) diffusion of precursor into the swollen capsid through the permeable protein layer, (3) shrinking of the virus capsid, and (4) the synthesis of non-genomic material induced by inner surface functionalities.

The abundantly present functional groups at the cavity interface bear the role as nucleation points during the mineralization process and therefore strongly determine the type of non-genomic material producible inside the respective virus capsid. For example, native RNA viruses such as cowpea chlorotic mottle virus (CCMV) or brome mosaic virus (BMV) express a multitude of basic amino acid moieties on the inner capsid interface whose dense positive charge interacts with the viral genome ensuring the assembly of uniformly sized capsids.[14, 315, 345, 357, 371] These functionalities allow highly efficient nucleation and mineralization of different materials such as the oxometallates tungstate WO_4^{2-} and the vanadate species $V_{10}O_{28}^{6-}$ [17] but only with an anionic starting material. An optimized engineering of the capsomers to obtain a negatively charged inner surface is required to extend the applicability of the "nanoreactor" approach for the VLP generation also to materials derived from cationic ions. The feasibility of this necessary step was shown by replacing the basic with acidic amino acids side chains enabling the mineralization of Fe_2O_3, Fe_3O_4, or Co_2O_3, inside a virus capsid.[361, 372] The accessibility of complementary inner surface characteristics and differing

symmetries of various virus capsids led to the generation of nanoparticles or nanowires made of various materials inside a virus capsid. The potential materials include, in addition to the examples mentioned before, metals[16, 313, 317, 363, 367, 369], metal oxides[14, 361, 362, 370], bimetallic alloys[368, 373], and semiconductors[370].

Complementary to the approach mentioned before, the core material synthesis can be performed prior to the actual VLP generation which involves the so-called "encapsulation" (Figure 2.10). This process relies on the efficient self-assembly of the capsomers around the negatively charged nanomaterial core acting as the nucleation grain.
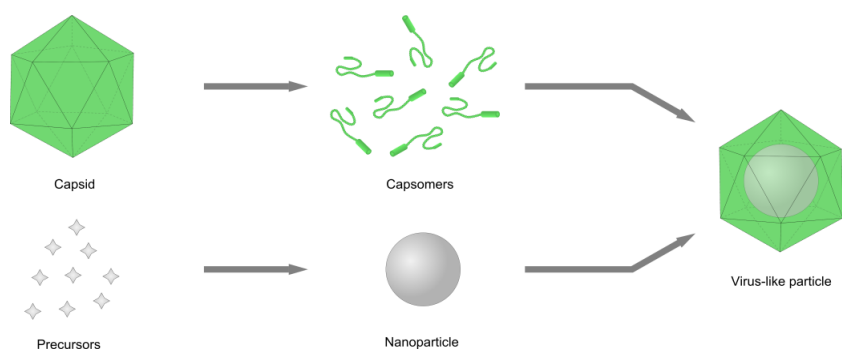
Figure 2.10 VLP synthesis via the "encapsulation" route including firstly a disassembly of the virus capsid (top) and independent nanoparticle synthesis in parallel (bottom) and secondly a reassembly of the capsomers around the nanoparticle as the nucleation grain provided suitable surface engineering**.**

This split synthesis way allows a highly versatile choice of the capsid/core combination[13, 374], since (a) a biocompatibility of the reaction conditions during core synthesis including temperature, pH, and solvent is not mandatory, (b) usable core material is not restricted by the functionalities of the inner cavity surface making capsomer engineering optional not obligatory, and (c) the surface of the core material can be tailored to optimally meet the requirements for encapsulation[12, 14]. While polymers present themselves as potential nucleation grains due to their flexibility similar to the native RNA or DNA, the reduced number of degrees of freedom of nanoparticles strongly simplifies the assembly process around these solid nanostructures.[13] However, several parameters have to be optimized to ensure encapsulation of nanoparticles whose efficiency can be determined by the following arbitrary equation:

$$\eta = N_{VLP}/N_{NP}$$

with N_{VLP} the number of virus-like particles with a complete capsid shell and N_{NP} the overall number of nanoparticles both observed in transmission electron microscopy[12, 317].

The most decisive nanoparticle characteristics for a feasible encapsulation are the diameter, the surface composition, and the surface charge density of the respective core. Their importance was

proven by studies on different virus capsids, nanoparticles and encapsulation protocols which will be described in the following. Nanoparticles smaller than the cavity size of the respective capsid can easily be incorporated inside the protein cage with a potential encapsulation of more than one core.[375] In contrast, a larger diameter leads only to the formation of a disorganized capsid and prevents any kind of self-assembly of an intact capsid around the core.[317, 359] Interestingly, for some virus types the size of the non-genomic core also influences the symmetry of the formed virus capsid. A decrease of the diameter starting close to the cavity size of the capsid results in a reduction of the triangulation number from T = 3 (180 subunits) and pseudoT = 2 (120 subunits) to T = 1 (60 subunits).[317] This alteration of T strongly influences the capsid symmetry, since hexameric substructures disappear in the process and a transformation of a truncated icosahedron (T = 3) into a dodecahedron (T = 1) as the geometric form takes place. Furthermore, the choice of the surface ligands on the nanoparticle surface shows a tremendous effect on the encapsulation efficiency. The utilization of citrate, phosphine, or DNA to imitate the negative charge of the viral RNA/DNA results in an encapsulation efficiency of only 2-3%. An inappropriate stoichiometric capsomer/nanoparticle ratio due to aggregation problems, a formation competition between encapsulated nanoparticles and empty capsids favoring the latter, or random and unspecific interactions between capsomers and nanoparticle can be named as potential reasons.[12, 16, 313, 321, 376] A thorough optimization drastically improves the encapsulation probability, especially by the introduction of a biocompatible polymer such as polyethylene glycol to avoid non-specific binding of the capsomers to the nanoparticle surface during the assembly process yielding an encapsulation efficiency of 95%.[16] Some ligands can be applied for different core materials with consistent result improvements[12, 16, 375] indicating a dependency of the efficiency solely on the surface composition and not on the core itself. Especially for viruses which show a non-specific interaction between the genome and the capsomers, the negative charge density of the surface is crucial for a feasible encapsulation process. Since the first step during self-assembly is an electrostatic interaction between the core and the capsomers that is followed by a rearrangement of the proteins to form the actual capsid by pH reduction, the initial assembly phase can be described by a micelle model.[13, 317] Therefore, any decrease of the number of negatively charged surface functionalities from the highest possible inevitably leads to a deterioration of the encapsulation efficiency until the charge density falls below a specific threshold and no VLP generation occurs.[13]

A more virus-related factor influencing the encapsulation efficiency is the presence or absence of a part of the original genome for a feasible VLP generation. Capsids of different viruses including for example the Red Clover necrotic mosaic virus (RCNMV) need a specific part of their native viral genome for the VLP formation. The oligonucleotides attached to the nanoparticle core then act as a sort of nucleation starting point during self-assembly by directed interaction with the

capsomers.[359, 377, 378] In contrast, for viruses relying on more non-specific interaction of the core with the capsomers, such as BMV or CCMV mentioned earlier, no additional modification of the core with a native RNA/DNA strand is needed which drastically simplifies the nanoparticle synthesis and VLP generation process.[12, 317, 371] Nanoparticles with no viral RNA/DNA modification curiously can even act as suitable core for encapsulation by bioengineered capsomers, while the native virus genome is incapable of performing this task.[315] Consequently, the capsid of the brome mosaic virus as the encapsulating protein cage received considerable attention in research including theoretical calculations[379] and in practical applications. The resulting VLPs contain for example nanoparticles consisting of gold[16, 313, 317], iron oxide[14], or semiconducting material[375] and show the same physicochemical properties as the native virus[323].

In conclusion, virus-like particles (VLP) can be prepared from a wide variety of different virus capsids and non-genomic materials. Especially the prior synthesis and potential optimization of the respective cargo together with a subsequent encapsulation process is a suitable way to create UCNPs with a biomimetic surface. Consequently, the preparation of VLPs from UCNPs with an optimized surface composition and the convenient quasi-spherical BMV capsid was studied in this thesis regarding its feasibility and adaptability to differently functionalized artificial nucleation grains.

2.5 Imaging in Bioanalysis

Imaging is one of the most important methods for the investigation of biological samples and systems, both *in vitro* and *in vivo*. Imaging information like the temporal or spatial resolution or the creation of three-dimensional images as well as instrument-related factors like sensitivity, costs, or accuracy have to be taken into account to choose a suitable imaging technique to obtain the desired information.[380, 381] Among the wide variety of detectable measurands in imaging applications such as magnetism or radioactivity, luminescence is highly favored in research[18, 20, 23, 24, 92, 97, 128], since techniques based on it are non-invasive, versatile, and specific[1, 127, 382, 383] with a high detection sensitivity of the respective target[1, 162, 384, 385]. Additionally, the fast and robust implementation[97, 162] allows measurements of a variety of potential measurement signals, e.g. intensity, lifetime, or spectral characteristics[1, 386], with a high spatial[127, 162, 383, 384, 387-389] and temporal[127, 387-389] resolution. Furthermore the spectral resolution[389] enables multicolor imaging and a multiplexed readout.

These beneficial characteristics led to the development of imaging concepts based on luminescence that employ a multitude of various luminophores as contrast agents for imaging including organic dyes, fluorescent proteins, metal nanoparticles, or quantum dots.[111, 127, 165] The use of several fluorescent labels in one application enables a multiplexed readout by multicolor staining, i.e. the

simultaneous imaging of different biological structures or functions.[18, 24, 390] However, conventional contrast agents, more precisely the required excitation wavelength, also cause detrimental phenomena which hamper or almost prevent the feasibility to obtain informative images. Visible or UV light only marginally penetrates biological tissue[20, 92, 128, 162, 165, 388], is strongly scattered during the pass through the specimen[128, 162, 165], and causes severe damages to the DNA and potentially leads to cell death, especially after long exposure times[20, 23, 92, 128, 165, 388]. The arising autofluorescence originating from endogenous species[24, 198, 199] such as flavins, NADH, or porphyrins greatly affects the imaging results, since it leads to a low signal-to-noise ratio and diminishes the achievable spatial and temporal resolution and the detection sensitivity.[20, 23, 24, 92, 128, 162, 165, 263, 388]

Additionally, since a clear spectral separation is required for multiplexing, the number and range of suitable contrast agents is limited due to the broad emission bands of most organic dyes and fluorescent proteins.[24, 391] the application of a post-processing of the obtained data is an option to reduce the impact of both autofluorescence and to a minor part the overlapping of emission peaks. There are several analysis algorithms accessible for this purpose that can help to differentiate between the various luminescence signals of the contrast agent and the background but they all have their limitations in efficiency and do not improve the imaging depth.[24, 162, 381, 389, 391]

The definition of several demands towards the luminescent label employed and their realization in form of optimized contrast agents enables a reduced background from the start and makes any post-analysis redundant. Firstly, the excitation and emission should be in the range of the biological window (750 nm - 1000 nm) to ensure good tissue penetration, low photodamage, low scattering, and reduced autofluorescence by endogenous species.[18, 162, 390, 392] Secondly, a large spectral shift between excitation and emission light is beneficial to further diminish background fluorescence.[392] Thirdly, the quantum efficiency of the emission and thus the brightness of the contrast agent should be high.[18, 162, 390, 392] Consequently, the excitation power densities used can be lower and the tissue penetration of the emission light is enhanced. Fourthly, the contrast agents should be photostable, even after extended irradiation times.[18, 162, 392] Fifthly and finally, the cytotoxicity of the agent as well as any changes in the pharmacokinetics of biomolecules after agent binding should be low to reduce damages to the specimen and ensure an unaltered targeting ability.[162, 390] These label requirements can be consulted for *in vitro* and *in vivo* applications to find the suitable contrast agent for the respective purpose and optimally allows its use in both application types with satisfactory results[18]. Since for *in vivo* imaging the label is exposed to more complex biological influences and mechanisms, the biological stability can be named as a sixth demand. The degradation or clearance from the system, for example, hampers the efficiency of the label, especially in respect to targeting. This results in a potential different behavior of the label in *in vitro* and *in vivo* applications.[390]

Developments and optimizations of new labels based on these demands led to two types of contrast agents that display either NIR emission generated by a Stokes process or visible/NIR emission based on an Anti-Stokes process[162] after NIR excitation. The preference of NIR excitation[18, 21, 392, 393] for imaging application can be attributed to the deeper tissue penetration, since an inefficient excitation strongly diminishes the use of a suiting bright label with a high quantum yield[390]. Although the generation of a favored NIR emission[192, 394] can also be realized by UV/VIS excitation, shown for special quantum dots[381, 392], these labels suffer from an increased chemical instability[392]. Therefore, the combined NIR excitation and NIR emission in form of a NIR-to-NIR system is highly favored[123, 164, 390, 395] but current labels lack a sufficient brightness and biocompatibility[395]. The use of a two-photon excitation[263, 392], i.e. an Anti-Stokes process, is another way to exploit the favorable NIR excitation with a potential NIR emission. As a result, imaging techniques based on this phenomenon were developed including the two-photon fluorescence imaging (TPFI)[92, 128, 165]. However, organic dyes, quantum dots or plasmonic nanoparticles only show a low cross section of the two-photon absorption decreasing the emission efficiency. The absence of suitable instruments for *in vivo* imaging also limits the feasibility of the two-photon process for imaging applications.[392]

Consequently, the use of the upconversion process, more precisely upconverting nanoparticles (UCNPs), for imaging extensively solves most of the problems of organic fluorophores or quantum dots with NIR excitation/emission. The excitation with NIR light utilizing an inexpensive low-energy continuous wave laser diode generates visible and NIR light depending on the doping. No autofluorescence of endogenous species is generated due to the large Anti-Stokes shift, especially for the visible peaks[19, 49, 58], which is highly accommodating for imaging applications. The low photobleaching, low toxicity and possible multiplexing of these contrast agents[19, 49, 58] also improve their suitability for applications *in vitro* and *in vivo*. These types of studies strongly differ in regard of their research focus and investigation method. While *in vitro* applications employ microscopy techniques to study individual cells in an artificial environment, the behavior of cell organizations in natural surroundings is detected by whole animal imaging for answering *in vivo* questions.[396]

2.5.1 *In Vitro* Imaging Methods

Microscopy techniques are the major tools for *in vitro* imaging of cells and their response to exterior factors.[198, 391] Since the first beginnings with a transmitted-light microscope several more sophisticated and more informative instruments, mostly based on luminescence, were developed such as wide-field microscopy, confocal microscopy, and two-photon microscopy.[198, 391] These techniques significantly differ in detection sensitivity, speed of acquisition, and viability of the biological sample[391]. A differentiation regarding the way of image acquisition can also be made with

the non-scanning way acquiring the whole image simultaneously and the scanning way assembling smaller sections to build the image whose data is collected separately.[397] The wide-field fluorescence microscopy allows a short image acquisition speed in a non-scanning way with moderate illumination intensities, but the high amount of detected out-of-focus fluorescence (up to 90%) and the diminished intensity of in-focus fluorescence reaching the detector by scattering strongly lowers the image resolution, contrast and potential 3D information.[198, 396-398]

The invention of the confocal microscopy led to a reduced detection of scattered or out-of-focus fluorescence due to a pinhole in the confocal plane in all microscope designs. These instruments predominantly work in the scanning mode and thus a computerized data evaluation is required to obtain the actual images. The resulting images show an improved spatial resolution and a depth distinction of the fluorescence origin. This feature allows the generation of three dimensional images by additional post-processing.[198, 397, 398] A drawback of the pinhole introduction is the decreased overall emission reaching the detector that is intended in the first place by eliminating unwanted fluorescence but necessitates the use of high excitation power densities which strongly enhances photobleaching. This phenomenon is not limited to the in-focus fluorophores in contrast to the detected fluorescence and results in an even damage to both in-focus and out-of-focus fluorophores. Consequently, the feasibility of elongated irradiation times or the imaging of several specimen planes is strongly hampered.[198, 396-398] Also the primary use of UV light as the excitation source entails a comparatively short tissue penetration and photodamage to the biological sample.[198]

A further method development uses the Anti-Stokes process of two-photon absorption as the basic concept of a microscopy technique. The two-photon microscopy shows the same scanning option as confocal microscopy to acquire the image but shows the following improvements.[396] The excitation process includes the absorption of two low-energy photons almost simultaneously (within 10^{-18} s)[399] and its probability is close to zero outside of the focus plane leading to an emission only in a very small volume. Therefore, the excitation wavelength inevitable lies in the NIR range, preferably in the biological window, with all its benefits such as deep tissue penetration, reduced photobleaching and photodamage outside the excited volume, and lower scattering.[2, 198, 398, 399] Additional to an improved three dimensional resolution, the background fluorescence is further decreased due to the small overall emitting volume and the low two-photon cross section of most biomolecules responsible for autofluorescence.[198, 398] This technique is also not limited to the two-photon processes but can be extended to processes based on multi-photon absorption or second- or third-harmonic generation.[399] However, being a Anti-Stokes process relying mostly on virtual energy levels, the two-photon microscopy needs extremely high excitation power densities to generate a detectable emission.[399, 400] Since no biological specimen tolerates this enormous intensity all at once,

expensive lasers producing very short pulses (ca. 10^{-13} s) are needed for this microscopy technique.[198, 399] Furthermore, the photobleaching rate and the extent of photodamage is still high in the small excitation volume[198] and the range of two-photon labels show mostly also a low two-photon absorption cross section[398].

Established labels for these different microscopy techniques include additional to conventional organic fluorophores also nanomaterials such as silica-based nanoparticles, gold nanorods, quantum dots or rods.[398] However, in recent years more and more research efforts are focused on UCNPs as contrast agents for imaging applications. The microscopy techniques used for this purpose included both established techniques such as conventional fluorescence microscopy[18, 21, 111, 127, 168, 401] or confocal microscopy[20, 23, 58, 92, 97, 106, 124, 185, 388] and optimized methods adapted to the optical characteristics of UCNPs such as laser scanning upconversion luminescence microscopy[19, 199, 261]. These optimized microscopes have the potential to strongly improve the image quality acquired from UCNP-labeled cells compared to other designs.[199] The feasibility of *in vitro* applications with these techniques was shown for a variety of UCNP dopings including erbium, thulium, or holmium ions using either one or all of their emission wavelengths as the detection signal. While the red emissions of the respective UCNPs[124, 199, 388] played a minor role as the detection signal, the green emission of Er^{3+}-doped UCNPs[19, 21, 23, 58, 97, 111, 127, 128, 165, 168] was favored due to its high emission intensity. For Tm^{3+}-doped UCNPs the focus was on the NIR emission[18, 106, 162] due to its deep tissue penetration.

Since UCNPs are hydrophobic after most syntheses, their surface has to be modified with hydrophilic components such as citrate[58, 261], silica[21, 92, 128, 165, 388], or hydrophilic polymers[23, 111, 127, 162] to enable imaging. This nanoparticle design allows a cell labeling by nonspecific interactions[58, 162, 165] and a potential internalization[18, 19, 106, 111, 128, 165, 261, 388] for example by endocytosis without the need of targeting functionalities. However, for most *in vitro* imaging applications a directed detection of biological structures or cell receptors is desired to be able to discriminate between healthy cells and cancer cells which are known to show an overexpression of specific groups on their surface. Any species, predominantly biological, can be used as a targeting functionality that specifically recognize the target including small biomolecules such as folic acid[19, 23, 124, 168, 199], proteins like transferrin[401] or a cell- or structure-recognizing antibody[20, 21, 185] such as anti-claudin-4 and anti-mesothelin antibodies[97]. Consequently, a directed and specific attachment to the cell surface[20, 21, 124, 168, 199, 401] and an efficient uptake of the contrast agent into the targeted cell[97, 168] can be achieved.

Thorough studies verified a high photostability[165, 199] of the UCNPs in *in vitro* imaging and the expected independency of the measurement noise on laser intensity[20, 128]. Since the emission peaks of UCNPs are very narrow compared to other contrast agents and the emission can be tuned by the dopant type and concentration, multiplex labeling in form of a multicolor readout is easily realized.[21]

2.5.2 *In Vivo* Imaging Methods

The imaging of whole animals puts new demands on the contrast agent used, since the complexity of the biological system increases drastically compared to *in vitro* applications. Consequently, great efforts were made by researchers, especially for diagnostic purposes, to develop methods that meet these requirements including target specificity and sensitivity, penetration depth, 3D tomography, real-time imaging, high spatial resolution, accuracy and cost[380]. (Bio)luminescence-based imaging, magnetic resonance imaging (MRI), positron emission tomography (PET), X-ray computed tomography (X-ray CT), single photon emission computed tomography (SPECT), and ultrasound (US) imaging showed thereby the highest potential.[122, 380, 381, 390, 402] These methods can be roughly divided into the two groups of functional (e.g. luminescence imaging, PET) or structural (MRI, CT) techniques.[122]

Optical imaging based on luminescence excels in spatial resolution and sensitivity[97, 123, 124, 380, 403] reaching almost to the single molecule level[97]. The implementation of this technique is also quite robust to outer influences, inexpensive, and portable.[97] However, the potential autofluorescence of biological specimen induced by the UV excitation light limits the spatial resolution and accuracy of the imaging and the low penetration depth of the excitation irradiation in tissue prevents any access to anatomical or physiological information.[123, 124, 380, 402] Radionuclide imaging such as PET is based on the detection of gamma rays emitted by the radioactive contrast agent which drastically increases the penetration depth and spatial resolution compared to luminescence imaging.[402] Being another functional imaging technique PET shows a relatively high sensitivity ranging in the picomolar domain[123, 124, 403] and allows the computational reconstruction of 3D images[404]. Despite recent improvements the achievable spatial resolution is still comparatively low for *in vivo* applications[123, 124] due to the lack of recognizable anatomical structures in the PET images[380]. For this purpose, structural imaging techniques have to be applied like MRI which relies on changes in the dipolar movement of hydrogen atoms in magnetic fields with the spin-lattice (T_1) and spin-spin (T_2) relaxation as the detection signals.[402] MRI features the highest spatial resolution compared to the other imaging methods[123, 402], a good temporal resolution[403] and together with the good in-depth imaging ability[97, 123] the realization of 3D tomography with a high anatomical information content is made greatly feasible[123, 380]. However, as a structural imaging technique MRI suffers from a low sensitivity and the miss of cellular information.[97, 123, 380]

Since all imaging techniques have their advantages and disadvantages and thus no method is superior in all demands for *in vivo* applications, combinations of the different modalities have been investigated. The introduction of this highly favored multimodality greatly improves the informative

value of the images by using synergistic effects[122, 380], i.e. the compensation of one modality's drawback by an advantage of another modality[123, 124]. Beneficial dual- or even tri-modalities can be especially obtained by the combination of a functional and a structural method, stated by the high preference of luminescence/MRI methods[97, 122, 123, 380] but also dual-modalities like PET/MRI[380], luminescence/PET[380, 394, 405] or tri-modalities like MRI/luminescence/PET[124, 403] were realized.

Nanoparticles are favored as contrast agents compared to organic dyes, since they are photostable in most instances and improve the achievable imaging contrast.[392] Additionally, they significantly increase the blood circulation time and enable the mentioned introduction of several modalities (e.g. fluorescence, PET or MRI imaging) for multimodal applications.[405] The large surface of nanoparticles is accessible to modification with biomolecules in high numbers[97, 392, 405], also of different functionality, which simplifies the generation of multivalency[402]. A targeting ability of nanoparticles can be realized by the attachment of a variety of different biomolecules such as peptides, proteins, antibodies, aptamers, or DNA oligonucleotides.[192] However, their comparatively large size entails more complex mechanisms for body clearance which majorly employ either ways over the liver and the bile instead of the simpler renal system of the kidney or an uptake by the reticuloendothelial system which diminishes the imaging efficiency. A potential toxicity of the nanoparticles for the animal has to be excluded from the start or at least greatly reduced if imaging with these contrast agents is envisioned.[390]

Similar to *in vitro* applications, the use of UCNPs as contrast agents for *in vivo* imaging focused on Tm^{3+}- and Er^{3+}-doped UCNPs with the NIR[18, 19, 162, 212, 261] and green[124, 128, 212] emission, respectively, as the detection signal. However, most studies were performed with self-made[19, 124, 261, 265] or at least modified[18, 162, 212] instruments due to the lack of commercially available devices with an NIR excitation source. Nonetheless, the upconversion process allows deep tissue penetration and high signal-to-noise ratio without any tissue damages even after elongated exposure times.[265] Therefore, both animal pretreatments for imaging such as shaving[18, 162] or skin removal[19] are redundant and disadvantageous tissue features such as black skin with its increased absorption and scattering effect can be ignored[261]. The expected lack of measurement interference by autofluorescence[199] also enables the imaging of very small body structures like the lymphatic system whose differentiation potential can be further improved by an adjusted excitation intensity power.[19] Since the emission peaks of UCNPs are very narrow and are spectrally good distinguishable, UCNPs doped with different activators and/or modified with various downconverting components allow the creation of multicolor contrast agents for a multiplexed *in vivo* imaging of different regions of interest.[24, 212] Tumor imaging studies crucial for any diagnostic applications also gave evidence that the design of

UCNPs with a targeting capability remains unchanged in the complex biological systems of animals and allowed a targeted imaging with high accuracy and specificity towards the target structure.[199]

Additional to the feasibility of targeted imaging, the biodistribution of non-targeting UCNP and potential accompanying toxicity is an important factor of their applicability as contrast agents. Since the liver with its phagocytic cells and the spleen as the biggest organ of the immune system belong to the main elimination routes for foreign particles, a fast accumulation in these organs with a comparatively slow excretion is predicted and observed.[18, 124, 125] Even the use of targeting functionalities cannot avoid a certain degree of uptake by these two organs.[199] However, the aggregation of the nanoparticles can also lead to an observable luminescence in the lungs[124, 128], while most other organs like the kidney normally show no increased UCNP accumulation[125, 128]. Since the clearance routes via liver and spleen are quite efficient and fast, the UCNP blood circulation is quite short which can be detrimental for the imaging application, especially if targeting is envisioned.[125, 128, 199] During these biodistribution studies no toxicity was observed indicated by a good health and normal behavior of the laboratory animals during the time of in vivo imaging and nanoparticle excretion which ranged between a few days and several months.[125, 162]

3. Materials & Methods

3.1 Chemicals

	Chemical	Purity	Supplier[a]
A	Acetone	For analysis	Merck
	Acetic acid	For analysis (99.8%)	Sigma-Aldrich
	Alkyne-PEG5-acid	-----	Sigma-Aldrich
	3-(Aminopropyl)triethoxysilan (APTES)	≥ 98%	Sigma-Aldrich
	Ammonia solution (25%)	For analysis	Merck
	Antibody Goat-anti-Mouse 10 nm gold label, IgG, secondary antibody	Optical density $OD_{520nm} = 1.0$	Aurion
	Antibody Goat-anti-Rabbit 10 nm gold label, IgG, secondary antibody	Optical density $OD_{520nm} = 1.0$	Aurion
	L(+)-ascorbic acid, sodium salt	≥ 99%	Sigma-Aldrich
	(3-Azidopropyl)diethoxy (hydroxyl)silane	-----	University Regensburg
B	Boric acid	For analysis (≥ 99.5%)	Merck
C	Calcium chloride dihydrate	For analysis (≥ 99%)	Roth
	Carboxyethylsilanetriol, sodium salt, 25% in water	-----	ABCR
	Chloroform	For analysis (≥ 99%)	Merck
	Copper(II) sulfate pentahydrate	For analysis (≥ 99%)	Merck
	Cyclohexane	100%	VWR
D	Dimethylformamide	99.8%	Sigma-Aldrich
E	Ethanol	Absolute (99.8%)	Sigma-Aldrich
F	6-Fluorescein-Azide	>95%	Jena Bioscience
H	Hydrochloric acid (37%)	For analysis	Merck
I	Igepal® CO-520 (M_n = 441 g/mol)	-----	Sigma-Aldrich
M	Magnesium acetate tetrahydrate	For analysis (≥ 99.5%)	Merck
	Magnesium chloride hexahydrate	For analysis (≥ 99%)	Merck
	3-Mercaptopropionic acid	For Synthesis (> 98%)	Merck
N	Nitrosyl tetrafluoroborate	95%	Sigma-Aldrich
O	1-Octanthiol	97%	Sigma-Aldrich
	Ortho-phosphoric acid	For analysis (85%)	Merck

P	Polyacrylic acid (M_r = 2100), sodium salt	-----	Sigma-Aldrich
	Polyacrylic acid (M_r = 5100), sodium salt	-----	Sigma-Aldrich
	Potassium chloride	For analysis (≥ 99.5%)	Merck
	Propargylamine	98%	Sigma-Aldrich
	O-(propargyloxy)-N-(triethoxysilylpropyl)urethane	90%	ABCR
S	Sodium acetate trihydrate	For analysis (≥ 99%)	Merck
	Sodium chloride	For analysis (≥ 99.5%)	Merck
T	Tetraethyl orthosilicate (TEOS)	For synthesis (99.9%)	Merck / ABCR
	Toluene	For analysis (99.99%)	Acros organics
	Triethoxyoctylsilane	For synthesis	Merck
	Triethylamine	For synthesis	Merck
	3-(Trihydroxysilyl)propyl-methylphosphonate, sodium salt solution, 42 wt% in water	-----	Sigma-Aldrich
	Tris(hydroxymethyl)aminomethane	99.8%	Merck
U	10-Undecynylphosphonic acid	≥ 95%	Sikémia

[a] Supplier contacts:

ABCR	www.abcr.de
Acros	www.acros.com
Aurion	www.aurion.nl
Jena Bioscience	www.jenabioscience.com
Merck	www.merck.de
Roth	www.carlroth.com
Sigma-Aldrich	www.sigmaaldrich.com
Sikémia	www.sikemia.com
VWR	www.vwr.com

Additionally, the brome mosaic virus (BMV) in a virus inoculum and the rabbit-anti-BMV antibody (IgG, polyclonal) was purchased from the DMSZ Plant Virus Collection Braunschweig (www.dmsz.de). The azide silane (3-azidopropyl)diethoxy(hydroxyl)silane and the alkyne fluorophore 4-amino-N-(2-propynyl)-1,8-naphthalimide was provided by Raphaela Liebherr at the Department of Analytical Chemistry, Chemo- and Biosensors, University of Regensburg.

3.2   Instruments

Upconversion luminescence spectra were recorded with a Varian Cary Eclipse Fluorescence Spectrophotometer, modified with a continuous-wave diode laser with a wavelength of 980 nm and an adjustable power input (P_{max} = 5 W). A Hidex Plate Chameleon Multilabel Detection Platform (Figure 3.1) was used for microtiter plate measurements and scanning applications of UCNPs. The instrument was equipped with a NIR laser diode (λ = 980 nm, P = 4 W) as the excitation source and an excitation long pass filter (Schott RG-850, www.schott.com). The upconversion emission was selected by a short pass filter ($\lambda_{cut\text{-}off}$ = 525 nm, $\varnothing$ = 25 mm), a band pass filter (535 nm CWL, 25 nm FWHM, $\varnothing$ = 25 mm) or a band pass filter (800 nm CWL, 25 nm FWHM, $\varnothing$ = 25 mm). The short pass filter and 800 nm band pass filter were purchased from Edmund Optics (www.edmundoptics.de), while the 535 nm band pass filter was purchased from Hidex (www.hidex.com).
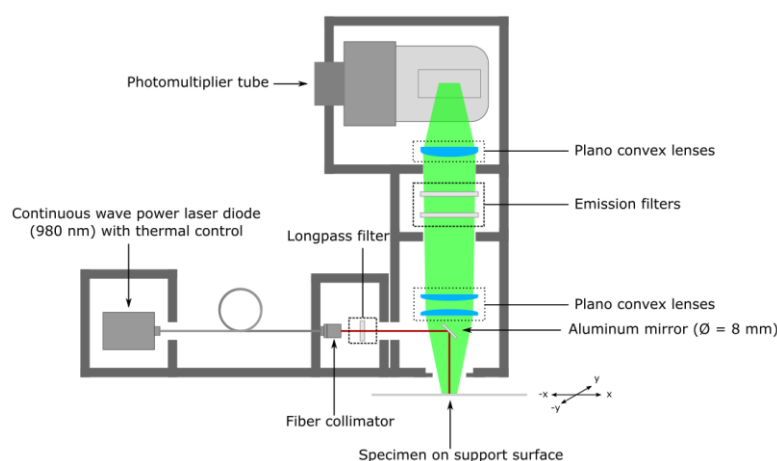
Figure 3.1 Schematic illustration of the Hidex Plate Chameleon Multilabel Detection Platform (Chameleon reader)

Transmission electron microscopy (TEM) images were recorded with a ZEISS LEO912AB 120 kV at the Institute of Pathology of the University Hospital Regensburg by Heiko Siegmund or with a Philips CM12 120 kV at the department of experimental and applied physics, chair Prof. Back, University of Regensburg by Stefan Wilhelm.

The size and zeta potential measurements were performed with a Malvern Zetasizer Nano Series Nano-ZS at the Department of Pharmaceutical Technology, University of Regensburg.

Fluorescence spectra were recorded with an Aminco-Bowman Series 2 Luminescence Spectrometer and fluorescence measurements of microtiter plates with a Tecan GENios Plus. Protein absorption was measured with a Varian Cary 50 Bio UV-Vis Spectrophotometer.

Infrared spectra of both dry and dispersed UCNPs were recorded with a Varian 670-IR FT-IR Spectrometer equipped with PIKE GladiATR unit.

The immunogold staining automat was a Leica EM Immunogold-Labeling-machine (IGL) at the Institute of Pathology of the University Hospital Regensburg.

For the surface modification of UCNPs with a silanized silica shell a Hettich Zentrifugen EBA 12 centrifuge (Rotor 4: max. 4,000 rcf, 6x120 g, Rotor 7: max. 36,000 rcf, 12x3 g) centrifuge was employed, while the functionalization with polyacrylic acid via ligand exchange was performed with a Hettich Zentrifugen Mikro 200 R (max. 21,000 rcf, 24x3 g). An Eppendorf Centrifuge 5415 R centrifuge (max. 16,100 rcf, 24x3,75 g, cooling option) was used in the preparation of virus-like particles (VLP) for the removal of viral RNA.

Dialysis was performed with GE Healthcare Mini Dialysis kits with an 8 kDa cut-off and a volume of 250 µL. The incubation for a constant temperature during click chemistry was performed in an Eppendorf Thermomixer Comfort (1.5 mL). A Bandelin Sonorex R4100 was used for the sonication treatment of UCNP dispersions.

3.3 Upconverting Nanoparticles

The upconverting nanoparticles used for all studies were synthesized according to literature[93] by Stefan Wilhelm, Verena Muhr and Nadja Leibl. The nanoparticles of the type $NaYF_4$:Yb^{3+}, X^{3+} showed a diameter of 30 nm for X^{3+} = Er^{3+} and 23 nm for X^{3+} = Tm^{3+}, respectively. The additional doping with gadolinium (Gd^{3+}) resulting in $NaYF_4$:Yb^{3+}, Er^{3+}, Gd^{3+} nanoparticles decreased the overall diameter to 12 nm. All these UCNPs were coated with oleic acid and dispersed in cyclohexane and characterized by the group of Dr. Thomas Hirsch. The citrate-coated UCNPs with a diameter of 14 nm were obtained by a ligand exchange reaction of oleic acid by citric acid which was performed by Stefan Wilhelm according to literature[269].

3.4 Surface Modification of Upconverting Nanoparticles

3.4.1 Silica Coating

The synthesis of UCNP@SiO_2 based on a microemulsion technique was performed according to literature[128]. The UCNP dispersion was diluted with cyclohexane to obtain a final nanoparticle concentration of 0.76 mg/mL. A UCNP dispersion volume of 10 mL were mixed with 50 µL of Igepal CO-520 and stirred for 5 minutes. The remaining 450 µL of Igepal CO-520 together with 80 µL of ammonia (25%) were added to this mixture and the reaction vessel sonicated for about 20 minutes

after sealing. Depending on the desired silica shell thickness a specific volume of tetraethyl orthosilicate was given into the reaction mixture which was then rotated at 4°C for 2 days.

After the silica shell growth was completed 5 mL of acetone were added to the reaction mixture and the reaction vessel was shaken manually so that the nanoparticles started to settle down. The resulting nanoparticles were washed immediately with ethanol/water (2:1 v/v) three times by centrifugation (1,800 rcf, 10 minutes) and sonication. Finally, the UCNP@SiO$_2$ nanoparticles were redispersed in 7 mL water and stored under rotation at 4°C.

3.4.2 Silanization

Two synthesis process based on the microemulsion technique were utilized for the silanization of a silica shell on the UCNP surface. The first way of silanization used in this work was performed simultaneous to the silica shell growth described in chapter 3.4.1 and was performed accordingly. The only change was the addition of the respective silane in excess subsequent to TEOS to the reaction mixture. In this way, silica-coated UCNPs functionalized with amine, alkyne, azide, or phosphonate groups were obtained.

The second method is adapted from literature[248] and also relies on the microemulsion technique but differs from the previously mentioned technique regarding the synthesis order and the solvents used for work up. Additionally, the protocol was optimized regarding solvents used for work up and amount of silane used leading to the following general implementation. An amount of 4.3 mg of UCNPs dispersed in cyclohexane was diluted to a final concentration of 0.43 mg/mL. This dispersion with a volume of 10 mL was mixed with 500 µL Igepal CO-520 and 80 µL aqueous ammonia (25%) and stirred at 600 rpm for 10 minutes. After the addition of 46 µL TEOS the mixture was stirred for 3 h at 25°C. Afterwards, 46 µL carboxyethylsilanetriol (CEST) was added and the dispersion sonicated for 30 minutes. The resulting slightly turbid mixture was stirred at 600 rpm for 2 days on a multiposition magnetic stirrer.

Ethanol with a volume of 5 mL was added to the less turbid dispersion for work up and the mixture was shaken to start the settling down of nanoparticles. After the removal of the reaction solvent by centrifugation (1800 rcf, 15 minutes) the modified UCNPs were washed three times with ethanol (1,800 rcf, 15 minutes) and two times with a Britton-Robinson buffer (15 mM phosphoric acid, boric acid, acetic acid) with pH = 10 (19,000 rcf, 30 minutes). The resulting functionalized UCNPs were dispersed in the Britton-Robinson buffer and stored at 4°C.

This method was mainly employed for the silanization with carboxylic acid groups but was later also used for the simultaneous functionalization with carboxylic acid and azide groups. While the general process remained unchanged for this bifunctional modification, the amounts of chemicals had to be adjusted due to an increase of the nanoparticle diameter from 12 to 24 nm in order to match the new surface area of the UCNPs. Consequently, a volume of 58.8 µL ammonia (25%) and 367 µL Igepal CO-520 was added to the UCNP dispersion (β = 0.43 mg/mL, V = 8.6 mL). The amount of TEOS and silane (5% azide silane + 95% CEST) was decreased to 44.2 µL.

3.4.3   Coating with Polyacrylic Acid

The surface modification of hydrophobic UCNPs with polyacrylic acid (PAA) was performed by a ligand exchange reaction according to literature[269] with minor modifications and employed $NOBF_4$ as a temporary surface ligand. At first, a cyclohexane dispersion of UCNP with a nanoparticle concentration of 5 mg/mL and a volume of 2 mL was mixed with the same volume of dimethylformamide (DMF) to form a two-phase system. After the addition of 30 mg of $NOBF_4$ the mixture was stirred vigorously for 10 minutes to ensure a complete phase transfer of the nanoparticles from the cyclohexane into the DMF phase. The clear cyclohexane phase is removed without shaking up the DMF phase and is partitioned equally on two centrifuge tubes and washed three times with chloroform (2,000 rcf, 5 minutes) and once with a DMF/chloroform mixture (1:1 v/v, 2,000 rcf, 5 minutes). The purified UCNPs were redispersed in 2 mL DMF.

Two types of PAA with different molecular masses (2,100 g/mol and 5,100 g/mol) were chosen as the new surface ligand of the UCNPs. 30 mg of each polymer were solved in double-distilled water with a maximal volume of 0.5 mL and 1 mL of the BF_4^--stabilized UCNP dispersion was added to each sample. The mixture was stirred for 20 minutes and diluted with double-distilled water to a final nanoparticle concentration of 5 mg/mL.

3.4.4   Implementation of Click Chemistry

The Huisgen cycloaddition, i.e. the 1,3-dipolar cycloaddition of an azide with a terminal alkyne, was implemented according to a previously reported protocol[10] with minor changes. For most click reactions azide-functionalized UCNPs were employed, while the alkyne-modification of UCNPs played only a secondary role in this work and their use was limited to a modification with an azide-functionalized fluorophore. Therefore, the click reaction process as described below is focused on the azide-modified UCNPs and molecules containing alkyne groups, although the two functionalities are exchangeable without any changes of the reaction protocol.

An aqueous dispersion of azide-modified UCNPs (β = 1.08 mg/mL) was mixed with ethanol resulting in a water/ethanol dispersion of 1:1 (v/v). A solution of copper sulfate (5 µL, 20 mM), a solution of sodium ascorbate (5 µL, 100 mM) and 5 µL of triethylamine was added to 1 mL of the nanoparticle dispersion. Finally, a clickable reagent was added to this reaction mixture which was then shaken at 500 rpm in a thermomixer at 35°C for at least 14 h, mostly overnight. The resulting dispersion was centrifuged (22,000 rcf, 30 minutes) and washed three times with ethanol (22,000 rcf, 30 minutes). The UCNPs obtained were redispersed in 1mL water and stored at 4°C.

The Click reaction with azide-functionalized UCNPs with different clickable reagents yielded nanoparticles with phosphonate, carboxylic acid, or amine groups. Clickable fluorophores acted as sensitive labels to verify a successful click reaction by fluorescence spectroscopy for both azide- and alkyne-modified UCNPs. Click reactions without copper and/or with UCNPs coated with a pure silica shell were used as negative controls in these experiments with the fluorophore.

3.4.5 Zetasizer & Transmission Electron Microscopy

Both the hydrodynamic radius and the zeta potential were determined by a zetasizer device for all UCNP dispersions after surface modifications.

For the size measurements at the zetasizer the aqueous UCNP dispersion with a volume of 1 mL was transferred into a disposable polystyrene fluorimeter cuvette. The settings of the zetasizer for size measurements included the refractive index and absorption of the nanoparticle material $NaYF_4$, the refractive index and viscosity of the aqueous dispersant, the equilibration time of the temperature (at least 60 seconds), and the "normal" size distribution mode. The measurement position in the cuvette and attenuator position were automatically optimized by the software. The measurement consisting of at least 10 runs with a duration of at least 10 seconds was performed three to five times and an average was derived by the zetasizer software. The resulting distribution graph was given in the "intensity" version and the polydispersity index (PdI) was calculated by the software. A data processing to obtain the "number" version of the distribution graph required the refractive index (RI = 1.5) and the absorption coefficient (A = 0) of the host material $NaYF_4$. This conversion avoided an overrepresentation of larger particles owing to their higher scattering behavior.

The zeta potential determination of the aqueous UCNP dispersions was performed in a clear disposable zeta cell. The UCNP dispersion with a volume of approximately 700 µL was filled slowly into the cell so that the gold electrodes were inside the dispersant and the liquid level just below the filling opening. Afterwards the cell was inserted correctly in the cell holder of the zetasizer. Additional to the settings for the size measurements the dielectric constant of the aqueous

dispersant has to be known for zeta potential measurements. The set voltage was optimized by a test run to obtain a current below 0.5 mA to avoid sample degradation and electrode contamination. The measurement was performed in the distribution mode to record the potential distribution. Since the zeta cells can be used several times before disposal, after each measurement the cells were first cleaned with ethanol, flushed with a large amount of distilled water and dried with compressed air.

In some cases, also the absolute nanoparticle diameter was also determined by Heiko Siegmund or by Stefan Wilhelm via TEM imaging. Furthermore, the detection of BMV capsids or capsomers was carried out by TEM including a negative staining with phosphotungstic acid.

3.5   Synthesis of Virus-Like Particles

3.5.1   General Implementation

The preparation of virus-like particles was performed according to literature[375] and consists of two parts: Firstly, the disassembly of the brome mosaic virus capsid into the single capsomer proteins and the removal of virus RNA and secondly, the encapsulation of the UCNP by the reassembly of the capsomers by using the nanoparticle as the new nucleation grain. Except for centrifugation to remove the virus RNA, the only technique used for the whole VLP synthesis is dialysis at 4°C for 24 h against different buffer systems (Table 3.1).

Table 3.1 Dialysis buffer composition for VLP synthesis

Buffer	Components				pH
1	0.5 M $CaCl_2$				
2	0.01 M Tris				7.4
3	0.01 M Tris	1.0 M KCl	0.005 M $MgCl_2$		7.4
4	0.05 M Tris	0.05 M NaCl	0.01 M KCl	0.005 M $MgCl_2$	7.4
5	0.05 M NaAc	0.008 M $MgAc_2$			4.5

The disassembly of the capsids started with the dialysis against buffer 1 containing a high concentration of calcium ions in order to break the virus capsid and release the viral RNA strands. The subsequent centrifugation at 4°C and with a speed of 16,000 g removed these RNA strands that would otherwise compete with the UCNPs for the role as the nucleation grain for the capsid self-assembly. The resulting protein solution was then first dialyzed against buffer 2 to remove the Ca^{2+} ions, then against buffer 3, the storage buffer for the capsomers, to stabilize the proteins and finally stored at 4°C.

The capsomers can reassemble to form the viral capsid in presence of an UCNP acting as a nucleation grain provided a suiting ratio between nanoparticles and capsomers is given. Therefore, a mixture of the UCNPs dispersion and the BMV capsomers solution was prepared to yield a UCNP/capsomer ratio of 1:180. This mixture was dialyzed against buffer 4, the reassembly buffer, to enable the self-assembly of the capsomers. Finally, a dialysis against buffer 5, the VLP storage buffer, was performed to stabilize the VLPs. The VLP dispersion was again stored at 4°C to avoid any kind of degradation.

3.5.2 Dialysis

Since the sample volumes for the VLP synthesis range from 50 - 200 μL and conventional dialysis tubes normally have a minimum volume of over 1 mL to simplify handling, special dialysis cups were used for the VLP synthesis (Figure 3.2A). These cups from GE Healthcare Life Sciences have a maximal volume of 250 μL and are equipped with a dialysis membrane with a molecular weight cut-off of 8 kDa. Since the BMV capsomers have a molecular weight over 20 kDa, the cut-off is sufficient for the capsid encapsulation of the UCNPs. The general dialysis performance with these cups is shown in Figure 3.2B. Since the dialysis cups are suitable for centrifugation, the necessary quantitative recovery of the reaction mixture for further use by this method is nearly 100 %.
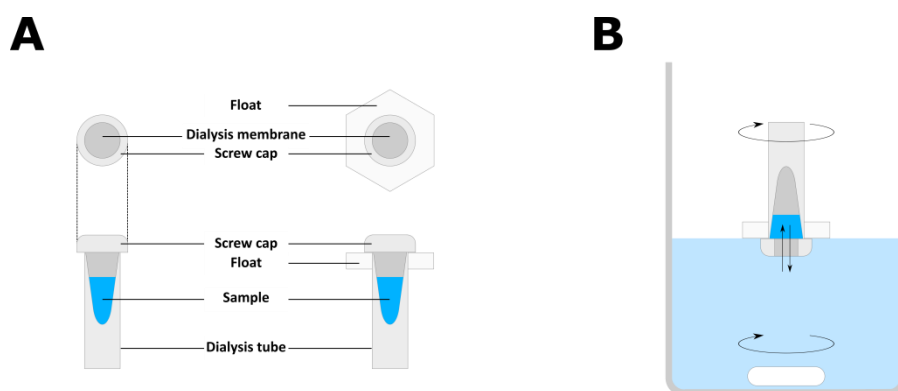
Figure 3.2 Dialysis tube setup (A) with part names and general use (B) during VLP synthesis.

3.5.3 Absorption Spectroscopy

For VLP synthesis the concentration of the capsomer solution after the capsid disassembly was determined by absorption spectroscopy. Consequently, an absorption measurement of the protein solution at 280 nm in a quartz cuvette was performed. After background correction the absorption value was measured at least ten times and the resulting average value was used for the concentration calculations, described in chapter 5.3.

3.5.4 Immunogold Staining

The immunogold staining method was applied on the VLP samples in addition to the negative staining with phosphotungstic acid due to its higher specificity. The staining was performed at the University Hospital Regensburg under guidance of Heiko Siegmund and except the Rabbit-anti-BMV antibody and the Goat-anti-Rabbit antibody all chemicals and solutions were provided. All antibody solutions were centrifuged at 8,800 rcf for 2 minutes. Two controls for each sample were subjected in parallel to the staining procedure. The secondary Goat-anti-Rabbit antibody was replaced by a Goat-anti-Mouse antibody for the first control (Con 1) and the Rabbit-anti-BMV was replaced by a simple PBS solution for the second control (Con 2).

The pretreatment of the nickel grids (SCI - Science Services, Munich, Type 400 Mesh Square Nickel) included (1) a covering with Formvar plastic foil using a 1% (w/v) Formvar solution in chloroform, (2) a deposition of a carbon layer in an evaporation chamber (Leica BAL-TEC CTA005), and (3) a change of the surface from hydrophobic to hydrophilic by glow discharging in the same device. A drop of the VLP samples and the respective controls were applied on a Parafilm strip and the pretreated nickel grids were laid on top of the drops for incubation. After the removal of excess sample solution, a blocking step with a PBS/BSA solution (Dulbecco's Phosphate Buffered Saline, Sigma) was performed twice which included also an excess solution removal. The as-prepared grids were brought into a Leica IGL instrument, an immunogold staining automat, which performed the following steps automatically:

Table 3.2 Preparation steps for the immunogold staining performed by the Leica IGL device

Step	Incubation with	Solution volume per grid	Duration per step
1	Primary antibody solution	7 µL	60 min
2-6	PBS/BSA solution	30 µL	1 min
7	Secondary antibody solution	7 µL	30 min
8-10	PBS/BSA solution	30 µL	1 min
11-12	PBS solution	30 µL	1 min
13	Glutaraldehyde (2%) solution	30 µL	10 min
14-15	Double-distilled water	30 µL	1 min

After the removal of residual liquid from the grids outside of the device, the different samples were incubated with a 2 % solution of phosphotungstic acid and the grids were air-dried.

3.6   Chameleon Reader

3.6.1   Determination of Limit of Detection

The limit of detection (LOD) of the Chameleon reader was determined for unmodified UCNPs with a diameter of 12 nm. After preliminary studies setting the approximate concentration range a stock dispersion of these UCNPs with a concentration of 19.6 mg/mL was diluted twice to obtain two dispersions, one for an upper concentration range ranging from 50 to 1000 ng/mL and one for lower concentrations ranging from 1 to 10 ng/mL. Each concentration and pure cyclohexane as a blank with a volume of 200 μL was filled in five wells each of a 96 well microtiter plate (Greiner bio-one, polystyrole, flat bottom). The upconversion luminescence measurement was performed in the chameleon instrument with λ_{exc} = 980 nm and λ_{em} = 535 nm and each well was measured five times. The LOD was derived from the calibration curve obtained and the equation for the lowest detectable intensity (LDI)

$$LDI = x_{bg} + 3 \cdot \sigma_{bg}$$

with x_{bg} the average and σ_{bg} the standard deviation of the background intensity.

3.6.2   Scanning Mode

The scanning mode of the chameleon reader was implemented in the Chameleon software "Hidex CommFiler 2" (Version 2.64.00) by adjusting the following setting options:

- position of scan area
- number and spacing of scan points
- collecting time of the emission signal
- emission filter(s) employed

Preset parameters that are based on conventional microtiter plates with their respective dimensions or custom-made parameters can be used to create specified locations on a support. For this location programming the dimensions of the support, the number of locations desired and their relative positions on the support have to be known.

The total width W_{total} and the total height H_{total} is generally fixed by the plate holder of the Chameleon reader designed for microtiter plates and thus are set to 127.80 mm and 85.60 mm, respectively (Figure 3.3).
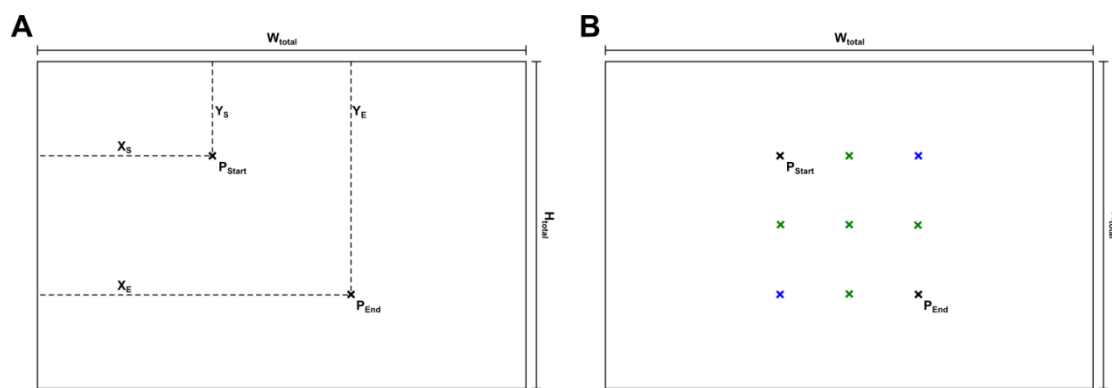
Figure 3.3 Support dimensions (W_{total} & H_{total}) and relative positions of the starting position (X_s/Y_s) and the ending position (X_E/Y_E) in relation to the upper left corner (A). The software defines according to this starting and end position (black crosses) and the overall number of desired positions the remaining positions (2x2 matrix: black & blue crosses; 3x3 matrix: all crosses) to form a rectangular matrix (B).

The location positions are defined by firstly configuring the vertical and horizontal distance of the upper left position (start position) and the lower right position of the desired quadratic matrix. These distances, i.e. the horizontal distance X_s and the vertical distance Y_s for the start position and the horizontal distance X_E and the vertical distance Y_E for the end position, are in relation to the upper left corner of the support (Figure 3.3A). According to these start and end positions and the set number of locations the software determines the positions of the remaining locations to form a square pattern resulting for example in a 2x2 (Figure 3.3B, black & blue crosses) or a 3x3 matrix (Figure 3.3B, all crosses).

These set positions form the centers of the scan areas and simultaneously determine the size of the scan areas. Since the scan areas measured are square-shaped and should fit together to form a continuous area without overlaps or gaps, the side length of the scan area equals the distance of the center positions (Figure 3.4).
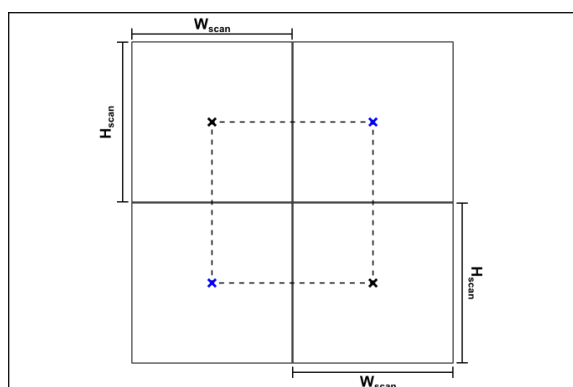
Figure 3.4 Dimensions of the optimal scan area (width W_{scan} x height H_{scan}). The four areas fit together to form a larger continuous scanned area ($2W_{scan}$ x $2H_{scan}$) without overlaps or gaps due to the optimal side length equaling the center distance.

These scan area dimensions are set by the number of scanning points and their distance to each other. For example, with a position distance of 9 mm both a number of 324 scan spots (18x18 square, Figure 3.5A) with a distance of 500 µm and a number of 1296 scan spots (36x36 square, Figure 3.5B) with a distance of 250 µm can be set to obtain the predefined side length of 9 mm. During the scan these spots are measured sequentially starting from the lower left to the upper right position line-by-line starting from the left (Figure 3.5C).
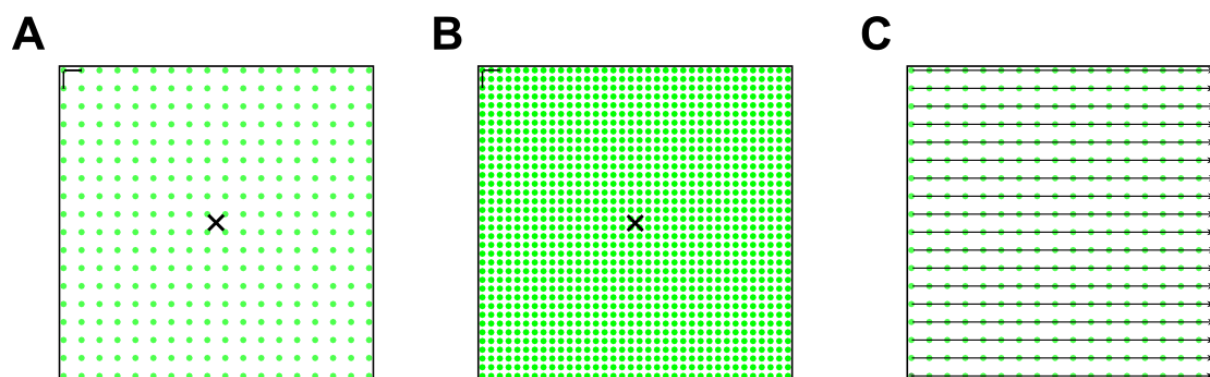
Figure 3.5 Scan area (center position indicated by black cross) with 324 scan spots (A) and 1296 scan spots (B). The black bars in both images indicate 500 µm. The scan order of these points is line-by-line from the left starting with the lower left spot and ends with the upper right spot (C), depicted for 324 scan spots.

Additionally, the collecting time at a single position defines the intensity of the detection signal and the measurement period. Furthermore, the emission filters chosen for the scan have to match the upconversion luminescence of the UCNPs labels, since they define the emission detected by the photomultiplier tube. Figure 3.6 shows the emission spectra of erbium- or thulium-doped UCNPs and the matching filter(s).
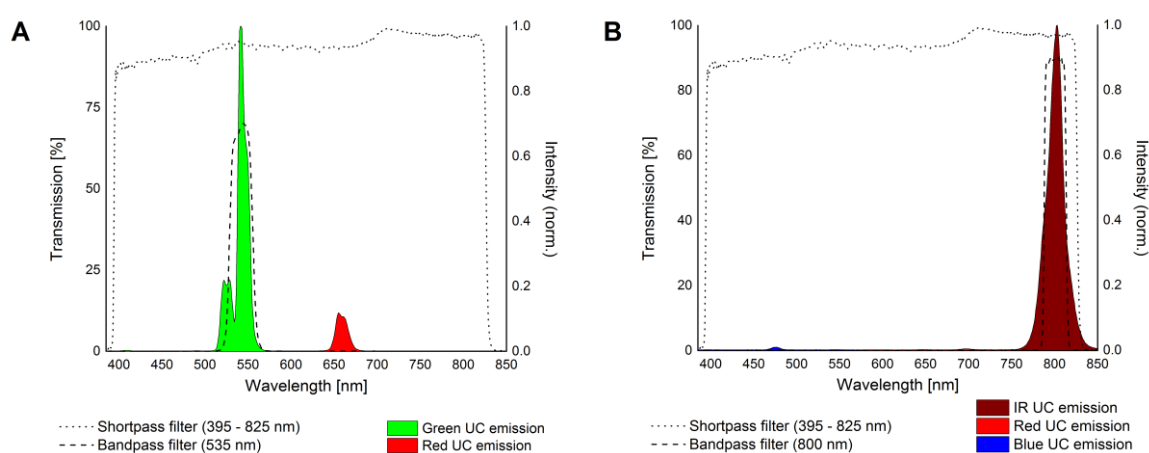
Figure 3.6 Transmission spectra of optical filters and the emission spectra of UCNPs doped with erbium (A) or thulium (B).

The shortpass filter is usable for both nanoparticle types to obtain scans with the overall emission as the measurement signal. If solely the green emission of $NaYF_4$:Yb, Er ranging from 510 to 560 nm or the IR emission of $NaYF_4$:Yb, Tm ranging from 775 to 825 nm is to be recorded, the respective

bandpass filter can be used. Their combination with the shortpass filter enables scan measurements with reduced background due to a more sufficient exclusion of excitation light.

For the scan itself the sample has to be fixed on a solid and even support whose material is not subjected to any limitations. The scan can then be performed to obtain either an image of the whole specimen or several smaller images with different settings by dividing the area into smaller subareas depending on the region of interest. The resulting data set was converted into a 2D matrix and in the case of subareas recomposed to an overall 2D matrix of the whole specimen. Finally, this matrix was used to create a pseudo-color image of the specimen with a color-coded intensity scale using the software "OriginPro 9" (Version 9.0.0).

3.7   Gel Electrophoresis

The separation of UCNPs by gel electrophoresis was performed by Dr. Antonín Hlaváček at the Central European Institute of Technology (CEITEC) of Masaryk University in Brno. The detailed nanoparticle preparation and electrophoresis implementation is given in literature[260].

3.8   Preparation of Lateral Flow Assays

The lateral flow assays were prepared by the group of Paul L. A. M. Corstjens at the department of molecular cell biology of the Leiden University Medical Center. A specific monoclonal mouse-anti-CAA antibody (MACAA) for the analyte *Schistosoma* circulating anodic antigen and a polyclonal goat-anti-mouse antibody (GAM, purchased from Sigma-Aldrich) were bound on a laminated nitrocellulose membrane (Millipore) by a Linomat 5 device (Camag Scientific, www.camag.com) to form the test and the control line, respectively. Assays with a width of 4 mm were prepared according to literarture[407] after the introduction of a glass fiber sample as the application pad and a paper absorbent pad. Additionally, the UCNPs of the type $Y_2O_2S:Yb^{3+},Er^{3+}$ coated with a layer of silica were modified with the MACAA[213] to introduce a recognition capability during labeling.

The dilution of the crude *Schistosoma* extract in immunochromatography buffer (100 mM HEPES, 270 mM NaCl, 0.5 % (w/v) of Tween 20, 1% (w/v) of BSA, pH 7.2) yielded a series of solution concentrations ranging from 10 to 10,000 pg/mL. These samples were applied to one assay each with one assay treated with buffer only serving as the negative control. The resulting lateral flow assays were treated with 100 ng of modified UCNPs for labeling and subsequently dried for storage.

3.9   Wafer Preparation

The potential plasmonic enhancement of the upconversion luminescence by a gold surface was studied on the surface of commercially available silica wafers with a size of 10 mm x 3 mm and gold layers with two possible formats (Figure 3.7) but otherwise same characteristics. The gold layers with a thickness of 300 nm were deposited on the silica surface by vapor deposition and had an overall area of approximately 4 mm^2.

The microelectrodes were coated with the same functionality on both silica and gold to ensure that changes in intensity solely results from the plasmonic enhancement by the gold surface.
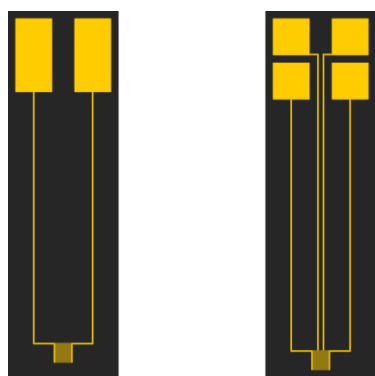
Figure 3.7 Scheme of silica microelectrodes with 2x1 (left) and 2x2 (right) setup of gold electrodes with an area of 4 mm^2.

The functionalization process was performed as follows. The wafers were first cleaned overnight in 1 mL ethanol under shaking at 500 rpm to remove any residues from the wafer preparation and impurities. The silanization of the silica surface was carried out in a 5% toluene solution of the octanyl or carboxyl silane overnight. After a washing step in ethanol to remove any residual silanes the wafers were immersed in an ethanol solution of the respective thiol with a concentration of 3 mmol/L and shaken overnight. Any access thiols were subsequently removed by washing, at least two times, with ethanol and the solvent was allowed to evaporate to dry the wafers.

4. Surface Modifications for Biofunctionalization

4.1 Demands on Upconverting Nanoparticle for Encapsulation

Upconverting nanoparticles after surface modification had to fulfill three requirements to be suitable cores for the generation of virus-like particles (VLP) by capsid encapsulation. Firstly, a general dispersibility of the nanoparticles in aqueous media involved a shift of the nanoparticle surface from hydrophobic to hydrophilic and thus only polar or ionic groups were reasonable choices as surface functionalities. Secondly, the nanoparticles had to be smaller than the diameter of the inner cavity of the virus capsid (18 nm for the BMV capsid) with a narrow size distribution, i.e. monodispersity, to allow a general encapsulation. Thirdly, a negatively charged UCNP surface at physiological pH 7.4 was mandatory for the self-assembly of the virus capsid by taking on the role of the original viral RNA.

Nanoparticles in dispersion scatter light depending on their size which is the measurement principle of the dynamic light scattering (DLS) method utilized for characterization. Additionally, this techniques are predominantly non-destructive and do not affect the sample enabling a subsequent use without any limitations. Therefore, DLS was suitable to determine the monodispersity of modified nanoparticles. Especially the polydispersity index (PdI) was a measure of the nanoparticle size distribution and was informative about the uniformity of the nanoparticle size, both of aggregates and single nanoparticles. While a narrow size distribution and thus monodispersity was given for polydispersity indices of 0.1 or lower, the nanoparticles were polydisperse with a moderate (0.1 < PdI < 0.4) or a broad (PdI > 0.4) size distribution.[408]

Although the hydrodynamic diameter, i.e. the sum of the actual nanoparticle diameter and thickness of its solvation shell, and not the actual nanoparticle size was determined by DLS techniques, a precise overview of the whole dispersion regarding aggregates or single nanoparticles was evaluated. The distribution of the hydrodynamic diameters was represented by the detected intensity or the number of nanoparticles (Figure 4.1).
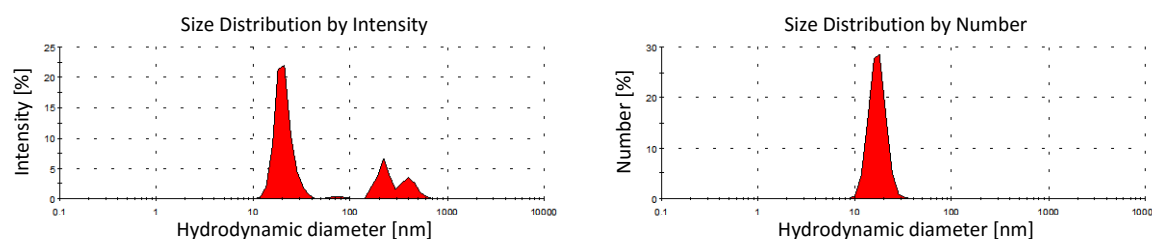

Figure 4.1 Exemplary distributions of the hydrodynamic diameter by the detected intensity (left) or the number of nanoparticles (right).

The distribution by intensity was directly obtained by the DLS measurement and the hydrodynamic diameter was depicted regarding the intensity of the scattered light caused by the respective nanoparticle fraction. Since there is a proportionality between this signal intensity and the sixth power of the (nano)particle diameter[409], larger nanoparticles have higher peaks in this distribution diagram. The data conversion by the instrument software to obtain the distribution according to number leveled out this overrepresentation. Therefore, the distribution of the hydrodynamic diameter is represented more accurately but depiction according to number is more affected by arising errors during data evaluation by the software. Consequently, its informative value was limited, yet a general conclusion about aggregation or the presence of small nanoparticles was still possible, especially when the distribution according to intensity was also taken into account for evaluation.

The actual size of a modified UCNP decided about the fit of the nanoparticle into the cavity of the virus capsid. Transmission electron microscopy (TEM) is capable to illustrate both UCNPs and a potential silica shell with a high contrast owing to their high and distinguishable electronic densities. Therefore, an accurate determination of the actual nanoparticle diameter was realized which allowed statements about the encapsulation probability, since sizes larger than the inner cavity of the capsid of 18 nm excluded encapsulation feasibility. A maximum diameter of 16 nm was chosen to take into account the contribution of the surface functionalities to the nanoparticle size since they were not detectable by TEM. Furthermore, TEM images also confirmed the presence of aggregates and additionally their structure. However, since TEM was time consuming and costly, the sampling number had to be restricted to one testing per batch. In combination with DLS measurements this imaging was sufficiently representative for the whole sample, although only a small volume fraction was analyzed.

An additional characterization method for nanoparticles relies on the determination of the zeta potential. It is an informative indicator for the surface charge of a modified UCNP and its absolute value allows conclusions about the stability of the nanoparticle dispersion. The zeta potential is the electric potential present at the outer border, i.e. slipping layer, of the electrostatic double layer forming on the surface of a charged nanoparticle (Figure 4.2). The net charge of this nanoparticle surrounded by ions in the Stern and slipping layer defines a specific electrophoretic mobility which can be harnessed to determine the zeta potential. The measurement principle of this mobility, more precisely the velocity of the charged nanoparticles in an applied electric field, is based on intensity fluctuations caused by the combination of the scattered light and a laser reference beam. The information is converted to the zeta potential by the instrument software.[409]
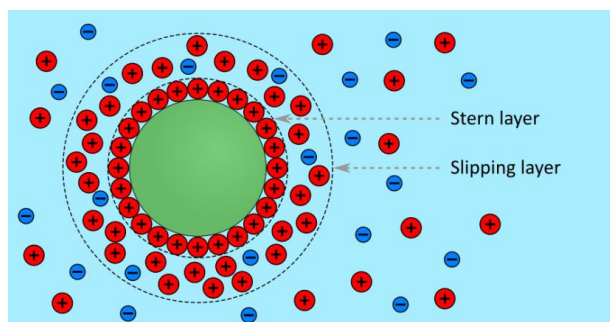
Figure 4.2 Schematic illustration of a negatively charged nanoparticle in dispersion with its electrical double layer including the Stern layer consisting of positively charged ions strongly bound to the nanoparticle surface and the slipping layer containing both positively and negatively charged ions with a more diffuse order.

The actual zeta potential of nanoparticle dispersion was measured in the distribution mode. This measurement type allowed a detailed presentation of the zeta potential regarding its maximum, average, and standard deviation which was especially important for samples with several nanoparticle fractions. The zeta potential of the nanoparticle sample provided information about the dispersion stability. The border between a stable and unstable dispersions is generally accepted as a potential of +30 mV and -30 mV, respectively, and thus an absolute value higher than 30 mV indicates a good dispersion stability.[409] Furthermore, since the nanoparticles acted as a replacement of the original RNA of the virus, only UCNPs with a negative zeta potential were logical options for the generation of VLPs by encapsulation.

The utilization of these methods to characterize UCNP modified with diverse surface functionalities provided satisfactory information about the monodispersity, absolute diameter and surface charge. Consequently, an informative conclusion about the suitability of these nanoparticles for the generation of VLPs was made by consulting these characteristics.

4.2   Silica Shell & Control of Thickness

Silica is a convenient material both to create a hydrophilic surface on the UCNP surface crucial for bioanalytical applications and to introduce a wide variety of useful functionalities such as amines, phosphonates, or carboxylic acids. Furthermore, the omnipresent silanol groups with a higher acidity than the aliphatic alcohols can be deprotonated in aqueous solution. The resulting negatively charged nanoparticle surface stabilizes the hydrophilic nanoparticles in dispersion by electrostatic repulsion. The silica-coated UCNPs (UCNP@SiO$_2$) were prepared according to literature[128] and the thickness of the silica shell was optimized by the adjustment of added tetraethoxy orthosilicate (TEOS).

An approximate correlation between the shell thickness and the TEOS amount was determined by the addition of 10, 5, or 4 µL of TEOS to the synthesis batch of UCNP@SiO$_2$ utilizing UCNPs with a diameter of 12 nm. The absolute diameter of these nanoparticles determined by transmission electron microscopy (TEM) is given in Table 4.1.

Table 4.1 TEM results of the silica coating of UCNPs with varying TEOS volumes

Code	UCNP diameter [nm]	TEOS volume [µL]	Shell thickness [nm]	Overall diameter [nm]
UCNP@SiO$_2$-10	12 - 15	10	5 - 6	22 - 27
UCNP@SiO$_2$-5	12 - 15	5	3 - 4	16 - 23
UCNP@SiO$_2$-4	12 - 15	4	1 - 2	14 - 19

Both the shell thickness and the absolute diameter of the UCNP@SiO$_2$ decreased logarithmically by the reduction of the TEOS volume added during synthesis. Furthermore, the synthesis using 4 µL yielded nanoparticles (UCNP@SiO$_2$-4) with an average overall size of 16.5 nm sufficient for encapsulation (Figure 4.3). A TEOS volume below this 4 µL may lead to a silica shell growth with a more uniform thickness of 1 nm for all nanoparticles but also an insufficient coating of the UCNP surface with silica becomes more probable. Furthermore, studies about the monodispersity of the different types of UCNP@SiO$_2$ revealed an opposite trend regarding the aggregation tendency. The polydispersity indices of the different UCNP@SiO$_2$ ranging between 0.20 and 0.35 suggested a moderate size distribution of the nanoparticles with an increased polydispersity observable for thinner silica shells. Additional to these aggregates found in the respective TEM images, DLS studies showed a strong increase of the average hydrodynamic diameter from 330 nm to 3100 nm (Figure 9.1-9.3). Especially the data comparison of UCNP@SiO$_2$-4 and UCNP@SiO$_2$-10 confirmed the formation of larger aggregates due to a thinner silica shell which was also found for the silica coating of other kinds of nanoparticles[410, 411]. This reduced stabilization of UCNP@SiO$_2$ with decreasing shell thickness was also indicated by the investigation of the zeta potential which decreases from -30 mV to -15 mV. However, the coating of UCNPs with pure silica created a negatively charged surface despite this decline in its absolute value.

Consequently, a reduction of the thickness of the silica could only be obtained by accepting an increased aggregation tendency of the nanoparticles, apparent in the hydrodynamic and absolute diameter of the coated UCNPs and their zeta potential. This phenomenon was traced back to three potential causes. Firstly, an incomplete surface coating of the UCNPs by the silica shell may cause electrostatic attraction of the resulting "naked" UCNP surface with its positive charge originating from the trivalent lanthanide dopants and the negatively charged silica surface of other (partly)

coated UCNPs. Secondly, if highly reactive silanol groups remain on the nanoparticle surface, covalent bonding reactions between two nanoparticle surfaces in close proximity might occur which led to an irreversible formation of larger aggregated structures. During work up an enhanced aggregation arises especially by centrifugation necessary for pellet formation or drying of the nanoparticles. Thirdly, a covalent surface linkage can also be promoted by any impurities in the reaction vessel initiating aggregation by nucleation during shell growth.

Figure 4.3 TEM image of UCNP@SiO$_2$-4 (*left*: 10,000x magnification, scale bar: 1 μm; *right*: 160,000x magnification, scale bar: 50 nm).

In conclusion, the generation of pure silica shells and a good control over the resulting shell thickness could be achieved by an adjustment of the TEOS amount added as suggested by literature[239]. The increasing aggregation tendency strongly hampered the suitability of silica-coated UCNPs for (bio)analytical application, although these nanoparticles with their small absolute size owing to the very thin shell and negative surface charge were potential initiators for capsid encapsulation. A simultaneous silanization was a new approach to increase the nanoparticle stability in dispersion and to introduce more accessible functionalities for future modifications while maintaining the beneficial low thickness of the silica shell. Organyl silanes with different functional groups such as amines, carboxylic acids, or phosphonates were suitable for this modification.

4.3 Amine Functionalization

The functionalization of UCNPs with amines (UCNP@SiO$_2$-NH$_2$) by silanization with 3-(aminopropyl)triethoxysilane (APTES) creates an accessible surface for the introduction of a magnitude of different species of biological compounds. These functionalities allow a fast, robust and simple linkage of different (bio)molecules or nanostructures, especially with activated carboxylic acids via ethyl(dimethylaminopropyl) carbodiimide (EDC) and N-hydroxysuccinimide (NHS). Furthermore, the dominant positive charge of ammonium ions formed by the protonation of amines

at physiological pH potentially stabilizes the modified UCNPs in dispersion owing to electrostatic repulsion.

The conversion of the negative charge of pure silica by the silanization with amines was recognizable in the strongly differing zeta potential of the UCNP@SiO$_2$-NH$_2$ (+21.8 mV, Figure 9.20) and the reference sample (UCNP@SiO$_2$, -4.2 mV) which was synthesized according to the same protocol but without the amine silane. In addition, this change in sign of the potential verified the presence of amines on the nanoparticle surface. The decrease of the polydispersity index (0.134) and the hydrodynamic diameter (460 nm) indicated an improvement of the monodispersity and general size of the as-modified UCNPs compared to non-functionalized nanoparticles (UCNP@SiO$_2$-4) with the same thin shell. Consequently, a simultaneous silanization during silica shell growth exerted a beneficial effect on the nanoparticle quality. Its compatibility with the coating process to obtain a thin silica shell was demonstrated by TEM imaging (Figure 4.4) showing a thickness of 1-2 nm. However, both DLS and TEM measurements revealed a strong aggregation tendency of the UCNP@SiO$_2$-NH$_2$ and significant multicore encapsulation by silica similar to the modification with pure silica (Figure 4.3).
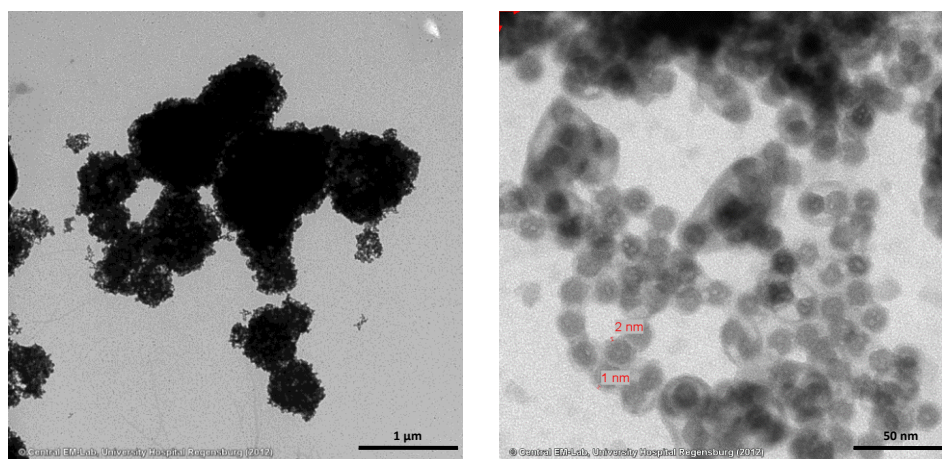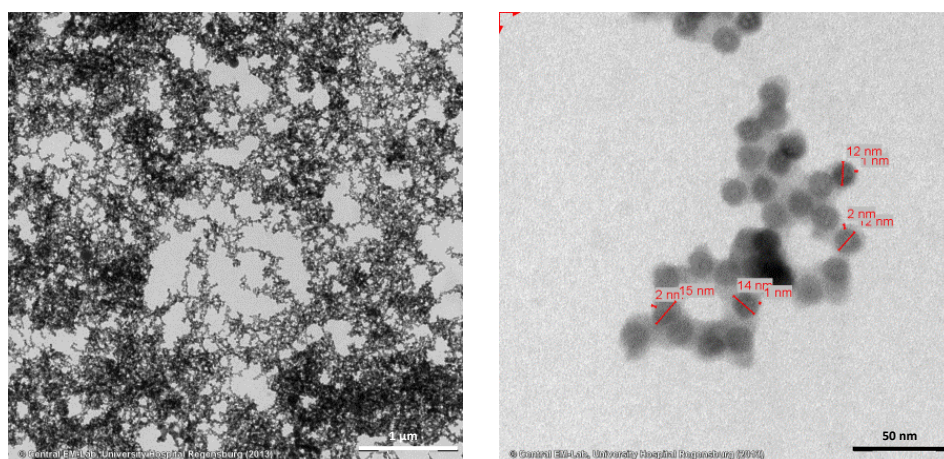

Figure 4.4 TEM image of UCNP@SiO$_2$-NH$_2$ (*left*: 10,000x magnification, scale bar: 1 µm; *right*: 200,000x magnification, scale bar: 50 nm).

This strong susceptibility of these nanoparticles to aggregation was explained by amine-specific electrostatic interactions with negatively charged surfaces. An insufficient conversion of silanol groups into amines creates positively charged subareas on the UCNP surface whereas the remaining surface keeps its negative charge. These opposite charges lead to an attraction of different nanoparticles and enhance the aggregation of the nanoparticles. Furthermore, a back bonding of the positively charged amines to the negative silica surface of the same nanoparticle can occur which was also found for amine-functionalized silica nanoparticles[8]. The resulting cancellation of the stabilizing positive charges leads to an increased aggregation tendency.

In conclusion, the improved monodispersity and smaller hydrodynamic diameter of UCNP@SiO$_2$-NH$_2$ demonstrated the positive influence of the simultaneous silanization on the stability of modified UCNPs. However, for the encapsulation with the BMV capsid the intrinsic positive surface charge excluded the utilization of these nanoparticles. In contrast, the fast and simple coupling chemistry of amines with carboxylic groups of biomolecules using EDC/NHS activation is a promising way for the attachment to the UCNP surface as long as the still remaining strong aggregation is addressed by future optimization. The resulting monodisperse nanoparticles with a specific recognition entity like antibodies are of great interest especially for bioanalytical targeting applications.

4.4 Carboxylic Acid Functionalization

In contrast to amine functionalities, carboxylic groups feature an intrinsic negative charge at physiological pH leading to a good stabilization of as-modified UCNPs and they are accessible to well established coupling reactions at the same time. Especially the EDC/NHS activation mentioned before is a general coupling option for a fast and efficient biomolecule attachment. Furthermore, an incomplete surface modification by carboxyl functionalities has a lower impact on aggregation, since the present electrostatic interactions of carboxyl and silanol groups are of repulsive nature. These advantageous characteristics led to a more thorough study and optimization of the UCNPs modified with carboxylic groups (UCNP@SiO$_2$-COOH).

The influence of the pH on the dispersion stability of UCNP@SiO$_2$-COOH was investigated by using a buffer system with a neutral pH 7 or alkaline pH 9 which simultaneously counteracts acid-base-reactions by the carboxyl functionalities. Acidic buffer systems were ignored since UCNP@SiO$_2$-COOH strongly aggregate below a pH of 6 due to the loss of the negative surface charge[248]. The two batches studied were synthesized by the same route for improved comparability. The zeta potential as an informative indicator for dispersion stability averaged about -25 mV for the UCNP@SiO$_2$-COOH batches of both pHs. In contrast to this similarity in the overall potential of both samples, the distribution of the zeta potential for pH 9 featured a single peak with a maximum of -35 mV (Figure 9.21) indicating a high potential uniformity, whereas a partitioning into three subdivisions occurred for a neutral pH with the major fraction with a maximum potential of -11 mV (Figure 9.22). Alkaline buffers were thus favorable for the work up and storage of UCNP@SiO$_2$-COOH, since an improved dispersion stability was realized owing to a more homogeneous and stable surface charge.

Furthermore, the adaption of the preparation protocol of UCNP@SiO$_2$-NH$_2$ for the synthesis of UCNP@SiO$_2$-COOH nanoparticles necessitated a process adjustment. There were three major focuses for this optimization studies.

Firstly, the breaking of the nanoparticle-containing micelles in the microemulsion of the same UCNP@SiO$_2$-COOH batch was induced either by acetone according to the synthesis of UCNP@SiO$_2$-NH$_2$ (work up **A**) or ethanol according to literature[248] (work up **B**). The impact of these solvents on nanoparticle aggregation was assessed by differences in the hydrodynamic diameter of the UCNP@SiO$_2$-COOH. The precipitation of the nanoparticles by acetone in work up **A** seemed to lead to a stronger temporary destabilization and thus a slightly enhanced formation of aggregates (Figure 9.5). In comparison, the addition of ethanol in work up **B** (Figure 9.6) to the microemulsion destabilized the UCNP@SiO$_2$-COOH to a lesser extent resulting in predominantly monodisperse small nanoparticles. Both work up designs were repeated for different batches confirming a high reproducibility despite minor variations which justified the preference of work up **B**.

Secondly, a change in purpose of the threefold washing of the nanoparticles by centrifugation was determined during the optimization studies of the work up protocol. While a removal of reaction components including organic solvent, detergent, TEOS, and organyl silanes was initially anticipated by this process, the high stability of UCNP@SiO$_2$-COOH in dispersion caused instead a separation of aggregates from smaller nanoparticles. This new function of the three washing steps *I-III* was verified by investigating the different washing solutions regarding the hydrodynamic diameter of dispersed nanoparticles. The first washing solution (Figure 9.7) contained primarily nanoparticles with a very small size (hydrodynamic diameter: 18 nm) and good monodispersity (PdI 0.275) and their zeta potential of approximate -25 mV as well as visual long-term controls for nanoparticle precipitation confirmed their good stabilization in dispersion. The larger hydrodynamic diameters (105 - 300 nm) with hardly any indication of smaller nanoparticles and the broader size distribution (PdI 0.595) for washing solutions *II* confirmed a nearly complete transfer of larger aggregates to this dispersion by centrifugation (Figure 9.8). A slight shift to larger diameters for the washing step III indicates only minor separation of the large nanoparticle aggregates.

Thirdly, the volume of added TEOS and CEST for the synthesis of UCNP@SiO$_2$-COOH had to be adjusted to take into account the differences in mass concentration, size and surface area of the nanoparticles utilized in this thesis and literature[248]. The detailed calculation for this adjustment to obtain the conversion factor is given in chapter 9.5 in the Appendix. The necessary volumes of TEOS and CEST were determined with the calculated factor of 2.06 ensuring a good conformity of the adapted synthesis with literature (Table 4.2). The minimal volume of 41 µL for TEOS and CEST to obtain a complete silica coating and functionalization was increased to an actual volume of 46 µL to ensure an efficient shell growth and simultaneous silanization. A CEST volume of 60 µL had no influence on nanoparticle stabilization or aggregation behavior which was checked in additional experiments.

Table 4.2 TEOS and CEST volumes needed for adapted synthesis from literature with a correction factor of 2.06

	V_{TEOS} [µL]	V_{CEST} [µL]
Literature[248]	20	20
Adaption	41	41
Actual used	46	46

Consequently, these investigations of the UCNP@SiO$_2$-COOH synthesis led to the utilization of ethanol instead of acetone as the precipitation solvent, the isolation of monodisperse small nanoparticles by the washing step *I*, and the increased TEOS and CEST volume of 46 µL compared to the original 20 µL and yielded the general procedure described in the Experimental Part.

The qualitative detection of carboxylic acids on the nanoparticle surface was realized by infrared spectroscopy due to the strong IR-activity of these functionalities. A requirement for an unambiguous detection is the absence of other carboxyl species like acetic acid, e.g. as a buffer component, in the measured sample. Furthermore, IR spectroscopy allows a measuring of nanoparticles in both dry and dispersed state. Especially, the dried sample gave good informative IR spectra (Figure 4.5) owing to the absence of the very strong O-H valence band originating from water molecules. These findings allowed an unambiguous detection of carboxyl functionalities with a high reliability and thus a confirmation of a successful functionalization process.
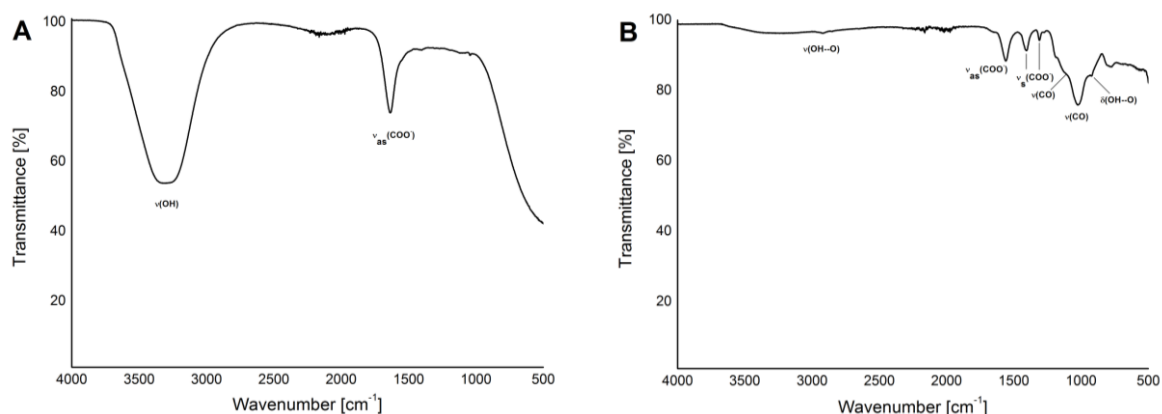
Figure 4.5 Infrared (IR) spectra of UCNP@SiO$_2$-COOH (A) in dispersion and (B) as dried powder with vibration assignments[412].

The optimized UCNP@SiO$_2$-COOH featured a very small hydrodynamic diameter of about 18 nm (Figure 9.9) with a good monodispersity (PdI 0.271). The majority of nanoparticles in the dispersion were of this small size, whereas aggregates formed a nearly insignificant fraction. Furthermore, a negative surface charge of the UCNP@SiO$_2$-COOH was confirmed by the average zeta potential of -19 mV (Figure 9.23) indicating a moderate dispersion stability and this potential was reproducibly

observable for different synthesis batches of UCNP@SiO$_2$-COOH. Precipitation studies by bare eye and determinations of the hydrodynamic diameter revealed no aggregation over several weeks. TEM imaging showed an absolute diameter of 13 nm for UCNP@SiO$_2$-COOH and confirmed the high monodispersity and small size of these nanoparticles (Figure 4.6, left) with hardly any observation of larger aggregates (Figure 4.6, right).
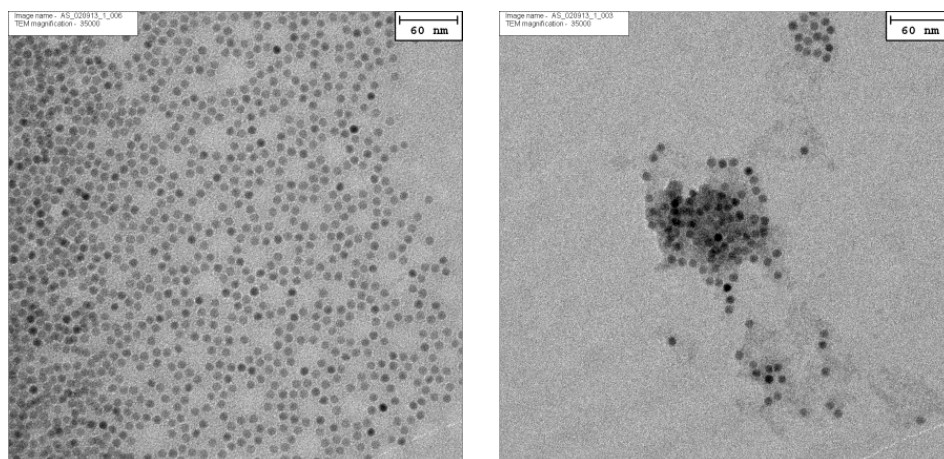
Figure 4.6 TEM image of UCNP@SiO$_2$-COOH (*left*: 3,500x magnification, scale bar: 60 nm; *right*: 3,500x magnification, scale bar: 60 nm).

In conclusion, UCNP@SiO$_2$-COOH nanoparticles were monodisperse with a very low aggregation tendency. The low diameter as well as the negative surface charge of these single nanoparticles enabled their use for the encapsulation by the BMV capsid to form VLPs.

4.5   Coating with Polyacrylic Acid

A renunciation from a covalent approach toward non-covalent methods for the generation of UCNPs equipped with carboxylic groups entails several advantages for the nanoparticle surface modification. A drastically reduced expenditure of time and simplified work up procedure with minimized chances for aggregation can be achieved and are met by the ligand exchange performed according to the NOBF$_4$ method[269]. The polymer polyacrylic acid (PAA) has a multitude of acidic groups suitable for surface coordination and functionality introduction. Additional to studies about the general suitability of this polymer for the coating of UCNPs by the NOBF$_4$ method two different molecular masses, 2100 g/mol and 5100 g/mol, were utilized to investigate potential influences of the chain length on the stabilization efficiency and yielded nanoparticles of the type UCNP@PAA(2100 g/mol) and UCNP@PAA(5100 g/mol).

A zeta potential above -35.0 mV for both nanoparticle types demonstrated a high dispersion stability as well as a strongly negative surface (Figure 9.24-9.25). Furthermore, the hydrodynamic diameter of

UCNP@PAA(5100 g/mol) which was determined by DLS to be 12 nm according to the number representation was slightly larger than the 10 nm of UCNP@PAA(2100 g/mol) (Figure 9.10-9.11). A reason for this increase of the solvation layer thickness around a nanoparticle was reduced to a stronger attraction of water molecules by PAA with molecular mass of 5100 g/mol due to its higher number of negatively charged carboxylic groups.

Moreover, a moderate size distribution of UCNP@PAA(5100 g/mol) was assumed apparent in a PdI of 0.270, whereas the UCNP@PAA(2100 g/mol) seem to be strongly polydisperse (PdI 0.609). However, the hydrodynamic diameter according to nanoparticle number featured a quite narrow size distribution with a maximum around 10 nm without any indication of aggregates and the zeta potential suggested a low tendency for aggregation. The measured broad size distribution was attributed to the presence of contaminations in the dispersion which had no unfavorable interference on the encapsulation process, as shown later. Consequently, the UCNP@PAA(2100 g/mol) were assumed to have similar degree of monodispersity as the UCNP@PAA(5100 g/mol) which was also supported by the high similarity of the hydrodynamic diameters of both nanoparticle types.

The determination of the absolute diameter of UCNP@PAA(5100 g/mol) by TEM (Figure 4.7) revealed a nanoparticle size of only 7-8 nm which was lower by a third than the assumed diameter of 12 nm.
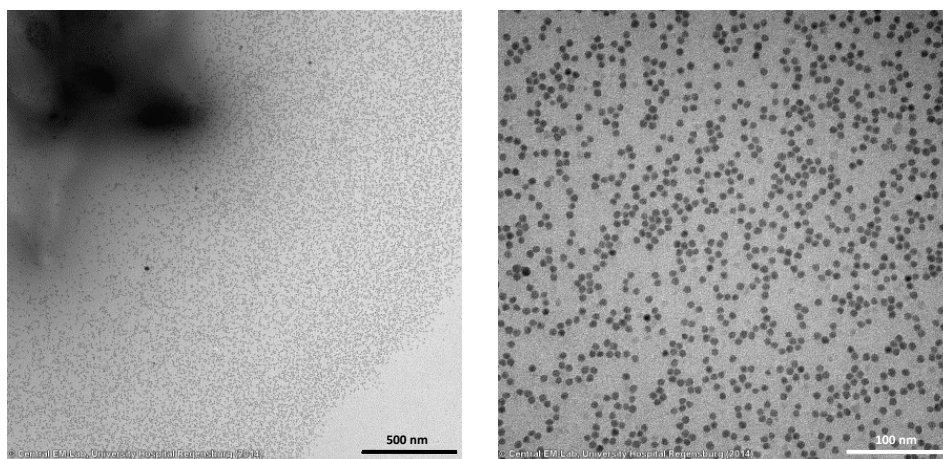
Figure 4.7 TEM image of UCNP@PAA(5100) (*left*: 40,000x magnification, scale bar: 500 nm; *right*: 200,000x magnification, scale bar: 100 nm).

Consequently, for the investigation of this discrepancy also the original oleate-coated UCNPs utilized for the synthesis of both types of PAA-coated UCNPs were imaged by TEM. A comparison of their absolute size to the diameter of UCNP@PAA(5100 g/mol) showed a high conformity in size of both nanoparticle types (Figure 4.8). This result was also an explanation for the high difference between the expected and the actual hydrodynamic diameter of the PAA-coated UCNPs. This dimension has to

be larger than the absolute diameter of the nanoparticle due to the inclusion of the solvation shell around the nanoparticle. However, the hydrodynamic diameter of UCNP@PAA(2100 g/mol) or UCNP@PAA(5100 g/mol) was 10 nm and 12 nm, respectively, which was equal to or smaller than the assumed absolute diameter of 12 nm. The lower absolute diameter of 7-8 nm found by TEM explained these results.
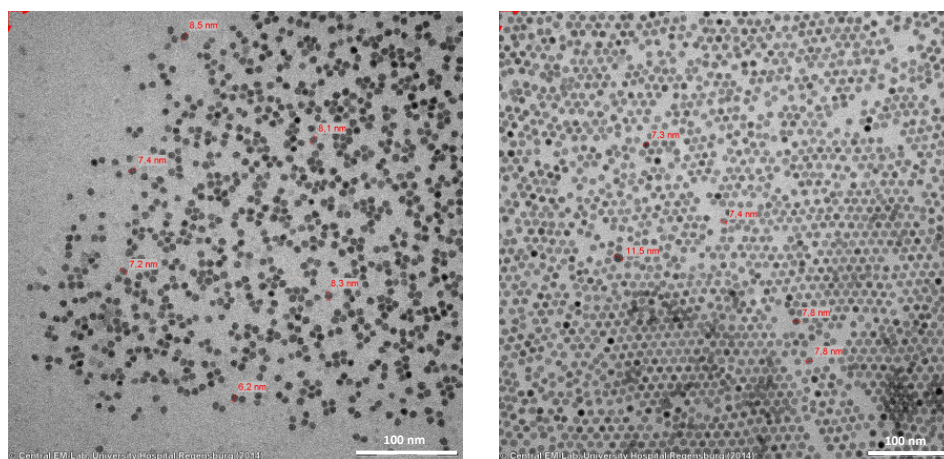
Figure 4.8 TEM images for size comparison between UCNP@PAA(5100) (*left*: 200,000x magnification, scale bar: 100 nm) and unmodified UCNP in cyclohexane (*right*: 200,000x magnification, scale bar: 100 nm).

Finally, the functionalization of UCNPs with PAA was shown to be realizable, also with different molecular masses of the polymer. These nanoparticles fulfilled the requirements of a high monodispersity and negative surface charge which were necessary for the encapsulation by the BMV capsid. The formation of VLPs was also unaffected by the lower absolute diameter compared to the assumed size.

4.6 Phosphonate Functionalization

A more realistic imitation of the native phosphate backbone of the viral genome compared to a modification with carboxylic acid is the introduction of phosphonate groups on the UCNP surface. Since a functionalization with the silane 3-(trihydroxysilyl)propyl-methylphosphonate (TPMS) showed a high stabilization capability of as-modified UCNPs[8], this organic silane was chosen for the UCNP modification (UCNP@SiO$_2$-Ph). The obtained phosphonate-modified surface might be capable to be the nucleation grain in the self-assembly process of the capsid.

DLS measurements revealed that UCNP@SiO$_2$-Ph feature a very high monodispersity (PdI 0.072) and a hydrodynamic diameter of 333 nm (Figure 9.12). Consequently, this type of nanoparticles seemed to form aggregates with a high size uniformity, in contrast to most other modified UCNPs described in this work. Furthermore, the imaging of the UCNP@SiO$_2$-Ph by TEM (Figure 4.9) showed circular

structures containing nanoparticles with an absolute diameter of 13 nm. The high number of UCNP@SiO$_2$-Ph as well as the high electronic density by overlapping was also shown (Figure 4.9, inset). A hypothesis for this phenomenon was a higher attraction of the modified nanoparticles to each other than to the surrounding aqueous medium. The zeta potential of -32 mV confirmed a negatively charged surface and high stability in dispersion of these aggregates (Figure 9.26). In addition, a low impact of external influences was demonstrated, since extensive washing did not affect the integrity of these aggregates.
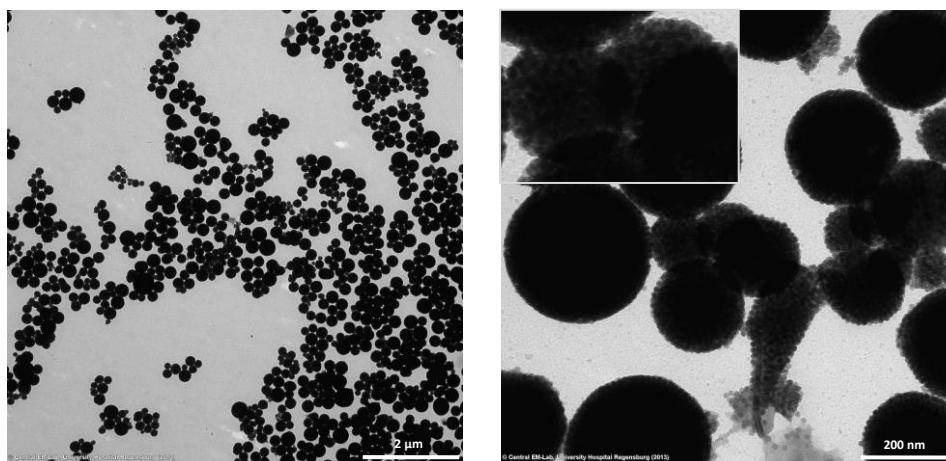
Figure 4.9 TEM image of UCNP@SiO$_2$-Ph (*left*: 10,000x magnification, scale bar: 2 μm; *right*: 100,000x magnification, scale bar: 200 nm).

In conclusion, the strong negative surface charge as well as the absolute nanoparticle diameter of 13 nm enables the use of UCNP@SiO$_2$-Ph as artificial cores for the VLP synthesis but the high affinity of the nanoparticles to each other might hamper the self-assembly process of the capsid due to the low number of singe nanoparticles.

4.7   Alkyne & Azide Functionalization

The functionalities mentioned in the previous chapters are omnipresent in biological systems but their high abundance has the disadvantage of a reduced selectivity and efficiency of their coupling reactions in *in vitro* and *in vivo* systems. In contrast, so-called bioorthogonal functionalities such as organic azides and terminal alkynes show no interaction with biological species and thus no interference with biochemical processes. Azides and alkynes are naturally absent in biological systems and can be coupled by the highly selective copper-catalyzed azide-alkyne cycloaddition (CuAAC) which is a Click reaction. An efficient linkage of (bio)molecules to the nanoparticle surface can be realized with these clickable functionalities without disturbances by the biological system.

The existence of these functionalities on the nanoparticle surface as well as the feasibility of the CuAAC coupling reaction was investigated fluorometrically after the attachment of a fluorophore with the complementary functionality (Figure 4.10). Furthermore, the need of the copper catalyst on the coupling reaction was verified during these studies.
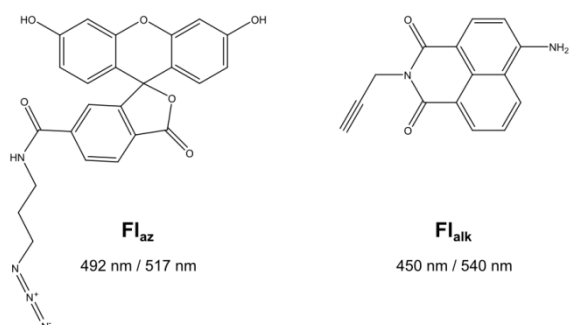
Figure 4.10 6-Fluorescein-azide (Fl$_{az}$) and 4-amino-N-(2-propynyl)-1,8-naphthalimide (Fl$_{alk}$) with their respective $\lambda_{exc}/\lambda_{em}$ utilized as clickable fluorophores.

In a first study, a surface functionalization with alkynes allowed the coupling of azide-containing species to the nanoparticle. The presence of these groups on these UCNPs (UCNP@SiO$_2$-Alk) was confirmed by the attachment of a fluorescein derivative Fl$_{az}$ (λ_{exc} = 492 nm, λ_{em} = 517 nm), UCNP@SiO$_2$ nanoparticles as the negative control and a fluorescein solution as the positive control. Together with the study of the copper catalyst efficiency, the four samples UCNP@SiO$_2$-Alk with or without Cu(II) ions (**F$^+$/F$^-$**) and UCNP@SiO$_2$ with or without Cu(II) ions (**O$^+$/O$^-$**) were investigated. The fluorescence spectra of the different samples are given in Figure 4.11 which were recorded under the same conditions to ensure comparability.
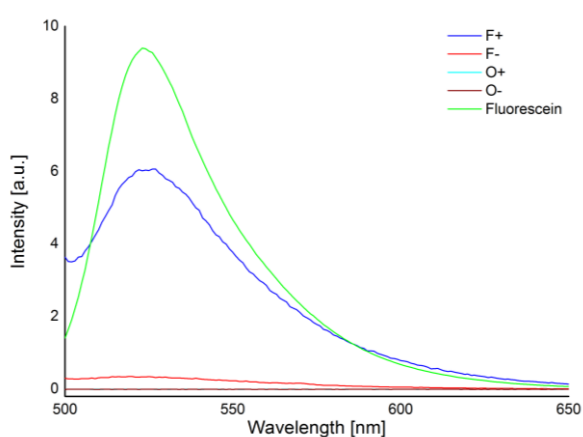
Figure 4.11 Fluorescence spectra of the F$^+$, F$^-$, O$^+$, and O$^-$ samples of UCNP@SiO$_2$-Alk after Click reaction with Fl$_{az}$ with a fluorescein solution as the reference

The spectra unambiguously illustrated a successful labeling of only the UCNP@SiO$_2$-Alk in presence of the copper catalyst. **F$^+$** shows a distinct peak at 525 nm similar to the pure fluorescein with a

negligible red shift compared to the expected 520 nm. The controls **O$^+$** and **O$^-$** cannot be distinguished in the spectrum since they show no emission at any wavelength. The weak signal of **F$^-$** is attributed to the occurrence of a minor coprecipitation of Fl$_{az}$ due to aggregation of UCNP@SiO$_2$-Alk during the labeling and washing processes.

The strong aggregation was assumed to be a result of the unpolar character of the alkyne functionalities leading to a hydrophobic character of the UCNP@SiO$_2$-Alk surface. Its occurrence was observed by the bare eye in form of rapid precipitation both during work up and storage. Furthermore, these aggregates featured a high polydispersity (PdI 0.548) and their hydrodynamic diameter of over 1000 nm (Figure 9.13) was only reliably detectable if visible precipitates were permitted to settle for a longer period of time. The zeta potential of +5 mV (Figure 9.27) confirmed the insufficient stabilizing effect of the hydrophobic alkyne groups and indicated a close to neutrality charged nanoparticle surface owing to the lack of a real charge or at least a significant dipole moment. TEM imaging revealed an absolute diameter of 13 nm of the UCNP@SiO$_2$-Alk and also the high number and large size of the aggregates were observable (Figure 4.12), partially covering whole grid sections. Similar to UCNP@SiO$_2$-Ph the higher attraction of the nanoparticles among each other was evident but the bulky and shapeless structures suggested a more undirected hydrophobic interaction.
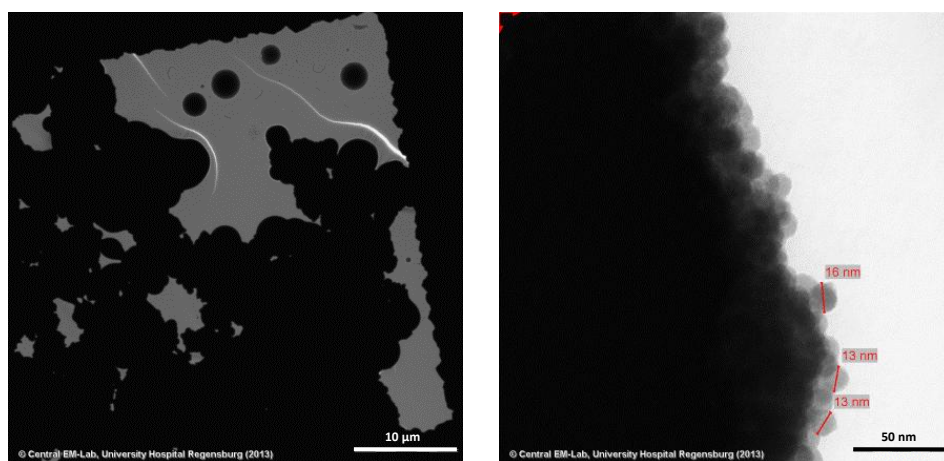
Figure 4.12 TEM image of UCNP@SiO$_2$-Alk (*left*: 1,000x magnification, scale bar: 10 μm; *right*: 200,000x magnification, scale bar: 50 nm).

In a second study, the clickable groups were exchanged so that the UCNPs were modified with azides which could be coupled with species featuring alkyne moieties. The existence of azide groups on the UCNP surface (UCNP@SiO$_2$-Az) and a feasible coupling reaction was again verified fluorometrically after the attachment of the naphtalimide fluorophore Fl$_{alk}$ (λ_{exc} = 450 nm, λ_{em} = 540 nm, Figure 4.10) with UCNP@SiO$_2$ nanoparticles serving as the negative control. Furthermore, the addition or omission of a copper(II) species was performed for catalyst studies as for UCNP@SiO$_2$-Alk. The

fluorescence of the four samples UCNP@SiO$_2$-Az with or without Cu(II) ions (**F$^+$/F$^-$**) and UCNP@SiO$_2$ with or without Cu(II) ions (**O$^+$/O$^-$**) was detected (Figure 4.13) using the same measurement settings to ensure comparability.
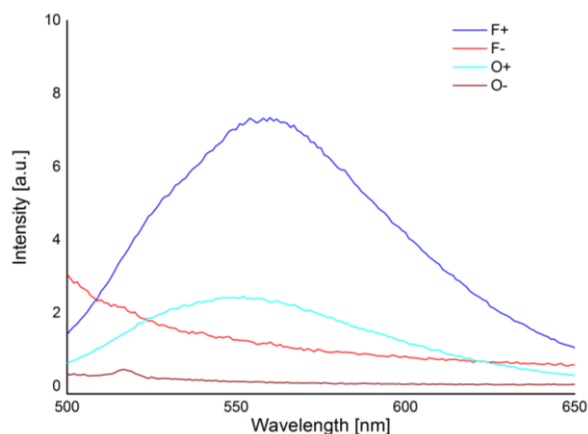
Figure 4.13 Fluorescence spectra of the F$^+$, F$^-$, O$^+$, and O$^-$ samples of UCNP@SiO$_2$-Az after Click reaction with Fl$_{alk}$

The high fluorescence of **F$^+$** provided direct proof of azide functionalities on the surface of UCNP@SiO$_2$-Az. The copper-free controls **F$^-$** and **O$^-$** showed no emission in the relevant wavelength range around the assumed maximum of 540 nm showing the importance of the copper(II) species for the CuAAC. An unspecific binding of the fluorophore to the silica surface of the UCNP@SiO$_2$ was indicated by the fluorescence signal of sample **O$^+$** which was anticipated to be reduced after additional washing steps.

Furthermore, dispersions of UCNP@SiO$_2$-Az had a satisfactory size distribution (PdI 0.169) and the hydrodynamic diameter of the majority of nanoparticles was around 300 nm (Figure 9.14). These improved characteristics compared to the also clickable UCNP@SiO$_2$-Alk were attributed to the dipolar nature of azide functionalities and indicate a good hydrophilicity of the nanoparticle surface. A negative surface charge of the nanoparticles was confirmed by a zeta potential of -28 mV (Figure 9.28) which suggested a moderate dispersion stabilization. The presence of small or medium sized aggregates was also demonstrated by TEM (Figure 4.14) and UCNP@SiO$_2$-Az had an absolute diameter of 13 nm. Moreover, the simultaneous existence of single nanoparticles suggested a weaker driving force of aggregation, in contrast to UCNP@SiO$_2$ and UCNP@ SiO$_2$-NH$_2$.

In conclusion, the introduction of the clickable alkyne of azide groups was demonstrated and their presence on the nanoparticle surface was verified by the detection of an attached fluorophore. Both functionalities were generally accessible binding sites for the attachment of (bio)molecules via the bioorthogonal coupling reaction CuAAC. Despite the high accessibility of these functional groups the stability characteristics of these as-modified UCNPs differed significantly. While single UCNP@SiO$_2$-Az

nanoparticles were prepared with a high reproducibility and stability in dispersion, UCNP@SiO$_2$-Alk featured a hydrophobic surface with a nearly neutral charge leading to strong aggregation of the nanoparticles in aqueous dispersion. Consequently, UCNP@SiO$_2$-Az nanoparticles were solely utilized for the more detailed investigation of the CuAAC as a bioorthogonal coupling reaction for different molecules in chapter 4.9.
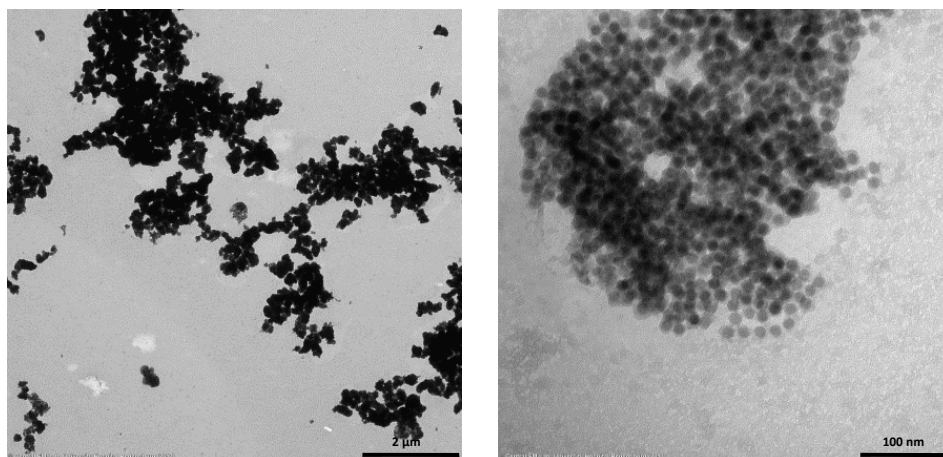
Figure 4.14 TEM image of UCNP@SiO$_2$-Az (*left*: 10,000x magnification, scale bar: 2 μm; *right*: 200,000x magnification, scale bar: 100 nm).

4.8   Carboxylic Acid & Azide Functionalization

A surface modification of UCNPs with more than one functional group has the potential to harness synergistic effects. A multifunctional nanoparticle features improved properties such as dispersion stability, selectivity of coupling reaction, or biocompatibility compared to a monofunctionalization. The combination of azides and carboxylic acids create synergetic nanoparticles with a high stability in dispersion due to electrostatic repulsion and an exceptional selectivity of their surface binding sites due to bioorthogonality. These UCNP@SiO$_2$-COOH/Az nanoparticles were synthesized by using UCNPs with a diameter of 25 nm instead of 12 nm as for the other functionalizations. The resulting brighter upconversion emission due to reduced quenching effects is beneficial for labeling purposes. The adjustments of the synthesis procedure consisting of a change in the silane volumes due to a larger nanoparticle surface were in accordance to the calculations described for UCNP@SiO$_2$-COOH in chapter 9.5 in the Appendix. The percentage of azide and carboxylic groups on the nanoparticle surface was defined by the volume ratio of the respective silanes during silanization. An amount of 5% azide was chosen as a compromise between stabilization efficiency and guaranteed presence of a sufficient number of Click functionalities on the surface of each UCNP.

The hydrodynamic diameter of UCNP@SiO$_2$-COOH/Az around 70 nm (Figure 9.15) was significantly lower than for the purely azide functionalized UCNP@SiO$_2$-Az owing to the presence of carboxylic

groups if the larger absolute diameter is taken into consideration. However, there was an increase in polydispersity (PdI 0.388) which varies for different batches of UCNP@SiO$_2$-COOH/Az and thus suggested optimization of the synthesis. Furthermore, the predominant presence of carboxylic groups on the nanoparticle surface was proven by the zeta potential (-18 mV) of these nanoparticles with a high similarity to the UCNP@SiO$_2$-COOH. This additionally confirmed good dispersion stability. The detection of the azide functionalities was achieved by the attachment of the fluorophore Fl$_{alk}$ via CuAAC, as for UCNP@SiO$_2$-Az, which led to a significant fluorescence of the washed nanoparticles. TEM imaging to determine the absolute diameter was omitted, since the UCNP@SiO$_2$-COOH/Az nanoparticles were not considered for the VLP synthesis by capsid encapsulation.

Consequently, a simultaneous modification of UCNPs with carboxyl and azide groups has been demonstrated which allowed the preparation of efficiently stabilized nanoparticles in dispersion with highly specific binding sites for the bioorthogonal CuAAC. The small number of azides is especially useful for single targeting functionality on the UCNP surface ensuring improved labeling efficiency. A detailed study about the influence of the azide percentage of the UCNP functionalization on the nanoparticle characteristics as well as an investigation about the attachment of biomolecules by CuAAC are the main focus of the master thesis of Uwe Käfer[413] and were thus not further pursued.

4.9 Functionalization by Click Chemistry

The main attention of the studies concerning the potential subsequent functionalization of UCNPs by Click chemistry was on UCNP@SiO$_2$-Az nanoparticles, since they featured a moderate dispersion stability in contrast to UCNP@SiO$_2$-Alk. These nanoparticles can be modified with a large variety of new functionalities such as carboxylic, amine or phosphonate groups which can act as binding sites for biomolecules. Another option is the direct attachment by the CuAAC reaction to biomolecules if they were previously equipped with an alkyne group. The selection of clickable compounds for this thesis (Figure 4.15) was chosen according to their specific properties. Furthermore, such an approach offered the possibility to compare the properties of as-modified UCNPs with nanoparticles modified directly with the respective functionality.
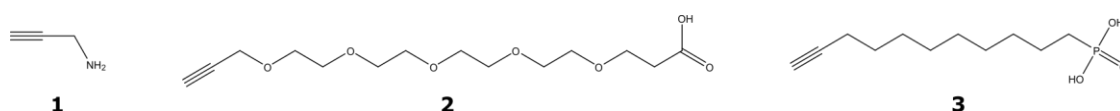

Figure 4.15 Overview of the Click compound utilized including propargylamine (1), alkyne-PEG5-acid (2), and 10-undecynylphosphonic acid (3).

The small size of propargylamine (**1**) enables a coupling to a high number of azide groups on the nanoparticle surface without any steric hindrance during the process. These amine-functionalized

nanoparticles by Click chemistry (UCNP@SiO$_2$-Az-NH$_2$) featured a hydrodynamic diameter larger than 250 nm (Figure 9.16) and moderate polydispersity (PdI 0.254). Consequently, the nanoparticle size hardly changed after the Click reaction but the size distribution broadened significantly compared to the original UCNP@SiO$_2$-Az acting as a reference (chapter 4.7). This broadening was explained by a slightly increased aggregation due to altered interactions between the nanoparticle surfaces. The comparison to UCNP@SiO$_2$-NH$_2$ synthesized by silanization revealed a high conformity of the hydrodynamic diameter but with a higher variation in the size (chapter 4.3). TEM images of UCNP@SiO$_2$-Az-NH$_2$ showed the presence of smaller aggregates (Figure 4.16) which formed larger network-like structures similar to UCNP@SiO$_2$-NH$_2$ which verified the size broadening observed by DLS studies. However, the zeta potential (+31 mV, Figure 9.30) proved a higher dispersion stability of the UCNP@SiO$_2$-Az-NH$_2$ nanoparticles and aggregates, in contrast to the UCNP@SiO$_2$-NH$_2$ (+21.8 mV, Figure 9.20). This difference in the zeta potential implied a reduced probability for back bonding of the ammonium groups and thus a higher number of positive surface charges remain.

Figure 4.16 TEM image of UCNP@SiO$_2$-Az-NH$_2$ (*left*: 10,000x magnification, scale bar: 2 µm; *right*: 250,000x magnification, scale bar: 50 nm).

The carboxyl species alkyne-PEG5-acid (**2**) is assumed to prevent aggregation and non-specific binding due to the steric repulsion by its polyethylene glycol (PEG) spacer. The hydrodynamic diameter of the as-modified UCNPs (UCNP@SiO$_2$-Az-COOH) at approximately 300 nm (Figure 9.17) showed a high similarity in size compared to the original UCNP@SiO$_2$-Az. However, the size distribution was improved apparent in a PdI of 0.067 and thus a high monodispersity of the UCNP@SiO$_2$-Az-COOH was concluded. Consequently, a good stabilization of the previously formed aggregates of UCNP@SiO$_2$-Az by the new carboxyl and PEG functionality was found including a prevention of further aggregation. The zeta potential (-19 mV, Figure 9.31) gave information about a moderate stability of the dispersion and the binding of **2** could only be concluded from the decrease of the absolute value of the potential compared to UCNP@SiO$_2$-Az. TEM studies of UCNP@SiO$_2$-Az-COOH showed a drastic decrease of the overall number of observable nanoparticles (Figure 4.17). In

addition to a few single nanoparticles only smaller aggregates were present with similar structures as the UCNP@SiO$_2$-Az aggregates. This observation confirmed the narrowing of the size distribution and suggested a removal of larger aggregates by sedimentation.

Figure 4.17 TEM image of UCNP@SiO$_2$-Az-COOH (*left*: 10,000x magnification, scale bar: 2 µm; *right*: 200,000x magnification, scale bar: 100 nm).

The introduction of phosphonates in form of 10-undecynylphosphonic acid (**3**) with its two negative charges has the advantage of a stronger electrostatic repulsion due to a higher charge density on the nanoparticle surface compared to functionalities with only a single negative charge. Although the hydrodynamic diameter of these nanoparticles (UCNP@SiO$_2$-Az-Ph) increased (Figure 9.18) compared to UCNP@SiO$_2$-Az, the polydispersity decreased significantly (PdI 0.095). An improved dispersion stability of the aggregates was indicated by these results similar to the UCNP@SiO$_2$-Az-COOH. The zeta potential (-14 mV) was conclusive about the moderate stability of the nanoparticles in dispersion (Figure 9.32) and only indicated a different surface composition modified by the Click reaction with **3**. In addition, the TEM studies of the UCNP@SiO$_2$-Az-Ph showed a good conformity to the UCNP@SiO$_2$-Az-COOH in regard of number and size of the nanostructures (Figure 4.18).

In conclusion, nanoparticles of the type UCNP@SiO$_2$-Az were successfully modified with different clickable compounds. While a strongly positive surface charge can be created by the functionalization with propargylamine (**1**), a strong aggregation due to electrostatic attraction was observed similar to UCNP@SiO$_2$-NH$_2$. The attachment of alkyne-PEG5-acid (**2**) or 10-undecynylphosphonic acid (**3**) allowed an improvement of the stability against aggregation of the as-modified nanoparticles. However, since the original UCNP@SiO$_2$-Az already formed aggregates during synthesis, this stabilization is limited to small aggregates and a minority of single nanoparticles. Therefore, an optimization of the synthesis process to obtain single UCNP@SiO$_2$-Az is preferable to take full advantage of the beneficial effects of the compounds **2** and **3**.
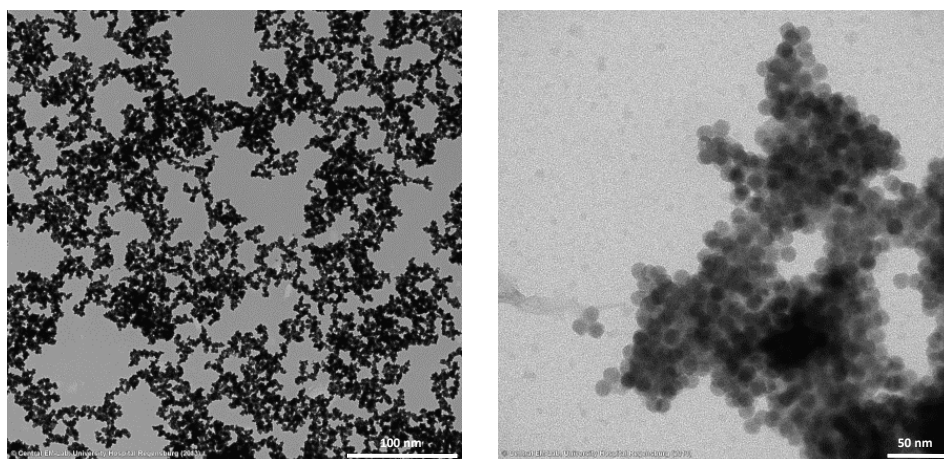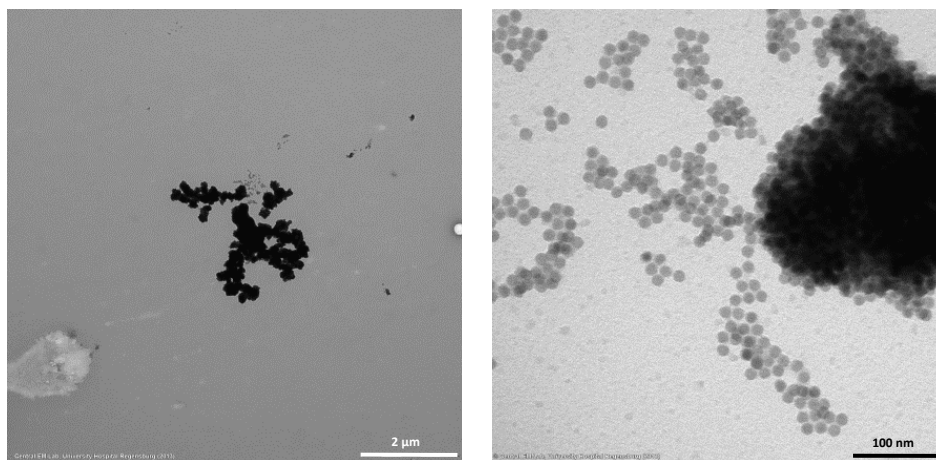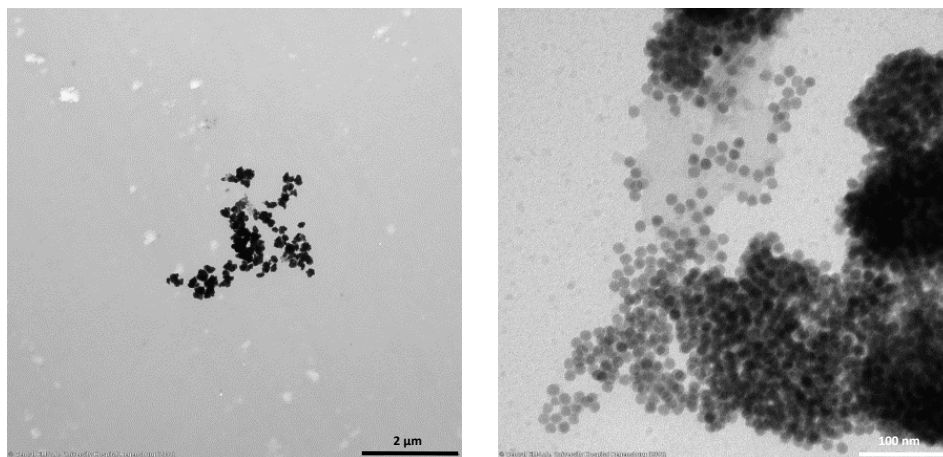
Figure 4.18 TEM image of UCNP@SiO$_2$-Az-Ph (*left*: 10,000x magnification, scale bar: 2 µm; *right*: 200,000x magnification, scale bar: 100 nm).

4.10 Summary

The modified UCNPs described in the chapters 4.2 - 4.8 featured different properties regarding their dispersion behavior and surface. The polydispersity index (PdI), hydrodynamic diameter, absolute nanoparticle size determined by TEM, and the zeta potential were the respective indicators for the monodispersity, aggregation tendency, nanoparticle size, or surface charge. These characteristics of the differently modified UCNPs allowed statements about the suitability for an encapsulation by the BMV capsid to generate VLPs and are summarized in Table 4.3.

The fulfillment of the three requirements of a hydrophilic surface to ensure dispersibility in aqueous systems, an absolute nanoparticle size below 16 nm to fit in the cavity of the BMV capsid, and a negative surface charge to imitate the viral RNA was proven by the nanoparticle size and the zeta potential. Firstly, most functionalities utilized for UCNP modification were hydrophilic and thus generate water-dispersible nanoparticles. The only exception was alkynes owing to their hydrophobic nature. Secondly, the size of a single nanoparticle was below the limit of 16 nm for almost all modifications. Only the nanoparticles coated with pure silica of the type UCNP@SiO$_2$-10 and UCNP@SiO$_2$-5 and the intrinsically larger UCNP@SiO$_2$-COOH/Az exceeded the suitable maximal size. Thirdly, except a functionalization with amine or alkyne groups all surface modifications of UCNPs resulted in the necessary negative surface charge at physiological pH. Since a simultaneous satisfaction of these requirements by one nanoparticle type is a challenging aim, the presence of aggregates of small or moderate size as indicated by the hydrodynamic diameter or the polydispersity index (PdI) were accepted. In conclusion, the selection for the generation of VLPs included UCNPs directly functionalized with carboxyl groups (UCNP@SiO$_2$-COOH, UCNP@PAA(2100), UCNP@PAA(5100)), with a thin silica shell (UCNP@SiO$_2$-4), or with phosphonate groups

(UCNP@SiO$_2$-Ph). Moreover, amine- and azide-functionalized UCNPs might be beneficial for other bioanalytical applications such as labeling, targeting, or sensor development. Amines can be efficiently used for binding reactions by well established processes such as the EDC/NHS activation, while the bioorthogonal azides and their coupling reaction CuAAC allow an unaffected binding process in *in vitro* and *in vivo* systems.

Table 4.3 Overview of nanoparticle characteristics described in chapter 4.2 - 4.8 and their suitability for encapsulation

Code	Nanoparticle size [nm]	Zeta potential [mV]	PdI	Hydrodynamic diameter [nm]	Suitability
UCNP@SiO$_2$-10	25	-30	0.215	142	–
UCNP@SiO$_2$-5	20	-3	0.343	1990	–
UCNP@SiO$_2$-4	17	-16	0.293	3091	+
UCNP@SiO$_2$-NH$_2$	14	+22	0.134	295	–
UCNP@SiO$_2$-COOH	13	-19	0.271	18	++
UCNP@PAA(2100)	-----	-46	0.609	10	++
UCNP@PAA(5100)	8	-41	0.270	12	++
UCNP@SiO$_2$-Ph	13	-32	0.072	255	+
UCNP@SiO$_2$-Alk	13	+5	0.548	2737	–*)
UCNP@SiO$_2$-Az	13	-28	0.169	295	+*)
UCNP@SiO$_2$-COOH/Az	-----	-20	0.388	28	–*)
UCNP@SiO$_2$-Az-NH$_2$	13	+31	0.254	255	–*)
UCNP@SiO$_2$-Az-COOH	13	-18	0.067	295	+*)
UCNP@SiO$_2$-Az-Ph	13	-13	0.095	342	+*)

*) Nanoparticles not considered for encapsulation

5.   Synthesis of Virus-Like Particles

5.1   Disassembly & Reassembly of Virus Capsids

The preparation of virus-like particles (VLPs) by encapsulation relies on three basic steps: firstly, the efficient and complete disassembly of the virus capsid into its single components capsomers and viral RNA; secondly, the removal of the whole genetic material of the virus; thirdly, the reassembly of the capsomers around a negatively charged artificial nucleation grain, in this case an UCNP core. A first basic study focused on the dis- and reassembly of the virus capsid and aimed for an exclusion of any effects on the VLP synthesis which were unrelated to the modified UCNP utilized as an artificial nucleation grain.

In general, the disassembly of the virus capsid included three dialysis steps with different functions (Figure 5.1). The actual breaking of the virus capsid already occurred during the first solvent exchange by buffer 1. The dialysis against buffer 2 removed Ca^{2+} ions from this capsomer solution, while buffer 3 stabilized these proteins during storage in solution.
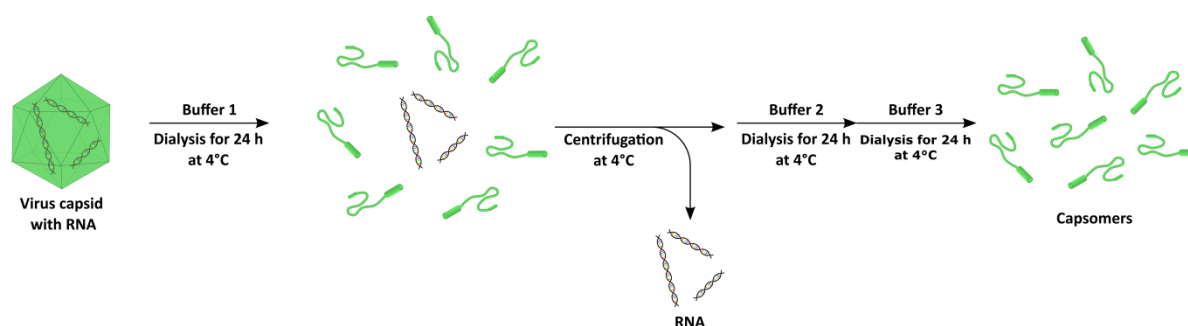
Figure 5.1 Scheme of the general disassembly process of brome mosaic virus (BMV) capsids via three dialysis steps and a centrifugation step.

The interposed centrifugation step at 4°C was meant to remove the viral RNA and thus only the artificial core induced the reassembly of the capsomers to form an unaltered BMV capsid. The omission of this step for this study enabled a reassembly to demonstrate the general feasibility of the complete dis- and reassembly process. The detection of the capsomers was carried out by TEM imaging (Figure 5.2) using a negative staining by phosphotungstic acid (PTA) to allow an illustration of these proteins. The images clearly demonstrated the presence of biological material in high abundance. Most of this material formed self-contained structures with even boundaries and were in a similar size range (Figure 5.2). Larger species with a more irregular shape and outer limit constituted only a minor percentage of the overall biological species. A classification of these components as viral capsomers was plausible, since this protein type was the predominant biological component in the solution.

Figure 5.2 TEM images of disassembled BMV capsids with PTA negative staining (*left*: 10,000x magnification, scale bar: 1 µm; *right*: 100,000x magnification, scale bar: 100 nm).

The actual VLP synthesis started with the reassembly of the capsomers around the artificial UCNP core. A ratio of 180:1 of the absolute protein and nanoparticle number had to be set in the respective synthesis batch to enable encapsulation by reassembly, since 180 capsomers form one complete virus capsid. The process itself was triggered by a change in the solvent composition caused by dialysis against buffer 4 (Figure 5.3). The negatively charged UCNP acted as the nucleation grain during this self-assembly process which leads to the formation of VLPs. The final dialysis against buffer 5 changed the salt composition and ensured a stabilization of the VLPs dispersed.
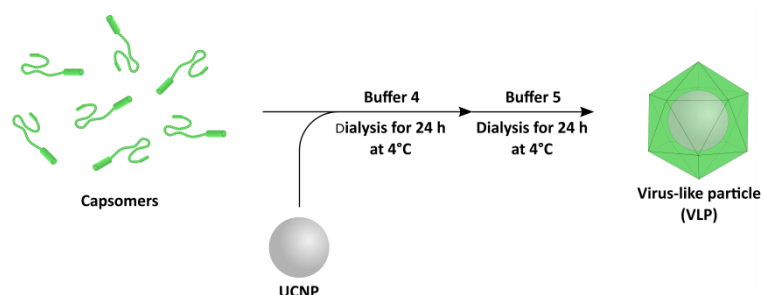
Figure 5.3 Scheme of the general reassembly process of a BMV capsid around an artificial UCNP core.

For the feasibility study of the complete process sequence the reassembly of the BMV capsids was performed in presence of the viral RNA to act as the nucleation grain. Images of the self-assembled biological structures of the capsomers were recorded by TEM (Figure 5.4) including negative staining. Several nanostructures (Figure 5.4, right, 1) with similar size and shape were distinguishable from smaller aggregates of biological materials. Their high uniformity suggested a specific formation and thus was identified as reassembled brome mosaic viruses with a high reliability. While there were some structures resembling disassembled capsomers (Figure 5.4, right, 2), a very low number of only partially assembled capsids was observed (Figure 5.4, right, 3). Consequently, the virus capsids were

predominantly formed to completion with only a minor tendency towards incomplete protein cages and the capsomers were either part of a complete capsid or remain as individual unities.
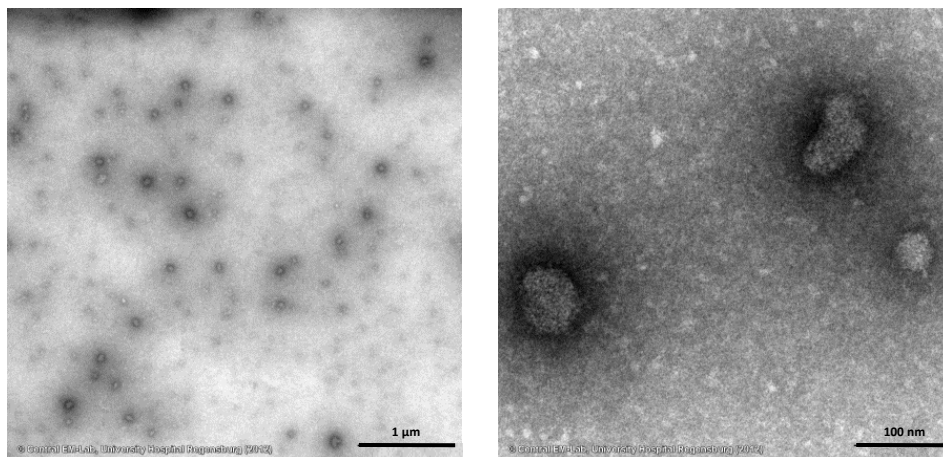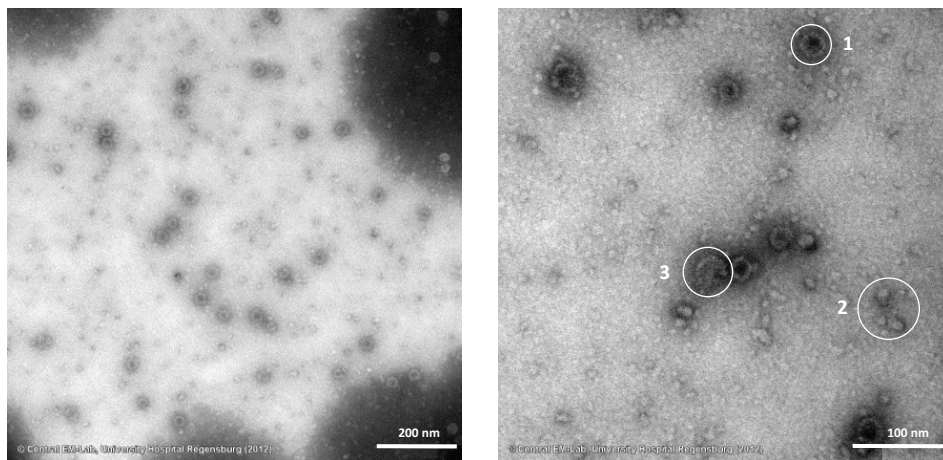

Figure 5.4 TEM images of reassembled BMV capsids with PTA negative staining (*left*: 40,000x magnification, scale bar: 200 nm; *right*: 100,000x magnification, scale bar: 100 nm).

A comparison of these reassembled BMV with a native virus solution yielded information about potential changes in the number or shape of the virus capsids. The TEM images allowed also a direct diameter comparison of the native and reassembled BMV capsids (Figure 5.5).
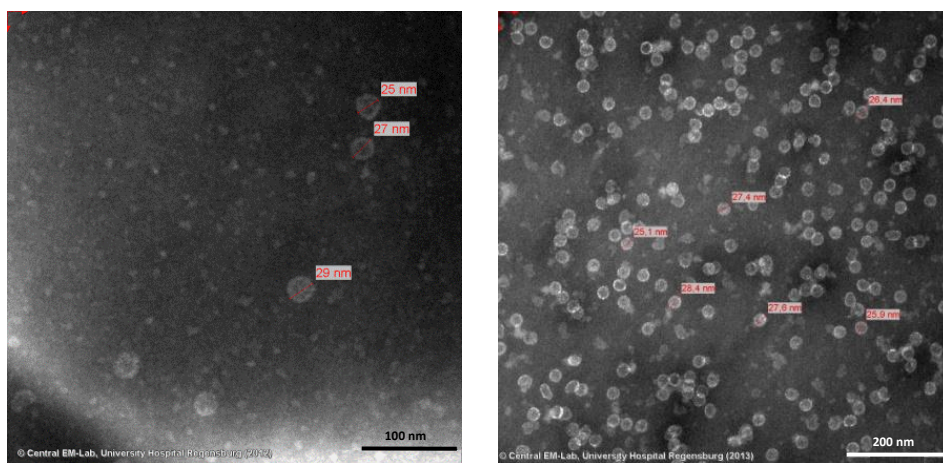
Figure 5.5 TEM images of reassembled BMV capsids (*left*: 100,000x magnification, scale bar: 100 nm) and native BMV (*right*: 100,000x magnification, scale bar: 200 nm) with PTA negative staining.

The size and shape of the capsids remained unchanged with an average diameter of 27 nm. The drastically reduced number of BMVs after the dis- and reassembly process was attributed to dilution phenomena during dialysis. Furthermore the solution of disassembled capsomers was partitioned for several reassembly tests. In conclusion, both the capsid disassembly to obtain single capsomers and the capsomer reassembly to generate either native BMVs or VLPs were feasible with only minor drawbacks regarding the reassembly efficiency and final capsid number.

5.2   Dialysis during the Synthesis of Virus-Like Particles

The encapsulation of optimized UCNPs by the reassembly of capsomers was only realizable when these nanoparticles were accessible in dispersion for the proteins. Since surface adsorption can reduce the overall number of dispersed UCNPs, the adsorption tendency to the walls and membrane of the dialysis tube used for VLP preparation was investigated by upconversion luminescence measurements. An exemplary UCNP batch dialyzed against buffer 4 was chosen for this study since this dialysis step was meant to induce the actual VLP generation and this purpose was affected the most by a nanoparticle attachment to the dialysis tube surfaces.

The samples studied were the dispersion inside the dialysis tube (*T*), the dispersion of UCNPs extracted from the dialysis membrane by sonication and shaking (*M*), the dialysis buffer volume itself (*B*), the original UCNP batch as the positive control (*C*) and pure Britton-Robinson buffer as the blank. The volume of the dialysis buffer was reduced by evaporation to take into account its higher volume compared to the other sample volumes and the related dilution effects. The blank-corrected luminescence of the samples using the green emission for detection is depicted in Figure 5.6.
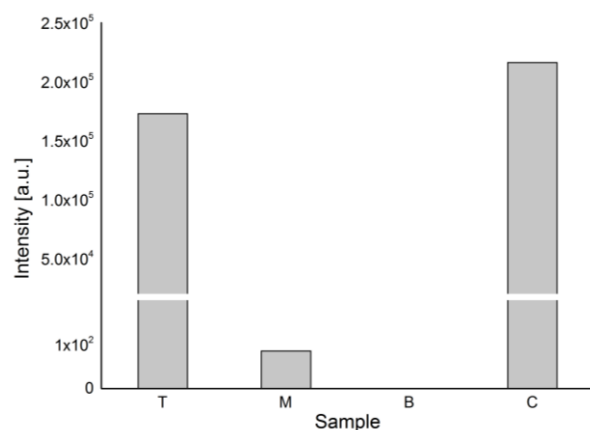
Figure 5.6 Upconversion emission intensities of the dispersion in the dialysis tube (T), extracted dispersion of the membrane (M), the dialysis buffer (B), and the original UCNP batch (C) acting as the control.

While the luminescence of sample *T* was in the same range of magnitude as the control *C*, the signals of the samples *M* and *B* were close to the background. The small difference in intensity of *T* compared to *C* was attributed to losses of UCNPs during sample handling and was insignificant for the current investigation. Consequently, a predominant presence of the UCNPs in dispersion with only minor adsorption tendencies to the dialysis membrane was confirmed and a removal of UCNPs by surface adsorption and thus a reduced accessibility of these nanoparticles were excluded during the VLP preparation.

5.3   Calculations of Capsomer Concentration

After the disassembly the concentration of capsomers dissolved in stabilizing buffer was determined by the absorption at 280 nm based on the UV-absorbing amino acids tryptophan and tyrosine and disulfide bonds, also called cystine, in the capsomer. The amino acid sequence was available in the free online protein database "www.uniprot.org" and stated the presence of three tryptophan, five tyrosine and no cystine units.

The molar absorption coefficient necessary for concentration determination was calculated (Eq. 1) according to literature[414].

$$\varepsilon_{280nm} = 5500 \cdot N_{Trp} + 1490 \cdot N_{Tyr} + 125 \cdot N_{Cys} \quad [\frac{L}{mol \cdot cm}] \quad \textbf{Eq. 1}$$

with the molar absorption coefficient ε_{280nm} of the capsomer at a wavelength of 280 nm and the number of occurrence N_x of the respective amino acid in the capsomer. For the BMV capsomer a molar absorption coefficient of 23,950 L/mol·cm^{-1} was determined.

The inclusion of the molar mass of the capsomer (20,385 g/mol) enabled the calculation (Eq. 2) of the specific absorption coefficient.

$$^{0.1\%}A_{280nm} = \frac{\varepsilon_{280nm}}{M_{Capsomer}} \quad [\frac{cm^2}{mg}] \quad\quad\quad \textbf{Eq. 2}$$

with the specific absorption coefficient $^{0.1\%}A_{280nm}$ at the wavelength 280 nm of a 0.1% protein solution, the molar absorption coefficient ε_{280nm} at a wavelength of 280 nm and the molar mass $M_{Capsomer}$ of the capsomer. Calculations yielded a specific absorption coefficient of 1.174 cm^2/mg for the BMV capsid protein.

The absorption of the capsomer solution was measured in a quartz glass cuvette due to its low absorption in the UV range and could be easily converted into the capsomer concentration by Eq. 3.

$$c_{Capsomer} = \frac{A_{280nm}}{^{0.1\%}A_{280nm} \cdot d} \quad [\frac{mg}{mL}] \quad\quad\quad \textbf{Eq. 3}$$

with the concentration $c_{Capsomer}$ of the capsomer in the respective solution, the absorption A_{280nm} measured at 280 nm for the respective solution and the specific absorption coefficient $^{0.1\%}A_{280nm}$ at the wavelength 280 nm of a 0.1% capsomer solution.

This concentration allowed the determination of the absolute number of capsomers in the solution by calculations including the Avogadro constant, the molar mass and the respective volume. This number was used to define the volume ratio of the capsomer solution and the UCNP dispersion to obtain a protein/nanoparticle ratio of 180:1 which was crucial to form complete virus capsids around an UCNP during self-assembly.

5.4   Upconverting Nanoparticles

The size as well as the surface characteristics of a modified UCNP was decisive for the encapsulation by a BMV capsid to generate VLPs. The considered diameter of the nanoparticle included both the UCNP core and the functionalization layer and had to be lower than the size of capsid cavity. While hydrophilic surface groups allowed a general dispersibility in aqueous systems, their intrinsic negative charge imitated the viral RNA and thus induced the reassembly process of the capsomers. These requirements and high monodispersity with a complete absence of aggregates were difficult to ensure simultaneously. Therefore, a small size and a negative surface charge of the nanoparticle were prioritized for the choice of modified UCNPs suitable for encapsulation. Additional to citrate-coated nanoparticles (UCNP@Cit) several modified UCNPs from chapter 4 were selected for the investigation of the VLP synthesis (Table 5.1).

Table 5.1 Overview of surface functionalities used for VLP synthesis with their respective introduction method

Code	Surface species/ligand	Surface functionality	Introduction method
UCNP@Cit	Citric acid	Carboxylic acid	Ligand exchange (NOBF$_4$ method) *)
UCNP@SiO$_2$	Silica	Silanol groups	Shell growth
UCNP@SiO$_2$-COOH	Propionic acid	Carboxylic acid	Silanization
UCNP@PAA	Polyacrylic acid	Carboxylic acid	Ligand exchange (NOBF$_4$ method)
UCNP@SiO$_2$-Ph	Propylphosphonic acid	Phosphonate	Silanization

*) Synthesis by Stefan Wilhelm

5.5   UCNP@Cit as Artificial Cores

Citric acid with its three carboxylic groups efficiently coordinates to the UCNP surface and generates a hydrophilic and negatively charged surface at physiological pH. It is commonly used for ligand exchange modifications to create nanoparticles dispersible in water or buffers. This hydrophilic character allows a good dispersibility of UCNP@Cit dried for storage. Since the nanoparticles were weighed in and dispersed in double distilled water, an adjustment of an exact nanoparticle

concentration in dispersion was enabled which simplified the ratio setting of the nanoparticle and capsomer number (1:180) for the VLP synthesis. After the encapsulation procedure the UCNP@Cit were imaged by TEM (Figure 5.7) including a negative staining with PTA.

Figure 5.7 TEM images of VLP with UCNP@Cit as artificial core (left: 10,000x magnification, scale bar: 1 µm; right: 40,000x magnification, scale bar: 200 nm) with PTA negative staining.

Despite some UCNP aggregates in very low number the images were nearly void of any single nanoparticles. The biological material present featured a larger structure with a more irregular shape comparable to some forms of disassembled capsomers. Additionally, the expected structural characteristics of VLPs according to literature[16] were not observable in the sample. Consequently, the preparation of VLP was not feasible with UCNP@Cit as the nucleation grain. The main reason was a nearly complete absence of any kind of nanoparticles due to destabilization effects on the nanoparticles during VLP synthesis leading to their precipitation. This phenomenon was explained by detachment of the surface ligands. Since the citrate molecules were bound non-covalently to the UCNP surface, a detachment/reattachment equilibrium of these ligands took place. However, the citrate molecule featured a smaller size than the cut-off size of the dialysis membrane and thus the balancing of the detachment/reattachment was severely disturbed by the removal of free citrate molecules during dialysis. Additionally, the long process time, 24h on the average, and the high buffer volume compared to the VLP sample strongly promoted the clearance of citric acid from the reaction system.

5.6 UCNP@SiO$_2$ as Artificial Cores

Covalent functionalizations like the growth of a silica shell are free of any functionality detachment problems from the nanoparticle surface during dialysis. At pH 7.4 present during encapsulation the silanol groups of a silica shell are negatively charged and a nanoparticle diameter about 16 nm was achievable after the optimization of the shell growth process yielding nanoparticles of the type

UCNP@SiO$_2$-4. Therefore, the encapsulation of these nanoparticles was studied by TEM (Figure 5.8), although the aggregation of the UCNP@SiO$_2$-4 presented a problem for the accessibility of single nanoparticles.

Figure 5.8 TEM images of VLP with UCNP@SiO$_2$-4 as artificial core (*left*: 40,000x magnification, scale bar: 200 nm; *right*: 40,000x magnification, scale bar: 200 nm) with negative staining.

The images demonstrated a complete lack of single UCNPs in the VLP sample, while biological material was detected after negative staining. A proceeding aggregation of the UCNP@SiO$_2$-4 was confirmed as the cause for the missing of detectable UCNPs by a comparison with the native UCNP@SiO$_2$-4 dispersion (Figure 4.3). A disappearance of the originally present smaller aggregates and single nanoparticles from dispersion was shown thereby. Furthermore, several VLP synthesis studies with UCNP@SiO$_2$ indicated an attachment of capsomers to the silica surface by unspecific binding (Figure 5.9).
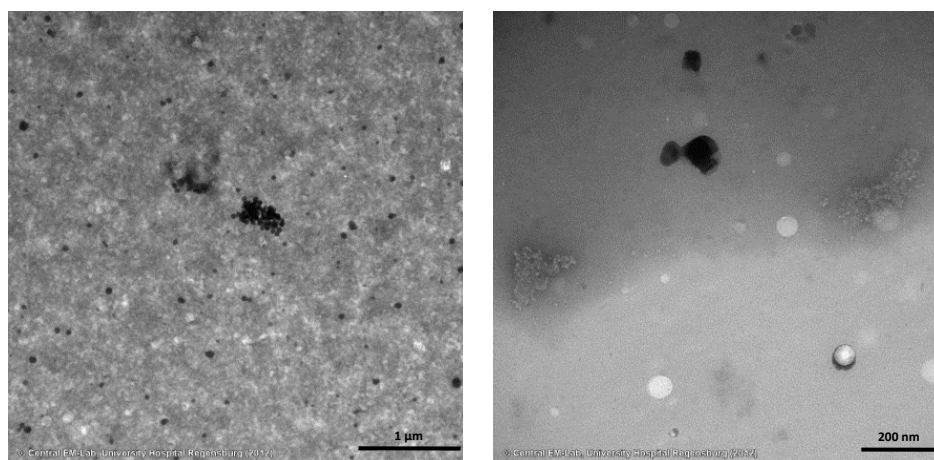

Figure 5.9 TEM images of VLP with UCNP@SiO$_2$ as artificial core (*left*: 10,000x magnification, scale bar: 1 μm; *right*: 40,000x magnification, scale bar: 200 nm) with negative staining.

Additional to a reduction in number of capsomers capable to undergo self-assembly this binding led to an enhancement of nanoparticle aggregation. A bridging effect of the proteins by the attachment

to more than one nanoparticle surface was named as a potential driving force. Consequently, the failure of the VLP synthesis with silica-coated UCNPs as the cores was caused by the high aggregation tendency proceeding both in storage and during synthesis and the affinity of capsomers to the silica surface reducing their accessible number in dispersion.

5.7   UCNP@SiO$_2$-COOH as Artificial Cores

The silanization of silica-coated UCNPs with carboxylic groups allows a prevention of aggregation due to the strong electrostatic repulsion. In addition to an absolute diameter of 13 nm and a satisfactory negative surface charge at pH 7.4 the as-modified UCNPs were highly monodisperse and stable in dispersion as shown in chapter 4.4. The preparation of VLPs with these nanoparticles was highly promising and was studied by TEM imaging (Figure 5.10)
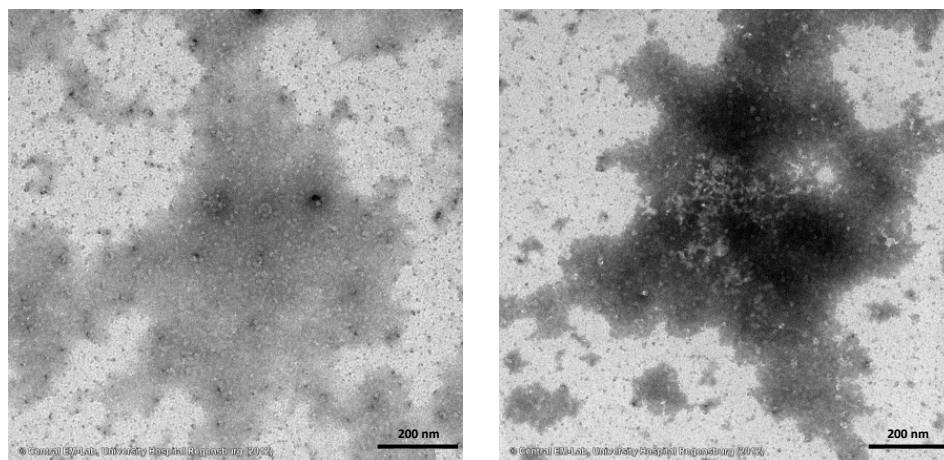

Figure 5.10 TEM images of VLP with UCNP@SiO$_2$-COOH as artificial core (left: 100,000x magnification, scale bar: 200 nm; right: 160,000x magnification, scale bar: 100 nm) with PTA negative staining.

The high abundance of nanoparticles demonstrated their high stability in dispersion in contrast to UCNPs coated with pure silica. Most UCNP@SiO$_2$-COOH nanoparticles were part of larger structures which were predominantly formed by a bridging effect of the virus proteins and only to a minor extent by aggregation. Indicators for this effect were the low overall density and an intermediate area between the individual UCNPs with moderate brightness, in contrast to the dark UCNP structures observable for other modified nanoparticles such as UCNP@SiO$_2$-4. In addition to attached capsomers, there was also free biological material observable which most likely could be defined as unassembled capsomers. However, the most striking observation was the resemblance of specific species to the expected VLP structure in literature[16] (Figure 5.10, right and inset). Despite the small number of these structures their existence led to the assumption of a potential encapsulation of the UCNP@SiO$_2$-COOH by the virus capsid. Consequently, immunogold staining was performed for a more reliable verification (chapter 5.9).

5.8   UCNP@PAA as Artificial Cores

A ligand exchange with the polymer polyacrylic acid (PAA) is a way to introduce a high number of negatively charged carboxylate groups on the UCNP surface without the risk of aggregation or unspecific binding of proteins due to the growth of a silica shell. This polymer showed a lower probability of detachment from the UCNP surface compared to citrate due to its multidentate property. Furthermore, the negative surface charge as well as the high monodispersity of the PAA-modified UCNPs confirmed the suitability of these nanoparticles as potential nucleation grains for the virus capsid reassembly. The TEM images of the VLP synthesis with UCNPs coated with the low weight PAA (2100 g/mol) as the artificial core are given in Figure 5.11.

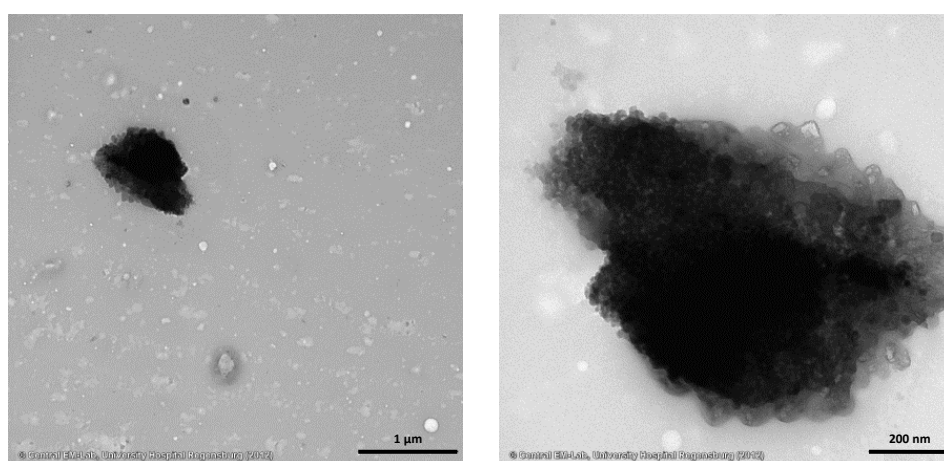**Figure 5.11** TEM images of VLP with UCNP@PAA(2100) as artificial core (left: 40,000x magnification, scale bar: 500 nm; right: 200,000x magnification, scale bar: 100 nm) with negative staining.

Both nanoparticles and biological material was clearly detected in high numbers by TEM after negative staining. Their close proximity indicated a strong interaction between both species in form of an almost complete enclosing of the UCNP@PAA(2100) by the capsomers. However, the binding organization was strongly disordered in contrast to the structured and uniform appearance of a VLP shown in literature[16] for gold nanoparticles. The attachment of the capsomers to the nanoparticle surface was thus unspecific and included no directed interaction. A specific coordination of the positively charged side chains of the capsomers to the negatively charged nanoparticle surface was yet indispensible for an organized capsid assembly. Furthermore, for the formation of the capsid the capsomers had to interact at their specific binding groups but this process was disturbed by the polymer.

The VLP preparation with the high-weight polymer (5100 g/mol) as the surface modification of the UCNPs, in contrast, yielded differing results (Figure 5.12).
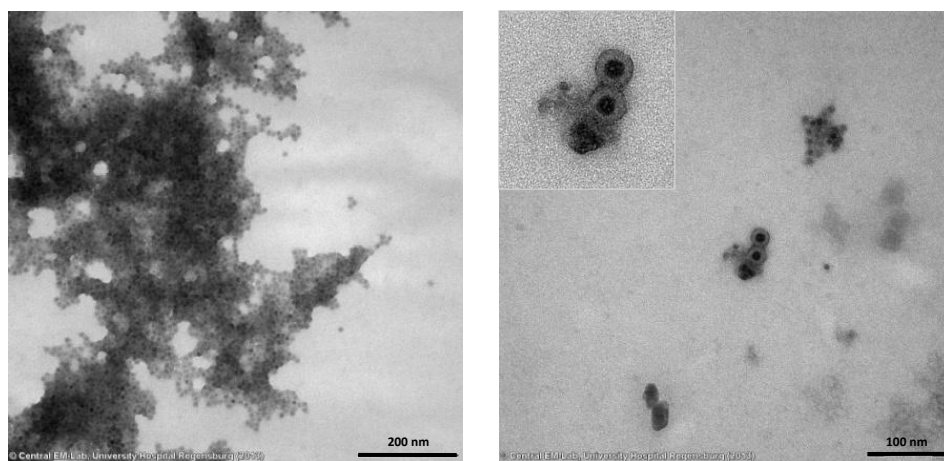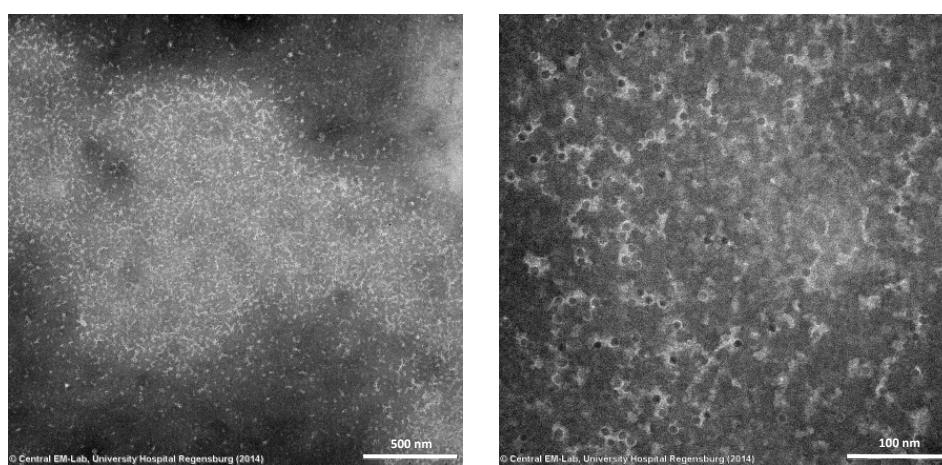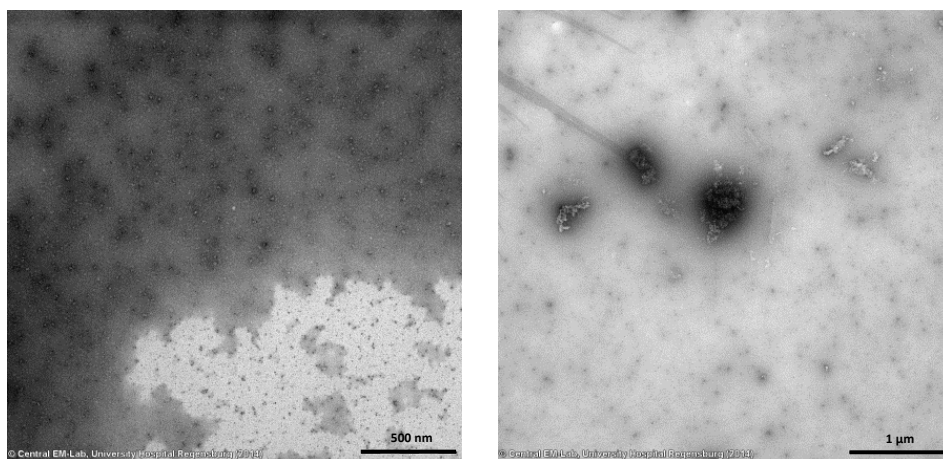
Figure 5.12 TEM images of VLP with UCNP@PAA(5100) as artificial core (left: 40,000x magnification, scale bar: 500 nm; right: 20,000x magnification, scale bar: 1 µm) with PTA negative staining.

The UCNP@PAA(5100) nanoparticles were only detected in moderate numbers unlike the high abundance in the original nanoparticle dispersion. The present biological material was classified as capsomers, since they had a similar structure as disassembled capsomers. There was no apparent interaction between the UCNP@PAA(5100) nanoparticles and the virus proteins in contrast to the unspecific interactions observable for UCNP@PAA(2100). These results were explained by two reasons for the arising effects during the VLP synthesis. Firstly, the high weight PAA partially lost its stabilization efficiency of the nanoparticles. This assumption can be attributed to enhanced bridging effects of longer polymer chains after partial detachment from the nanoparticle surface. Secondly, the absence of any unspecific binding of the capsomers might be caused by different surface characteristics compared to the low weight polymer. A reduced negative charge density on the nanoparticle surfaces and increased steric hindrance by the longer polymer chain might diminish effective electrostatic interactions with the proteins which were crucial for the initiation of the self-assembly.

5.9 Immunogold Staining

The promising results of the VLP synthesis using UCNP@SiO$_2$-COOH as the artificial core led to an investigation of the VLP samples with the immunogold staining technique (Figure 5.13). The utilization of antibodies for this method allowed a selective labeling of the BMV capsomers with gold nanoparticles and thus their specific identification by TEM imaging. Therefore, more detailed information about the potential encapsulation of UCNP@SiO$_2$-COOH was obtained compared to a simple but unspecific negative staining with PTA.

The general immunogold staining process included the recognition of and binding to the BMV capsid, more precisely the BMV capsomers, by the primary antibody. The secondary antibody reacted with

the primary antibody and carried a gold nanoparticle with a fixed size which was detectable by TEM. This identification specificity of both antibodies improved the accuracy of this staining method. The secondary antibody was selected according to the host animal the primary antibody was isolated from. Furthermore, secondary antibodies not binding to the primary antibody were utilized for the negative controls during the staining investigation. The gold nanoparticle bound to the secondary antibody for both the sample and the control had to be chosen according to their size so that they were detectable by TEM and distinguishable from the UCNPs.
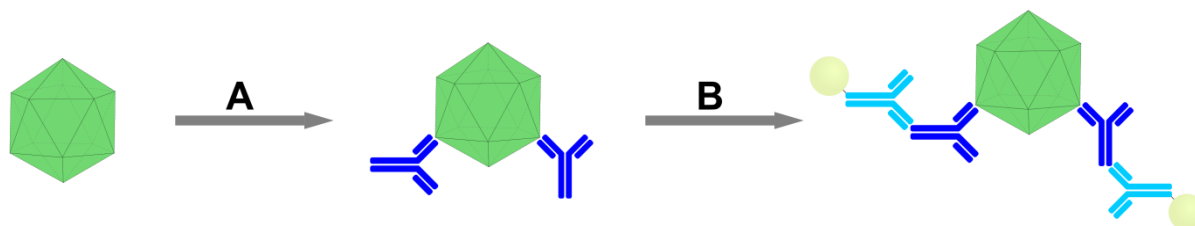
Figure 5.13 Schematic illustration of the immunogold staining principle including (A) the selective binding of the primary antibody to the BMV capsid and (B) the recognition of the secondary antibody labeled with a gold nanoparticle of the primary antibody.

The negative controls of the immunogold staining studied the impact of the antibody selectivity and of unspecific binding on the labeling efficiency and thus were crucial to exclude any false positive results. For the investigation the secondary (control 1) or primary (control 2) antibodies were replaced by a mismatching substitute. Consequently, while the actual sample should feature a high number of bound gold nanoparticles in the respective TEM images, a complete absence of these labels was expected for both controls in the case of a high antibody selectivity and low unspecific binding. The primary/secondary combinations and actual species used in this thesis are given in Table 5.2 with (*+*) for matching and (**–**) for mismatching antibodies.

Table 5.2 Combinations of primary and secondary antibody for sample and controls with respective example

Code	Primary antibody	Secondary antibody	Example
Sample	*+*	*+*	Rabbit-anti-BMV Goat-anti-rabbit
Control 1	*+*	**–**	Rabbit-anti-BMV Goat-anti-mouse
Control 2	**–**	*+*	PBS buffer Goat-anti-rabbit

The first sample studied by the immunogold staining technique was a native BMV solution to verify the general applicability of the method for BMV capsomer detection and to obtain TEM pictures of labeled capsids (Figure 5.14) for comparison with the actual VLP samples.

Figure 5.14 TEM images of sample of BMV virus for immunogold staining (left: 20,000x magnification, scale bar: 1 µm; right: 100,000x magnification, scale bar: 200 nm) with negative staining.

The multitude of observable gold nanoparticles verified the high binding affinity of both primary and secondary antibody. Additionally, an apparent increased accumulation of the gold labels around uniform biological material (Figure 5.14, right) showed the potential detection of BMV capsids by this staining method. However, the missing high abundance of intact capsids in contrast to the native sample (Figure 5.5, right) suggested a disassembly effect during the immunogold staining procedure. The staining conditions potentially caused a disassembly of capsids in the process. Furthermore, if the epitope of the capsomer for the primary antibody was not positioned at the outer and accessible surface of the capsid, the antibody attachment might have caused a denaturation of the viral protein. A simultaneous dilution effect was excluded due to the presence of the gold nanoparticles in the images in high numbers. TEM studies of the controls 1 (Figure 5.15, top) and 2 (Figure 5.15, bottom) allowed to conclude that this observation was a result of an effective binding and not of potential unspecific binding of both antibodies.

Only isolated gold nanoparticles (Figure 5.15, top left & bottom right, white circle) were found in the TEM images for both control 1 and 2 while biological structures were observable in higher amount (Figure 5.15, top right, white circle). Therefore, the primary and secondary antibody was highly selective and unspecific binding of the antibodies was nearly absent. Furthermore, the disassembly phenomenon mentioned for the BMV sample could be majorly attributed to the staining conditions, since the number of capsids was similarly low for control 2 despite the omission of the primary antibody. In conclusion, the immunogold staining of BMV capsids was feasible with a high selectivity of the two antibodies and a high detection sensitivity of the gold nanoparticles.
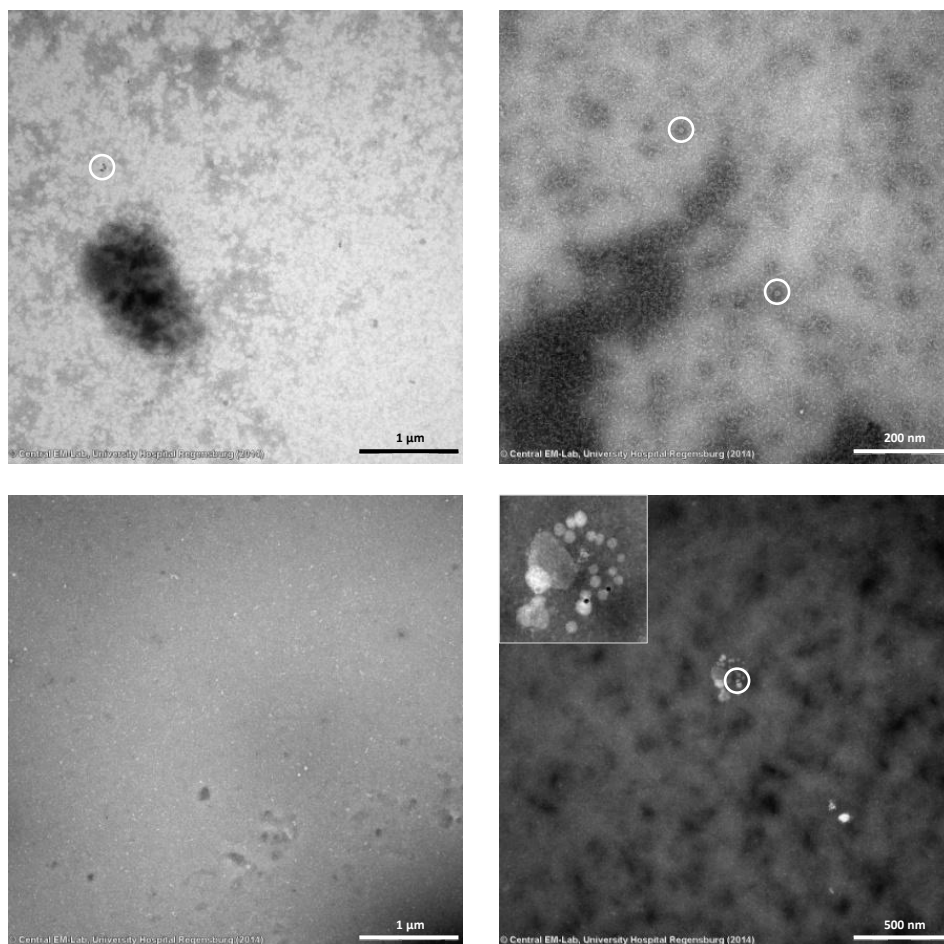
Figure 5.15 TEM images of control 1 (top) and control 2 (bottom) of BMV virus for immunogold staining (top left: 20,000x magnification, scale bar: 1 µm; top right: 100,000x magnification, scale bar: 200 nm, bottom left: 20,000x magnification, scale bar: 1 µm; bottom right: 40,000x magnification, scale bar: 500 nm) with negative staining.

The immunogold staining of the VLP sample described in chapter 5.7 should allow an identification of the found encapsulated product (Figure 5.10, right) which resembled the appearance of VLPs in literature[16]. However, the TEM images of the sample after staining revealed a low number (Figure 5.16).

The absence of UCNPs in the images was explained by their aggregation and precipitation during the sample preparation for the immunogold staining. After the deposition of the TEM grid on the top of a sample drop the dispersed species attached to the grid by electrostatic or dispersion forces, whereas larger aggregates precipitated and thus were not bound to the grid. This phenomenon is even more pronounced for an increasing aggregation tendency. Furthermore, the very low number of gold nanoparticles suggested an altered behavior of the antibodies in this sample, especially regarding selectivity, or a degradation of the capsomers during longer storage times. In consequence of these results, no TEM images of the two controls were recorded.
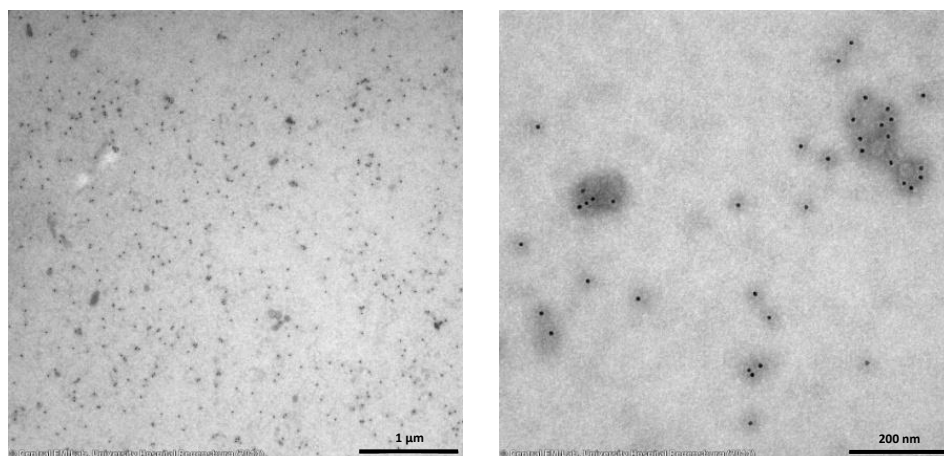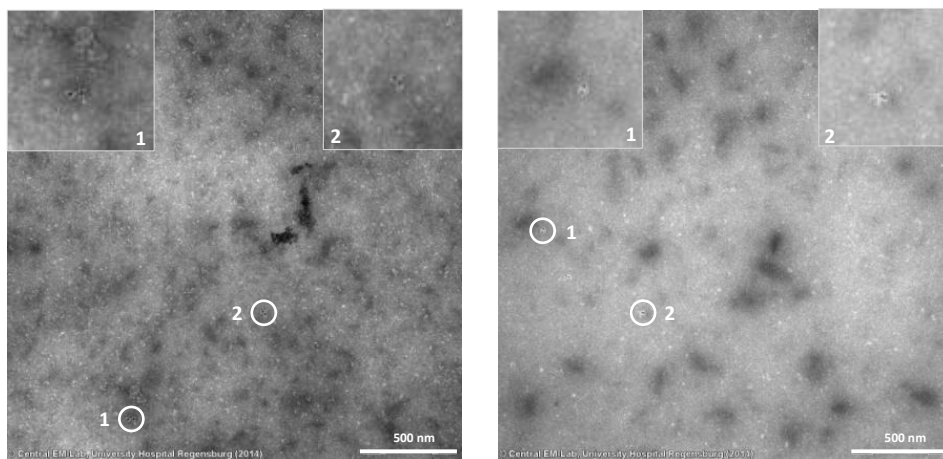
Figure 5.16 TEM images of first sample of VLP for immunogold staining (*left*: 40,000x magnification, scale bar: 500 nm; *right*: 40,000x magnification, scale bar: 500 nm) with negative staining.

A repeated preparation and staining of VLPs with UCNP@SiO$_2$-COOH nanoparticles as the artificial core was performed for a more detailed study but yielded similar results (Figure 5.17).
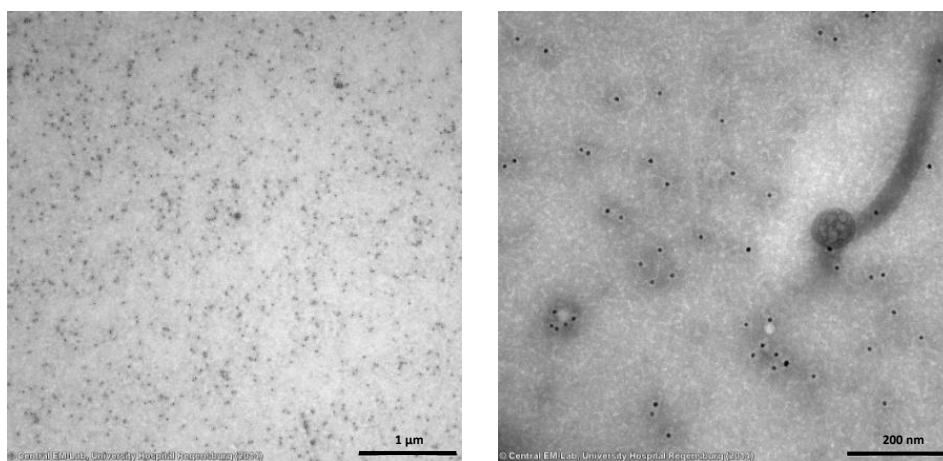
Figure 5.17 TEM images of sample of second VLP sample for immunogold staining (*left*: 20,000x magnification, scale bar: 1 µm; *right*: 100,000x magnification, scale bar: 200 nm) with negative staining.

Although the number of detectable gold nanoparticles drastically increased and matched the results of the BMV sample, no UCNPs in form of single nanoparticles or aggregates were observable in the images. These findings further confirmed the assumptions made for the previous VLP sample. Firstly, a great majority of UCNPs were removed from the sample during the preparation for the immunogold staining, also owing to enhanced aggregation tendencies. Secondly, the capsomers were not stable over longer storage times (more than a month) in the storage buffer for the VLPs (buffer 5), since this VLP sample was prepared only a few days before staining and showed a high number of detectable capsomer entities. The complete absence of any structures resembling the one found in chapter 5.7 in both VLP samples allowed the conclusion that the nanostructure found was a random accumulation of UCNPs with biological material which not necessarily was capsomers.

5.10 Summary

The preparation of virus-like particles (VLP) by the encapsulation with a BMV capsid was studied utilizing UCNPs with different negatively charged surface functionalities. Citrate as the surface ligand led to negatively charged nanoparticles dispersible in aqueous systems but they were prone to removal during VLP synthesis. Since their molecular mass was far below the cut-off size of the dialysis membrane, they easily diffused out of the reaction system after detachment from the nanoparticle surface. Consequently, precipitation of the UCNPs occurred due to the loss of stabilization by the negative charge of citrate ligands. In contrast, silanol groups of a silica shell are stable during dialysis due to a covalent modification process. However, silica-coated UCNPs strongly aggregated both in storage and VLP synthesis and were thus unusable for encapsulation despite the reduced shell thickness (UCNP@SiO$_2$-4). A silanization with carboxylic groups (UCNP@SiO$_2$-COOH) promised a stabilization of single nanoparticles also during the encapsulation process. Their use as artificial cores led to the formation of nanostructures resembling the VLPs described in literature and thus a more specific characterization method, the immunogold staining technique, was applied to directly identify the viral capsomers. Although the staining proved to be applicable for a native BMV sample showing high antibody selectivity and low unspecific binding, no evidence of a successful encapsulation was established by this method for two VLP syntheses with UCNP@SiO$_2$-COOH. The coating of UCNPs with polyacrylic acid was a non-covalent method to introduce carboxylic groups without the problem of ligand removal during dialysis, since its multidentate character reduced the probability of polymer detachment from the nanoparticle surface. While the high molecular mass polymer on the UCNP surface led to no initiation of self-assembly during the VLP synthesis, PAA with the lower mass on the surface interacted with the capsomers in the process. However, these interactions led to a disordered organization of the proteins around the nanoparticle indicating only an unspecific and not directed character. The functionalization with phosphonate groups were not shown since the studies of their VLP samples were strongly hampered by detection problems and the few informative images featured a high similarity to the preparations with citrate- or silica-coated UCNPs. In conclusion, no encapsulation by the BMV capsid was feasible with the modified UCNPs of this thesis acting as the artificial core. The promising tendencies of encapsulation found for carboxyl-modified UCNPs suggests a potential overcoming of the arising problems by proceeding optimizations, for example by the introduction of PEG spacer to avoid non-specific binding which was described for the encapsulation of gold nanoparticles by BMV capsids[16].

6.   Scan mode & Limit of Detection of the Chameleon Reader

6.1   Upconverting Nanoparticles

The second focus of this thesis was on the UCNP detection system "Hidex Plate Chameleon Multilabel Detection Platform", in short Chameleon reader. This microtiter plate reader equipped with excitation laser of 980 nm was utilized for the detection of UCNP both in dispersion and in a dried state. While dispersed nanoparticles were measured in conventional microtiter plates and are of great interest for labeling or assay applications, an even support for dried UCNPs could be imaged by the so-called "scan mode" of the Chameleon reader whose development and application on real samples is described later. Since the excitation and detection system was recorded from above, a transparency of the plate or support was not mandatory and white materials have the advantage of total reflection of the upconversion luminescence.

The determination of the limit of detection (LOD) of UCNPs in dispersion is a fundamental characteristic for many bioanalytical applications using UCNPs as a luminescent label. This parameter was studied for unmodified erbium-doped UCNPs in cyclohexane with a diameter of 12 nm whose detection additionally confirmed the high sensitivity of the Chameleon reader due to their small size and the resulting lower brightness. A more thorough investigation of the potential detection of UCNPs dispersible in water is discussed in a master thesis with a priority more on assay applications[413].

The scan mode of Chameleon reader was investigated and optimized utilizing erbium- and thulium-doped UCNPs synthesized by the group of Thomas Hirsch at our institute. These nanoparticles with a size of 30 or 23 nm featured an enhanced upconversion emission intensity which was beneficial for optimization of the device parameters. This stronger luminescence was especially important for the use of the scan mode for studies about the plasmon enhancement phenomenon of the upconversion luminescence and for real samples such as electrophoresis gels and lateral flow assays. While the enhancement effect of the surface plasmon resonance of a gold surface was investigated with the same UCNPs as for the mode optimization, the nanoparticles for the real samples were prepared by the respective cooperation partner and subsequently employed in the intended application. An overview of the UCNPs employed during development and application of the scan mode are given in Table 6.1.

Table 6.1 Overview of UCNPs used for both optimization and application of the scanning method

Code	Size	Host	Dopants	Surface
UCNP-Er$_1$	30 nm	NaYF$_4$	Yb^{3+} / Er^{3+}	Oleic acid
UCNP-Er$_2$	12 nm	NaYF$_4$	Yb^{3+} / Er^{3+} / Gd^{3+}	Silica shell (funct.) *$^{)}$
UCNP-Er$_3$	24 nm	NaYF$_4$	Yb^{3+} / Er^{3+} / Gd^{3+}	Silica shell (funct.) *$^{)}$
UCNP-Er$_4$	400 nm	Y$_2$O$_2$S	Yb^{3+},Em^{3+}	Silica shell
UCNP-Tm	23 nm	NaYF$_4$	Yb^{3+} / Tm^{3+}	Oleic acid

*$^{)}$ funct.: Functionalized with carboxylic groups and fluorescein

6.2   Limit of Detection in Dispersion

The general limit of detection (LOD) of the upconversion luminescence is an important parameter about the sensitivity of the respective detection method. Therefore, the lowest detectable concentration of UCNPs with a diameter of 12 nm was determined for a concentration range of 10 - 1000 ng/mL or of 1 - 10 ng/mL. After two intermediate dilution steps of the stock dispersion the final concentrations were prepared by a direct dilution inside the respective five wells of the mictrotiter plate with cyclohexane yielding the calibration concentrations 10 / 50 / 100 / 500 / 1000 ng/mL for the range 10 - 1000 ng/mL or the concentrations 1 / 2 / 4 / 6 / 8 / 10 ng/mL for the range 1 - 10 ng/mL. The upconversion luminescence was measured threefold for each well yielding 15 values for each concentration and the cyclohexane blank to allow an informative statistical evaluation. After blank correction the respective calibration curves of the two concentration ranges were determined by a linear fit (Figure 6.1).
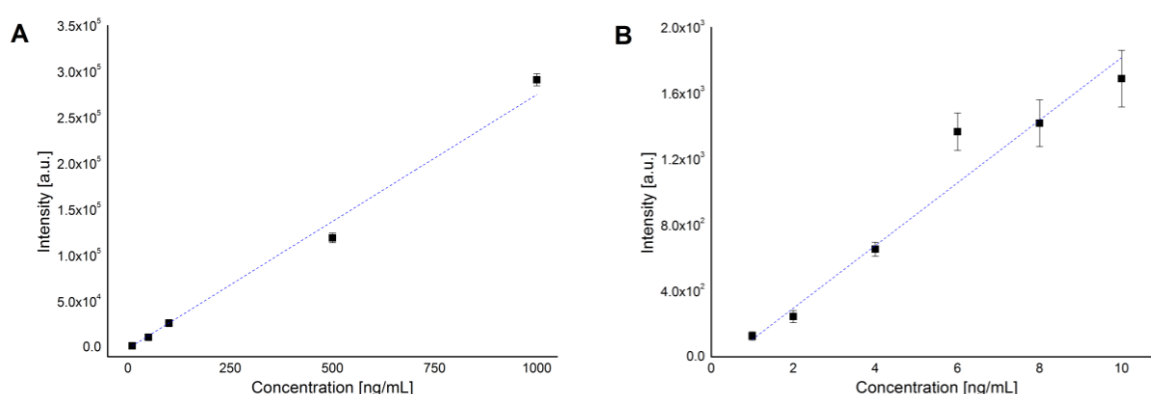
$$I = 276.2 \ \frac{mL}{ng} \cdot c \ [\frac{ng}{mL}] - 1109.1$$

$$R^2 = 0.9897$$

$$I = 190.1 \ \frac{mL}{ng} \cdot c \ [\frac{ng}{mL}] - 84.5$$

$$R^2 = 0.9585$$

Figure 6.1 Calibration curves for the LOD determination in the concentration range (A) 10 - 1000 ng/mL and (B) 1 - 10 ng/mL with the resulting linear equation and coefficient of determination R^2.

The curve for 10 - 1000 ng/mL demonstrated a good fit with only minor deviations which was also evident from the coefficient of determination R^2. The larger deviations for the lower concentration range led to a lower matching of the fit. These results were attributed to a larger variation of the intensity values for the different wells of one concentration which is also indicated by comparatively high standard deviation. The stronger impact of dilution inaccuracies for lower concentrations was assumed as a reason for this observation.

These fits with their respective linear equation enabled the calculation of the LOD by determining the respective intensity. This lowest detectable intensity (LDI) was defined as the intensity that was at least three times the standard deviation higher than the background and thus could be significantly distinguished from the background. The calculations were performed with equation (Eq. 4).

$$\text{LDI [a.u.]} = x_{bg} + 3 \cdot \sigma_{bg} \qquad\qquad \textbf{Eq. 4}$$

with the average x_{bg} and the standard deviation σ_{bg} of the background intensity. For the background of the two calibrations the LDI are given in Table 6.2.

Table 6.2 Calculation of the lowest detectable upconversion luminescence intensity

x_{bg} [a.u.]	σ_{bg} [a.u.]	LDI [a.u.]
259.14	14.97	304.06

Finally, the lowest concentration detectable by the Chameleon reader was calculated by converting this intensity into a mass concentration by the two linear equations (Table 6.3). Similar to these calculations the LOD can also be determined for the whole measured concentration range.

Table 6.3 Calculation of the LOD for both concentration ranges and the overall concentration range

	Concentration range 10 - 1000 ng/mL	Concentration range 1 - 10 ng/mL	Concentration range 1 - 1000 ng/mL
LOD [ng/mL]	5.1	2.0	2.1

In conclusion, an UCNP concentration of 5 ng/mL was detected in dispersion with high significance and low standard deviation. For a calibration with low concentrations this limit was reduced to 2 ng/mL but a stronger impact of measurement uncertainties on the results was assumed. A linear fitting of all concentrations from 1 - 1000 ng/mL resulted in a similar LOD which confirmed a sufficient high determination accuracy of this concentration for the 1 - 10 ng/mL and a low influence of determination uncertainties on the LOD. Therefore, the lowest detectable concentration of oleic acid-coated UCNPs in cyclohexane was defined as 2 ng/mL with high reliability. This general low limit

of detection is an even more informative indicator for a high sensitivity, since the UCNPs employed had a size of only 12 nm and thus had a reduced brightness compared to larger nanoparticles due to the stronger impact of quenching effects on their upconversion emission. Therefore, the utilization of UCNPs with a larger diameter should enable a reduction of the LOD and thus an improvement of the detection sensitivity of the Chameleon reader.

6.3   General Optimization Settings for the Scan Mode

The "scan mode" of the Chameleon reader was the second utilization option studied for bioanalysis and its implementation development and optimization as well as its application for real samples were the second major focus of thesis besides the UCNP modification and VLP preparation. The most crucial instrument parameters for the mode development included the following settings whose optimization studies are given in the indicated chapters:

- collecting time   Chapter 6.4
- filter combination   Chapter 6.5
- number of the scanning points   Chapter 6.6
- distance of the scanning points   Chapter 6.6

Firstly, the collecting time defined the period of time for which the detector records upconversion luminescence at a single scan point. Consequently, the measurement time for one scan process as well as the exposure of a scan point to the NIR laser was adjusted to both minimize the expenditure of time for a scan and to avoid sample damages due to heating effects. In addition, since the collecting time was the only instrument setting that the detected maximal luminescence intensity nearly exclusively depended on, this parameter was utilized to obtain intensity signals below 3.0×10^8 a.u. to spare the detector from oversaturation.

Secondly, the choice of filter or filter combination defined the wavelength range of the detected upconversion luminescence. While the utilization of a shortpass filter (395 - 825 nm) allowed signal recording over the whole emission range of the respective UCNP, the bandpass filter focused on the emission of a narrow wavelength section. Furthermore, a combination of filters improved the signal-to-noise ratio of the scan and suppressed the influence of scattering effects of the excitation light on the scan results.

Thirdly, the number and distance of the measurement points were essential for the definition of the size of the scan area and the lateral resolution. Since the scan area had a quadratic form, the scan points per line or column comprised the square root of the overall number of scan points. Together

with the preset point distance this number defined the edge length and thus the size of the scan area which ranged from 81 mm^2 (edge length: 9 mm) to 2025 mm^2 (edge length: 45 mm). Moreover, both settings allowed the optimization of the lateral resolution which is an important indicator for the differentiability of structural characteristics.

6.4   Collecting Time

The duration of intensity recording at one single spot, i.e. the collecting time, was crucial for the development studies to achieve a compromise between significant signal detection and short measurement time. Longer collecting times during scanning allowed a detection of very small amounts of UCNPs in the specimen. However, they soon meet their limits of practicability since the achievable information content remained constant for increasing collecting times whereas the time for a single scan increased. Consequently, the optimization of this parameter targeted a collecting time short enough for a good time practicability of the scan procedure without any significant information losses. The studies for this purpose included the scans of the same UCNP spots whose inhomogeneous form was caused by dispersion spreading during application. The set of collecting times studied started with 500 ms (Figure 6.2).
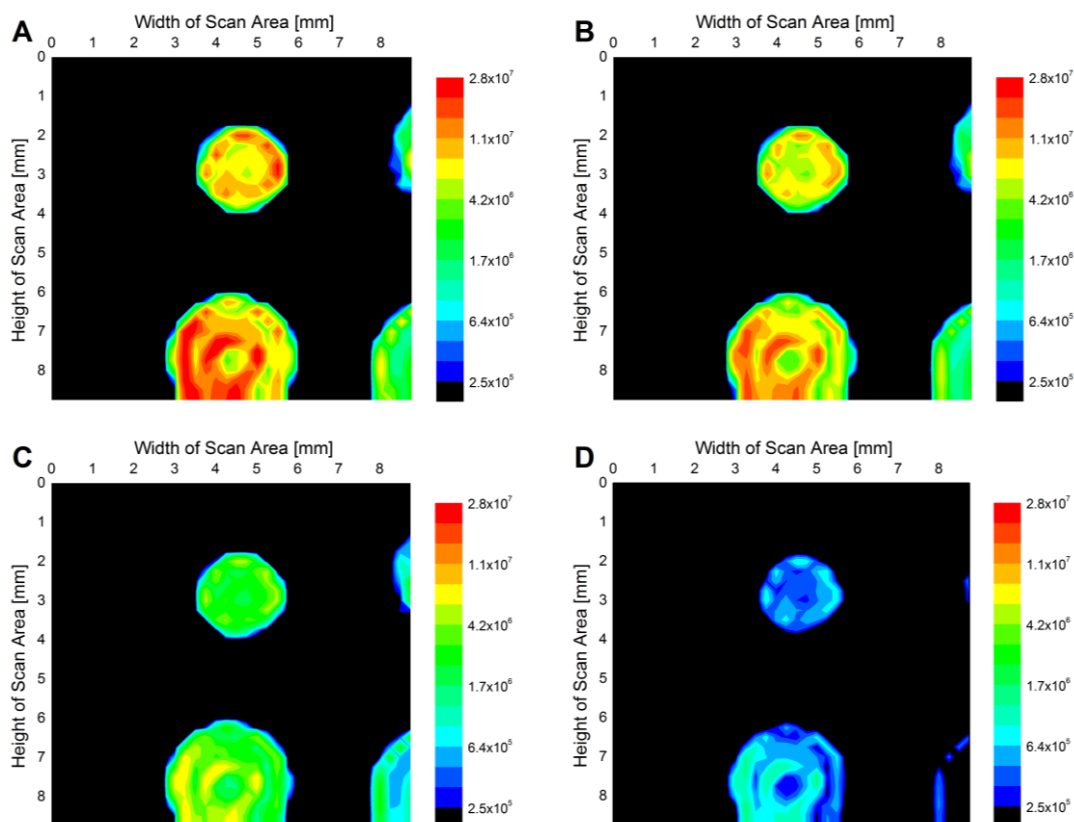
Figure 6.2 Scan images of UCNP-Er$_1$ using a collecting time of (A) 500 ms, (B) 400 ms, (C) 300 ms or (D) 250 ms; the same pseudo-color and logarithmic scale is used to ensure comparability and a background correction of the data was performed.

The maximal intensity was reduced with decreasing recording time per spot but for 250 ms a sufficient high signal was achievable. The identical logarithmic scale of the same intensity range was applied for all images to ensure comparability. However, areas with a lower UCNP concentration disappeared for shorter collecting times apparent for 250 ms (Figure 6.2D, right side) leading to a potential missing of information. A rescaling could counteract this information loss for shorter collecting times but a simultaneous increase of the background noise limited this improvement. However, an additional reduction below 250 ms revealed significant limiting factor for the choice of the collecting time (Figure 6.3).
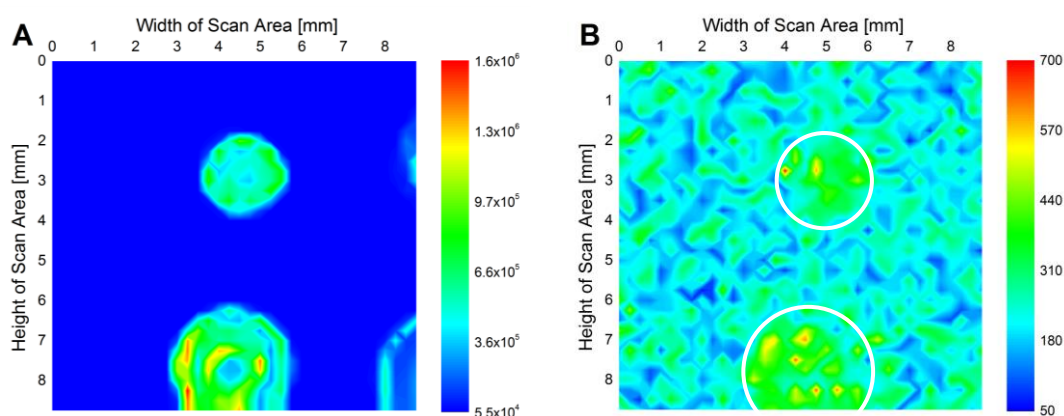
Figure 6.3 Scan images of UCNP-Er_1 using a collecting time of (A) 250 ms or (B) 200 ms utilizing a pseudo-color linear scale

The comparatively high background and weak signal intensity of the emitting areas for a collecting time of 200 ms (Figure 6.3B) led to indistinct outlines of the UCNP spots in contrast to the well defined structures for a collecting time of 250 ms. This low contrast originated from restrictions by the start-up time of the NIR laser until an even excitation intensity was reached. Durations lower than 250 ms were too short for the laser to build up a homogeneous excitation density and only an insufficient amount of UCNPs showed detectable luminescence signals.

In conclusion, a collecting time of at least 250 ms was suitable for a scan of the specimen detecting nearly all emissive areas. A scan with longer recording times, favorably for 500 ms, visualized more details, since weak emitting structures were additionally illustrated. Collecting times higher than 500 ms were also studied but showed no improvement of the information content of the resulting images. A collecting time of 500 ms was thus a good compromise between high information content and a short scan time. Additional to these instrumental factors the sample imaged and the UCNPs utilized had to be taken into account for the choice of the optimal collecting time. Since the NIR laser (P = 4 W) induced also a heating effect in the sample, the thermal resistance of the sample materials defined their susceptibility to damages or destruction by NIR laser. Shorter collecting times thus were advantageous to prevent any damages to the specimen. Furthermore, the size of the UCNP labels

strongly influenced the choice of the optimal collecting time. While for smaller nanoparticles a longer recording time was beneficial for efficient luminescence detection, UCNPs with larger diameters, e.g. in the micron range, required shorter durations especially to avoid an oversaturation of the detector.

6.5   Choice of Filters

The emission filters utilized for the scan measurement defined and set either the sum of all upconversion luminescence emissions, called overall emission, or a selected emission of a narrow wavelength range, called single wavelength emission, as the detection signal. A shortpass filter with cut-off wavelength below the 980 nm was chosen for the overall emission which featured high signal intensity and thus enabled an improved sensitivity. The single wavelength emissions were more promising to blend out any scattering of the excitation light and a bandpass filter for the green or NIR range was selected due to the highest emission intensity for erbium- and thulium-doped UCNPs, respectively, in this spectral domain. A combination of the shortpass filter and a bandpass filter had the potential to additionally improve the scan results. Consequently, a shortpass filter and two bandpass filters were studied for the optimization of the scan method (Table 6.4).

Table 6.4 Selection of emission filters utilized for scan applications with their respective characteristics

Filter for	Type	Cut-off wavelength / Bandwidth	Transmitted wavelengths
Overall emission	shortpass	825 nm	395 - 825 nm
Green emission	bandpass	535 ± 25 nm	510 - 560 nm
Infrared emission	bandpass	800 ± 25 nm	775 - 825 nm

The shortpass filter and the bandpass filter for the green range were used individually or in combination for the scan of erbium-doped UCNPs (UCNP-Er$_1$) to study their effect on the scan images (Figure 6.4). A logarithmic pseudo-color scale was chosen to take into account the broad intensity range of the upconversion emission, especially if the overall emission was the detection signal.

The highest luminescence signal was found for the shortpass filter (Figure 6.4A), whereas the average intensity decreased by a factor of 0.47 for the bandpass filter only or a factor of 0.44 for the shortpass/bandpass filter combination. This reduction of signal intensity was a result of the complete shielding of the complete red and parts of the green emission, in particular the second emission peak around 523 nm. The minor difference between the reduction factors for the bandpass filter or the filter combination confirmed the usability of both filter settings for the detection of the upconversion luminescence in the green spectral range. However, the combination (Figure 6.4C) excelled in regard of the detection suppression of scattered light indicated by the uniform spot shape and even

background intensity. In contrast, more irregular spot shapes (Figure 6.4A) or an inhomogeneous background intensity (Figure 6.4B) were found for the shortpass filter or the bandpass filter alone. The combination of the shortpass filter and a bandpass filter was thus preferable for scans with a single wavelength emission as detection signal.
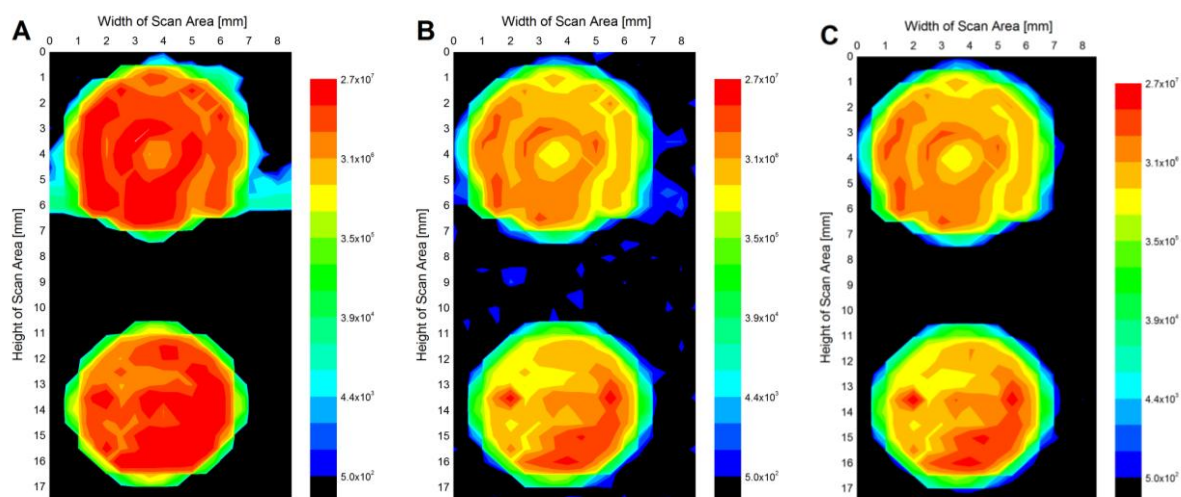
Figure 6.4 Scan images of UCNP-Er$_1$ using (A) a shortpass filter (395 - 825 nm), (B) a bandpass filter (535 ± 25 nm), or (C) a shortpass/bandpass filter combination (395 - 825 nm / 535 ± 25 nm); an identical pseudo-color and logarithmic scale is used for all images to ensure comparability and a background correction was performed.

Studies for thulium-doped UCNPs of the type UCNP-Tm focused on the shortpass filter for the overall emission and the shortpass/bandpass filter combination for the IR emission. A pseudo-color logarithmic scale of the same intensity range was again chosen to ensure compatibility of the scan images (Figure 6.5). The maximal intensity of overall emission was in the same intensity range as for UCNP-Er$_1$ and a reduced background noise was again present for the filter combination compared to the overall emission scan, similar to the erbium-doped UCNPs. However, the intensity for the single wavelength emission scan decreased by a factor of 0.66 although the IR emission at 800 nm represented the majority of the overall upconversion emission of UCNP-Tm. An explanation for this phenomenon was the varying sensitivity of the detector for different wavelength ranges. While the photomultiplier tube was sensitive in the visible range peaking in the green domain, the sensitivity at 800 nm diminished to 2.4% referred to the green wavelength range. Consequently, the low sensitivity of the detector hampered the exploitation of the strong NIR emission of thulium-doped UCNPs for scan applications despite its stronger emission signal compared to the green emission of erbium-doped UCNPs.
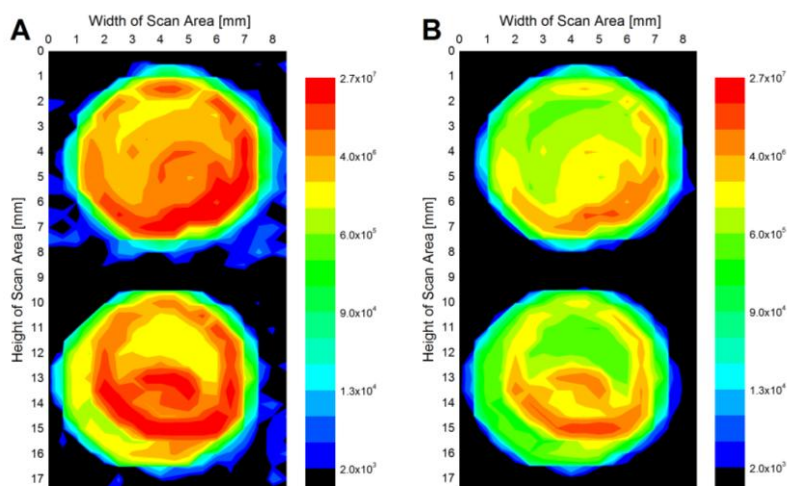
Figure 6.5 Scan images of UCNP-Tm using (A) a shortpass filter (395 - 825 nm) or (B) shortpass/bandpass filter combination (395 - 825 nm / 800 ± 25 nm); an identical pseudo-color and logarithmic scale is used for all images to ensure comparability and a background correction was performed.

The signal-to-noise (STN) ratio was an indicator for the potential discrimination between the upconversion emission and the background and gave information about the quality of the scan images achievable by the different filter settings. A normalized intensity, i.e. the average intensity of a single scan point, of the UCNP or background area was favorable for the calculation since dilution effects by spreading during the nanoparticle application on the scan support were taken into account. The comparison of these intensities for erbium- and thulium-doped UCNPs with the average background intensity showed general similarities of both nanoparticle types (Figure 6.6).
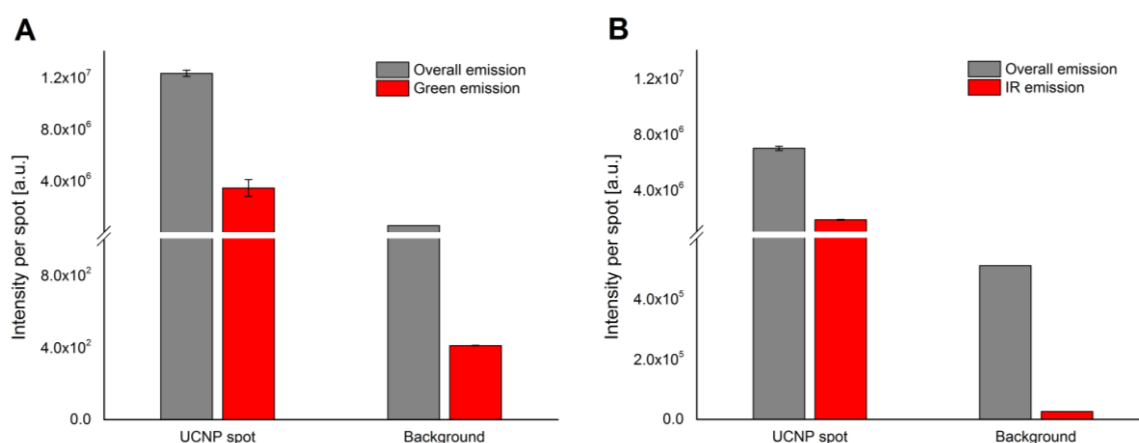
Figure 6.6 Intensity of upconversion luminescence and background for (A) UCNP-Er$_1$ and (B) UCNP-Tm using either the overall emission (grey bar) or the green and IR emission (red bar), respectively, as the detection signal. The luminescence intensity is the average of all scanning points used for evaluation.

The intensity per scanning point was significantly higher than the background for both overall emissions and single wavelength emissions. However, there was a noticeable increase of the background for both UCNP types if the shortpass filter was employed only. Additionally, the absolute intensity value of the UCNP-Er$_1$ (Figure 6.6A) was higher compared to the UCNP-Tm (Figure 6.6B)

which confirmed the higher sensitivity of the detector for green and a restricted detection of NIR emission. The calculated signal-to noise ratios for both types of UCNP and of detection signals are given in Table 6.5.

Table 6.5 Signal-to-noise ratios for the overall and single wavelength emission of erbium- or thulium-doped UCNPs

Dopant	Signal-to-noise ratio for overall emission	Signal-to-noise ratio for single wavelength emission
Erbium	24	8383
Thulium	14	72

The green emission as the detection signal allowed the best discrimination between the upconversion luminescence and the background among all nanoparticle and signal options, especially due to the very low background intensity for these scans. The intensity of the overall emission for both nanoparticle types was high enough compared to the background for a reliable detection despite the increase of the background intensity. However, differentiation problems might arise for lower nanoparticle concentrations due to a decreased intensity and they were thoroughly studied by the determination of the limit of detection (LOD) described in chapter 6.7. Furthermore, the small STN ratio for the overall and the single wavelength emission of UCNP-Tm nanoparticles was attributed to the low detector sensitivity for the NIR emission of only 2.4% referred to the green emission of erbium-doped UCNPs.

In conclusion, both the overall emission as well as a single wavelength emission of erbium- and thulium-doped UCNPs was a useful detection signal for scan applications. While the detection of all upconversion emissions by using a shortpass filter as the emission filter was favorable for maximal signal intensity, the combination of the shortpass and a bandpass filter allowed an improved discrimination between upconversion emission and the background. Moreover, the high NIR emission intensity of thulium-doped UCNPs was only limited detectable and thus suitable for sensitive imaging since the detector showed only a reduced sensitivity in the NIR range. An improvement of this NIR sensitivity by a detector replacement might improve the signal-to-noise ratio for the NIR emission. A Hamamatsu photomultiplier tube R12829 or R12896, for example, feature a quantum efficiency of 10% or 7% at 800 nm which is at least one magnitude higher than other photomultiplier tubes.[415, 416] Moreover, the anode dark current, i.e. the small current present while operating in the complete dark, is comparatively high for detectors with a high NIR sensitivity and one of the major causes is the thermionic emission of electrons. Therefore, a general cooling of the detector leads to a reduction of the background noise and thus increase of the signal-to-noise ratio in the NIR range.[417]

6.6   Lateral Resolution

The lateral resolution is a crucial factor for the content of structural information achievable by an imaging method and defines the discriminability of luminescent areas from each other or from the background. The focusing of the NIR laser diode as the excitation source had the advantage of a smaller area of illumination than conventional lamps important for high resolutions. The circular-shaped excitation area on the scan surface with a diameter of 0.8 mm featured a higher excitation density in its center than in its outer rim which allowed the realization of a lateral resolution far below this diameter.

The highest lateral resolution, i.e. the shortest possible distance between two scan spots, was investigated by the scanning of gel bands in close proximity with varying distances between two scan spots (Figure 6.7). Gel bands were selected as the studied objects due to their uniform shape without any inhomogeneity in the signal distribution. The discriminability of luminescent structures was the chosen indicator for an improved illustration of structural characteristics. The shortpass/bandpass filter combination was chosen to detect the green emission of UCNP-Er_2 described in chapter 6.5.
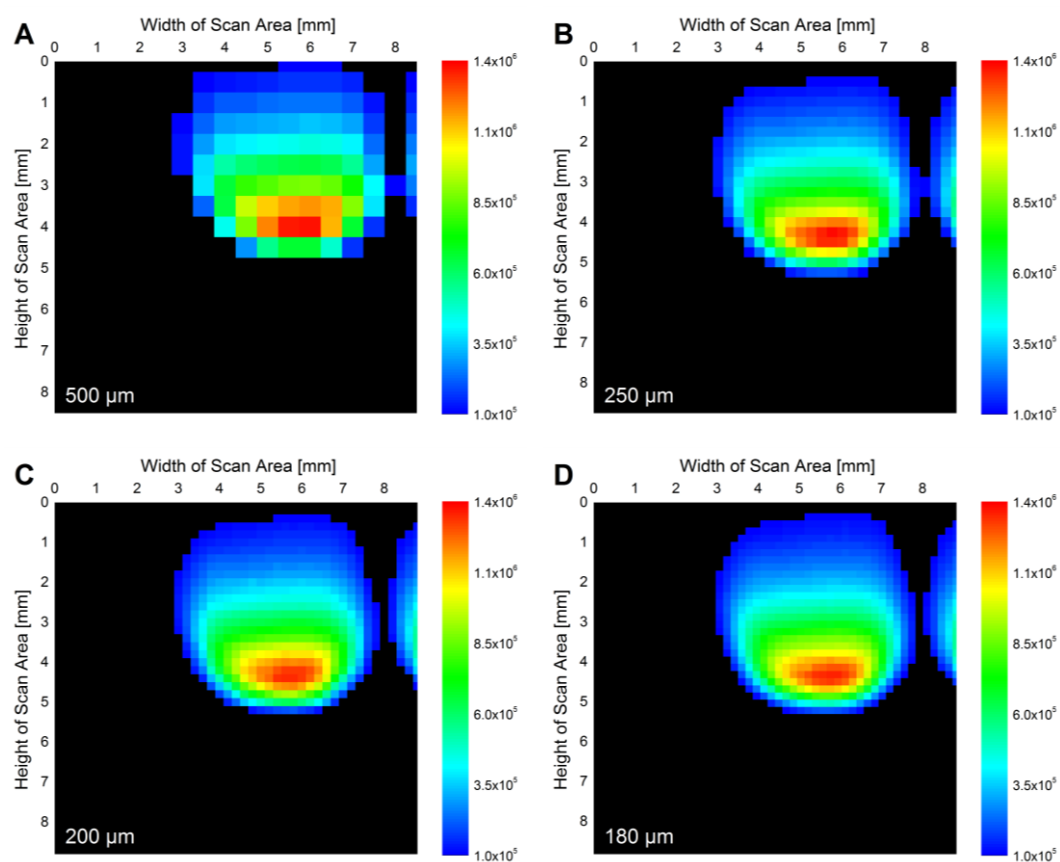
Figure 6.7 Scan images of UCNP-Er_2 with a lateral resolution of (A) 500 µm, (B) 250 µm, (C) 200 µm or (D) 180 µm and a direct display of scanning points; an identical pseudo-color scale is used for all images to ensure comparability.

The structural information was improved by reducing the distance of the scanning points from 500 μm to 180 μm. The single scan points were illustrated as pixels for better illustration. The contours of the UCNP bands became more smooth leading to an improvement of the overall shape of the gel bands. Furthermore, areas of different intensities inside the bands were more refined which allowed a better localization of the majority of UCNPs in the respective band especially important for preparative electrophoresis. Furthermore, neighboring structures were more distinguishable from each other apparent in the gap between the two bands for lateral resolutions of 200 and 180 μm. The structural information content of the images yet remained the same for these distances (Figure 6.7C/D) which was shown by nearly coinciding border smoothness and band differentiation.

Moreover, the application of software algorithms allowed a post-treatment of the scan images (Figure 6.8). A smoothening of contours (Figure 6.8B) improved the shape illustration and border separation of luminescence areas. In contrast to a simple grayscale (Figure 6.8D) a pseudo-color scaling (Figure 6.8A/C) enabled a better recognition of luminescent structures and their discriminability from the background. An increased color number allowed a better distinction of areas with different intensities by a more significant segmentation (Figure 6.8C). Therefore, all data of the scan measurements were presented in a pseudo-color scale with a smoothening algorithm.
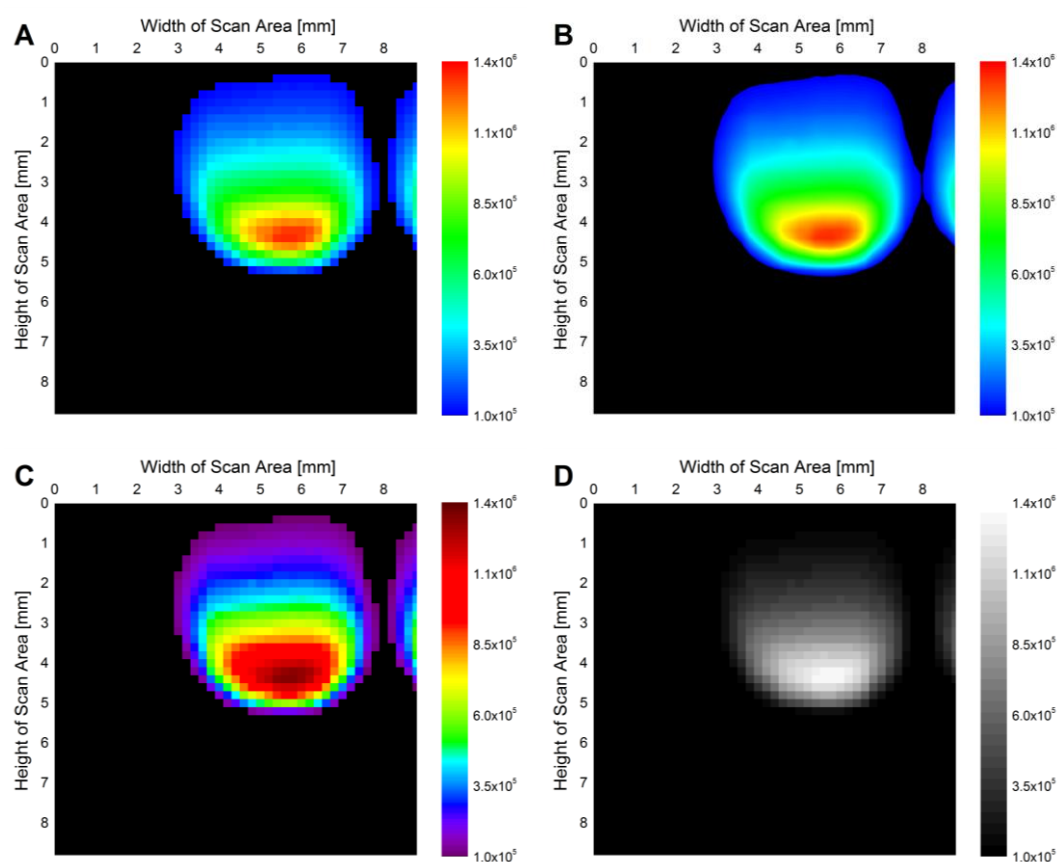
Figure 6.8 Scan images of UCNP-Er$_2$ with a lateral resolution of 200 μm (A) before and (B) after smoothening, (C) and (D) with an alternate pseudo-color and grey scale, respectively; an identical scale is used for all images to ensure comparability.

6.7   Limit of Detection

The lowest detectable nanoparticle amount, also called the limit of detection (LOD), is a good indicator for the sensitivity of the imaging method. Specific amounts of UCNPs were applied on multiple positions of a scan surface with pure cyclohexane as the background. The relation between these nanoparticle amounts and the obtained luminescence signal allowed the determination of the LOD achievable by different detection signals.

The scan of erbium-doped UCNPs (UCNP-Er$_1$) with masses per spot ranging from 1 - 100 ng is given in Figure 6.9. Since the green emission featured a better signal-to-noise ratio than the overall emission, a lower minimum intensity of 100 a.u. instead of 400,000 a.u. could be chosen for the images without any interferences of the background on image evaluation. A qualitative evaluation revealed that an UCNP amount of 1 ng or 5 ng for the green and the overall emission, respectively, was detectable significantly compared to the cyclohexane background sample (0 ng).
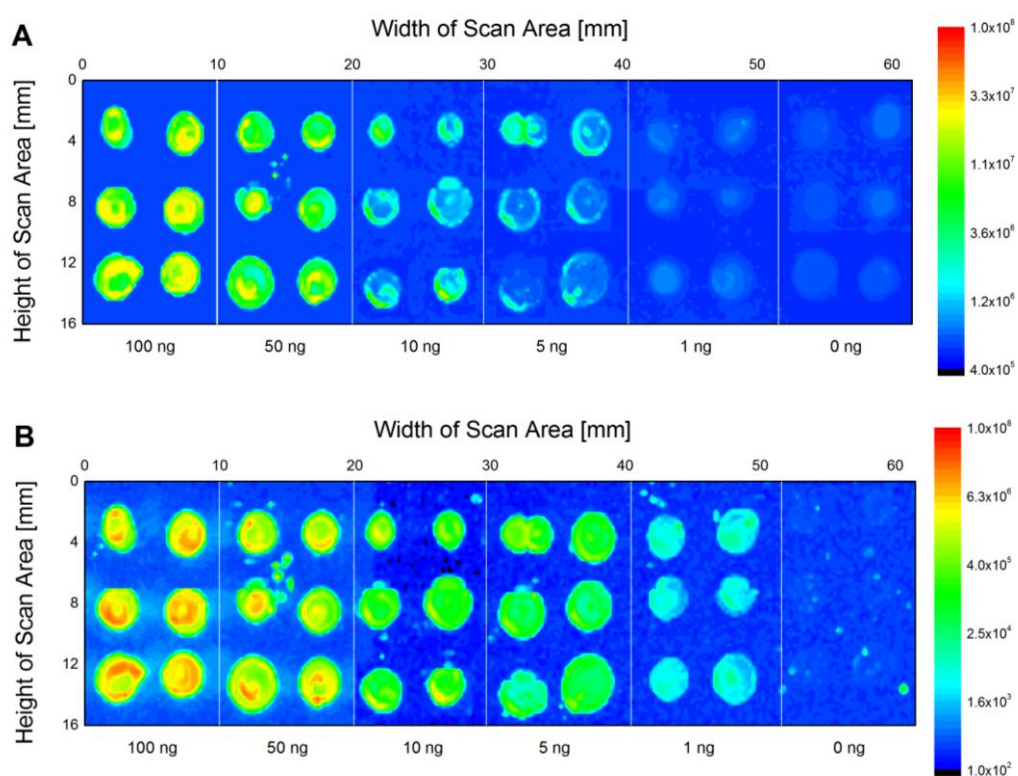
Figure 6.9 Scan images of UCNP-Er$_1$ amounts ranging from 1 to 100 ng for LOD determination utilizing the (A) overall and (B) green emission as the detection signal; a pseudo-color and logarithmic scale is used for both images to visualize the broad intensity range.

For a more quantitative determination of the LOD a calibration curve was derived from these images by using the normalized intensity, i.e. the average intensity of a single scan point, as the measurand (Figure 6.10).

$$I = 5.77 \cdot 10^5 \; \frac{1}{ng} \cdot m \; [ng] + 1.39 \cdot 10^5$$

$$R^2 = 0.9985$$

$$I = 5.08 \cdot 10^4 \; \frac{1}{ng} \cdot m \; [ng] - 4.58 \cdot 10^4$$

$$R^2 = 0.9967$$

Figure 6.10 Calibration curves in an amount range of UCNP-Er$_1$ from 1 to 100 ng with (A) overall and (B) green emission as the detection signal and a normalization to a single scanning point; the linear equation and coefficient of determination R^2 are given below.

A linear correlation between the upconversion luminescence intensity and the UCNP amount was confirmed by these fittings which featured a good conformity indicated by the high coefficient of determination R^2. The calculation of the LOD was analogue to the determination of the LOD of UCNPs in dispersion described in chapter 6.2. The LODs for both emission types (Table 6.6) proved a very good sensitivity enabling the significant detection of 1 ng UCNP.

Table 6.6 Lowest detectable intensity (LDI) and limit of detection (LOD) of UCNP-Er$_1$ with the respective detection signal

Detection signal	LDI [a.u.]	LOD [ng]
Overall emission	7.22 x 10^5	1.04
Green emission	3.04 x 10^2	0.91

The scan of different amounts of thulium-doped UCNPs (UCNP-Tm) showed that an amount of 5 ng UCNPs were distinguishable from the background for both emission types by a qualitative evaluation (Figure 6.11).
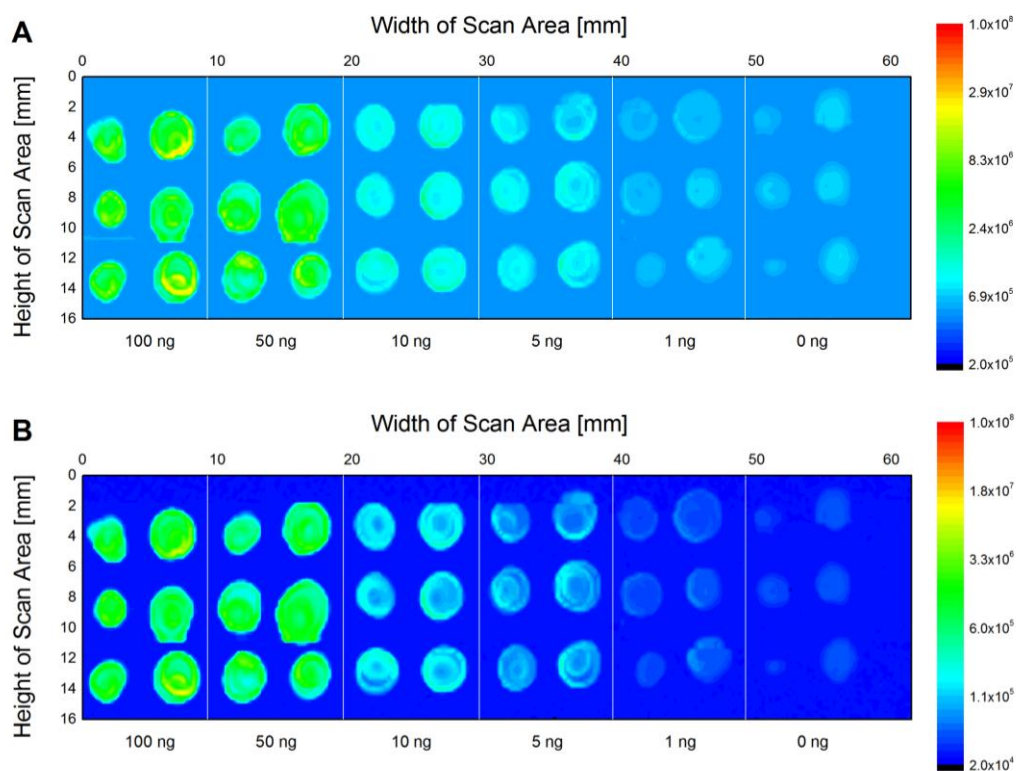
Figure 6.11 Scan images of UCNP-Tm amounts ranging from 1 to 100 ng for LOD determination utilizing the (A) overall and (B) infrared emission as the detection signal; an identical pseudo-color and logarithmic scale is used for both images to visualize the broad intensity range.

The calibration for the LOD determination again included the plotting of the average intensity of a single scanning spot over the UCNP amount (Figure 6.12).
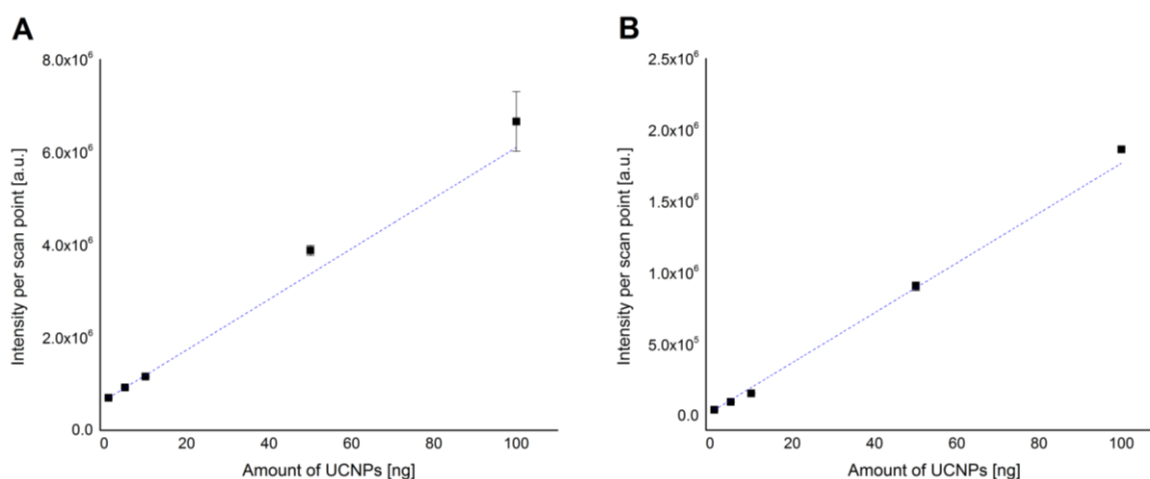
$$I = 5.46 \cdot 10^4 \ \frac{1}{ng} \cdot m \ [ng] + 64.3 \cdot 10^4$$

$$R^2 = 0.9852$$

$$I = 1.74 \cdot 10^4 \ \frac{1}{ng} \cdot m \ [ng] + 2.40 \cdot 10^4$$

$$R^2 = 0.9816$$

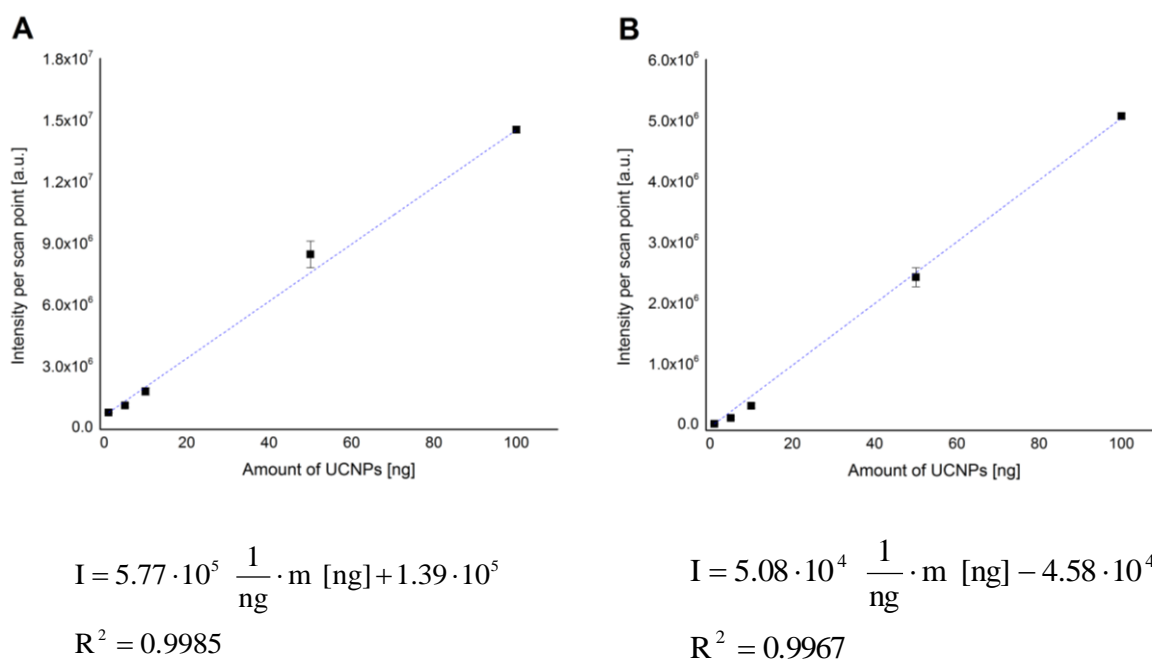**Figure 6.12** Calibration curves in an amount range of UCNP-Tm from 1 to 100 ng with (A) overall and (B) green emission as the detection signal; the linear equation and coefficient of determination R^2 are given below.

A linear fit again verified a linear correlation between UCNP amount and upconversion emission intensity indicated by the coefficients of determination R^2. Analogue calculation as for erbium-doped UCNP nanoparticles revealed a LOD in the range of 1 ng (Table 6.7). The higher LOD for the overall emission was explained by the comparatively high background of the scan images leading to a lower signal-to-noise ratio.

Table 6.7 Lowest detectable intensity (LDI) and limit of detection (LOD) of UCNP-Tm with the respective detection signal

Detection signal	LDI [a.u.]	LOD [ng]
Overall emission	7.25×10^5	1.51
Infrared emission	4.10×10^4	0.98

In conclusion, both UCNP types showed a linear correlation between the upconversion luminescence and the UCNP amount. Calculations yielded a LOD around 1 ng for the overall and the single wavelength emission of erbium- or thulium-doped UCNPs. Consequently, they are suitable as luminescent labels for (bio)analytical applications, especially for assay techniques where only low nanoparticle amounts have to be detectable. An improvement of the LOD might be realizable if the determination process is optimized by ensuring a reproducible spot size with distinct boundaries or if the sensitivity of the detector is enhanced, especially important for NIR emission of thulium-doped UCNPs. Furthermore, since a hydrophilic surface is indispensable for bioanalysis but causes a reduction of the upconversion luminescence due to quenching effects, the influence of these surface modifications on the LOD is important to determine.

6.8   Scan of Electrophoresis Gels

The applicability of the scan mode on real samples was investigated after the development and optimization of the general scan process including studies about the lateral resolution, the limit of detection and the signal-to-noise ratio. The imaging of UCNPs in electrophoresis gels by their upconversion luminescence was hampered for a long time due to the lack of commercially available instruments with a NIR excitation source and thus luminescence substitutes such as organic fluorophores had to be employed. Despite these instrumental limitations for a direct upconversion detection gel electrophoresis proved to be a convenient method both for the separation of modified UCNPs from aggregates and for the isolation of single nanoparticles[260]. Consequently, the first imaging studies of electrophoresis gels by the scan mode of the Chameleon reader focused on its general feasibility. The nanoparticles employed (UCNP-Er$_2$) were silica-coated and functionalized with carboxylic groups to ensure dispersibility in the aqueous electrophoresis system and electrophoretic

mobility. Additionally, the organic fluorophore fluorescein was introduced into the silica shell to allow a comparison of conventional fluorescence imaging methods.

An electrophoresis gel of a UCNP batch after surface modification was imaged with the overall or the green emission serving as the detection signal (Figure 6.13). The undiluted and two diluted dispersions of this batch were applied twofold on neighboring lanes. A lower minimum intensity of 200 a.u. for the green emission was chosen for the images, since a better signal-to-noise ratio was given for this emission type.
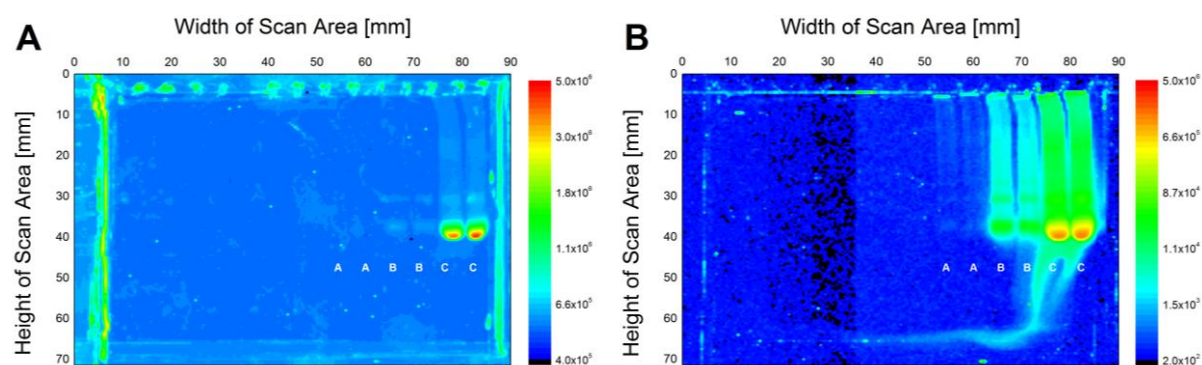
Figure 6.13 Scan images of the exemplary electrophoresis gel after the separation of UCNP-Er$_2$ utilizing the (A) overall and (B) green emission as the detection signal; an pseudo-color and logarithmic scale is used for both images to visualize the broad intensity range.

Both lanes of the undiluted and the higher concentrated diluted sample of the UCNP-Er$_2$ nanoparticles displayed two sets of luminescent bands for both emissions which confirmed the method feasibility for electrophoresis gels. The detection of two bands in each lane was attributed to two subpopulations of nanoparticles in the UCNP batch and their varying migration distance indicated a difference in size of these nanoparticles. The same position of these bands for both the undiluted and diluted samples confirmed the absence of any overlapping of bands and thus the only presence of these subpopulations. Furthermore, also structural characteristics of the gel itself such as the gel edges and the gel pockets were depicted in the images which simplified lane identification.

While these observations were conformably found for both the overall and the single wavelength emission, there were also differences in the content of information for these detection signals. The image of the overall emission showed a good discrimination of the luminescence signals from each other and from the background. However, an illustration was hampered for lower nanoparticle concentration which was verified by missing luminescent bands in the two lanes A (Figure 6.13A). In contrast, the image of the green emission indicated the gel bands of the lowest UCNP concentration but it suffered from a strongly increased background inside the lanes B and C (Figure 6.13B). A partial obscuring of UCNP bands was evident for the upper weaker emission band in lane C. Since this high background was detectable only in the sample lanes and was absent in the sample-free lanes, a

scattering effect of the synthesis components was a potential cause for this raise in intensity. In conclusion, although the overall emission allowed a good distinction between the UCNP bands and the background, an improved sensitivity was achieved by utilizing the green emission of the UCNP-Er$_2$ but along with an increased background in the sample lanes.

After the general feasibility of the scan mode for electrophoresis gels was demonstrated, the electrophoresis and subsequent upconversion scan were investigated as a UCNP characterization method during surface modification studies. The functionalization of UCNPs by the growth of a silica shell and the simultaneous silanization with carboxylic groups was chosen for this purpose, since its modification process was well understood (chapter 4.4) and showed a dependency of the nanoparticle characteristics on the silane amount during synthesis. Therefore, nanoparticles were synthesized with varying TEOS and CEST volumes (Table 6.8) for the investigation of this dependency and separated by gel electrophoresis. A simultaneous fluorescein labeling with a fluorescein-labeled amine silane (FITC-APTES) enabled an imaging with a conventional fluorescence technique important for a method comparison. Both the nanoparticle synthesis and the subsequent electrophoretic separation were performed by Dr. Antonín Hlaváček.

Table 6.8 Volume ratios of TEOS/FITC-APTES and CEST utilized for UCNP-Er$_3$ preparation

Code	TEOS/FITC-APTES volume [µL]	CEST [µL]
UCNP-Er$_3$-A	1.0	0.8
UCNP-Er$_3$-B	1.0	1.7
UCNP-Er$_3$-C	1.0	3.4
UCNP-Er$_3$-D	2.0	0.8
UCNP-Er$_3$-E	2.0	1.7
UCNP-Er$_3$-F	2.0	3.4

The image obtained of the electrophoresis gel by the scan mode of the Chameleon reader is shown in Figure 6.14. A distance of 500 µm of the scanning points was enough to obtain a sufficient resolution of the different gel bands and a logarithmic pseudo-color scale chosen to take into account the broad intensity range of the upconversion emission.

The two gel scans were informative about the quality of the synthesis optimization process. Except for the UCNP-Er$_3$-D sample all nanoparticle types migrated into the gel and were separated into two bands, at least to a certain extent. Especially, the UCNP-Er$_3$-C and UCNP-Er$_3$-F nanoparticles featured high uniformity of their electrophoretic separation and their similar surface characteristics were confirmed by the same position of their lower band with high emission intensity. In contrast, the

major part of the other nanoparticle types, above all UCNP-Er$_3$-A and UCNP-Er$_3$-E, remained in the well pockets indicating a strong aggregation of these as-modified UCNPs. Consequently, a high nanoparticle stabilization was guaranteed by a large CEST volume, while the amount of added TEOS played only a minor role. The scan images also confirmed the differing illustration characteristics for the overall and green emission as described before for the feasibility study (Figure 6.13) such as the increased background luminescence for the green emission.
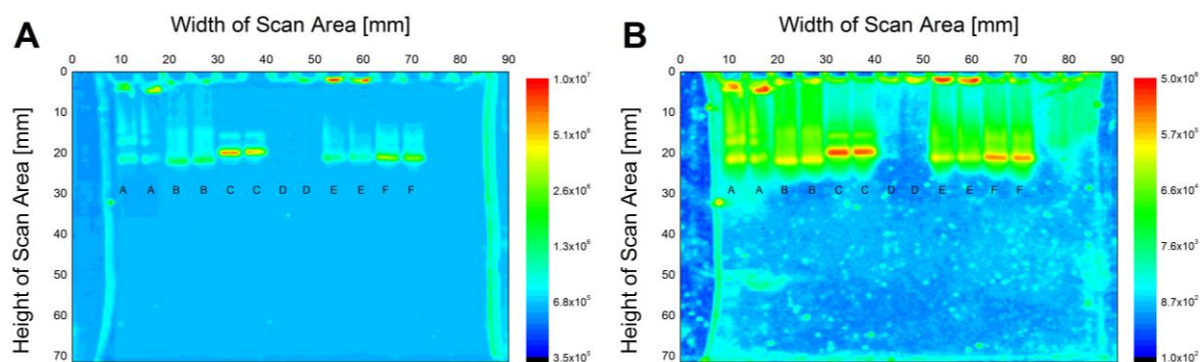
Figure 6.14 Scan images of the electrophoresis gel after the separation of UCNP-Er$_2$ synthesized with varying silane volumes utilizing the (A) overall and (B) green emission as the detection signal; a pseudo-color and logarithmic scale is used for both scan images to visualize the broad intensity range and the codes of the different nanoparticle types are stated for a simpler assignment.

A comparison with the fluorescence image (Figure 6.15) recorded with an excitation wavelength of 488 nm and an emission wavelength of 532 nm was informative about the result comparability of the new scan method with well established techniques. The position and the relative intensity of the gel bands coincided in the fluorescence and upconversion image (Figure 6.14). The differing band shape in the images was attributed to the larger excitation area of NIR laser and the resulting luminescence emission of UCNPs excited by the outer rim of the laser. However, the upconversion scan allowed an illustration of bands with a weak intensity which partly disappeared into the background for the fluorescence image, for example in lane C, which confirmed the higher detection sensitivty of UCNPs compared to conventional fluorophores. The large fluorescent area below the bands in the fluorescence image was identified as unbound fluorophore whose presence was explained by the application of the UCNP sample directly on the gel without any purification steps. The absence of this area in the upconversion scan images verified an independence of the UCNP and fluorophore detection which enables a bimodal readout without any impact of the other label necessary for multiplexing applications. Furthermore, the sole illustration of UCNPs in the upconversion images is advantageous for preparative approaches where a nanoparticle identification is mandatory to allow an isolation of a single subpopulation of UCNPs with a high purity.
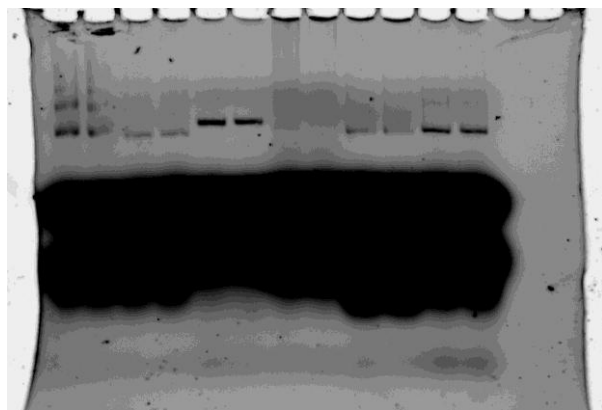
Figure 6.15 Fluorescence image of the electrophoresis gel after the separation of UCNP-Er$_2$

In conclusion, the scan mode of the Chameleon reader was applicable to electrophoresis gels. The agarose gel proved to be resistant against heating effects by the NIR laser indicated by the absence of any damages, even after repeated scans. The utilization of the overall and the green emission allowed the detection of all luminescent bands containing UCNPs as well as the gel edges and pockets with similar contents of information. However, while the green emission was favorable to detect very weak UCNP bands but caused an obscuring effect of the gel bands by increased background intensity, the overall emission resulted in images with a low background but lacked a sufficient resolution of lower UCNP concentrations. Consequently, a scan of an electrophoresis gel with both emissions yielded different information about the presence and amount of UCNP and thus can be employed as complementary measurements.

6.9   Scans of Lateral Flow Assays

The imaging of lateral flow assays (LFA) was the second application option of the scan mode on a real sample. The general design of these assays comprised a mixing zone and at least two reaction stripes. The first reaction stripe passed by the sample fluid is the actual detection line, the so-called test line, while the second reaction stripe, the so-called flow control line, serves as a confirmation of the process completion. As an exemplary analyte the *Schistosoma* circulating anodic antigen (CAA) originating from the parasitic worm *Schistosoma* was quantified by such lateral flow assays. The assays comprised a nitrocellulose membrane as the support matrix, an application pad made of glass fiber, a filter paper pad for waste absorption, and a laminate foil covering the actual assay compartment of the nitrocellulose membrane. The monoclonal mouse-anti-CAA antibody (MACAA) was immobilized on the test line to bind the CAA analyte solved in the sample, while a polyclonal goat-anti-mouse (GAM) antibody was bound on the flow control line owing to its specificity against the MACAA. A MACAA antibody labeled with nanoparticles of the type UCNP-Er$_4$ acted as the detection component of both antigen bound to the test line and GAM antibody bound to the flow

control line. For a quantification of the CAA analyte by the LFA technique, a dilution series of a crude worm extract were prepared (Table 6.9) and an individual assay was performed with each of these samples. The preparation and performance of the lateral flow assays were performed by the group of Dr. Paul Corstjens resulting in dried assays ready for imaging.

Table 6.9 CAA concentration applied to the different lateral flow assays

	Assay 1	Assay 2	Assay 3	Assay 4	Assay 5	Assay 6	Assay 7	Assay 0
Code	A1	A2	A3	A4	A5	A6	A7	B
CAA concentration [pg/mL]	10	31.6	100	316	1000	3162	10000	0

The overall and the green emission of the UCNP-Er$_4$ nanoparticles were utilized as the detection signal for the CAA quantification (Figure 6.16). A lateral resolution of 500 µm was sufficient to discriminate the test and the flow control line of the assays from the background. The collecting time had to be optimized, since the laminate foil cover of the nitrocellulose membrane was strongly heat sensitive. A collecting time of 250 ms reduced the probability of occurrence of damages and also avoided any oversaturation of the photomultiplier tube due to the higher brightness of the large UCNP-Er$_4$.
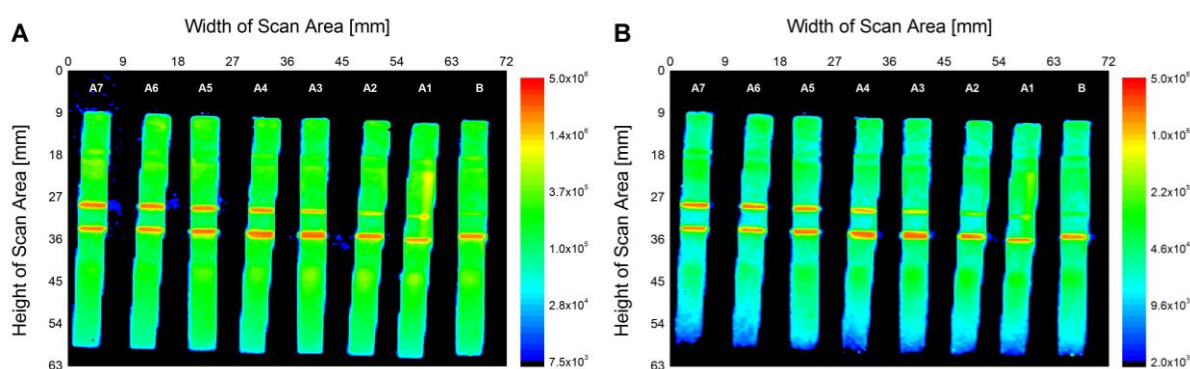
Figure 6.16 Scan images of the lateral flow assays with UCNP-Er$_4$ as the luminescent label synthesized utilizing the (A) overall and (B) green emission as the detection signal; a pseudo-color and logarithmic scale is used for both scan images to visualize the broad intensity range and the codes of the assays are stated for a simpler assignment.

The whole assay was imaged by the scan mode of the Chameleon reader using the overall (Figure 6.16A) or the green (Figure 6.16B) emission as the detection signal. The assay support matrix of white nitrocellulose showed a high scattering and reflection capability of the upconversion luminescence which resulted in an intensity increase between the assay and the scan support and thus enabled the illustration of the assay. This difference in intensity led to a background correction of the images in Figure 6.16 utilizing the average of the detected intensity of the nitrocellulose membrane. Furthermore, after this correction a sensitive and accurate detection of the test and the flow control line was realizable. The upconversion luminescence of the test line (upper band) decreased due to

the reduction of the CAA concentration from A7 to A1, while the intensity signal of the flow control line (lower band) remained constant.

For the quantitative evaluation of the scan images the sum intensity of each test and flow control line was determined which were also corrected by the intensity of the test line of the blank assay B. The resulting sum intensity of the flow control line strongly varied between the assays A1-A7 (Figure 9.37A) which indicated differences in the assay preparation such as flow characteristics of the sample or binding efficiency of the antibody. A ratiometric evaluation was performed in form of the intensity ratio of test and flow control line (I_T/I_C) to take account of these variations and to level out their influence (Figure 9.37B). The I_T/I_C ratios were fitted with a logistic 4-parameter function (Figure 6.17). While a coefficient of determination R^2 of 0.9901 for the green emission confirmed a high conformity of the fit to the data, a coefficient of 0.9257 for the overall emission was determined. Consequently, the utilization of the shortpass/bandpass filter combination for the green emission was of great advantage for scans of real samples, since the strongly improved signal-to-noise ratio and a lower background signal compared to the overall emission allowed a better signal detection.
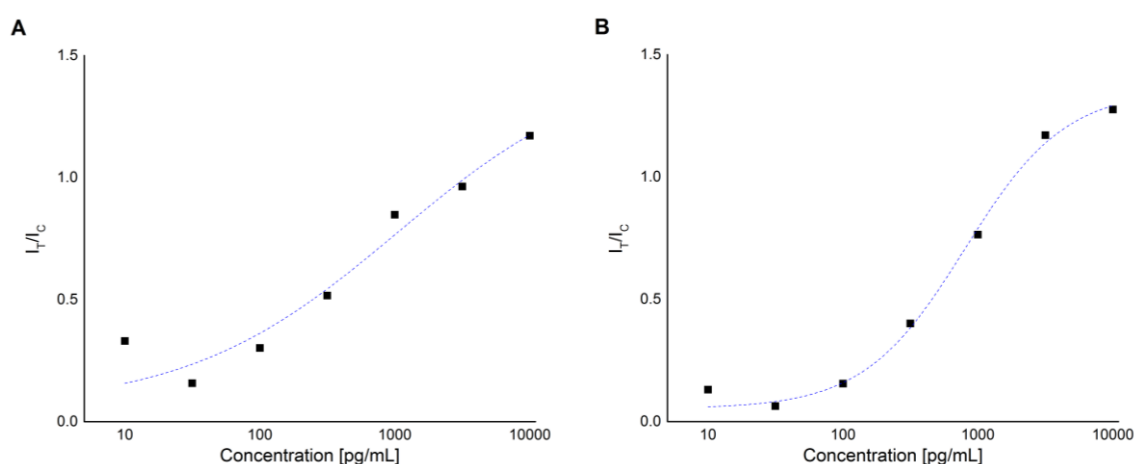
Figure 6.17 Intensity ratio of test (I_T) and control (I_C) strip for the different UCNP concentrations with a logistic 4-parameter function fit utilizing the overall (A) or the green (B) emission as the detection signal

A second study of these assays focused on the influence of the assay state, i.e. dry or wet, on the evaluation, since the emission of UCNPs is quenched by water molecules due to their high vibrational states. Therefore, the dried assays were wetted by applying 200 µL of double-distilled water onto the application pad and after the removal of excess fluid the assays were imaged with the same settings as before. The comparison of the evaluation data (Figure 9.38) revealed a very low influence of the assay state on the intensity ratios of the test and flow control line apparent in the high conformity of the ratios for the dried and the wet assays. Consequently, an imaging and evaluation of the lateral flow assays was realizable both in a wet state and after drying for storage without any losses of information.

Finally, a calculation of the limit detection (LOD) was performed for the assays in the dried and the wet state. A linear fit of the dynamic range and the lower limit of the respective logistic 4-parameter function were determined and the intersection of the linear regressions was utilized to calculate the LOD (Table 6.10).

Table 6.10 Limit of detection (LOD) of UCNP-Er$_4$ with the respective detection signal and assay condition

Detection signal	Condition	LOD [pg/mL]
Overall emission	Dry	64.11
	Wet	43.98
Green emission	Dry	130.46
	Wet	119.62

The general low detectable concentrations confirmed a high detection sensitivity of the UCNP labels used for lateral flow assays. Furthermore, a wetting of the assays seemed to improve the LOD as indicated by the lower concentrations of detectable nanoparticles for the wet state. Furthermore, the assays were also evaluated by the group of Corstjens using a Packard scanner or an ESE Quant scanner suitable for UCNP detection. The measurements with these instruments were performed in a line scan mode and the upconversion emission was detected along the vertical middle line of the assay. Consequently, the luminescence of only a small part of the test and flow control line of the assay was measured by this mode in contrast to the detection of the complete lines by the scan mode of the Chameleon reader. Evaluations of the line scans revealed a limit of detection of 129 pg/mL for a Packard scanner and of 120 pg/mL for an ESE Quant scanner. The scan mode of the Chameleon reader was capable to detected UCNPs at least in the same concentration range (green emission) or lower concentrations (overall emission) compared to these detection devices which was also attributed to the utilization of the whole test and flow control line for evaluation.

In conclusion, the scan mode of the Chameleon reader was able to image lateral flow assays both in a dried and a wet state. A ratiometric method utilizing the sum intensity ratios of the test and flow control lines allowed an evaluation unaffected by differences in the assay preparations such as flow characteristics. A fitting with a logistic 4-parameter function proved to be in good conformity with the data and was used to determine the limit of detection of UCNPs for the wet and dry assays. Especially the overall emission as the detection signal enabled a lowest detectable nanoparticle concentration far below the LOD of other instruments employed for assay evaluation. These results confirmed the high detection sensitivity of the scan mode for UCNPs and suggested a good usability of such nanoparticles as luminescent probes for lateral flow assay applications.

6.10 Luminescence Enhancement by Surface Plasmon Resonance

The enhancement of the upconversion luminescence is one of the most important aspects of the design optimization of the UCNP. Additional to a shielding of the nanoparticle surface from quenchers by bulky ligands or an additional shell, there is also an enhancing effect on the upconversion luminescence by the surface plasmon resonance of a gold surface. Studies of this effect using the scan mode of the Chameleon reader were performed by depositing UCNPs on the gold or silica surface of a shared support. Commercially available silica wavers with gold electrodes usually used for electrochemical (bio)analysis were selected as this scan support since they featured a small size enabling short scan times and the presence of silica and gold areas large enough for UCNP application allowing a direct referencing. A modification of the gold and silica surface with an identical functionality, i.e. an alkyl chain or a carboxylic group, was performed to introduce a spacing layer between the UCNPs and the gold surface and to generate a surface with the same chemical characteristics. Especially the hydrophilicity of the microelectrode surface determined the spreading of the UCNP dispersion.

A functionalization with a thiol and a silane featuring the same functional group was studied with non-functionalized electrodes as references (Figure 9.39). The modification with a layer of long-chained octanyl groups created a surface with a very hydrophobic character leading to significant spreading of the applied UCNP dispersion in cyclohexane. The water droplet test showed a lower spreading compared to non-functionalized surfaces confirming a functionalization with hydrophobic groups. Images of the as-modified microelectrode recorded by a digital camera (Figure 9.40) demonstrated an even functionalization without any indications of contaminations during the modification process. The reduced number of prior present dust or other contaminations was attributed to the extensive washing of the surface before and after functionalization and the storage in ethanol to avoid new contaminations. Consequently, the microelectrodes modified with octanyl groups were suitable for the investigation of the surface plasmon enhancement of the upconversion luminescence.

An analogue modification process was performed for the functionalization of the microelectrode with carboxylic groups utilizing the respective thiol and silane component. The creation of a highly hydrophilic surface was confirmed by the strong spreading of a water droplet. However, the silica surface of the as-functionalized microelectrodes was coated with a layer of precipitate visible both by the naked eye and a digital camera (Figure 9.41) after the silanization step. While the gold electrodes remain almost free of any contamination, the silica surface was nearly completely covered by this amorphous layer. This dependence on the surface material suggested a strong interaction of this

contamination with the unmodified silica surface. A scratch test revealed a simple removability of the contamination layer and an uncovering of an unaffected silica surface (Figure 9.42) which confirmed the non-covalent character of the interaction between contamination and surface and excluded any degradation processes of the silica. Therefore, the contamination layer originated from a precipitation of the carboxyl silane during silanization which was induced by the solvent change from an aqueous solution to the hydrophobic toluene phase as the reaction system. The high affinity of this precipitate to the silica surface only was attributed to a similar polarity of both materials.

The surface plasmon enhancement studies focused on the microelectrodes modified with octanyl groups as the UCNP support due to the difference in modification efficiency. The UCNP-Er_1 or UCNP-Tm dispersions were applied onto the gold and silica surface of the microelectrodes by a steel wire onto the microelectrode to ensure a small spot size. The filters chosen for the imaging included the shortpass filter and the two band pass filter for respective single wavelength emission of erbium- or thulium-doped UCNPs. Additionally, the red emission of erbium-doped UCNPs was recorded by using the combination of the longpass filter (395 - 825 nm) and a shortpass filter (600 - 2000 nm). An individual study of the blue or red emission of UCNP-Tm type was neglected, since the NIR emission presented nearly the complete upconversion emission of these nanoparticles. The scan images of both UCNP types with the overall emission as the detection signal are given in Figure 6.18 and the microelectrode outline was illustrated for the identification of the UCNP spots on the gold electrodes.
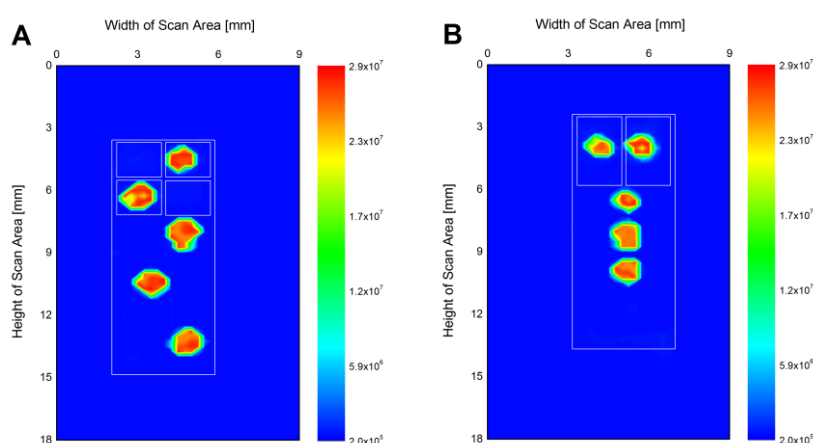
Figure 6.18 Exemplary scan images of microelectrode modified with octanyl groups utilizing the overall emission of UCNPs doped (A) with erbium or (B) with thulium as the detection signal; a pseudo-color scale is used and an approximate schematic illustration of the respective microelectrode layout including the overall dimensions (large rectangular) and the gold electrodes areas (smaller rectangles).

Two microelectrodes were utilized for each UCNP doping resulting in four or six evaluable spots on the gold and silica surface, respectively. The statistical evaluation included the determination of the average intensity of the UCNP spots on gold and silica and the standard deviation between the

different spots on the same surface material. The gold/silica intensity ratio was calculated to directly show an enhancement (> 1) or a quenching (< 1) of the upconversion emission by the surface plasmon resonance of gold (Figure 6.19).
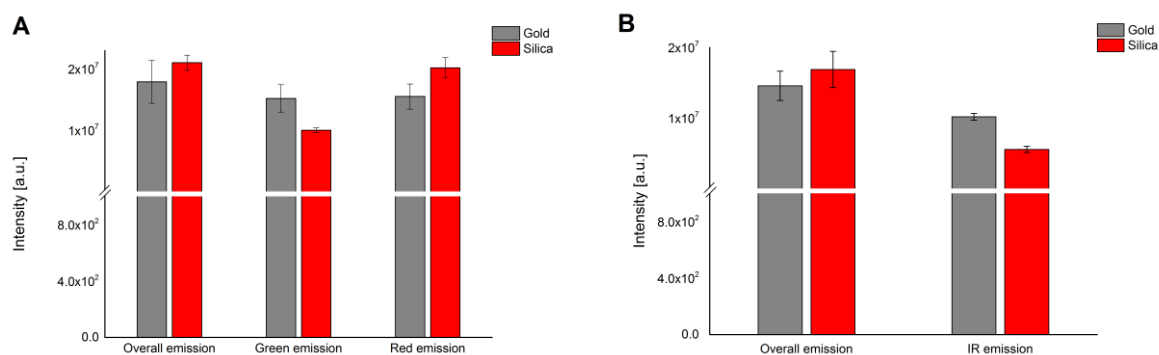
Dopant		Intensity ratio (gold : silica)
Erbium	Overall emission	0.85
	Green emission	1.52
	Red emission	0.77
Thulium	Overall emission	0.86
	Infrared emission	1.83

Figure 6.19 Average intensities of a single scanning point on a gold or silica surface modified with octanyl groups of UCNPs doped (A) with erbium or (B) with thulium using different emissions as the detection signal; the resulting quenching (< 1) or enhancement (> 1) factors are given below.

While the signal intensity of both overall emissions was reduced by the gold surface, an enhancement of the green or infrared emission of UCNP-Er$_1$ and UCNP-Tm, respectively, was evident. However, the red emission for the erbium-doped nanoparticles was also quenched by the gold surface similar to the overall emission. Consequently, the kind of influence of the plasmon resonance of a gold surface on the upconversion emission strongly depended on the wavelength. A reason for this dependency might be a shift in the transition probabilities towards a higher population of the green-emitting energy states of the erbium ions. An intensity comparison of the green and red emission of erbium-doped UCNPs was determined to study this dependency. While the intensities at both wavelengths were almost identical for a gold surface, the red emission was stronger on a silica surface. This alignment in intensity by a change in the support material from silica to gold suggested an intensity increase of the green emission with a simultaneous decrease of the red emission intensity. However, since the overall emission was decreasing, the enhancement of the green emission signal could not compensate the intensity reduction of the red emission.

In conclusion, the gold and silica surface of commercially available microelectrodes were successfully modified with hydrophobic octanyl chains. The upconversion luminescence of UCNPs on these surfaces was determined by the scan mode of the Chameleon reader to study the influence of a gold

surface on the emission intensity of these nanoparticles. While an enhancement was indicated for the green or infrared emissions of erbium- or thulium-doped UCNPs, the overall emission seemed to be quenched by the gold surface. A comparison between the red and green emission of erbium-doped UCNPs revealed a strong wavelength dependency of the luminescence enhancement by the surface plasmon resonance of a gold surface. However, since the overall emission decreased for UCNPs on gold, a predominant quenching effect was assumed.

7. Summary

7.1 In English

The surface modification of upconverting nanoparticles was a main focus of this thesis and a wide variety of different functionalities were introduced on the nanoparticle surface in the process. The growth of a silica shell with a preferably simultaneous silanization proved to be a convenient way to create both a hydrophilic surface crucial for bioanalytical applications and an accessible functionality for subsequent modification. The utilization of silanol, amine, carboxyl, or phosphonate groups yielded UCNPs with strongly differing stabilities in dispersion and surface charges. A strong aggregation was observed for both an amine modification and the non-modified silanol groups of a pure silica shell with a tendency enhancement for a reduced shell thickness. Furthermore, surface phosphonate groups led to the formation of aggregates with high uniformity in both size and shape. In contrast, an optimized modification process to introduce carboxylic acids on the surface yielded monodisperse UCNPs with a diameter of 13 nm that are efficiently stabilized in aqueous dispersion. The presence of these predominantly single nanoparticles in high abundance was confirmed both by dynamic light scattering and transmission electron microscopy studies. This high monodispersity was also realizable by a ligand exchange utilizing the polymer polyacrylic acid. The method applied relied on a prior exchange of the hydrophobic oleic acid with BF_4^- ions allowing a subsequent modification with the polymer with simplified process conditions and reduced expenditure of time.

Furthermore, the copper-catalyzed azide-alkyne cycloaddition (CuAAC) was studied as a potential beneficial coupling reaction since it merged the advantages of the "Click chemistry" and "bioorthogonal reactions" concept. The associated alkyne and azide groups were bound to the nanoparticle surface by silanization of silica-coated UCNPs and the nanoparticles differed drastically in their dispersion stability. While an azide-functionalized surface exerted a certain degree of stabilization, alkyne functionalities led to a strong nanoparticle aggregation and precipitation in a very short time. However, both functional groups allowed an efficient and highly specific binding of their respective counterpart shown by an exemplary Click reaction with a fluorophore and also the important role of the copper(I) catalyst was demonstrated. The attachment of more complex molecules including biochemical functionalities or additionally stabilizing moieties revealed a good feasibility of a modification by the copper-catalyzed azide-alkyne cycloaddition. A simultaneous modification of the UCNPs with azide and carboxyl groups led to an enhanced nanoparticle stability compared to a pure azide functionalization.

Studies about the creation of a biomimetic nanoparticle surface comprised the encapsulation of UCNPs by virus capsid leading to the formation of virus-like particles (VLPs). After the process feasibility was confirmed to both dissemble and reassemble the capsid of a brome mosaic virus (BMV), small nanoparticles with an optimized surface were utilized to act as an artificial nucleation grain for self-assembly. These modified UCNPs met the three requirements for encapsulation: a hydrophilic surface to be dispersible in aqueous systems, an absolute diameter below 16 nm to fit in the capsid cavity of the BMV, and a negative surface charge to initiate the self-assembly of the capsomers similar to the viral RNA. In addition to the options described, citric acid was investigated as a potential surface ligand. While silanol and phosphonate groups were inappropriate to induce any kind of self-assembly, a form of unspecific interaction of the viral proteins with carboxylic acids was found both for covalent and non-covalent methods. An exception was citric acid, since it was prone to an irreversible removal from the UCNP surface during the VLP preparation process. However, for all nanoparticles with a modified surface no clear evidence of encapsulation was found as confirmed by both TEM imaging and immunogold staining.

The second research focus of this thesis was the development of a new imaging method of UCNPs. At first, different imaging parameters of the scan mode of a Hidex Plate Chameleon Multilabel Detection Platform with a 980 nm excitation source were studied and optimized for UCNPs of the type $NaYF_4$: Yb^{3+}, Er^{3+} or NaY_4:Yb^{3+}, Tm^{3+}. A collecting time from 250 to 500 ms was sufficient to obtain an upconversion emission signal distinguishable from the background and to minimize laser-induced damages to the sample due to heating effects. Furthermore, both the overall emission of the UCNPs and the emission in a narrow wavelength domain were suitable as the detection signal for the image acquisition. The respective filter or filter combination additionally influenced the signal-to-noise ratio and thus the detection sensitivity. While the green emission of erbium-doped UCNPs was favorable in this regard, limitations of the detector sensitivity in the near infrared range hampered the utilization of the strong near infrared emission of thulium-doped UCNPs for scans with sensitive detection. The lateral resolution of the resulting scan images was reduced to 200 μm providing both a good resolution of luminescent structures and a good discrimination of signal and background. Since a lower scan point distance resulted in longer scan times without additional structural information, a lateral resolution of 200 μm was defined as the lower limit of the lateral resolution of the scan modus. Finally, a limit of detection of 1 ng was determined for both erbium- and thulium-doped UCNPs with high accuracy regardless of the emission utilized as the detection signal.

The applicability of this optimized process to real samples was demonstrated for both electrophoresis gels and lateral flow assays. The imaging of these gels and assays showed a high accuracy and reproducibility and allowed a good discrimination of the UCNP signal from the

background and an illustration of differences in the UCNP concentrations or sample materials. Furthermore, the downconversion emission of fluorescein doped in the silica shell of the UCNPs allowed a comparison between the imaging methods based either on up- and downconversion. In addition to a high conformity of the images regarding the position and intensity of the gel bands the absence of any signal from the fluorophore in the upconversion scan images of the gels confirmed a high discriminability of both signal types. This enables a bimodal readout. Moreover, the evaluation of the lateral flow assays yielded a limit of detection of the exemplary analyte "*Schistosoma* circulating anodic antigen (CAA)" of 44 or 64 pg/mL for the wet and dry condition of the array, respectively. For these measurements the the overall emission of the erbium-doped UCNPs was utilized as the detection signal. Consequently, a high sensitivity of this new imaging method was evident compared to other instrument options.

Finally, the scan mode of the Chameleon reader was also utilized for studies about a potential enhancement of the upconversion emission by surface plasmon resonance of a gold surface. Both $NaYF_4$: Yb^{3+}, Er^{3+} or NaY_4:Yb^{3+}, Tm^{3+} were applied on a gold or silica surface of a commercial wafer with gold electrodes whose complete surfce was modified before with the same functionality to ensure the same chemical properties. The comparison of the emission intensities of UCNP on the different surface materials indicated a strong dependency of the enhancement effect on the emission wavelength. While the intensity of the green or near infrared emission of erbium- or thulium-doped UCNPs was increased by the gold surface, the overall emission of both UCNP types was reduced indicating a simultaneous quenching of the upconversion emission at other wavelengths.

7.2   In German

Ein Schwerpunkt dieser Arbeit war die Oberflächenmodifikation von aufwärtskonvertierenden Nanopartikeln (eng.: upconverting nanoparticles, UCNP). Eine Vielzahl verschiedener Funktionalitäten wurde dafür auf der Nanopartikeloberfläche eingeführt. Das Aufbringen einer Silikaschicht mit einer vorzugsweise gleichzeitigen Silanisierung erwies sich dabei als praktischer Weg, um sowohl eine für bioanalytische Anwendungen wichtige hydrophile Oberfläche als auch eine für anschließende Modifikationen zugängliche Funktionalität zu erzeugen. Die Verwendung von Silanol-, Amin-, Carboxyl- oder Phosphonatgruppen ergaben UCNPs mit stark unterschiedlichen Dispersionsstabilitäten und Oberflächenladungen. Sowohl für eine Aminmodifikation als auch für nicht modifizierte Silanolgruppen einer reinen Silikahülle wurde eine starke Aggregation festgestellt, wobei eine Verstärkung dieses Prozesses bei einer Dickenverringerung der Silikahülle auftrat. Desweiteren führten Phosphonatgruppen auf der Oberfläche zur Bildung von Aggregaten mit einheitlicher Größe und Form. Demgegenüber lieferte ein optimierter Modifikationsprozess zur Anbringung von Carbonsäuren auf die Nanopartikeloberfläche monodisperse UCNPs mit einem Durchmesser von 13 nm und einer hohen Stabilität in wässriger Dispersion. Die überwiegende Anwesenheit einzelner Nanopartikel in großer Anzahl wurde durch Untersuchungen mittels dynamischer Lichtstreuung und Transmissionselektronenmikroskopie bestätigt. Diese hohe Monodispersität konnte auch bei einem Ligandenaustausch mit dem Polymer Polyacrylsäure realisiert werden. Dafür wurde die hydrophobe Ölsäure vorher durch BF_4^--Ionen ersetzt, um die anschließende Modifikation mit dem Polymer unter einfacheren Prozessbedingungen und mit geringerem Zeitaufwand zu ermöglichen.

Außerdem wurde die Kupfer-katalysierte Azid-Alkin-Cycloaddition als potenzielle Kupplungsreaktion untersucht, da sie die Vorteile der Konzepte "Click-Chemie" und "Bioorthogonalität" in sich vereinte. Die zugehörigen Alkin- und Azidgruppen wurden mittels einer Silanisierung der Silika-beschichteten UCNPs an die Nanopartikeloberfläche gebunden. Die erhaltenen Nanopartikel unterschieden sich drastisch in ihrer Dispersionsstabilität. Während eine Azid-funktionalisierte Oberfläche einen gewissen Grad an Stabilisierung ausübte, führten Alkinfunktionalitäten in kürzester Zeit zu einer starken Aggregation und Ausfällung der Nanopartikel. Beide funktionelle Gruppen erlaubten jedoch eine effiziente und höchst spezifische Anbindung des jeweiligen Gegenstücks durch eine Clickreaktion, testweise gezeigt mit einem passenden Fluorophor. Dabei wurde auch die entscheidende Rolle des Kupfer(I)-Katalysators demonstriert. Eine gut durchführbare Oberflächen-modifikation mittels einer Kupfer-katalysierte Azid-Alkin-Cycloaddition wurde durch die Ankopplung von komplexeren Molekülen, die biochemische oder zusätzlich stabilisierende Funktionalitäten

hatten, bewiesen. Eine gleichzeitige Modifikation der UCNPs mit Azid- und Carboxylgruppen führte zu einer erhöhten Nanopartikelstabilität verglichen mit einer reinen Azidfunktionalisierung.

Zur Erzeugung einer biomimetischen Nanopartikeloberlfäche wurden UCNPs mit einem Viruskapsid umhüllt. Dies führte zur Bildung von Virus-ähnlichen Partikeln (engl.: virus-like particles, VLPs). Nachdem die Umsetzbarkeit der Prozesse zum Auseinander- und Zusammenbauen von Kapsiden des Brommosaik-Virus (BMV) überprüft wurde, wurden kleine Nanopartikel mit einer optimierten Oberfläche verwendet, um als künstliche Nukleationskeime für die Selbstorganisation der Virusproteine zu dienen. Diese modifizierten UCNPs wiesen Eigenschaften auf, die die drei Anforderungen für eine Einkapselung erfüllten: eine hydrophile Oberfläche für ein mögliches Dispergieren in wässrigen Systemen, einen Durchmesser von unter 16 nm, um in den Kapsidhohlraum des BMV zu passen und eine negative Oberflächenladung für die Initiierung des Selbstzusammenbaus der Kapsomere wie mit der viralen RNA. Während Silanol- und Phosphonatgruppen ungeeignet waren, um eine Selbstorganisation der Kapsomere zu initiieren, wurden unspezifische Interaktionen der Virenproteine mit Carbonsäuren, die entweder durch kovalente oder nicht-kovalente Wechselwirkungen auf die Nanopartikeloberfläche eingeführt wurden, gefunden. Die zusätzlich untersuchte Oberflächenmodifikation mit Zitronensäure bildete eine Ausnahme, da dieser Ligand zu einer irreversiblen Ablösung von der UCNP-Oberfläche während der VLP-Herstellung neigte. Ein eindeutiger Beweis für eine Umhüllung eines Nanopartikels mit modifizierter Oberfläche wurde aber nicht gefunden, weder in TEM-Aufnahmen noch bei einer Immunogold-Anfärbung.

Der zweite Forschungsschwerpunkt dieser Arbeit war die Entwicklung einer neuen Abbildungsmethode von UCNPs. Zuerst wurden verschiedene Darstellungsparameter des Scanmodus einer "Hidex Plate Chameleon Multilabel Detection Platform" mit einer 980 nm Anregungsquelle untersucht und für UCNPs des Typs $NaYF_4$: Yb^{3+}, Er^{3+} oder NaY_4:Yb^{3+}, Tm^{3+} optimiert. Eine Detektionszeit von 250 bis 500 ms war ausreichend, um ein vom Hintergrund unterscheidbares Signal der Aufwärtskonversion-Emission zu erhalten und um Schäden an der Probe durch Erhitzungseffekte zu minimieren. Desweiteren waren sowohl die Gesamtemission als auch die Emission in einem schmalen Wellenlängenbereich als Detektionssignal für eine Bilderzeugung geeignet. Der jeweilige Filter oder die jeweilige Filterkombination beeinflusste auch das Signal-zu-Rauschen-Verhältnis und somit die Detektionsempfindlichkeit. Während die grüne Emission von Erbium-dotierten UCNPs sich diesbezüglich besonders auszeichnete, hemmte eine geringe Detektorempfindlichkeit im Nahinfrarot die Verwendbarkeit der starken Nahinfrarotemission von Thulium-dotierten UCNPs für Scans mit einer nachweisstarken Detektion. Die laterale Auflösung der Scanbilder wurde auf 200 μm verringert, wobei sowohl eine gute Auflösung lumineszierender Strukturen als auch eine gute

Unterscheidbarkeit von Signal und Hintergrund erreicht wurde. Da ein geringerer Abstand als 200 μm zwischen den Scanpunkten eine längere Scandauer ohne zusätzliche strukturelle Informationen zur Folge hatte, wurde diese laterale Auflösung als untere Auflösungsgrenze des Scan-Modus definiert. Schließlich wurde eine Nachweisgrenze von 1 ng mit hoher Genauigkeit mittels des Scanmodus sowohl für Erbium- wie auch Thulium-dotierten UCNPs realisiert. Dabei zeigte sich, dass diese niedrigste Konzentration von der als Detektionssignal verwendeten Emission unabhängig war.

Die Anwendung dieses optimierten Abbildungsprozesses auf Realproben wurde anhand von Elektrophoresegelen und Lateral-Flow-Assays gezeigt. Die Abbildung dieser Gele und Assays wies eine hohe Genauigkeit und Reproduzierbarkeit auf und erlaubte eine gute Unterscheidbarkeit des UCNP-Signals vom Hintergrund und eine Darstellung von Unterschieden in der UCNP-Konzentration oder im Probenmaterial. Außerdem erlaubte die abwärtskonvertierende Emission von Fluorescein, das in die Silikahülle der UCNPs eingebracht wurde, einen Vergleich zwischen den auf Aufwärts- oder Abwärtskonversion beruhenden Abbildungsmethoden. Zusätzlich zu einer hohen Übereinstimmung der Bilder bezüglich der Position und Intensität der Gelbanden bewies die Abwesenheit jeglichen Fluorophor-Signals in den Aufwärtskonversion-Bildern der Gele eine gute Unterscheidung beider Signaltypen. Dadurch wird ein bimodales Auslesen ermöglicht. Darüber hinaus ergab die Auswertung der Lateral-Flow-Assays eine Nachweisgrenze von 44 oder 64 pg/mL für den exemplarischen Analyten "*Schistosoma* circulating anodic antigen (CAA)" im feuchten bzw. trockenen Zustand des Assays. Bei deren Messung wurde die Gesamtemission der Erbium-dotierten UCNPs als Detektionssignal verwendet. Demzufolge ist eine hohe Empfindlichkeit dieser neuen Darstellungs-methode im Vergleich zu anderen Geräteoptionen offensichtlich.

Schließlich wurde der Scanmodus des Chameleon readers für Untersuchungen der möglichen Verstärkung der Aufwärtskonversion-Emission durch Oberflächenplasmonen einer Goldoberfläche eingesetzt. Sowohl $NaYF_4: Yb^{3+}, Er^{3+}$ als auch $NaY_4:Yb^{3+}, Tm^{3+}$ wurden auf eine Gold- oder Silikaoberfläche eines kommerziellen Wafers mit Goldelektroden aufgetragen, dessen gesamte Oberfläche vorher mit der gleichen Funktionalität modifiziert wurde, um gleiche chemische Eigenschaften sicherzustellen. Der Vergleich der Emissionsintensitäten der UCNP auf den verschiedenen Oberflächenmaterialien bestätigte eine starke Abhängigkeit des Verstärkungseffekts von der Emissionswellenlänge. Während die Intensität der grünen oder nahinfraroten Emission der Erbium- bzw. Thulium-dotierten UCNPs durch die Goldoberfläche verstärkt wurde, wurde die Gesamtemission beider UCNP-Typen verringert. Dies weist auf eine gleichzeitige Löschung der Aufwärtskonversion-emission bei anderen Wellenlängen hin.

8.   References

1   Nagl S, Stich MIJ, Schaferling M, Wolfbeis OS. **Method for simultaneous luminescence sensing of two species using optical probes of different decay time, and its application to an enzymatic reaction at varying temperature** (2009) Anal Bioanal Chem, *393*, 1199-1207.

2   Larson DR, Zipfel WR, Williams RM, Clark SW, Bruchez MP, Wise FW, Webb WW. **Water-soluble quantum dots for multiphoton fluorescence imaging in vivo** (2003) Science, *300*, 1434-1436.

3   Klostranec JM, Chan WCW. **Quantum dots in biological and biomedical research: Recent progress and present challenges** (2006) Adv. Mater., *18*, 1953-1964.

4   Goesmann H, Feldmann C. **Nanoparticulate Functional Materials** (2010) Angew. Chem. Int. Edit., *49*, 1362-1395.

5   Auzel F. **Upconversion and Anti-stokes processes with f and d ions in solids** (2004) Chem. Rev., *104*, 139-173.

6   Darbandi M, Lu WG, Fang JY, Nann T. **Silica encapsulation of hydrophobically ligated PbSe nanocrystals** (2006) Langmuir, *22*, 4371-4375.

7   Stöber W, Fink A, Bohn E. **Controlled Growth of Monodisperse Silica Spheres in Micron Size Range** (1968) J. Colloid Interface Sci., *26*, 62-69.

8   Bagwe RP, Hilliard LR, Tan WH. **Surface modification of silica nanoparticles to reduce aggregation and nonspecific binding** (2006) Langmuir, *22*, 4357-4362.

9   Brennan JL, Hatzakis NS, Tshikhudo TR, Dirvianskyte N, Razumas V, Patkar S, Vind J, Svendsen A, Nolte RJM, Rowan AE, Brust M. **Bionanoconjugation via click chemistry: The creation of functional hybrids of lipases and gold nanoparticles** (2006) Bioconjugate Chem., *17*, 1373-1375.

10 Mader HS, Link M, Achatz DE, Uhlmann K, Li XH, Wolfbeis OS. **Surface-Modified Upconverting Microparticles and Nanoparticles for Use in Click Chemistries** (2010) Chem. Eur. J., *16*, 5416-5424.

11 Sletten EM, Bertozzi CR. **From Mechanism to Mouse: A Tale of Two Bioorthogonal Reactions** (2011) Acc. Chem. Res., *44*, 666-676.

12 Aniagyei SE, DuFort C, Kao CC, Dragnea B. **Self-assembly approaches to nanomaterial encapsulation in viral protein cages** (2008) J. Mater. Chem., *18*, 3763-3774.

13 Daniel MC, Tsvetkova IB, Quinkert ZT, Murali A, De M, Rotello VM, Kao CC, Dragnea B. **Role of Surface Charge Density in Nanoparticle-Templated Assembly of Bromovirus Protein Cages** (2010) ACS Nano, *4*, 3853-3860.

14 Huang XL, Bronstein LM, Retrum J, Dufort C, Tsvetkova I, Aniagyei S, Stein B, Stucky G, McKenna B, Remmes N, Baxter D, Kao CC, Dragnea B. **Self-assembled virus-like particles with magnetic cores** (2007) Nano Lett., *7*, 2407-2416.

15 Lewis JD, Destito G, Zijlstra A, Gonzalez MJ, Quigley JP, Manchester M, Stuhlmann H. **Viral nanoparticles as tools for intravital vascular imaging** (2006) Nat. Med., *12*, 354-360.

16 Chen C, Daniel MC, Quinkert ZT, De M, Stein B, Bowman VD, Chipman PR, Rotello VM, Kao CC, Dragnea B. **Nanoparticle-templated assembly of viral protein cages** (2006) Nano Lett., *6*, 611-615.

17 Douglas T, Young M. **Host-guest encapsulation of materials by assembled virus protein cages** (1998) Nature, *393*, 152-155.

18 Nyk M, Kumar R, Ohulchanskyy TY, Bergey EJ, Prasad PN. **High Contrast in Vitro and in Vivo Photoluminescence Bioimaging Using Near Infrared to Near Infrared Up-Conversion in Tm^{3+} and Yb^{3+} Doped Fluoride Nanophosphors** (2008) Nano Lett., *8*, 3834-3838.

19 Cao TY, Yang Y, Gao YA, Zhou J, Li ZQ, Li FY. **High-quality water-soluble and surface-functionalized upconversion nanocrystals as luminescent probes for bioimaging** (2011) Biomaterials, *32*, 2959-2968.

20 Wang M, Mi CC, Wang WX, Liu CH, Wu YF, Xu ZR, Mao CB, Xu SK. **Immunolabeling and NIR-Excited Fluorescent Imaging of HeLa Cells by Using $NaYF_4$:Yb,Er Upconversion Nanoparticles** (2009) ACS Nano, *3*, 1580-1586.

21 Wang M, Mi CC, Zhang YX, Liu JL, Li F, Mao CB, Xu SK. **NIR-Responsive Silica-Coated $NaYbF_4$:Er/Tm/Ho Upconversion Fluorescent Nanoparticles with Tunable Emission Colors and Their Applications in Immunolabeling and Fluorescent Imaging of Cancer Cells** (2009) J. Phys. Chem. C, *113*, 19021-19027.

22 Xiong LQ, Chen ZG, Tian QW, Cao TY, Xu CJ, Li FY. **High Contrast Upconversion Luminescence Targeted Imaging in Vivo Using Peptide-Labeled Nanophosphors** (2009) Anal. Chem., *81*, 8687-8694.

23   Chatteriee DK, Rufalhah AJ, Zhang Y. **Upconversion fluorescence imaging of cells and small animals using lanthanide doped nanocrystals** (2008) Biomaterials, *29*, 937-943.

24   Tian Z, Chen GY, Li X, Liang HJ, Li YS, Zhang ZG, Tian Y. **Autofluorescence-free in vivo multicolor imaging using upconversion fluoride nanocrystals** (2010) Laser Med. Sci., *25*, 479-484.

25   Boyer JC, van Veggel FCJM. **Absolute quantum yield measurements of colloidal NaYF$_4$: Er^{3+}, Yb^{3+} upconverting nanoparticles** (2010) Nanoscale, *2*, 1417-1419.

26   Chen GY, Qju HL, Prasad PN, Chen XY. **Upconversion Nanoparticles: Design, Nanochemistry, and Applications in Theranostics** (2014) Chem. Rev., *114*, 5161-5214.

27   Auzel F. **Upconversion Processes in Coupled Ion Systems** (1990) J. Lumin., *45*, 341-345.

28   Wang F, Liu XG. **Recent advances in the chemistry of lanthanide-doped upconversion nanocrystals** (2009) Chem. Soc. Rev., *38*, 976-989.

29   Haase M, Schäfer H. **Upconverting Nanoparticles** (2011) Angew. Chem. Int. Edit., *50*, 5808-5829.

30   Dong B, Liu DP, Wang XJ, Yang T, Miao SM, Li CR. **Optical thermometry through infrared excited green upconversion emissions in Er^{3+}-Yb^{3+} codoped Al$_2$O$_3$** (2007) Appl. Phys. Lett., *90*, 181117.

31   Xu W, Xu S, Zhu YS, Liu T, Bai X, Dong BA, Xu L, Song HW. **Ultra-broad plasma resonance enhanced multicolor emissions in an assembled Ag/NaYF$_4$:Yb,Er nano-film** (2012) Nanoscale, *4*, 6971-6973.

32   Matsuura D. **Red, green, and blue upconversion luminescence of trivalent-rare-earth ion-doped Y$_2$O$_3$ nanocrystals** (2002) Appl. Phys. Lett., *81*, 4526-4528.

33   Wang X, Kong XG, Yu Y, Sun YJ, Zhang H. **Effect of annealing on upconversion luminescence of ZnO:Er^{3+} nanocrystals and high thermal sensitivity** (2007) J. Phys. Chem. C, *111*, 15119-15124.

34   Tripathi G, Rai VK, Rai SB. **Upconversion and temperature sensing behavior of Er^{3+} doped Bi$_2$O$_3$-Li$_2$O-BaO-PbO tertiary glass** (2007) Opt. Mater., *30*, 201-206.

35   Vetrone F, Boyer JC, Capobianco JA, Speghini A, Bettinelli M. **NIR to visible upconversion in nanocrystalline and bulk Lu$_2$O$_3$: Er^{3+}** (2002) J. Phys. Chem. B, *106*, 5622-5628.

36   Solìs D, López-Luke T, De la Rosa E, Salas P, Angeles-Chavez C. **Surfactant effect on the upconversion emission and decay time of ZrO$_2$:Yb-Er nanocrystals** (2009) J. Lumin., *129*, 449-455.

37   Chen XY, Ma E, Liu GK. **Energy levels and optical spectroscopy of Er^{3+} in Gd$_2$O$_3$ nanocrystals** (2007) J. Phys. Chem. C, *111*, 10404-10411.

38   Liu YX, Pisarski WA, Zeng SJ, Xu CF, Yang QB. **Tri-color upconversion luminescence of Rare earth doped BaTiO$_3$ nanocrystals and lowered color separation** (2009) Opt. Express, *17*, 9089-9098.

39   Hampl J, Hall M, Mufti NA, Yao YMM, MacQueen DB, Wright WH, Cooper DE. **Upconverting phosphor reporters in immunochromatographic assays** (2001) Anal. Biochem., *288*, 176-187.

40   Feng L, Wang J, Tang Q, Liang LF, Liang HB, Su Q. **Optical properties of Ho^{3+}-doped novel oxyfluoride glasses** (2007) J. Lumin., *124*, 187-194.

41   Du YP, Zhang YW, Sun LD, Yan CH. **Luminescent monodisperse nanocrystals of lanthanide oxyfluorides synthesized from trifluoroacetate precursors in high-boiling solvents** (2008) J. Phys. Chem. C, *112*, 405-415.

42   Pisarski WA, Goryuka T, Pisarska J, Dominiak-Dzik G, Ryba-Romanowski W. **Effect of heat treatment on Er^{3+} containing multicomponent oxyfluoride lead borate glass system** (2008) J. Non-Cryst. Solids, *354*, 492-496.

43   Heer S, Lehmann O, Haase M, Gudel HU. **Blue, green, and red upconversion emission from lanthanide-doped LuPO$_4$ and YbPO$_4$ nanocrystals in a transparent colloidal solution** (2003) Angew. Chem. Int. Edit., *42*, 3179-3182.

44   Aebischer A, Hostettler M, Hauser J, Krämer K, Weber T, Güdel HU, Bürgi HB. **Structural and spectroscopic characterization of active sites in a family of light-emitting sodium lanthanide tetrafluorides** (2006) Angew. Chem. Int. Edit., *45*, 2802-2806.

45   Schäfer H, Ptacek P, Zerzouf O, Haase M. **Synthesis and Optical Properties of KYF$_4$/Yb, Er Nanocrystals, and their Surface Modification with Undoped KYF$_4$** (2008) Adv. Funct. Mater., *18*, 2913-2918.

46   Joubert MF. **Photon avalanche upconversion in rare earth laser materials** (1999) Opt. Mater., *11*, 181-203.

47   Gamelin DR, Güdel HU. **Design of luminescent inorganic materials: New photophysical processes studied by optical spectroscopy** (2000) Acc. Chem. Res., *33*, 235-242.

48   Maciel GS, de Araújo CB, Messaddeq Y, Aegerter MA. **Frequency upconversion in Er^{3+}-doped fluoroindate-glasses pumped at 1.48 μm** (1997) Phys. Rev. B, *55*, 6335-6342.

49   Wang LY, Zhang Y, Zhu YY. **One-Pot Synthesis and Strong Near-Infrared Upconversion Luminescence of Poly(acrylic acid)-Functionalized YF$_3$:Yb^{3+}/Er^{3+} Nanocrystals** (2010) Nano Res., *3*, 317-325.

50   Qu YQ, Kong XG, Sun YJ, Zeng QH, Zhang H. **Effect of excitation power density on the upconversion luminescence of LaF$_3$:Yb^{3+}, Er^{3+} nanocrystals** (2009) J. Alloys Compd., *485*, 493-496.

51   Diamente PR, Raudsepp M, van Veggel FCJM. **Dispersible Tm^{3+}-doped nanoparticles that exhibit strong 1.47 μm photoluminescence** (2007) Adv. Funct. Mater., *17*, 363-368.

52   Suyver JF, Aebischer A, Biner D, Gerner P, Grimm J, Heer S, Krämer KW, Reinhard C, Güdel HU. **Novel materials doped with trivalent lanthanides and transition metal ions showing near-infrared to visible photon upconversion** (2005) Opt. Mater., *27*, 1111-1130.

53   Sedlmeier A, Gorris HH. **Surface modification and characterization of photon-upconverting nanoparticles for bioanalytical applications** (2015) Chem. Soc. Rev., *44*, 1526-1560.

54   Menyuk N, Pierce JW, Dwight K. **NaYF$_4$:Yb,Er - An Efficient Upconversion Phosphor** (1972) Appl. Phys. Lett., *21*, 159-161.

55   Krämer KW, Biner D, Frei G, Güdel HU, Hehlen MP, Lüthi SR. **Hexagonal sodium yttrium fluoride based green and blue emitting upconversion phosphors** (2004) Chem. Mater., *16*, 1244-1251.

56   Liu C, Wang H, Li X, Chen D. **Monodisperse, size-tunable and highly efficient β-NaYF$_4$:Yb,Er(Tm) up-conversion luminescent nanospheres: controllable synthesis and their surface modifications** (2009) J. Mater. Chem., *19*, 3546-3553.

57   Wang F, Han Y, Lim CS, Lu YH, Wang J, Xu J, Chen HY, Zhang C, Hong MH, Liu XG. **Simultaneous phase and size control of upconversion nanocrystals through lanthanide doping** (2010) Nature, *463*, 1061-1065.

58   Cao TY, Yang TS, Gao Y, Yang Y, Hu H, Li FY. **Water-soluble NaYF$_4$:Yb/Er upconversion nanophosphors: Synthesis, characteristics and application in bioimaging** (2010) Inorg. Chem. Commun., *13*, 392-394.

59   Kaminskii AA. **Achievements in the Field of Physics and Spectroscopy of Activated Laser Crystals** (1985) Phys. Status Solidi A, *87*, 11-57.

60   Liang LF, Wu H, Hu HL, Wu MM, Su Q. **Enhanced blue and green upconversion in hydrothermally synthesized hexagonal NaY$_{1-x}$Yb$_x$F$_4$: Ln^{3+} (Ln^{3+} = Er^{3+} or Tm^{3+})** (2004) J. Alloys Compd., *368*, 94-100.

61   Suyver JF, Grimm J, van Veen MK, Biner D, Krämer KW, Güdel HU. **Upconversion spectroscopy and properties of NaYF$_4$ doped with Er^{3+}, Tm^{3+} and/or Yb^{3+}** (2006) J. Lumin., *117*, 1-12.

62   Yin AX, Zhang YW, Sun LD, Yan CH. **Colloidal synthesis and blue based multicolor upconversion emissions of size and composition controlled monodisperse hexagonal NaYF$_4$:Yb,Tm nanocrystals** (2010) Nanoscale, *2*, 953-959.

63   Zhang L, Hu HF, Qi CH, Lin FY. **Spectroscopic properties and energy transfer in Yb^{3+}/Er^{3+}-doped phosphate glasses** (2001) Opt. Mater., *17*, 371-377.

64   Tikhomirov VK, Mortier M, Gredin P, Patriarche G, Görller-Walrand C, Moshchalkov VV. **Preparation and up-conversion luminescence of 8 nm rare-earth doped fluoride nanoparticles** (2008) Opt. Express, *16*, 14544-14549.

65   Glaspell G, Anderson J, Wilkins JR, Ei-Shall MS. **Vapor phase synthesis of upconverting Y$_2$O$_3$ nanocrystals doped with Yb^{3+}, Er^{3+}, Ho^{3+}, and Tm^{3+} to generate red, green, blue, and white light** (2008) J. Phys. Chem. C, *112*, 11527-11531.

66   Sivakumar S, van Veggel FCJM, May PS. **Near-infrared (NIR) to red and green up-conversion emission from silica sol-gel thin films made with La$_{0.45}$Yb$_{0.50}$Er$_{0.05}$F$_3$ nanoparticles, hetero-looping-enhanced energy transfer (Hetero-LEET): A new up-conversion process** (2007) J. Am. Chem. Soc., *129*, 620-625.

67   Wang F, Liu XG. **Upconversion multicolor fine-tuning: Visible to near-infrared emission from lanthanide-doped NaYF$_4$ nanoparticles** (2008) J. Am. Chem. Soc., *130*, 5642-5643.

68   Achatz DE, Ali R, Wolfbeis OS. **Luminescent Chemical Sensing, Biosensing, and Screening Using Upconverting Nanoparticles** (2011) Top. Curr. Chem., *300*, 29-50.

69   Bogdan N, Vetrone F, Ozin GA, Capobianco JA. **Synthesis of Ligand-Free Colloidally Stable Water Dispersible Brightly Luminescent Lanthanide-Doped Upconverting Nanoparticles** (2011) Nano Lett., *11*, 835-840.

70   Liu Y, Kobayashi T, Iizuka M, Tanaka T, Sotokawa I, Shimoyama A, Murayama Y, Otsuji E, Ogura S, Yuasa H. **Sugar-attached upconversion lanthanide nanoparticles: A novel tool for high-throughput lectin assay** (2013) Bioorgan. Med. Chem., *21*, 2832-2842.

71   Mai HX, Zhang YW, Sun LD, Yan CH. **Highly efficient multicolor up-conversion emissions and their mechanisms of monodisperse NaYF$_4$:Yb,Er core and core/shell-structured nanocrystals** (2007) J. Phys. Chem. C, *111*, 13721-13729.

72   Sun YJ, Chen Y, Tian LJ, Yu Y, Kong XG, Zhao JW, Zhang H. **Controlled synthesis and morphology dependent upconversion luminescence of NaYF$_4$:Yb, Er nanocrystals** (2007) Nanotechnology, *18*, 275609.

73   Vetrone F, Naccache R, Zamarrón A, de la Fuente AJ, Sanz-Rodríguez F, Maestro LM, Rodriguez EM, Jaque D, Solé JG, Capobianco JA. **Temperature Sensing Using Fluorescent Nanothermometers** (2010) ACS Nano, *4*, 3254-3258.

74   Boyer JC, Cuccia LA, Capobianco JA. **Synthesis of colloidal upconverting NaYF$_4$:Er^{3+}/Yb^{3+} and Tm^{3+}/Yb^{3+} monodisperse nanocrystals** (2007) Nano Lett., *7*, 847-852.

75   Yang LW, Han HL, Zhang YY, Zhong JX. **White Emission by Frequency Up-Conversion in Yb^{3+}-Ho^{3+}-Tm^{3+} Triply Doped Hexagonal NaYF$_4$ Nanorods** (2009) J. Phys. Chem. C, *113*, 18995-18999.

76   Wei Y, Lu FQ, Zhang XR, Chen DP. **Synthesis and characterization of efficient near-infrared upconversion Yb and Tm codoped NaYF$_4$ nanocrystal reporter** (2007) J. Alloys Compd., *427*, 333-340.

77   Chen GY, Ohulchanskyy TY, Kumar R, Agren H, Prasad PN. **Ultrasmall Monodisperse NaYF$_4$:Yb^{3+}/Tm^{3+} Nanocrystals with Enhanced Near-Infrared to Near-Infrared Upconversion Photoluminescence** (2010) ACS Nano, *4*, 3163-3168.

78   Soukka T, Rantanen T, Kuningas K. **Photon upconversion in homogeneous fluorescence-based bioanalytical assays** (2008) Ann. N.Y. Acad. Sci., *1130*, 188-200.

79   Shen J, Sun LD, Yan CH. **Luminescent rare earth nanomaterials for bioprobe applications** (2008) Dalton Trans., *42*, 5687-5697.

80   Yi GS, Lu HC, Zhao SY, Yue G, Yang WJ, Chen DP, Guo LH. **Synthesis, characterization, and biological application of size-controlled nanocrystalline NaYF$_4$:Yb,Er infrared-to-visible up-conversion phosphors** (2004) Nano Lett., *4*, 2191-2196.

81   Wang LY, Yan RX, Hao ZY, Wang L, Zeng JH, Bao H, Wang X, Peng Q, Li YD. **Fluorescence resonant energy transfer biosensor based on upconversion-luminescent nanoparticles** (2005) Angew. Chem. Int. Edit., *44*, 6054-6057.

82   Li ZQ, Zhang Y. **An efficient and user-friendly method for the synthesis of hexagonal-phase NaYF$_4$:Yb, Er/Tm nanocrystals with controllable shape and upconversion fluorescence** (2008) Nanotechnology, *19*, 345606.

83   Ehlert O, Thomann R, Darbandi M, Nann T. **A four-color colloidal multiplexing nanoparticle system** (2008) ACS Nano, *2*, 120-124.

84   Wang GF, Peng Q, Li YD. **Upconversion Luminescence of Monodisperse CaF$_2$:Yb^{3+}/Er^{3+} Nanocrystals** (2009) J. Am. Chem. Soc., *131*, 14200-14201.

85   Yang J, Zhang CM, Peng C, Li CX, Wang LL, Chai RT, Lin J. **Controllable Red, Green, Blue (RGB) and Bright White Upconversion Luminescence of Lu$_2$O$_3$:Yb^{3+}/Er^{3+}/Tm^{3+} Nanocrystals through Single Laser Excitation at 980 nm** (2009) Chem. Eur. J., *15*, 4649-4655.

86   Patra A, Friend CS, Kapoor R, Prasad PN. **Upconversion in Er^{3+}: ZrO$_2$ nanocrystals** (2002) J. Phys. Chem. B., *106*, 1909-1912.

87   Chen GY, Liu HC, Somesfalean G, Liang HJ, Zhang ZG. **Upconversion emission tuning from green to red in Yb^{3+}/Ho^{3+}-codoped NaYF$_4$ nanocrystals by tridoping with Ce^{3+} ions** (2009) Nanotechnology, *20*, 385704.

88   Liang HJ, Chen GY, Li L, Liu Y, Qin F, Zhang ZG. **Upconversion luminescence in Yb^{3+}/Tb^{3+}-codoped monodisperse NaYF$_4$ nanocrystals** (2009) Opt. Commun., *282*, 3028-3031.

89   Wang X, Zhuang J, Peng Q, Li YD. **Hydrothermal synthesis of rare-earth fluoride nanocrystals** (2006) Inorg. Chem., *45*, 6661-6665.

90   Zhang CL, Yuan YX, Zhang SM, Wang YH, Liu ZH. **Biosensing Platform Based on Fluorescence Resonance Energy Transfer from Upconverting Nanocrystals to Graphene Oxide** (2011) Angew. Chem. Int. Edit., *50*, 6851-6854.

91   Liu YS, Tu DT, Zhu HM, Chen XY. **Lanthanide-doped luminescent nanoprobes: controlled synthesis, optical spectroscopy, and bioapplications** (2013) Chem. Soc. Rev., *42*, 6924-6958.

92   Li ZQ, Zhang Y, Jiang S. **Multicolor Core/Shell-Structured Upconversion Fluorescent Nanoparticles** (2008) Adv. Mater., *20*, 4765-4769.

93   Wilhelm S, Kaiser M, Würth C, Heiland J, Carrillo-Carrion C, Muhr V, Wolfbeis OS, Parak WJ, Resch-Genger U, Hirsch T. **Water dispersible upconverting nanoparticles: effects of surface modification on their luminescence and colloidal stability** (2015) Nanoscale, *7*, 1403-1410.

94   Boyer JC, Vetrone F, Cuccia LA, Capobianco JA. **Synthesis of colloidal upconverting NaYF$_4$ nanocrystals doped with Er^{3+}, Yb^{3+} and Tm^{3+}, Yb^{3+} via thermal decomposition of lanthanide trifluoroacetate precursors** (2006) J. Am. Chem. Soc., *128*, 7444-7445.

95   Shan J, Qin X, Yao N, Ju Y. **Synthesis of monodisperse hexagonal NaYF$_4$: Yb, Ln (Ln = Er, Ho and Tm) upconversion nanocrystals in TOPO** (2007) Nanotechnology, *18*, 445607.

96   Wang HQ, Nann T. **Monodisperse Upconverting Nanocrystals by Microwave-Assisted Synthesis** (2009) ACS Nano, *3*, 3804-3808.

97   Kumar R, Nyk M, Ohulchanskyy TY, Flask CA, Prasad PN. **Combined Optical and MR Bioimaging Using Rare Earth Ion Doped NaYF$_4$ Nanocrystals** (2009) Adv. Funct. Mater., *19*, 853-859.

98   Shan JN, Ju YG. **Controlled synthesis of lanthanide-doped NaYF$_4$ upconversion nanocrystals via ligand induced crystal phase transition and silica coating** (2007) Appl. Phys. Lett., *91*, 123103.

99   Heer S, Kömpe K, Güdel HU, Haase M. **Highly efficient multicolour upconversion emission in transparent colloids of lanthanide-doped NaYF$_4$ nanocrystals** (2004) Adv. Mater., *16*, 2102-2105.

100   Schäfer H, Ptacek P, Kömpe K, Haase M. **Lanthanide-doped NaYF$_4$ nanocrystals in aqueous solution displaying strong up-conversion emission** (2007) Chem. Mater., *19*, 1396-1400.

101   Yi GS, Chow GM. **Synthesis of hexagonal-phase NaYF$_4$:Yb,Er and NaYF$_4$:Yb,Tm nanocrystals with efficient up-conversion fluorescence** (2006) Adv. Funct. Mater., *16*, 2324-2329.

102   Chen DQ, Yu YL, Huang F, Lin H, Huang P, Yang AP, Wang ZX, Wang YS. **Lanthanide dopant-induced formation of uniform sub-10 nm active-core/active-shell nanocrystals with near-infrared to near-infrared dual-modal luminescence** (2012) J. Mater. Chem., *22*, 2632-2640.

103   Cui XX, She JB, Gao C, Cui K, Hou CQ, Wei W, Peng B. **Luminescent properties of Nd^{3+}-doped LaF$_3$ core/shell nanoparticles with enhanced near infrared (NIR) emission** (2010) Chem. Phys. Lett., *494*, 60-63.

104   Abel KA, Boyer JC, Andrei CM, van Veggel FCJM. **Analysis of the Shell Thickness Distribution on NaYF$_4$/NaGdF$_4$ Core/Shell Nanocrystals by EELS and EDS** (2011) J. Phys. Chem. Lett., *2*, 185-189.

105   Yi GS, Chow GM. **Water-soluble NaYF$_4$:Yb,Er(Tm)/NaYF$_4$/polymer core/shell/shell nanoparticles with significant enhancement of upconversion fluorescence** (2007) Chem. Mater., *19*, 341-343.

106   Boyer JC, Manseau MP, Murray JI, van Veggel FCJM. **Surface Modification of Upconverting NaYF$_4$ Nanoparticles with PEG-Phosphate Ligands for NIR (800 nm) Biolabeling within the Biological Window** (2010) Langmuir, *26*, 1157-1164.

107   Liebherr RB, Soukka T, Wolfbeis OS, Gorris HH. **Maleimide activation of photon upconverting nanoparticles for bioconjugation** (2012) Nanotechnology, *23*, 485103.

108   Sudarsan V, Sivakumar S, van Veggel FCJM, Raudsepp M. **General and convenient method for making highly luminescent sol-gel derived silica and alumina films by using LaF$_3$ nanoparticles doped with lanthanide ions (Er^{3+}, Nd^{3+}, and Ho^{3+})** (2005) Chem. Mater., *17*, 4736-4742.

109   Wang F, Wang JA, Liu XG. **Direct Evidence of a Surface Quenching Effect on Size-Dependent Luminescence of Upconversion Nanoparticles** (2010) Angew. Chem. Int. Edit., *49*, 7456-7460.

110   Deng RR, Xie XJ, Vendrell M, Chang YT, Liu XG. **Intracellular Glutathione Detection Using MnO$_2$-Nanosheet-Modified Upconversion Nanoparticles** (2011) J. Am. Chem. Soc., *133*, 20168-20171.

111   Jiang GC, Pichaandi J, Johnson NJJ, Burke RD, van Veggel FCJM. **An Effective Polymer Cross-Linking Strategy To Obtain Stable Dispersions of Upconverting NaYF$_4$ Nanoparticles in Buffers and Biological Growth Media for Biolabeling Applications** (2012) Langmuir, *28*, 3239-3247.

112   Naccache R, Vetrone F, Mahalingam V, Cuccia LA, Capobianco JA. **Controlled Synthesis and Water Dispersibility of Hexagonal Phase NaGdF$_4$:Ho^{3+}/Yb^{3+} Nanoparticles** (2009) Chem. Mater., *21*, 717-723.

113   Wang Y, Tu LP, Zhao JW, Sun YJ, Kong XG, Zhang H. **Upconversion Luminescence of β-NaYF$_4$: Yb^{3+}, Er^{3+}@β-NaYF$_4$ Core/Shell Nanoparticles: Excitation Power, Density and Surface Dependence** (2009) J. Phys. Chem. C, *113*, 7164-7169.

114   Couvreur P, Puisieux F. **Nanoparticles and Microparticles for the Delivery of Polypeptides and Proteins** (1993) Adv. Drug Deliv. Rev., *10*, 141-162.

115   Foster KA, Yazdanian M, Audus KL. **Microparticulate uptake mechanisms of in-vitro cell culture models of the respiratory epithelium** (2001) J. Pharm. Pharmacol., *53*, 57-66.

116   Win KY, Feng SS. **Effects of particle size and surface coating on cellular uptake of polymeric nanoparticles for oral delivery of anticancer drugs** (2005) Biomaterials, *26*, 2713-2722.

117   Xia YN. **Nanomaterials at work in biomedical research** (2008) Nat. Mater., *7*, 758-760.

118   Hodgson JT, Darnton A. **The quantitative risks of mesothelioma and lung cancer in relation to asbestos exposure** (2000) Ann. Occup. Hyg., *44*, 565-601.

119   Goodglick LA, Kane AB. **Cytotoxicity of Long and Short Crocidolite Asbestos Fibers Invitro and Invivo** (1990) Cancer Res., *50*, 5153-5163.

120   Wade MJ, Lipkin LE, Tucker RW, Frank AL. **Asbestos Cytotoxicity in a Long-Term Macrophage-Like Cell-Culture** (1976) Nature, *264*, 444-446.

121   Shan JN, Chen JB, Meng J, Collins J, Soboyejo W, Friedberg JS, Ju YG. **Biofunctionalization, cytotoxicity, and cell uptake of lanthanide doped hydrophobically ligated $NaYF_4$ upconversion nanophosphors** (2008) J. Appl. Phys., *104*, 094308.

122   Wang Y, Ji L, Zhang BB, Yin PH, Qiu YY, Song DQ, Zhou JY, Li Q. **Upconverting rare-earth nanoparticles with a paramagnetic lanthanide complex shell for upconversion fluorescent and magnetic resonance dual-modality imaging** (2013) Nanotechnology, *24*, 175101.

123   Zhou J, Yu MX, Sun Y, Zhang XZ, Zhu XJ, Wu ZH, Wu DM, Li FY. **Fluorine-18-labeled $Gd^{3+}/Yb^{3+}/Er^{3+}$ co-doped $NaYF_4$ nanophosphors for multimodality PET/MR/UCL imaging** (2011) Biomaterials, *32*, 1148-1156.

124   Liu Q, Sun Y, Li CG, Zhou J, Li CY, Yang TS, Zhang XZ, Yi T, Wu DM, Li FY. **^{18}F-Labeled Magnetic-Upconversion Nanophosphors via Rare-Earth Cation-Assisted Ligand Assembly** (2011) ACS Nano, *5*, 3146-3157.

125   Xiong LQ, Yang TS, Yang Y, Xu CJ, Li FY. **Long-term in vivo biodistribution imaging and toxicity of polyacrylic acid-coated upconversion nanophosphors** (2010) Biomaterials, *31*, 7078-7085.

126   Yuan PY, Lee YH, Gnanasammandhan MK, Guan ZP, Zhang Y, Xu QH. **Plasmon enhanced upconversion luminescence of $NaYF_4$:Yb, Er@SiO$_2$@Ag core-shell nanocomposites for cell imaging** (2012) Nanoscale, *4*, 5132-5137.

127   Wu ZN, Guo CR, Liang S, Zhang H, Wang LP, Sun HC, Yang B. **A pluronic F127 coating strategy to produce stable up-conversion $NaYF_4$:Yb,Er(Tm) nanoparticles in culture media for bioimaging** (2012) J. Mater. Chem., *22*, 18596-18602.

128   Jalil RA, Zhang Y. **Biocompatibility of silica coated $NaYF_4$ upconversion fluorescent nanocrystals** (2008) Biomaterials, *29*, 4122-4128.

129   Vetrone F, Naccache R, Mahalingam V, Morgan CG, Capobianco JA. **The Active-Core/Active-Shell Approach: A Strategy to Enhance the Upconversion Luminescence in Lanthanide-Doped Nanoparticles** (2009) Adv. Funct. Mater., *19*, 2924-2929.

130   El-Sayed MA. **Some interesting properties of metals confined in time and nanometer space of different shapes** (2001) Acc. Chem. Res., *34*, 257-264.

131   Liz-Marzán LM. **Tailoring surface plasmons through the morphology and assembly of metal nanoparticles** (2006) Langmuir, *22*, 32-41.

132   Pérez-Juste J, Pastoriza-Santos I, Liz-Marzán LM, Mulvaney P. **Gold nanorods: Synthesis, characterization and applications** (2005) Coord. Chem. Rev., *249*, 1870-1901.

133   Alivisatos P. **The use of nanocrystals in biological detection** (2004) Nat. Biotechnol., *22*, 47-52.

134   Bukasov R, Shumaker-Parry JS. **Highly tunable infrared extinction properties of gold nanocrescents** (2007) Nano Lett., *7*, 1113-1118.

135   Irit N, Bendikov TA, Doron-Mor I, Barkay Z, Vaskevich A, Rubinstein I. **Silica-stabilized gold island films for transmission localized surface plasmon sensing** (2007) J. Am. Chem. Soc., *129*, 84-92.

136   Xing SX, Tan LH, Yang MX, Pan M, Lv YB, Tang QH, Yang YH, Chen HY. **Highly controlled core/shell structures: tunable conductive polymer shells on gold nanoparticles and nanochains** (2009) J. Mater. Chem., *19*, 3286-3291.

137   Hägglund C, Zäch M, Kasemo B. **Enhanced charge carrier generation in dye sensitized solar cells by nanoparticle plasmons** (2008) Appl. Phys. Lett., *92*, 013113.

138   Singh MP, Strouse GF. **Involvement of the LSPR Spectral Overlap for Energy Transfer between a Dye and Au Nanoparticle** (2010) J. Am. Chem. Soc., *132*, 9383-9391.

139   Zhao J, Jensen L, Sung JH, Zou SL, Schatz GC, Van Duyne RP. **Interaction of plasmon and molecular resonances for rhodamine 6G adsorbed on silver nanoparticles** (2007) J. Am. Chem. Soc., *129*, 7647-7656.

140   Chen Y, Munechika K, Ginger DS. **Dependence of fluorescence intensity on the spectral overlap between fluorophores and plasmon resonant single silver nanoparticles** (2007) Nano Lett., *7*, 690-696.

141   Noginov MA, Zhu G, Belgrave AM, Bakker R, Shalaev VM, Narimanov EE, Stout S, Herz E, Suteewong T, Wiesner U. **Demonstration of a spaser-based nanolaser** (2009) Nature, *460*, 1110-1113.

142   Munechika K, Chen Y, Tillack AF, Kulkarni AP, Plante IJL, Munro AM, Ginger DS. **Spectral Control of Plasmonic Emission Enhancement from Quantum Dots near Single Silver Nanoprisms** (2010) Nano Lett., *10*, 2598-2603.

143   Luther JM, Jain PK, Ewers T, Alivisatos AP. **Localized surface plasmon resonances arising from free carriers in doped quantum dots** (2011) Nat. Mater., *10*, 361-366.

144   Zhang H, Xu D, Huang Y, Duan XF. **Highly spectral dependent enhancement of upconversion emission with sputtered gold island films** (2011) Chem. Commun., *47*, 979-981.

145   Saboktakin M, Ye XC, Oh SJ, Hong SH, Fafarman AT, Chettiar UK, Engheta N, Murray CB, Kagan CR. **Metal-Enhanced Upconversion Luminescence Tunable through Metal Nanoparticle-Nanophosphor Separation** (2012) ACS Nano, *6*, 8758-8766.

146   Zhang H, Li YJ, Ivanov IA, Qu YQ, Huang Y, Duan XF. **Plasmonic Modulation of the Upconversion Fluorescence in NaYF$_4$:Yb/Tm Hexaplate Nanocrystals Using Gold Nanoparticles or Nanoshells** (2010) Angew. Chem. Int. Edit., *49*, 2865-2868.

147   Xu W, Chen BT, Yu W, Zhu YS, Liu T, Xu S, Min XL, Bai X, Song HW. **The up-conversion luminescent properties and silver-modified luminescent enhancement of YVO$_4$:Yb^{3+}, Er^{3+} NPs** (2012) Dalton Trans., *41*, 13525-13532.

148   Feng W, Sun LD, Yan CH. **Ag nanowires enhanced upconversion emission of NaYF$_4$:Yb,Er nanocrystals via a direct assembly method** (2009) Chem. Commun., *29*, 4393-4395.

149   Zhao P, Zhu YH, Yang XL, Fan KC, Shen JH, Li CZ. **Facile synthesis of upconversion luminescent mesoporous Y$_2$O$_3$:Er microspheres and metal enhancement using gold nanoparticles** (2012) R. Soc. Chem. Adv., *2*, 10592-10597.

150   Li ZQ, Li XD, Liu QQ, Chen XH, Sun Z, Liu C, Ye XJ, Huang SM. **Core/shell structured NaYF$_4$:Yb^{3+}/Er^{3+}/Gd^{3+} nanorods with Au nanoparticles or shells for flexible amorphous silicon solar cells** (2012) Nanotechnology, *23*, 025402.

151   Schietinger S, Aichele T, Wang HQ, Nann T, Benson O. **Plasmon-Enhanced Upconversion in Single NaYF$_4$:Yb^{3+}/Er^{3+} Codoped Nanocrystals** (2010) Nano Lett., *10*, 134-138.

152   Tu NN, Wang LY. **Surface plasmon resonance enhanced upconversion luminescence in aqueous media for TNT selective detection** (2013) Chem. Commun., *49*, 6319-6321.

153   Liu N, Qin WP, Qin GS, Jiang T, Zhao D. **Highly plasmon-enhanced upconversion emissions from Au@β-NaYF$_4$:Yb,Tm hybrid nanostructures** (2011) Chem. Commun., *47*, 7671-7673.

154   Kannan P, Rahim FA, Chen R, Teng X, Huang L, Sun HD, Kim DH. **Au Nanorod Decoration on NaYF$_4$:Yb/Tm Nanoparticles for Enhanced Emission and Wavelength-Dependent Biomolecular Sensing** (2013) ACS Appl. Mater. Interfaces, *5*, 3508-3513.

155   Liu S, Chen GY, Ohulchanskyy TY, Swihart MT, Prasad PN. **Facile Synthesis and Potential Bioimaging Applications of Hybrid Upconverting and Plasmonic NaGdF$_4$: Yb^{3+}, Er^{3+}/Silica/Gold Nanoparticles** (2013) Theranostics, *3*, 275-281.

156   Ge W, Zhang XR, Liu M, Lei ZW, Knize RJ, Lu YL. **Distance Dependence of Gold-Enhanced Upconversion luminescence in Au/SiO$_2$/Y$_2$O$_3$:Yb^{3+}, Er^{3+} Nanoparticles** (2013) Theranostics, *3*, 282-288.

157   Deng W, Sudheendra L, Zhao JB, Fu JX, Jin DY, Kennedy IM, Goldys EM. **Upconversion in NaYF$_4$:Yb, Er nanoparticles amplified by metal nanostructures** (2011) Nanotechnology, *22*, 325604.

158   Priyam A, Idris NM, Zhang Y. **Gold nanoshell coated NaYF$_4$ nanoparticles for simultaneously enhanced upconversion fluorescence and darkfield imaging** (2012) J. Mater. Chem., *22*, 960-965.

159   Zhang F, Braun GB, Shi YF, Zhang YC, Sun XH, Reich NO, Zhao DY, Stucky G. **Fabrication of Ag@SiO$_2$@Y$_2$O$_3$:Er Nanostructures for Bioimaging: Tuning of the Upconversion Fluorescence with Silver Nanoparticles** (2010) J. Am. Chem. Soc., *132*, 2850-2851.

160   Qian LP, Zhou LH, Too HP, Chow GM. **Gold decorated NaYF$_4$:Yb,Er/NaYF$_4$/silica (core/shell/shell) upconversion nanoparticles for photothermal destruction of BE(2)-C neuroblastoma cells** (2011) J. Nanopart. Res., *13*, 499-510.

161   Lakowicz JR. **Radiative decay engineering: Biophysical and biomedical applications** (2001) Anal. Biochem., *298*, 1-24.

162   Chen GY, Shen J, Ohulchanskyy TY, Patel NJ, Kutikov A, Li ZP, Song J, Pandey RK, Agren H, Prasad PN, Han G. α-NaYbF$_4$:Tm^{3+}/CaF$_2$ Core/Shell Nanoparticles with Efficient Near-Infrared to Near-Infrared Upconversion for High-Contrast Deep Tissue Bioimaging** (2012) ACS Nano, *6*, 8280-8287.

163   Fischer LH, Harms GS, Wolfbeis OS. **Upconverting Nanoparticles for Nanoscale Thermometry** (2011) Angew. Chem. Int. Edit., *50*, 4546-4551.

164   Hilderbrand SA, Weissleder R. **Near-infrared fluorescence: application to in vivo molecular imaging** (2010) Curr. Opin. Chem. Biol., *14*, 71-79.

165   Idris NM, Li ZQ, Ye L, Sim EKW, Mahendran R, Ho PCL, Zhang Y. **Tracking transplanted cells in live animal using upconversion fluorescent nanoparticles** (2009) Biomaterials, *30*, 5104-5113.

166   Shan JN, Budijono SJ, Hu GH, Yao N, Kang YB, Ju YG, Prud'homme RK. **Pegylated Composite Nanoparticles Containing Upconverting Phosphors and *meso*-Tetraphenyl porphine (TPP) for Photodynamic Therapy** (2011) Adv. Funct. Mater., *21*, 2488-2495.

167   Ali R, Saleh SM, Meier RJ, Azab HA, Abdelgawad II, Wolfbeis OS. **Upconverting nanoparticle based optical sensor for carbon dioxide** (2010) Sens. Actuators B, *150*, 126-131.

168   Li LL, Zhang RB, Yin LL, Zheng KZ, Qin WP, Selvin PR, Lu Y. **Biomimetic Surface Engineering of Lanthanide-Doped Upconversion Nanoparticles as Versatile Bioprobes** (2012) Angew. Chem. Int. Edit., *51*, 6121-6125.

169   Mader HS, Kele P, Saleh SM, Wolfbeis OS. **Upconverting luminescent nanoparticles for use in bioconjugation and bioimaging** (2010) Curr. Opin. Chem. Biol., *14*, 582-596.

170   Zhan QQ, Qian J, Liang HJ, Somesfalean G, Wang D, He SL, Zhang ZG, Andersson-Engels S. **Using 915 nm Laser Excited $Tm^{3+}/Er^{3+}/Ho^{3+}$-Doped $NaYbF_4$ Upconversion Nanoparticles for in Vitro and Deeper in Vivo Bioimaging without Overheating Irradiation** (2011) ACS Nano, *5*, 3744-3757.

171   Shen J, Chen GY, Vu AM, Fan W, Bilsel OS, Chang CC, Han G. **Engineering the Upconversion Nanoparticle Excitation Wavelength: Cascade Sensitization of Tri-doped Upconversion Colloidal Nanoparticles at 800 nm** (2013) Adv. Opt. Mater., *1*, 644-650.

172   Xie XJ, Gao NY, Deng RR, Sun Q, Xu QH, Liu XG. **Mechanistic Investigation of Photon Upconversion in Nd^{3+}-Sensitized Core-Shell Nanoparticles** (2013) J. Am. Chem. Soc., *135*, 12608-12611.

173   Yang YM, Shao Q, Deng RR, Wang C, Teng X, Cheng K, Cheng Z, Huang L, Liu Z, Liu XG, Xing BG. **In Vitro and In Vivo Uncaging and Bioluminescence Imaging by Using Photocaged Upconversion Nanoparticles** (2012) Angew. Chem. Int. Edit., *51*, 3125-3129.

174   Xu CT, Svenmarker P, Liu HC, Wu X, Messing ME, Wallenberg LR, Andersson-Engels S. **High-Resolution Fluorescence Diffuse Optical Tomography Developed with Nonlinear Upconverting Nanoparticles** (2012) ACS Nano, *6*, 4788-4795.

175   Wolfbeis OS. **An overview of nanoparticles commonly used in fluorescent bioimaging** (2015) Chem. Soc. Rev., *44*, 4743-4768.

176   Saleh SM, Ali R, Wolfbeis OS. **Quenching of the Luminescence of Upconverting Luminescent Nanoparticles by Heavy Metal Ions** (2011) Chem. Eur. J., *17*, 14611-14617.

177   Wang F, Zhang Y, Fan XP, Wang MQ. **Facile synthesis of water-soluble $LaF_3 : Ln^{3+}$ nanocrystals** (2006) J. Mater. Chem., *16*, 1031-1034.

178   Wang F, Chatterjee DK, Li ZQ, Zhang Y, Fan XP, Wang MQ. **Synthesis of polyethylenimine/$NaYF_4$ nanoparticles with upconversion fluorescence** (2006) Nanotechnology, *17*, 5786-5791.

179   Bünzli JCG. **Lanthanide Luminescence for Biomedical Analyses and Imaging** (2010) Chem. Rev., *110*, 2729-2755.

180   Yu XF, Li M, Xie MY, Chen LD, Li Y, Wang QQ. **Dopant-Controlled Synthesis of Water-Soluble Hexagonal $NaYF_4$ Nanorods with Efficient Upconversion Fluorescence for Multicolor Bioimaging** (2010) Nano Res., *3*, 51-60.

181   Gai SL, Yang PP, Li CX, Wang WX, Dai YL, Niu N, Lin J. **Synthesis of Magnetic, Up-Conversion Luminescent, and Mesoporous Core-Shell-Structured Nanocomposites as Drug Carriers** (2010) Adv. Funct. Mater., *20*, 1166-1172.

182   Gorris HH, Wolfbeis OS. **Photon-upconverting nanoparticles for optical encoding and multiplexing of cells, biomolecules, and microspheres** (2013) Angew. Chem. Int. Edit., *52*, 3584-3600.

183   Hu H, Xiong LQ, Zhou J, Li FY, Cao TY, Huang CH. **Multimodal-Luminescence Core-Shell Nanocomposites for Targeted Imaging of Tumor Cells** (2009) Chem. Eur. J., *15*, 3577-3584.

184   Wilhelm S, Hirsch T, Patterson WM, Scheucher E, Mayr T, Wolfbeis OS. **Multicolor Upconversion Nanoparticles for Protein Conjugation** (2013) Theranostics, *3*, 239-248.

185   Jiang S, Zhang Y, Lim KM, Sim EKW, Ye L. **NIR-to-visible upconversion nanoparticles for fluorescent labeling and targeted delivery of siRNA** (2009) Nanotechnology, *20*, 155101.

186   Eggeling C, Widengren J, Rigler R, Seidel CAM. **Photobleaching of fluorescent dyes under conditions used for single-molecule detection: Evidence of two-step photolysis** (1998) Anal. Chem., *70*, 2651-2659.

187   Wu XY, Liu HJ, Liu JQ, Haley KN, Treadway JA, Larson JP, Ge NF, Peale F, Bruchez MP. **Immunofluorescent labeling of cancer marker Her2 and other cellular targets with semiconductor quantum dots** (2003) Nat. Biotechnol., *21*, 41-46.

188   Medintz IL, Stewart MH, Trammell SA, Susumu K, Delehanty JB, Mei BC, Melinger JS, Blanco-Canosa JB, Dawson PE, Mattoussi H. **Quantum-dot/dopamine bioconjugates function as redox coupled assemblies for in vitro and intracellular pH sensing** (2010) Nat. Mater., *9*, 676-684.

189   Mattheakis LC, Dias JM, Choi YJ, Gong J, Bruchez MP, Liu JQ, Wang E. **Optical coding of mammalian cells using semiconductor quantum dots** (2004) Anal. Biochem., *327*, 200-208.

190   Resch-Genger U, Grabolle M, Cavaliere-Jaricot S, Nitschke R, Nann T. **Quantum dots versus organic dyes as fluorescent labels** (2008) Nat. Methods, *5*, 763-775.

191   Bogdan N, Vetrone F, Roy R, Capobianco JA. **Carbohydrate-coated lanthanide-doped upconverting nanoparticles for lectin recognition** (2010) J. Mater. Chem., *20*, 7543-7550.

192   Michalet X, Pinaud FF, Bentolila LA, Tsay JM, Doose S, Li JJ, Sundaresan G, Wu AM, Gambhir SS, Weiss S. **Quantum dots for live cells, in vivo imaging, and diagnostics** (2005) Science, *307*, 538-544.

193   Schlegel G, Bohnenberger J, Potapova I, Mews A. **Fluorescence decay time of single semiconductor nanocrystals** (2002) Phys. Rev. Lett., *88*, 137401.

194   Wu SW, Han G, Milliron DJ, Aloni S, Altoe V, Talapin DV, Cohen BE, Schuck PJ. **Non-blinking and photostable upconverted luminescence from single lanthanide-doped nanocrystals** (2009) Proc. Natl. Acad. Sci. USA, *106*, 10917-10921.

195   Ostrowski AD, Chan EM, Gargas DJ, Katz EM, Han G, Schuck PJ, Milliron DJ, Cohen BE. **Controlled Synthesis and Single-Particle Imaging of Bright, Sub-10 nm Lanthanide-Doped Upconverting Nanocrystals** (2012) ACS Nano, *6*, 2686-2692.

196   Ungun B, Prud'homme RK, Budijono SJ, Shan JN, Lim SF, Ju YG, Austin R. **Nanofabricated upconversion nanoparticles for photodynamic therapy** (2009) Opt. Express, *17*, 80-86.

197   Kumar M, Zhang P. **Highly Sensitive and Selective Label-Free Optical Detection of DNA Hybridization Based on Photon Upconverting Nanoparticles** (2009) Langmuir, *25*, 6024-6027.

198   Yu MX, Li FY, Chen ZG, Hu H, Zhan C, Yang H, Huang CH. **Laser Scanning Up-Conversion Luminescence Microscopy for Imaging Cells Labeled with Rare-Earth Nanophosphors** (2009) Anal. Chem., *81*, 930-935.

199   Xiong LQ, Chen ZG, Yu MX, Li FY, Liu C, Huang CH. **Synthesis, characterization, and in vivo targeted imaging of amine-functionalized rare-earth up-converting nanophosphors** (2009) Biomaterials, *30*, 5592-5600.

200   Gargas DJ, Chan EM, Ostrowski AD, Aloni S, Altoe MVP, Barnard ES, Sanii B, Urban JJ, Milliron DJ, Cohen BE, Schuck PJ. **Engineering bright sub-10-nm upconverting nanocrystals for single-molecule imaging** (2014) Nat. Nanotechnol., *9*, 300-305.

201   Kuningas K, Rantanen T, Karhunen U, Lövgren T, Soukka T. **Simultaneous use of time-resolved fluorescence and anti-stokes photoluminescence in a bioaffinity assay** (2005) Anal. Chem., *77*, 2826-2834.

202   Wang F, Zhang Y, Fan XP, Wang MQ. **One-pot synthesis of chitosan/LaF$_3$:Eu^{3+} nanocrystals for bio-applications** (2006) Nanotechnology, *17*, 1527-1532.

203   Li JJ, Wang YA, Guo WZ, Keay JC, Mishima TD, Johnson MB, Peng XG. **Large-scale synthesis of nearly monodisperse CdSe/CdS core/shell nanocrystals using air-stable reagents via successive ion layer adsorption and reaction** (2003) J. Amer. Chem. Soc., *125*, 12567-12575.

204   Somers RC, Bawendi MG, Nocera DG. **CdSe nanocrystal based chem-/bio-sensors** (2007) Chem. Soc. Rev., *36*, 579-591.

205   Sun L, Sung KB, Dentinger C, Lutz B, Nguyen L, Zhang JW, Qin HY, Yamakawa M, Cao MQ, Lu Y, Chmura AJ, Zhu J, Su X, Berlin AA, Chan S, Knudsen B. **Composite organic-inorganic nanoparticles as Raman labels for tissue analysis** (2007) Nano Lett., *7*, 351-356.

206   Shan JN, Ju YG. **A single-step synthesis and the kinetic mechanism for monodisperse and hexagonal-phase NaYF$_4$:Yb, Er upconversion nanophosphors** (2009) Nanotechnology, *20*, 275603.

207   Qiu PY, Zhou N, Chen HY, Zhang CL, Gao G, Cui DX. **Recent advances in lanthanide-doped upconversion nanomaterials: synthesis, nanostructures and surface modification** (2013) Nanoscale, *5*, 11512-11525.

208   Gorris HH, Ali R, Saleh SM, Wolfbeis OS. **Tuning the Dual Emission of Photon-Upconverting Nanoparticles for Ratiometric Multiplexed Encoding** (2011) Adv. Mater., *23*, 1652-1655.

209   Zhou HP, Xu CH, Sun W, Yan CH. **Clean and Flexible Modification Strategy for Carboxyl/Aldehyde-Functionalized Upconversion Nanoparticles and Their Optical Applications** (2009) Adv. Funct. Mater., *19*, 3892-3900.

210   Achatz DE, Meier RJ, Fischer LH, Wolfbeis OS. **Luminescent Sensing of Oxygen Using a Quenchable Probe and Upconverting Nanoparticles** (2011) Angew. Chem. Int. Edit., *50*, 260-263.

211   Sedlmeier A, Achatz DE, Fischer LH, Gorris HH, Wolfbeis OS. **Photon upconverting nanoparticles for luminescent sensing of temperature** (2012) Nanoscale, *4*, 7090-7096.

212   Cheng LA, Yang K, Shao MW, Lee ST, Liu ZA. **Multicolor In Vivo Imaging of Upconversion Nanopaticles with Emissions Tuned by Luminescence Resonance Energy Transfer** (2011) J. Phys. Chem. C, *115*, 2686-2692.

213   Corstjens PL, Li S, Zuiderwijk M, Kardos K, Abrams WR, Niedbala RS, Tanke HJ. **Infrared up-converting phosphors for bioassays** (2005) IEE proceedings. Nanobiotechnology, *152*, 64-72.

214   Cheng LA, Yang K, Zhang SA, Shao MW, Lee ST, Liu ZA. **Highly-Sensitive Multiplexed in vivo Imaging Using PEGylated Upconversion Nanoparticles** (2010) Nano Res., *3*, 722-732.

215   Niedbala RS, Feindt H, Kardos K, Vail T, Burton J, Bielska B, Li S, Milunic D, Bourdelle P, Vallejo R. **Detection of analytes by immunoassay using up-converting phosphor technology** (2001) Anal. Biochem., *293*, 22-30.

216   Ouellette AL, Li JJ, Cooper DE, Ricco AJ, Kovacs GTA. **Evolving Point-of-Care Diagnostics Using Up-Converting Phosphor Bioanalytical Systems** (2009) Anal. Chem., *81*, 3216-3221.

217   Ylihärsilä M, Valta T, Karp M, Hattara L, Harju E, Hölsä J, Saviranta P, Waris M, Soukka T. **Oligonucleotide Array-in-Well Platform for Detection and Genotyping Human Adenoviruses by Utilizing Upconverting Phosphor Label Technology** (2011) Anal. Chem., *83*, 1456-1461.

218   Rantanen T, Järvenpää ML, Vuojola J, Arppe R, Kuningas K, Soukka T. **Upconverting phosphors in a dual-parameter LRET-based hybridization assay** (2009) Analyst, *134*, 1713-1716.

219   Päkkilä H, Ylihärsilä M, Lahtinen S, Hattara L, Salminen N, Arppe R, Lastusaari M, Saviranta P, Soukka T. **Quantitative Multianalyte Microarray Immunoassay Utilizing Upconverting Phosphor Technology** (2012) Anal. Chem., *84*, 8628-8634.

220   Derfus AM, Chan WCW, Bhatia SN. **Probing the cytotoxicity of semiconductor quantum dots** (2004) Nano Lett., *4*, 11-18.

221   Kirchner C, Liedl T, Kudera S, Pellegrino T, Javier AM, Gaub HE, Stolzle S, Fertig N, Parak WJ. **Cytotoxicity of colloidal CdSe and CdSe/ZnS nanoparticles** (2005) Nano Lett., *5*, 331-338.

222   Limaye DA, Shaikh ZA. **Cytotoxicity of cadmium and characteristics of its transport in cardiomyocytes** (1999) Toxicol. Appl. Pharm., *154*, 59-66.

223   Clarke SJ, Hollmann CA, Zhang ZJ, Suffern D, Bradforth SE, Dimitrijevic NM, Minarik WG, Nadeau JL. **Photophysics of dopamine-modified quantumdots and effects on biological systems** (2006) Nat. Mater., *5*, 409-417.

224   Nann T, Mulvaney P. **Single quantum dots in spherical silica particles** (2004) Angew. Chem. Int. Edit., *43*, 5393-5396.

225   Dong BA, Xu S, Sun JA, Bi S, Li D, Bai X, Wang Y, Wang LP, Song HW. **Multifunctional NaYF$_4$: Yb^{3+}, Er^{3+}@Ag core/shell nanocomposites: integration of upconversion imaging and photothermal therapy** (2011) J. Mater. Chem., *21*, 6193-6200.

226   Gai SL, Li CX, Yang PP, Lin J. **Recent Progress in Rare Earth Micro/Nanocrystals: Soft Chemical Synthesis, Luminescent Properties, and Biomedical Applications** (2014) Chem. Rev., *114*, 2343-2389.

227   Muhr V, Wilhelm S, Hirsch T, Wolfbeis OS. **Upconversion Nanoparticles: From Hydrophobic to Hydrophilic Surfaces** (2014) Acc. Chem. Res., *47*, 3481-3493.

228   Gu ZJ, Yan L, Tian G, Li SJ, Chai ZF, Zhao YL. **Recent Advances in Design and Fabrication of Upconversion Nanoparticles and Their Safe Theranostic Applications** (2013) Adv. Mater., *25*, 3758-3779.

229   Mader H, Li XH, Saleh S, Link M, Kele P, Wolfbeis OS. **Fluorescent silica nanoparticles** (2008) Ann. N.Y. Acad. Sci., *1130*, 218-223.

230   Kobayashi M, Juillerat F, Galletto P, Bowen P, Borkovec M. **Aggregation and charging of colloidal silica particles: Effect of particle size** (2005) Langmuir, *21*, 5761-5769.

231   Nooney RI, McCormack E, McDonagh C. **Optimization of size, morphology and colloidal stability of fluorescein dye-doped silica NPs for application in immunoassays** (2012) Anal. Bioanal. Chem., *404*, 2807-2818.

232   Ow H, Larson DR, Srivastava M, Baird BA, Webb WW, Wiesner U. **Bright and stable core-shell fluorescent silica nanoparticles** (2005) Nano Lett., *5*, 113-117.

233 Sokolov I, Volkov DO. **Ultrabright fluorescent mesoporous silica particles** (2010) J. Mater. Chem., *20*, 4247-4250.

234 Taylor KML, Kim JS, Rieter WJ, An H, Lin WL, Lin WB. **Mesoporous silica nanospheres as highly efficient MRI contrast agents** (2008) J. Amer. Chem. Soc., *130*, 2154-2155.

235 Van Blaaderen A, Vrij A. **Synthesis and Characterization of Colloidal Dispersions of Fluorescent, Monodisperse Silica Spheres** (1992) Langmuir, *8*, 2921-2931.

236 Wang L, Tan WH. **Multicolor FRET silica nanoparticles by single wavelength excitation** (2006) Nano Lett., *6*, 84-88.

237 Wang L, Zhao WJ, O'Donoghue MB, Tan WH. **Fluorescent nanoparticles for multiplexed bacteria monitoring** (2007) Bioconjugate Chem., *18*, 297-301.

238 Schroedter A, Weller H, Eritja R, Ford WE, Wessels JM. **Biofunctionalization of silica-coated CdTe and gold nanocrystals** (2002) Nano Lett., *2*, 1363-1367.

239 Ding HL, Zhang YX, Wang S, Xu JM, Xu SC, Li GH. **Fe_3O_4@SiO_2 Core/Shell Nanoparticles: The Silica Coating Regulations with a Single Core for Different Core Sizes and Shell Thicknesses** (2012) Chem. Mater., *24*, 4572-4580.

240 Lei ZL, Pang XL, Li N, Lin L, Li YL. **A novel two-step modifying process for preparation of chitosan-coated Fe_3O_4/SiO_2 microspheres** (2009) J. Mater. Process. Technol., *209*, 3218-3225.

241 Lu ZY, Dai J, Song XN, Wang G, Yang WS. **Facile synthesis of Fe_3O_4/SiO_2 composite nanoparticles from primary silica particles** (2008) Colloids Surf. A, *317*, 450-456.

242 Morel AL, Nikitenko SI, Gionnet K, Wattiaux A, Lai-Kee-Him J, Labrugere C, Chevalier B, Deleris G, Petibois C, Brisson A, Simonoff M. **Sonochemical approach to the synthesis of Fe_3O_4@SiO_2 core-shell nanoparticles with tunable properties** (2008) ACS Nano, *2*, 847-856.

243 Yoon TJ, Yu KN, Kim E, Kim JS, Kim BG, Yun SH, Sohn BH, Cho MH, Lee JK, Park SB. **Specific targeting, cell sorting, and bioimaging with smart magnetic silica core-shell nanomateriats** (2006) Small, *2*, 209-215.

244 Graf C, Vossen DLJ, Imhof A, van Blaaderen A. **A general method to coat colloidal particles with silica** (2003) Langmuir, *19*, 6693-6700.

245 Schroedter A, Weller H. **Ligand design and bioconjugation of colloidal gold nanoparticles** (2002) Angew. Chem. Int. Edit., *41*, 3218-3221.

246 Saleh SM, Ali R, Hirsch T, Wolfbeis OS. **Detection of biotin-avidin affinity binding by exploiting a self-referenced system composed of upconverting luminescent nanoparticles and gold nanoparticles** (2011) J. Nanopart. Res., *13*, 4603-4611.

247 Darbandi M, Nann T. **One-pot synthesis of YF_3@silica core/shell nanoparticles** (2006) Chem. Commun., *7*, 776-778.

248 Liu FY, Zhao Q, You HP, Wang ZX. **Synthesis of stable carboxy-terminated $NaYF_4$:Yb^{3+}, Er^{3+}@SiO_2 nanoparticles with ultrathin shell for biolabeling applications** (2013) Nanoscale, *5*, 1047-1053.

249 Li ZQ, Zhang Y, Shuter B, Idris NM. **Hybrid Lanthanide Nanoparticles with Paramagnetic Shell Coated on Upconversion Fluorescent Nanocrystals** (2009) Langmuir, *25*, 12015-12018.

250 Hou ZY, Li CX, Ma PA, Li GG, Cheng ZY, Peng C, Yang DM, Yang PP, Lin J. **Electrospinning Preparation and Drug-Delivery Properties of an Up-conversion Luminescent Porous $NaYF_4$:Yb^{3+}, Er^{3+}@Silica Fiber Nanocomposite** (2011) Adv. Funct. Mater., *21*, 2356-2365.

251 Kumar M, Guo Y, Zhang P. **Highly sensitive and selective oligonucleotide sensor for sickle cell disease gene using photon upconverting nanoparticles** (2009) Biosens. Bioelectron., *24*, 1522-1526.

252 Li ZQ, Zhang Y. **Monodisperse silica-coated polyvinylpyrrolidone/$NaYF_4$ nanocrystals with multicolor upconversion fluorescence emission** (2006) Angew. Chem. Int. Edit., *45*, 7732-7735.

253 Chen ZG, Chen HL, Hu H, Yu MX, Li FY, Zhang Q, Zhou ZG, Yi T, Huang CH. **Versatile synthesis strategy for carboxylic acid-functionalized upconverting nanophosphors as biological labels** (2008) J. Amer. Chem. Soc., *130*, 3023-3029.

254 Lu HC, Yi GS, Zhao SY, Chen DP, Guo LH, Cheng J. **Synthesis and characterization of multi-functional nanoparticles possessing magnetic, up-conversion fluorescence and bio-affinity properties** (2004) J. Mater. Chem., *14*, 1336-1341.

255 Johnson NJJ, Sangeetha NM, Boyer JC, van Veggel FCJM. **Facile ligand-exchange with polyvinylpyrrolidone and subsequent silica coating of hydrophobic upconverting β-$NaYF_4$:Yb^{3+}/Er^{3+} nanoparticles** (2010) Nanoscale, *2*, 771-777.

256 Wang M, Hou W, Mi CC, Wang WX, Xu ZR, Teng HH, Mao CB, Xu SK. **Immunoassay of Goat Antihuman Immunoglobulin G Antibody Based on Luminescence Resonance Energy Transfer between Near-Infrared**

Responsive NaYF$_4$:Yb, Er Upconversion Fluorescent Nanoparticles and Gold Nanoparticles (2009) Anal. Chem., *81*, 8783-8789.

257   Huisgen R. **1,3-Dipolar Cycloadditions Past and Future** (1963) Angew. Chem. Int. Edit., *2*, 565-632.

258   Tornoe CW, Christensen C, Meldal M. **Peptidotriazoles on solid phase: [1,2,3]-triazoles by regiospecific copper(I)-catalyzed 1,3-dipolar cycloadditions of terminal alkynes to azides** (2002) J. Org. Chem., *67*, 3057-3064.

259   Rostovtsev VV, Green LG, Fokin VV, Sharpless KB. **A stepwise Huisgen cycloaddition process: Copper(I)-catalyzed regioselective "ligation" of azides and terminal alkynes** (2002) Angew. Chem. *114*, 2708-2711.

260   Hlaváček A, Sedlmeier A, Skládal P, Gorris HH. **Electrophoretic characterization and purification of silica-coated photon-upconverting nanoparticles and their bioconjugates** (2014) ACS Appl. Mater. Interfaces, *6*, 6930-6935.

261   Liu Q, Sun Y, Yang TS, Feng W, Li CG, Li FY. **Sub-10 nm Hexagonal Lanthanide-Doped NaLuF$_4$ Upconversion Nanocrystals for Sensitive Bioimaging in Vivo** (2011) J. Amer. Chem. Soc., *133*, 17122-17125.

262   Konishi T, Yamada M, Soga K, Matsuura D, Nagasaki Y. **PEG-based Surface Modification on Upconversion Nanophosphors for Bio-imaging under IR Excitation** (2006) J. Photopolym. Sci. Technol., *19*, 145-149.

263   Vinegoni C, Razansky D, Hilderbrand SA, Shao FW, Ntziachristos V, Weissleder R. **Transillumination fluorescence imaging in mice using biocompatible upconverting nanoparticles** (2009) Opt. Lett., *34*, 2566-2568.

264   Liu YS, Tu DT, Zhu HM, Li RF, Luo WQ, Chen XY. **A Strategy to Achieve Efficient Dual-Mode Luminescence of Eu^{3+} in Lanthanides Doped Multifunctional NaGdF$_4$ Nanocrystals** (2010) Adv. Mater., *22*, 3266-3271.

265   Hilderbrand SA, Shao FW, Salthouse C, Mahmood U, Weissleder R. **Upconverting luminescent nanomaterials: application to in vivo bioimaging** (2009) Chem. Commun., *28*, 4188-4190.

266   Budijono SJ, Shan JN, Yao N, Miura Y, Hoye T, Austin RH, Ju YG, Prud'homme RK. **Synthesis of Stable Block-Copolymer-Protected NaYF$_4$:Yb^{3+}, Er^{3+} Up-Converting Phosphor Nanoparticles** (2010) Chem. Mater., *22*, 311-318.

267   Zhang QB, Song K, Zhao JW, Kong XG, Sun YJ, Liu XM, Zhang YL, Zeng QH, Zhang H. **Hexanedioic acid mediated surface-ligand-exchange process for transferring NaYF$_4$:Yb/Er (or Yb/Tm) up-converting nanoparticles from hydrophobic to hydrophilic** (2009) J. Colloid Interface Sci., *336*, 171-175.

268   Shen J, Sun LD, Zhang YW, Yan CH. **Superparamagnetic and upconversion emitting Fe$_3$O$_4$/NaYF$_4$:Yb,Er hetero-nanoparticles via a crosslinker anchoring strategy** (2010) Chem. Commun., *46*, 5731-5733.

269   Dong AG, Ye XC, Chen J, Kang YJ, Gordon T, Kikkawa JM, Murray CB. **A Generalized Ligand-Exchange Strategy Enabling Sequential Surface Functionalization of Colloidal Nanocrystals** (2011) J. Amer. Chem. Soc., *133*, 998-1006.

270   Bao Y, Luu QAN, Lin CK, Schloss JM, May PS, Jiang CY. **Layer-by-layer assembly of freestanding thin films with homogeneously distributed upconversion nanocrystals** (2010) J. Mater. Chem., *20*, 8356-8361.

271   Kolb HC, Finn MG, Sharpless KB. **Click chemistry: Diverse chemical function from a few good reactions** (2001) Angew. Chem. Int. Edit., *40*, 2004-2021.

272   Kolb HC, Sharpless KB. **The growing impact of click chemistry on drug discovery** (2003) Drug Discov. Today, *8*, 1128-1137.

273   Becer CR, Hoogenboom R, Schubert US. **Click Chemistry beyond Metal-Catalyzed Cycloaddition** (2009) Angew. Chem. Int. Edit., *48*, 4900-4908.

274   Moses JE, Moorhouse AD. **The growing applications of click chemistry** (2007) Chem. Soc. Rev., *36*, 1249-1262.

275   Jorgensen KA. **Catalytic Asymmetric Hetero-Diels-Alder Reactions of Carbonyl Compounds and Imines** (2000) Angew. Chem. Int. Edit., *39*, 3558-3588.

276   Nandivada H, Jiang X, Lahann J. **Click Chemistry: Versatility and Control in the Hands of Materials Scientists** (2007) Adv. Mat., *19*, 2197-2208.

277   Gontcharov AV, Liu H, Sharpless KB. **Tert-butylsulfonamide. A new nitrogen source for catalytic aminohydroxylation and aziridination of olefins** (1999) Org. Lett., *1*, 783-786.

278   Sletten EM, Bertozzi CR. **Bioorthogonal Chemistry: Fishing for Selectivity in a Sea of Functionality** (2009) Angew. Chem. Int. Edit., *48*, 6974-6998.

279   Zhang L, Chen X, Xue P, Sun HH, Williams ID, Sharpless KB, Fokin VV, Jia G. **Ruthenium-catalyzed cycloaddition of alkynes and organic azides** (2005) J. Amer. Chem. Soc., *127*, 15998-15999.

280   Bock VD, Hiemstra H, van Maarseveen JH. **Cu^I-Catalyzed Alkyne–Azide "Click" Cycloadditions from a Mechanistic and Synthetic Perspective** (2006) Eur. J. Org. Chem., *2006*, 51-68.

281 Boren BC, Narayan S, Rasmussen LK, Zhang L, Zhao H, Lin Z, Jia G, Fokin VV. **Ruthenium-catalyzed azide-alkyne cycloaddition: scope and mechanism** (2008) J. Amer. Chem. Soc., *130*, 8923-8930.

282 Himo F, Lovell T, Hilgraf R, Rostovtsev VV, Noodleman L, Sharpless KB, Fokin VV. **Copper(I)-catalyzed synthesis of azoles. DFT study predicts unprecedented reactivity and intermediates** (2005) J. Amer. Chem. Soc., *127*, 210-216.

283 Hong V, Presolski SI, Ma C, Finn MG. **Analysis and optimization of copper-catalyzed azide-alkyne cycloaddition for bioconjugation** (2009) Angew. Chem. Int. Edit., *48*, 9879-9883.

284 Levengood MR, Kerwood CC, Chatterjee C, van der Donk WA. **Investigation of the substrate specificity of lacticin 481 synthetase by using nonproteinogenic amino acids** (2009) ChemBioChem, *10*, 911-919.

285 Nagaraj RH, Sell DR, Prabhakaram M, Ortwerth BJ, Monnier VM. **High correlation between pentosidine protein crosslinks and pigmentation implicates ascorbate oxidation in human lens senescence and cataractogenesis** (1991) Proc. Natl. Acad. Sci. USA, *88*, 10257-10261.

286 Kurpiers T, Mootz HD. **Bioorthogonal ligation in the spotlight** (2009) Angew. Chem. Int. Edit., *48*, 1729-1731.

287 Baskin JM, Prescher JA, Laughlin ST, Agard NJ, Chang PV, Miller IA, Lo A, Codelli JA, Bertozzi CR. **Copper-free click chemistry for dynamic in vivo imaging** (2007) Proc. Natl. Acad. Sci. USA, *104*, 16793-16797.

288 Kele P, Mezo G, Achatz D, Wolfbeis OS. **Dual labeling of biomolecules by using click chemistry: a sequential approach** (2009) Angew. Chem. Int. Edit., *48*, 344-347.

289 Rodionov VO, Fokin VV, Finn MG. **Mechanism of the ligand-free Cu^I-catalyzed azide-alkyne cycloaddition reaction** (2005) Angew. Chem. Int. Edit., *44*, 2210-2115.

290 Chassaing S, Sani Souna Sido A, Alix A, Kumarraja M, Pale P, Sommer J. **"Click chemistry" in zeolites: copper(I) zeolites as new heterogeneous and ligand-free catalysts for the Huisgen [3+2] cycloaddition** (2008) Chem. Eur. J., *14*, 6713-6721.

291 Chan TR, Hilgraf R, Sharpless KB, Fokin VV. **Polytriazoles as copper(I)-stabilizing ligands in catalysis** (2004) Org. Lett., *6*, 2853-2855.

292 Lewis WG, Magallon FG, Fokin VV, Finn MG. **Discovery and characterization of catalysts for azide-alkyne cycloaddition by fluorescence quenching** (2004) J. Amer. Chem. Soc., *126*, 9152-9153.

293 Sen Gupta S, Kuzelka J, Singh P, Lewis WG, Manchester M, Finn MG. **Accelerated bioorthogonal conjugation: a practical method for the ligation of diverse functional molecules to a polyvalent virus scaffold** (2005) Bioconjugate Chem., *16*, 1572-1579.

294 Rodionov VO, Presolski SI, Gardinier S, Lim YH, Finn MG. **Benzimidazole and related ligands for Cu-catalyzed azide-alkyne cycloaddition** (2007) J. Amer. Chem. Soc., *129*, 12696-12704.

295 Rodionov VO, Presolski SI, Diaz DD, Fokin VV, Finn MG. **Ligand-accelerated Cu-catalyzed azide-alkyne cycloaddition: a mechanistic report** (2007) J. Amer. Chem. Soc., *129*, 12705-12712.

296 Golas PL, Tsarevsky NV, Sumerlin BS, Matyjaszewski K. **Catalyst Performance in "Click" Coupling Reactions of Polymers Prepared by ATRP: Ligand and Metal Effects** (2006) Macromolecules, *39*, 6451–6457.

297 Agard NJ, Baskin JM, Prescher JA, Lo A, Bertozzi CR. **A comparative study of bioorthogonal reactions with azides** (2006) ACS Chem. Biol., *1*, 644-648.

298 Agard NJ, Prescher JA, Bertozzi CR. **A strain-promoted [3+2] azide-alkyne cycloaddition for covalent modification of biomolecules in living systems** (2004) J. Amer. Chem. Soc., *126*, 15046-15047.

299 Chang PV, Prescher JA, Sletten EM, Baskin JM, Miller IA, Agard NJ, Lo A, Bertozzi CR. **Copper-free click chemistry in living animals** (2010) Proc. Natl. Acad. Sci. USA, *107*, 1821-1826.

300 Urbani CN, Bell CA, Whittaker MR, Monteiro MJ. **Convergent Synthesis of Second Generation AB-Type Miktoarm Dendrimers Using "Click" Chemistry Catalyzed by Copper Wire** (2008) Macromolecules, *41*, 1057–1060.

301 Codelli JA, Baskin JM, Agard NJ, Berozzi CR. **Second-generation difluorinated cyclooctynes for copper-free click chemistry** (2008) J. Amer. Chem. Soc., *130*, 11486-11493.

302 Shea KJ, Kim JS. **Influence of Strain on Chemical Reactivity. Relative Reactivity of Torsionally Strained Double Bonds in 1,3-Dipolar Cycloadditions** (1992) J. Amer. Chem. Soc., *114*, 4846-4855.

303 Uetrecht C, Heck AJR. **Modern Biomolecular Mass Spectrometry and its Role in Studying Virus Structure, Dynamics, and Assembly** (2011) Angew. Chem. Int. Edit., *50*, 8248-8262.

304 Lawrence CM, Menon S, Eilers BJ, Bothner B, Khayat R, Douglas T, Young MJ. **Structural and functional studies of archaeal viruses** (2009) J. Biol. Chem., *284*, 12599-12603.

305   Pearson MN, Beever RE, Boine B, Arthur K. **Mycoviruses of filamentous fungi and their relevance to plant pathology** (2009) Mol. Plant. Pathol., *10*, 115-128.

306   Ackermann HW, Kropinski AM. **Curated list of prokaryote viruses with fully sequenced genomes** (2007) Res. Microbiol., *158*, 555-566.

307   Nelson RS, Citovsky V. **Plant viruses. Invaders of cells and pirates of cellular pathways** (2005) Plant Physiol., *138*, 1809-1814.

308   Suttle CA. **Viruses in the sea** (2005) Nature, *437*, 356-361.

309   Douglas T, Young M. **Viruses: Making friends with old foes** (2006) Science, *312*, 873-875.

310   Fauquet CM, Fargette D. **International Committee on Taxonomy of Viruses and the 3,142 unassigned species** (2005) Virology journal, *2*, 64.

311   Rohwer F, Edwards R. **The Phage Proteomic Tree: a genome-based taxonomy for phage** (2002) J. Bacteriol., *184*, 4529-4535.

312   Van Regenmortel MHV, Mahy BWJ. **Emerging Issues in Virus Taxonomy** (2004) Emerg. Infect. Dis., *10*, 8-13.

313   Dragnea B, Chen C, Kwak ES, Stein B, Kao CC. **Gold nanoparticles as spectroscopic enhancers for in vitro studies on single viruses** (2003) J. Amer. Chem. Soc., *125*, 6374-6375.

314   Fischlechner M, Donath E. **Viruses as building blocks for materials and devices** (2007) Angew. Chem. Int. Edit., *46*, 3184-3193.

315   Aniagyei SE, Kennedy CJ, Stein B, Willits DA, Douglas T, Young MJ, De M, Rotello VM, Srisathiyanarayanan D, Kao CC, Dragnea B. **Synergistic Effects of Mutations and Nanoparticle Templating in the Self-Assembly of Cowpea Chlorotic Mottle Virus Capsids** (2009) Nano Lett., *9*, 393-398.

316   Wang Q, Lin TW, Tang L, Johnson JE, Finn MG. **Icosahedral virus particles as addressable nanoscale building blocks** (2002) Angew. Chem. Int. Edit., *41*, 459-462.

317   Sun J, DuFort C, Daniel MC, Murali A, Chen C, Gopinath K, Stein B, De M, Rotello VM, Holzenburg A, Kao CC, Dragnea B. **Core-controlled polymorphism in virus-like particles** (2007) Proc. Natl. Acad. Sci. USA, *104*, 1354-1359.

318   Dasgupta R, Shih DS, Saris C, Kaesberg P. **Nucleotide sequence of a viral RNA fragment that binds to eukaryotic ribosomes** (1975) Nature, *256*, 624-628.

319   Ahlquist P, Luckow V, Kaesberg P. **Complete nucleotide sequence of brome mosaic virus RNA3** (1981) J. Mol. Biol., *153*, 23-38.

320   Dasgupta R, Kaesberg P. **Complete nucleotide sequences of the coat protein messenger RNAs of brome mosaic virus and cowpea chlorotic mottle virus** (1982) Nucleic Acids Res., *10*, 703-713.

321   Kao CC, Sivakumaran K. **Brome mosaic virus, good for an RNA virologist's basic needs** (2000) Mol. Plant. Pathol., *1*, 91-97.

322   Anderegg JW, Wright M, Kaesberg P. **An x-ray scattering study of bromegrass mosaic virus** (1963) Biophys. J., *3*, 175-182.

323   Lucas RW, Larson SB, McPherson A. **The crystallographic structure of brome mosaic virus** (2002) J. Mol. Biol., *317*, 95-108.

324   Bancroft JB, Hills GJ, Markham R. **A study of the self-assembly process in a small spherical virus. Formation of organized structures from protein subunits in vitro** (1967) Virology, *31*, 354-379.

325   She YM, Haber S, Seifers DL, Loboda A, Chernushevich I, Perreault H, Ens W, Standing KG. **Determination of the complete amino acid sequence for the coat protein of brome mosaic virus by time-of-flight mass spectrometry - Evidence for mutations associated with change of propagation host** (2001) J. Biol. Chem., *276*, 20039-20047.

326   Bancroft JB, Bracker CE, Wagner GW. **Structures derived from cowpea chlorotic mottle and brome mosaic virus protein** (1969) Virology, *38*, 324-335.

327   Bancroft JB, Hiebert E. **Formation of an Infectious Nucleoprotein from Protein and Nucleic Acid Isolated from a Small Spherical Virus** (1967) Virology, *32*, 354-356.

328   Manzenrieder F, Luxenhofer R, Retzlaff M, Jordan R, Finn MG. **Stabilization of Virus-like Particles with Poly(2-oxazoline)s** (2011) Angew. Chem. Int. Edit., *50*, 2601-2605.

329   Uchida M, Klem MT, Allen M, Suci P, Flenniken M, Gillitzer E, Varpness Z, Liepold LO, Young M, Douglas T. **Biological Containers: Protein Cages as Multifunctional Nanoplatforms** (2007) Adv. Mater., *19*, 1025–1042.

330   Varpness Z, Peters JW, Young M, Douglas T. **Biomimetic synthesis of a H$_2$ catalyst using a protein cage architecture** (2005) Nano Lett., *5*, 2306-2309.

331   Comellas-Aragonès M, Engelkamp H, Claessen VI, Sommerdijk NA, Rowan AE, Christianen PC, Maan JC, Verduin BJ, Cornelissen JJ, Nolte RJ. **A virus-based single-enzyme nanoreactor** (2007) Nat. Nanotechnol., *2*, 635-639.

332   Miller RA, Presley AD, Francis MB. **Self-assembling light-harvesting systems from synthetically modified tobacco mosaic virus coat proteins** (2007) J. Amer. Chem. Soc., *129*, 3104-3109.

333   Falkner JC, Turner ME, Bosworth JK, Trentler TJ, Johnson JE, Lin T, Colvin VL. **Virus crystals as nanocomposite scaffolds** (2005) J. Amer. Chem. Soc., *127*, 5274-5275.

334   Speir JA, Munshi S, Wang G, Baker TS, Johnson JE. **Structures of the native and swollen forms of cowpea chlorotic mottle virus determined by X-ray crystallography and cryo-electron microscopy** (1995) Structure, *3*, 63-78.

335   Flenniken ML, Liepold LO, Crowley BE, Willits DA, Young MJ, Douglas T. **Selective attachment and release of a chemotherapeutic agent from the interior of a protein cage architecture** (2005) Chem. Commun., *4*, 447-449.

336   Durham ACH, Witz J, Bancroft JB. **The Semipermeability of Simple Spherical Virus Capsids** (1984) Virology, *133*, 1-8.

337   Pfeiffer P, Durham AC. **The cation binding associated with structural transitions in bromegrass mosaic virus** (1977) Virology, *81*, 419-432.

338   Wang Q, Kaltgrad E, Lin TW, Johnson JE, Finn MG. **Natural supramolecular building blocks: Wild-type cowpea mosaic virus** (2002) Chem. Biol., *9*, 805-811.

339   Kickhoefer VA, Han M, Raval-Fernandes S, Poderycki MJ, Moniz RJ, Vaccari D, Silvestry M, Stewart PL, Kelly KA, Rome LH. **Targeting vault nanoparticles to specific cell surface receptors** (2009) ACS Nano, *3*, 27-36.

340   Koudelka KJ, Destito G, Plummer EM, Trauger SA, Siuzdak G, Manchester M. **Endothelial targeting of cowpea mosaic virus (CPMV) via surface vimentin** (2009) PLoS Pathog., *5*, e1000417.

341   Kurata N, Shishido T, Muraoka M, Tanaka T, Ogino C, Fukuda H, Kondo A. **Specific protein delivery to target cells by antibody-displaying bionanocapsules** (2008) J. Biochem., *144*, 701-707.

342   Chatterji A, Ochoa W, Shamieh L, Salakian SP, Wong SM, Clinton G, Ghosh P, Lin T, Johnson JE. **Chemical conjugation of heterologous proteins on the surface of Cowpea mosaic virus** (2004) Bioconjugate Chem., *15*, 807-813.

343   Vriezema DM, Comellas Aragonès M, Elemans JA, Cornelissen JJ, Rowan AE, Nolte RJ. **Self-assembled nanoreactors** (2005) Chem. Rev., *105*, 1445-1489.

344   Haselhorst T, Garcia JM, Islam T, Lai JC, Rose FJ, Nicholls JM, Peiris JS, von Itzstein M. **Avian influenza H5-containing virus-like particles (VLPs): host-cell receptor specificity by STD NMR spectroscopy** (2008) Angew. Chem. Int. Edit., *47*, 1910-1912.

345   Tang J, Johnson JM, Dryden KA, Young MJ, Zlotnick A, Johnson JE. **The role of subunit hinges and molecular "switches" in the control of viral capsid polymorphism** (2006) J. Struct. Biol., *154*, 59-67.

346   Zhao XX, Fox JM, Olson NH, Baker TS, Young MJ. *In Vitro* **Assembly of Cowpea Chlorotic Mottle Virus from Coat Protein Expressed in** *Escherichia coli* **and** *in Vitro*-**Transcribed Viral cDNA** (1995) Virology, *207*, 486-494.

347   Liu CM, Jin QL, Sutton A, Chen LH. **A novel fluorescent probe: Europium complex hybridized T7 phage** (2005) Bioconjugate Chem., *16*, 1054-1057.

348   Lee YJ, Yi H, Kim WJ, Kang K, Yun DS, Strano MS, Ceder G, Belcher AM. **Fabricating genetically engineered high-power lithium-ion batteries using multiple virus genes** (2009) Science, *324*, 1051-1055.

349   Chatterji A, Ochoa WF, Ueno T, Lin T, Johnson JE. **A virus-based nanoblock with tunable electrostatic properties** (2005) Nano Lett., *5*, 597-602.

350   Lim YB, Lee E, Yoon YR, Lee MS, Lee M. **Filamentous artificial virus from a self-assembled discrete nanoribbon** (2008) Angew. Chem. Int. Edit., *47*, 4525-4528.

351   Lee ES, Kim D, Youn YS, Oh KT, Bae YH. **A virus-mimetic nanogel vehicle** (2008) Angew. Chem. Int. Edit., *47*, 2418-2421.

352   Meunier S, Strable E, Finn MG. **Crosslinking of and coupling to viral capsid proteins by tyrosine oxidation** (2004) Chem. Biol., *11*, 319-326.

353   Caldeira JC, Peabody DS. **Stability and assembly in vitro of bacteriophage PP7 virus-like particles** (2007) J. Nanobiotechnology, *5*, 10.

354   Zochowska M, Paca A, Schoehn G, Andrieu JP, Chroboczek J, Dublet B, Szolajska E. **Adenovirus dodecahedron, as a drug delivery vector** (2009) PLoS One, *4*, e5569.

355   Esfandiary R, Kickhoefer VA, Rome LH, Joshi SB, Middaugh CR. **Structural stability of vault particles** (2009) J. Pharm. Sci., *98*, 1376-1386.

356   Zandi R, Reguera D, Bruinsma RF, Gelbart WM, Rudnick J. **Origin of icosahedral symmetry in viruses** (2004) Proc. Natl. Acad. Sci. USA, *101*, 15556-15560.

357   Krol MA, Olson NH, Tate J, Johnson JE, Baker TS, Ahlquist P. **RNA-controlled polymorphism in the in vivo assembly of 180-subunit and 120-subunit virions from a single capsid protein** (1999) Proc. Natl. Acad. Sci. USA, *96*, 13650-13655.

358   Goicochea NL, De M, Rotello VM, Mukhopadhyay S, Dragnea B. **Core-like particles of an enveloped animal virus can self-assemble efficiently on artificial templates** (2007) Nano Lett., *7*, 2281-2290.

359   Loo L, Guenther RH, Basnayake VR, Lommel SA, Franzen S. **Controlled encapsidation of gold nanoparticles by a viral protein shell** (2006) J. Amer. Chem. Soc., *128*, 4502-4503.

360   Young M, Willits D, Uchida M, Douglas T. **Plant viruses as biotemplates for materials and their use in nanotechnology** (2008) Annu. Rev. Phytopathol., *46*, 361-384.

361   Allen M, Willits D, Mosolf J, Young M, Douglas T. **Protein Cage Constrained Synthesis of Ferrimagnetic Iron Oxide Nanoparticles** (2002) Adv. Mat., *14*, 1562-1565.

362   Klem MT, Young M, Douglas T. **Biomimetic synthesis of β-TiO$_2$ inside a viral capsid** (2008) J. Mater. Chem., *18*, 3821–3823.

363   Kramer RM, Li C, Carter DC, Stone MO, Naik RR. **Engineered protein cages for nanomaterial synthesis** (2004) J. Amer. Chem. Soc., *126*, 13282-13286.

364   Mao C, Solis DJ, Reiss BD, Kottmann ST, Sweeney RY, Hayhurst A, Georgiou G, Iverson B, Belcher AM. **Virus-based toolkit for the directed synthesis of magnetic and semiconducting nanowires** (2004) Science, *303*, 213-217.

365   Bittner AM. **Biomolecular rods and tubes in nanotechnology** (2005) Naturwissenschaften, *92*, 51-64.

366   Gazit E. **Use of biomolecular templates for the fabrication of metal nanowires** (2007) FEBS J., *274*, 317-322.

367   Knez M, Bittner AM, Boes F, Wege C, Jeske H, Maiß E, Kern K. **Biotemplate Synthesis of 3-nm Nickel and Cobalt Nanowires** (2003) Nano Lett., *3*, 1079-1082.

368   Knez M, Sumser M, Bittner AM, Wege C, Jeske H, Martin TP, Kern K. **Spatially Selective Nucleation of Metal Clusters on the Tobacco Mosaic Virus** (2004) Adv. Funct. Mater., *14*, 116-124.

369   Lee SY, Culver JN, Harris MT. **Effect of CuCl$_2$ concentration on the aggregation and mineralization of Tobacco mosaic virus biotemplate** (2006) J. Colloid Interface Sci., *297*, 554-560.

370   Shenton W, Douglas T, Young M, Stubbs G, Mann S. **Inorganic–Organic Nanotube Composites from Template Mineralization of Tobacco Mosaic Virus** (1999) Adv. Mater., *11*, 253-256.

371   Belyi VA, Muthukumar M. **Electrostatic origin of the genome packing in viruses** (2006) Proc. Natl. Acad. Sci. USA, *103*, 17174-17178.

372   Douglas T, Strable E, Willits D, Aitouchen A, Libera M, Young M. **Protein Engineering of a Viral Cage for Constrained Nanomaterials Synthesis** (2002) Adv. Mater., *14*, 415-418.

373   Tsukamoto R, Muraoka M, Seki M, Tabata H, Yamashita I. **Synthesis of CoPt and FePt$_3$ Nanowires Using the Central Channel of Tobacco Mosaic Virus as a Biotemplate** (2007) Chem. Mater., *19*, 2389-2391.

374   De la Escosura AN, R. J. M. , Cornelissen JJLM. **Viruses and protein cages as nanocontainers and nanoreactors** (2009) J. Mater. Chem., *19*, 2274–2278.

375   Dixit SK, Goicochea NL, Daniel MC, Murali A, Bronstein L, De M, Stein B, Rotello VM, Kao CC, Dragnea B. **Quantum dot encapsulation in viral capsids** (2006) Nano Lett., *6*, 1993-1999.

376   Ueno T. **Functionalization of viral protein assemblies by self-assembly reactions** (2008) J. Mater. Chem., *18*, 3741–3745.

377   Linger BR, Kunovska L, Kuhn RJ, Golden BL. **Sindbis virus nucleocapsid assembly: RNA folding promotes capsid protein dimerization** (2004) RNA, *10*, 128-138.

378   Loo L, Guenther RH, Lommel SA, Franzen S. **Encapsidation of nanoparticles by red clover necrotic mosaic virus** (2007) J. Amer. Chem. Soc., *129*, 11111-11117.

379   Hagan MF. **A theory for viral capsid assembly around electrostatic cores** (2009) J. Chem. Phys., *130*, 114902.

380   Lee S, Chen X. **Dual-modality probes for in vivo molecular imaging** (2009) Mol. Imaging, *8*, 87-100.

381   Weissleder R. **A clearer vision for in vivo imaging** (2001) Nat. Biotechnol., *19*, 316-317.

382   Zheng QD, Xu GX, Prasad PN. **Conformationally restricted dipyrromethene boron difluoride (BODIPY) dyes: Highly fluorescent, multicolored probes for cellular imaging** (2008) Chem. Eur. J., *14*, 5812-5819.

383   Heilemann M, van de Linde S, Schuttpelz M, Kasper R, Seefeldt B, Mukherjee A, Tinnefeld P, Sauer M. **Subdiffraction-resolution fluorescence imaging with conventional fluorescent probes** (2008) Angew. Chem. Int. Edit., *47*, 6172-6176.

384   Michaelis J, Hettich C, Mlynek J, Sandoghdar VV. **Optical microscopy using a single-molecule light source** (2000) Nature, *405*, 325-328.

385   Chan WC, Nie S. **Quantum dot bioconjugates for ultrasensitive nonisotopic detection** (1998) Science, *281*, 2016-2018.

386   Lakowicz JR, Szmacinski H, Nowaczyk K, Berndt KW, Johnson M. **Fluorescence Lifetime Imaging** (1992) Anal. Biochem., *202*, 316-330.

387   Wallrabe H, Periasamy A. **Imaging protein molecules using FRET and FLIM microscopy** (2005) Curr. Opin. Biotechnol., *16*, 19-27.

388   Qian HS, Guo HC, Ho PCL, Mahendran R, Zhang Y. **Mesoporous-Silica-Coated Up-Conversion Fluorescent Nanoparticles for Photodynamic Therapy** (2009) Small, *5*, 2285-2290.

389   Farkas DL, Du C, Fisher GW, Lau C, Niu W, Wachman ES, Levenson RM. **Non-invasive image acquisition and advanced processing in optical bioimaging** (1998) Comput. Med. Imaging Graph., *22*, 89-102.

390   Kobayashi H, Ogawa M, Alford R, Choyke PL, Urano Y. **New strategies for fluorescent probe design in medical diagnostic imaging** (2010) Chem. Rev., *110*, 2620-2640.

391   Stephens DJ, Allan VJ. **Light microscopy techniques for live cell imaging** (2003) Science, *300*, 82-86.

392   Chen G, Ohulchanskyy TY, Liu S, Law WC, Wu F, Swihart MT, Agren H, Prasad PN. **Core/shell NaGdF$_4$:Nd^{3+}/NaGdF$_4$ nanocrystals with efficient near-infrared to near-infrared downconversion photoluminescence for bioimaging applications** (2012) ACS Nano, *6*, 2969-2977.

393   Nagarajan S, Li ZQ, Marchi-Artzner V, Grasset F, Zhang Y. **Imaging gap junctions with silica-coated upconversion nanoparticles** (2010) Med. Biol. Eng Comput., *48*, 1033-1041.

394   Cai W, Chen K, Li ZB, Gambhir SS, Chen X. **Dual-function probe for PET and near-infrared fluorescence imaging of tumor vasculature** (2007) J. Nucl. Med., *48*, 1862-1870.

395   Welsher K, Liu Z, Sherlock SP, Robinson JT, Chen Z, Daranciang D, Dai H. **A route to brightly fluorescent carbon nanotubes for near-infrared imaging in mice** (2009) Nat. Nanotechnol., *4*, 773-780.

396   Cahalan MD, Parker I, Wei SH, Miller MJ. **Two-photon tissue imaging: seeing the immune system in a fresh light** (2002) Nat. Rev. Immunol., *2*, 872-880.

397   Conchello JA, Lichtman JW. **Optical sectioning microscopy** (2005) Nat. Methods, *2*, 920-931.

398   Ohulchanskyy TY, Roy I, Yong KT, Pudavar HE, Prasad PN. **High-resolution light microscopy using luminescent nanoparticles** (2010) Wiley Interdiscip. Rev. Nanomed. Nanobiotechnol., *2*, 162-175.

399   Stutzmann GE, Parker I. **Dynamic multiphoton imaging: a live view from cells to systems** (2005) Physiology, *20*, 15-21.

400   Minck RW, Terhune RW, Wang CC. **Nonlinear Optics** (1966) Appl. Opt., *5*, 1595-1612.

401   Mi CC, Zhang JP, Gao HY, Wu XL, Wang M, Wu YF, Di YQ, Xu ZR, Mao CB, Xu SK. **Multifunctional nanocomposites of superparamagnetic (Fe$_3$O$_4$) and NIR-responsive rare earth-doped up-conversion fluorescent (NaYF$_4$:Yb, Er) nanoparticles and their applications in biolabeling and fluorescent imaging of cancer cells** (2010) Nanoscale, *2*, 1141-1148.

402   Ray P. **Multimodality molecular imaging of disease progression in living subjects** (2011) J. Biosci., *36*, 499-504.

403   Stelter L, Pinkernelle JG, Michel R, Schwartlander R, Raschzok N, Morgul MH, Koch M, Denecke T, Ruf J, Baumler H, Jordan A, Hamm B, Sauer IM, Teichgraber U. **Modification of aminosilanized superparamagnetic nanoparticles: feasibility of multimodal detection using 3T MRI, small animal PET, and fluorescence imaging** (2010) Mol. Imaging Biol., *12*, 25-34.

404   Pandey SK, Gryshuk AL, Sajjad M, Zheng X, Chen Y, Abouzeid MM, Morgan J, Charamisinau I, Nabi HA, Oseroff A, Pandey RK. **Multimodality agents for tumor imaging (PET, fluorescence) and photodynamic therapy. A possible "see and treat" approach** (2005) J. Med. Chem., *48*, 6286-95.

405   Kumar R, Roy I, Ohulchanskyy TY, Goswami LN, Bonoiu AC, Bergey EJ, Tramposch KM, Maitra A, Prasad PN. **Covalently dye-linked, surface-controlled, and bioconjugated organically modified silica nanoparticles as targeted probes for optical imaging** (2008) ACS Nano, *2*, 449-456.

406   Achatz D. **PhD thesis: Synthesis and Surface Modification of Luminescent Nanoparticles for Imaging and Sensing of Oxygen Using Near-Infrared Excitation** (2012) Institute of Analytical Chemisty, Chemo- and Biosensors, *University of Regensburg.*

407   Corstjens PL, van Lieshout L, Zuiderwijk M, Kornelis D, Tanke HJ, Deelder AM, van Dam GJ. **Up-converting phosphor technology-based lateral flow assay for detection of Schistosoma circulating anodic antigen in serum** (2008) Journal of clinical microbiology *46*, 171-176.

408   Malvern. **Polydispersity – what does it mean for DLS and chromatography?** (2014) www.material-talks.com.

409   Malvern. **Zetasizer Nano Series User Manual** (2004) Malvern Instruments Ltd., *Issue 1.1*.

410   Jana NR, Earhart C, Ying JY. **Synthesis of water-soluble and functionalized nanoparticles by silica coating** (2007) Chem. Mater., *19*, 5074-5082.

411   Parak WJ, Gerion D, Zanchet D, Woerz AS, Pellegrino T, Micheel C, Williams SC, Seitz M, Bruehl RE, Bryant Z, Bustamante C, Bertozzi CR, Alivisatos AP. **Conjugation of DNA to silanized colloidal semiconductor nanocrystalline quantum dots** (2002) Chem. Mater., *14*, 2113-2119.

412   Hesse M, Meier H, Zeeh B. **Spektroskopische Methoden in der Organischen Chemie** (2005) Georg Thieme Verlag - Stuttgart, *7., überarbeitete Auflage*, 33-73.

413   Käfer U. **Master thesis: Entwicklung eines Detektionssystems für Peptid- und Proteinphosphorylierungen basierend auf aufwärtskonvertierenden Nanopartikeln** (2014) Institute of Analytical Chemisty, Chemo- and Biosensors, *University of Regensburg.*

414   Pace CN, Vajdos F, Fee L, Grimsley G, Gray T. **How to measure and predict the molar absorption coefficient of a protein** (1995) Protein Sci., *4*, 2411-2423.

415   Hamamatsu Photonics. **Photomultiplier tube R12829** (2015) Hamamatsu Data Sheet.

416   Hamamatsu Photonics. **Photomultiplier tube R12896** (2015) Hamamatsu Data Sheet.

417   Hamamatsu Photonics. **Photomultiplier Tubes** (2015) Photomultiplier tubes and Related Products.

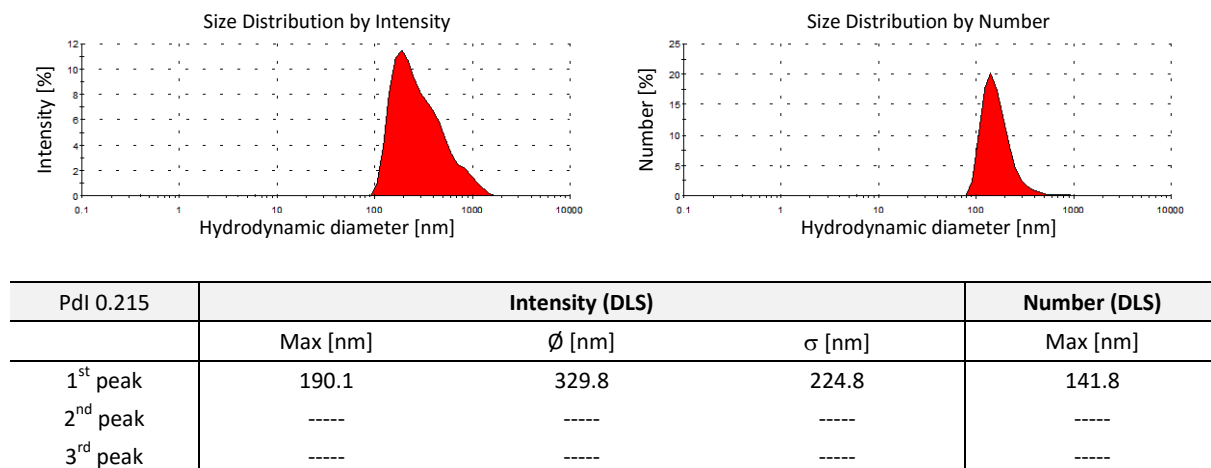# 9.   Appendix

9.1   Dynamic light scattering measurements

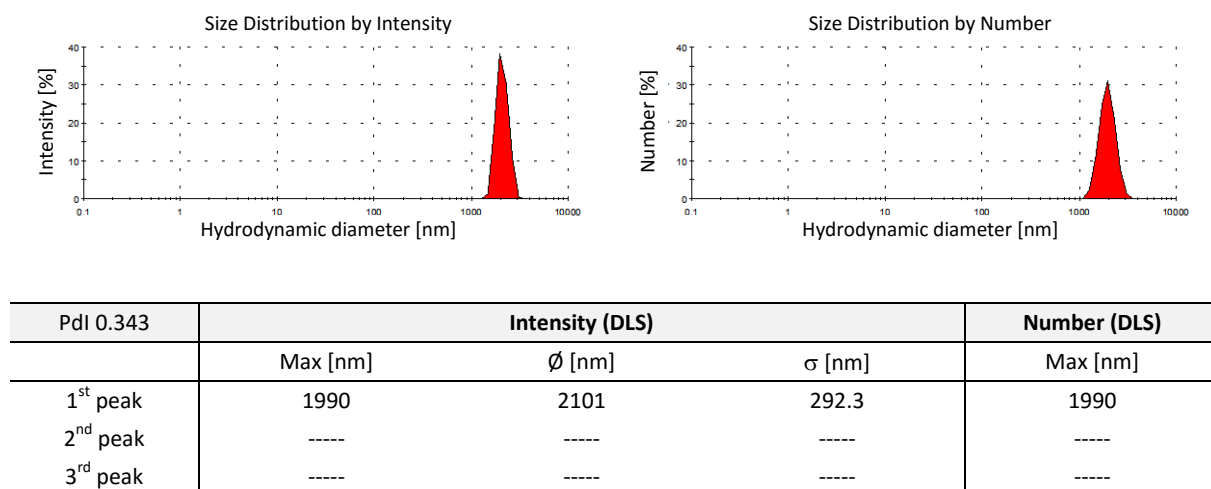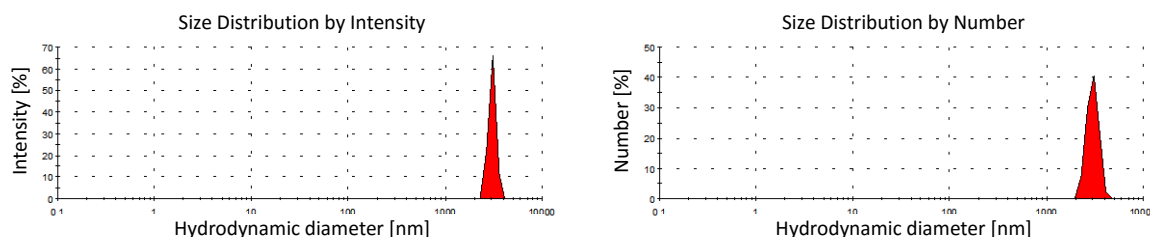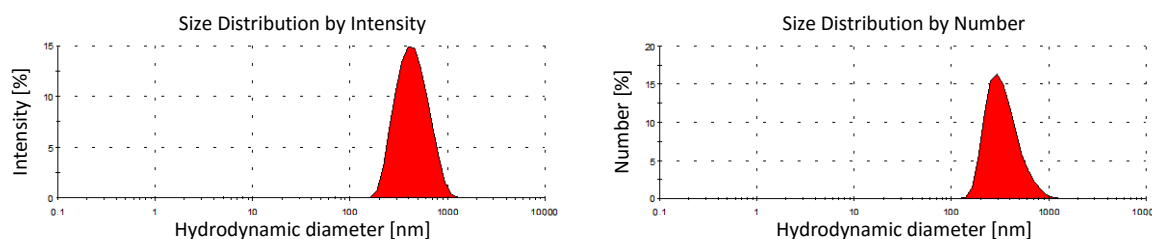| PdI 0.215	Intensity (DLS)			Number (DLS)
	Max [nm]	Ø [nm]	σ [nm]	Max [nm]
1st peak	190.1	329.8	224.8	141.8
2nd peak	-----	-----	-----	-----
3rd peak	-----	-----	-----	-----

Figure 9.1 Hydrodynamic diameter of UCNP@SiO$_2$-10: Size distribution according to signal intensity or nanoparticle number and peak data including maximum (Max), average (Ø), and deviation (σ).

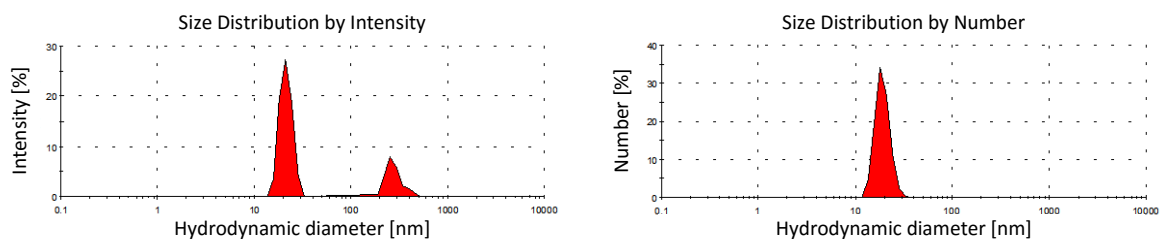| PdI 0.343	Intensity (DLS)			Number (DLS)
	Max [nm]	Ø [nm]	σ [nm]	Max [nm]
1st peak	1990	2101	292.3	1990
2nd peak	-----	-----	-----	-----
3rd peak	-----	-----	-----	-----

Figure 9.2 Hydrodynamic diameter of UCNP@SiO$_2$-5: Size distribution according to signal intensity or nanoparticle number and peak data including maximum (Max), average (Ø), and deviation (σ).

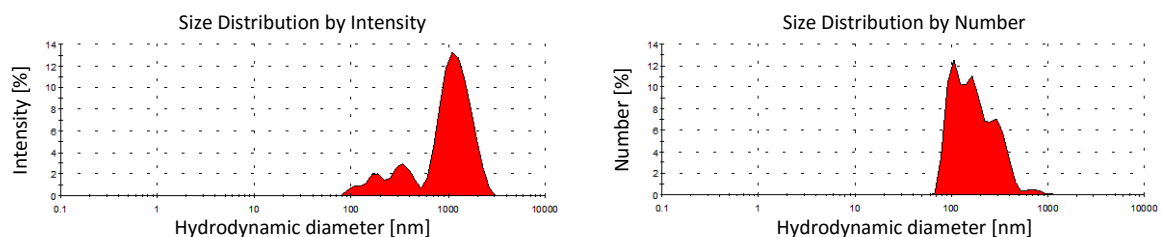| PdI 0.293	Intensity (DLS)			Number (DLS)
	Max [nm]	$\varnothing$ [nm]	σ [nm]	Max [nm]
1st peak	3091	3054	255.9	3091
2nd peak	-----	-----	-----	-----
3rd peak	-----	-----	-----	-----

Figure 9.3 Hydrodynamic diameter of UCNP@SiO$_2$-4: Size distribution according to signal intensity or nanoparticle number and peak data including maximum (Max), average ($\varnothing$), and deviation (σ).
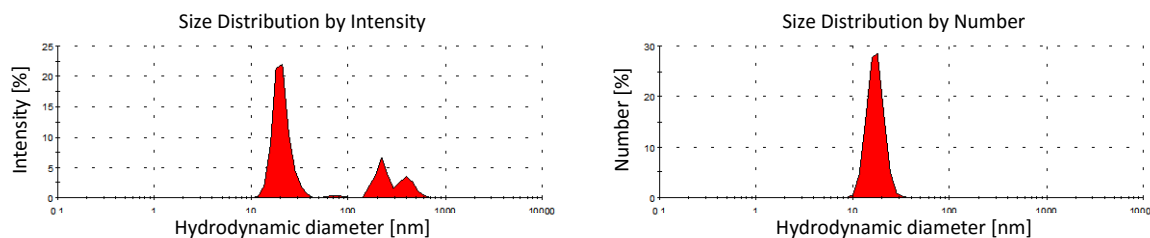

PdI 0.134	Intensity (DLS)			Number (DLS)
	Max [nm]	$\varnothing$ [nm]	σ [nm]	Max [nm]
1st peak	396.1	458.6	169.1	295.3
2nd peak	-----	-----	-----	-----
3rd peak	-----	-----	-----	-----

Figure 9.4 Hydrodynamic diameter of UCNP@SiO$_2$-NH$_2$: Size distribution according to signal intensity or nanoparticle number and peak data including maximum (Max), average ($\varnothing$), and deviation (σ).
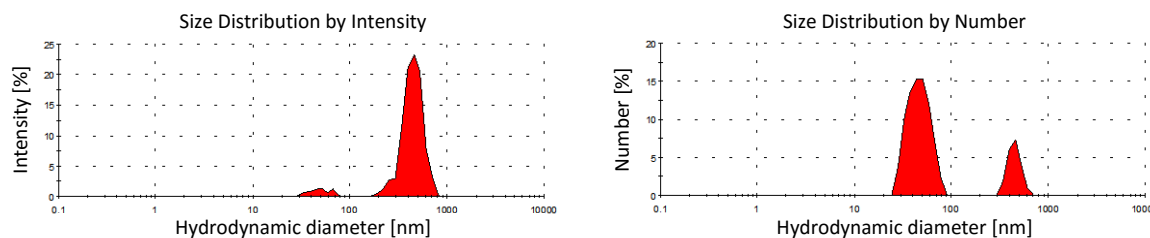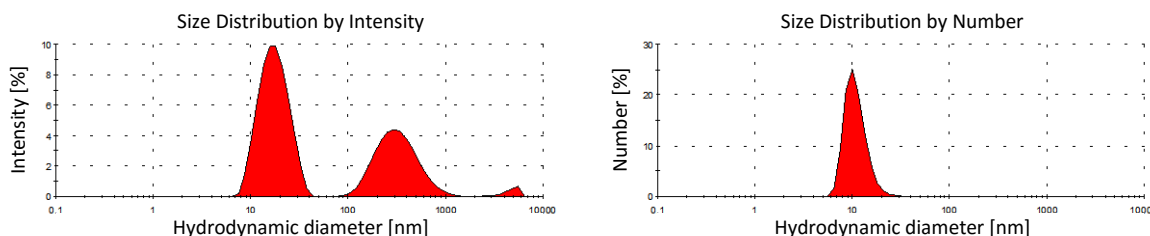

PdI 0.691	Intensity (DLS)			Number (DLS)
	Max [nm]	$\varnothing$ [nm]	σ [nm]	Max [nm]
1st peak	50.75	45.56	8.184	43.82
2nd peak	68.06	64.95	4.385	458.7
3rd peak	458.7	452.7	103.6	-----

Figure 9.5 Hydrodynamic diameter of UCNP@SiO$_2$-COOH with work up *A*: Size distribution according to signal intensity or nanoparticle number and peak data including maximum (Max), average ($\varnothing$), and deviation (σ).
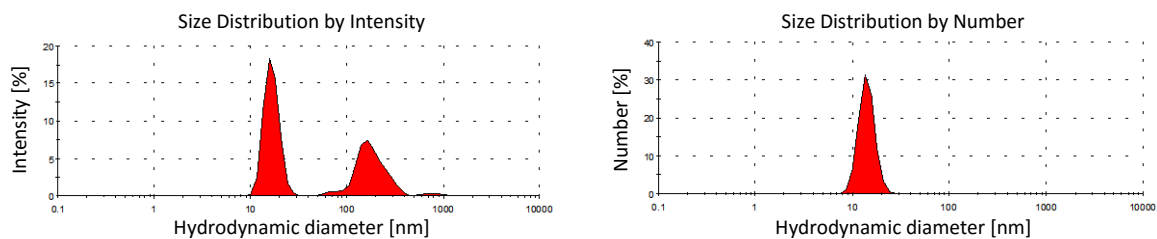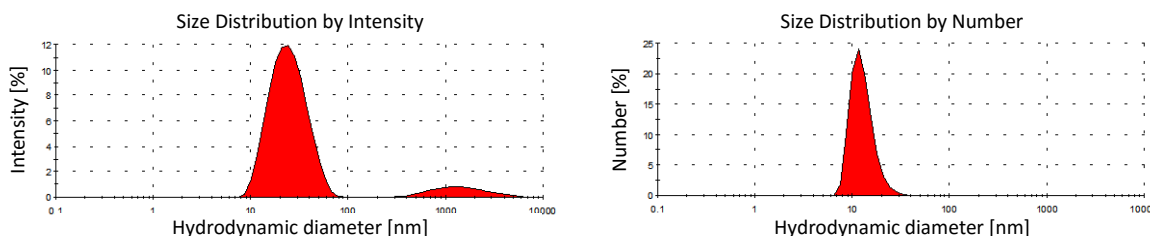
PdI 0.500	Intensity (DLS)			Number (DLS)
	Max [nm]	Ø [nm]	σ [nm]	Max [nm]
1st peak	15.69	16.75	3.002	13.54
2nd peak	164.2	182.4	64.78	-----
3rd peak	825.0	812.6	162.9	-----

Figure 9.6 Hydrodynamic diameter of UCNP@SiO$_2$-COOH with work up *B*: Size distribution according to signal intensity or nanoparticle number and peak data including maximum (Max), average (Ø), and deviation (σ).

PdI 0.275	Intensity (DLS)			Number (DLS)
	Max [nm]	Ø [nm]	σ [nm]	Max [nm]
1st peak	21.04	21.30	3.070	18.17
2nd peak	164.2	158.1	24.16	-----
3rd peak	255.0	281.8	58.26	-----

Figure 9.7 Hydrodynamic diameter of UCNP@SiO$_2$-COOH after washing step *I*: Size distribution according to signal intensity or nanoparticle number and peak data including maximum (Max), average (Ø), and deviation (σ).
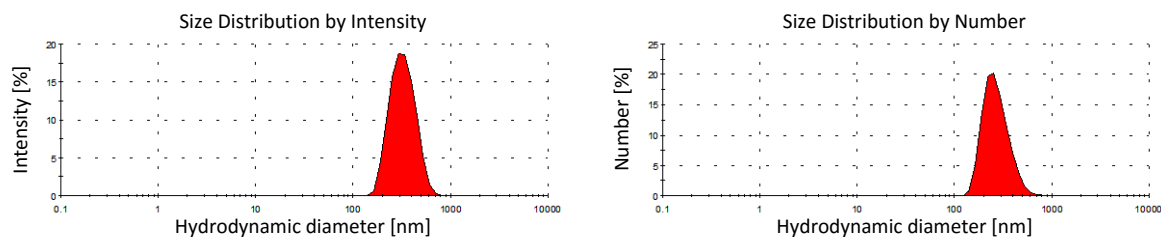

PdI 0.595	Intensity (DLS)			Number (DLS)
	Max [nm]	Ø [nm]	σ [nm]	Max [nm]
1st peak	190.1	174.6	31.06	105.7
2nd peak	342.0	340.3	82.88	164.2
3rd peak	1106	1261	426.5	295.3

Figure 9.8 Hydrodynamic diameter of UCNP@SiO$_2$-COOH after washing step *II*: Size distribution according to signal intensity or nanoparticle number and peak data including maximum (Max), average (Ø), and deviation (σ).
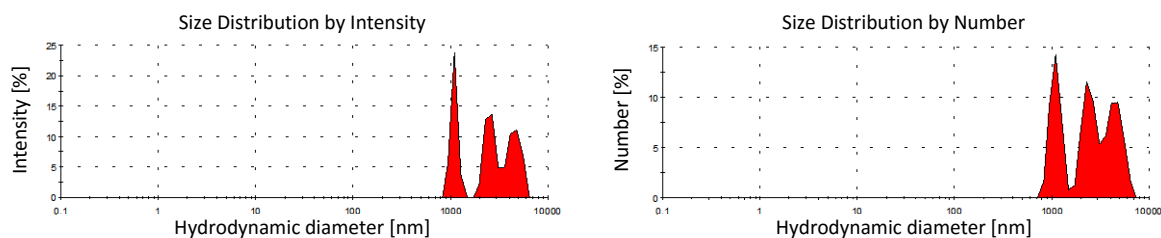
PdI 0.271	Intensity (DLS)			Number (DLS)
	Max [nm]	Ø [nm]	σ [nm]	Max [nm]
1st peak	21.04	20.65	4.258	18.17
2nd peak	220.2	222.1	35.30	-----
3rd peak	369.1	403.2	75.31	-----

Figure 9.9 Hydrodynamic diameter of UCNP@SiO$_2$-COOH after optimization: Size distribution according to signal intensity or nanoparticle number and peak data including maximum (Max), average (Ø), and deviation (σ).
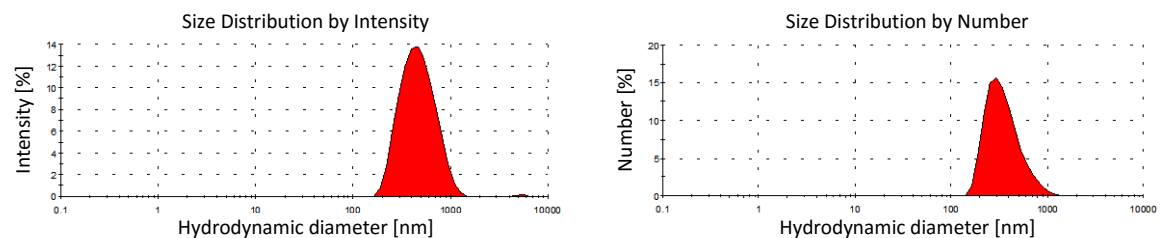

PdI 0.609	Intensity (DLS)			Number (DLS)
	Max [nm]	Ø [nm]	σ [nm]	Max [nm]
1st peak	18.17	18.13	6.062	10.10
2nd peak	295.3	348.4	176.6	-----
3rd peak	5560	4756	810.9	-----

Figure 9.10 Hydrodynamic diameter of UCNP@PAA(2100): Size distribution according to signal intensity or nanoparticle number and peak data including maximum (Max), average (Ø), and deviation (σ).
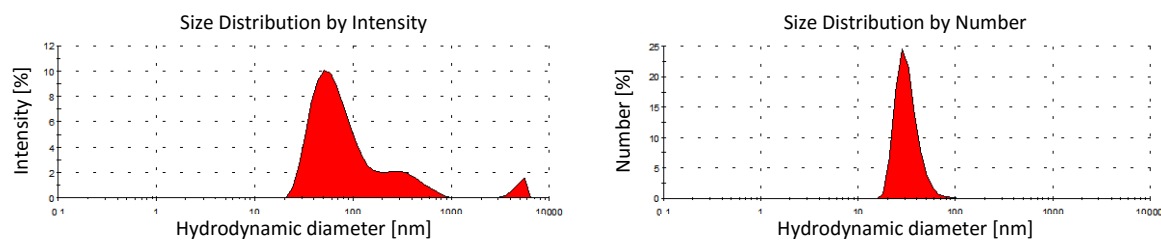

PdI 0.270	Intensity (DLS)			Number (DLS)
	Max [nm]	Ø [nm]	σ [nm]	Max [nm]
1st peak	24.36	26.03	11.07	11.70
2nd peak	1281	1621	1028	-----
3rd peak	-----	-----	-----	-----

Figure 9.11 Hydrodynamic diameter of UCNP@PAA(5100): Size distribution according to signal intensity or nanoparticle number and peak data including maximum (Max), average (Ø), and deviation (σ).
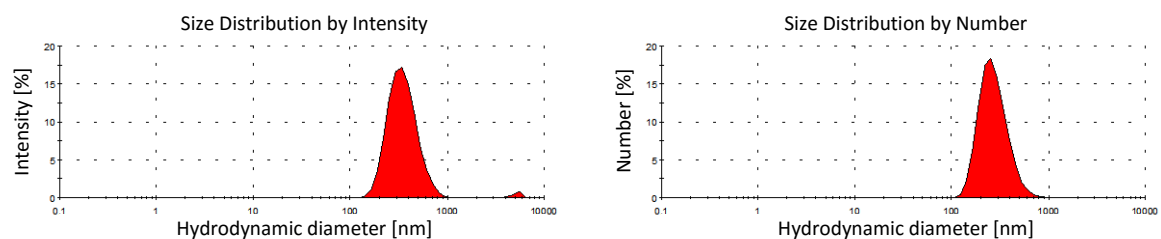
PdI 0.072	Intensity (DLS)			Number (DLS)
	Max [nm]	Ø [nm]	σ [nm]	Max [nm]
1st peak	295.3	333.3	95.62	255.0
2nd peak	-----	-----	-----	-----
3rd peak	-----	-----	-----	-----

Figure 9.12 Hydrodynamic diameter of UCNP@SiO$_2$-Ph: Size distribution according to signal intensity or nanoparticle number and peak data including maximum (Max), average (Ø), and deviation (σ).
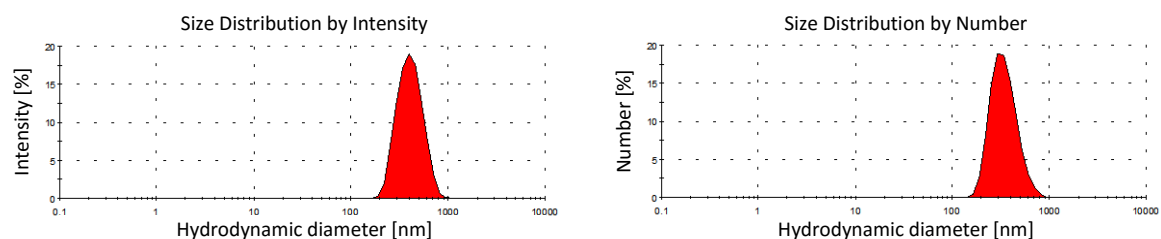

PdI 0.548	Intensity (DLS)			Number (DLS)
	Max [nm]	Ø [nm]	σ [nm]	Max [nm]
1st peak	1106	1100	85.54	1106
2nd peak	2669	2547	301.4	2305
3rd peak	4801	4387	780.5	4801

Figure 9.13 Hydrodynamic diameter of UCNP@SiO$_2$-Alk: Size distribution according to signal intensity or nanoparticle number and peak data including maximum (Max), average (Ø), and deviation (σ).
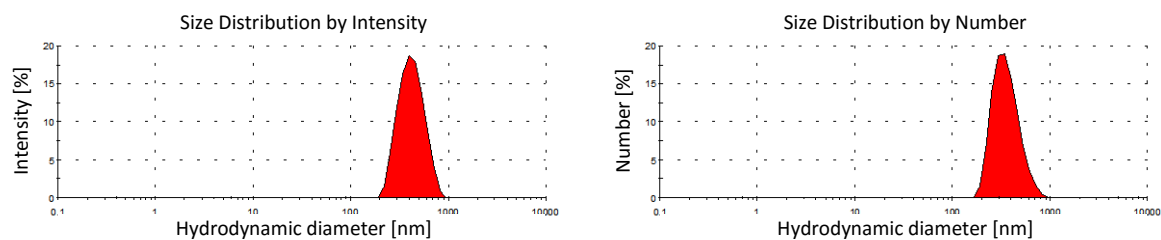

PdI 0.169	Intensity (DLS)			Number (DLS)
	Max [nm]	Ø [nm]	σ [nm]	Max [nm]
1st peak	458.7	491.1	196.9	295.3
2nd peak	5560	5198	475.4	-----
3rd peak	-----	-----	-----	-----

Figure 9.14 Hydrodynamic diameter of UCNP@SiO$_2$-Az: Size distribution according to signal intensity or nanoparticle number and peak data including maximum (Max), average (Ø), and deviation (σ).

| PdI 0.388	Intensity (DLS)			Number (DLS)
	Max [nm]	Ø [nm]	σ [nm]	Max [nm]
1st peak	50.75	70.00	36.95	28.21
2nd peak	295.3	354.6	154.1	-----
3rd peak	5560	4891	721.1	-----

Figure 9.15 Hydrodynamic diameter of UCNP@SiO$_2$-COOH/Az: Size distribution according to signal intensity or nanoparticle number and peak data including maximum (Max), average (Ø), and deviation (σ).

| PdI 0.254	Intensity (DLS)			Number (DLS)
	Max [nm]	Ø [nm]	σ [nm]	Max [nm]
1st peak	342.0	360.4	123.6	255.0
2nd peak	5560	5154	543.3	-----
3rd peak	-----	-----	-----	-----

Figure 9.16 Hydrodynamic diameter of UCNP@SiO$_2$-Az-NH$_2$: Size distribution according to signal intensity or nanoparticle number and peak data including maximum (Max), average (Ø), and deviation (σ).

PdI 0.067	Intensity (DLS)			Number (DLS)
	Max [nm]	Ø [nm]	σ [nm]	Max [nm]
1st peak	396.1	420.2	121.3	295.3
2nd peak	-----	-----	-----	-----
3rd peak	-----	-----	-----	-----

Figure 9.17 Hydrodynamic diameter of UCNP@SiO$_2$-Az-COOH: Size distribution according to signal intensity or nanoparticle number and peak data including maximum (Max), average (Ø), and deviation (σ).

PdI 0.095	Intensity (DLS)			Number (DLS)
	Max	Ø	σ	Max
	[nm]	[nm]	[nm]	[nm]
1st peak	396.1	432.5	125.0	342.0
2nd peak	-----	-----	-----	-----
3rd peak	-----	-----	-----	-----

Figure 9.18 Hydrodynamic diameter of UCNP@SiO$_2$-Az-Ph: Size distribution according to signal intensity or nanoparticle number and peak data including maximum (Max), average (Ø), and deviation (σ).

9.2   Zeta potential measurements
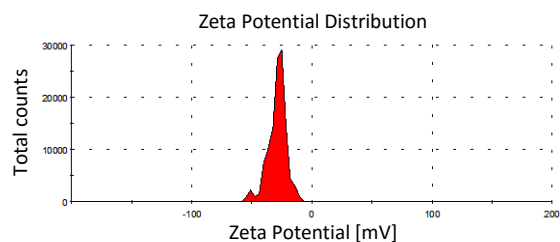
	Zeta potential distribution		
	Max [mV]	Ø [mV]	σ [mV]
1st peak	-51.2	-51.2	2.49
2nd peak	-28.0	-28.1	6.68
3rd peak	-----	-----	-----

Figure 9.19 Zeta potential of UCNP@SiO$_2$-10: Zeta potential distribution and peak data including maximum (Max), average (Ø), and deviation (σ).
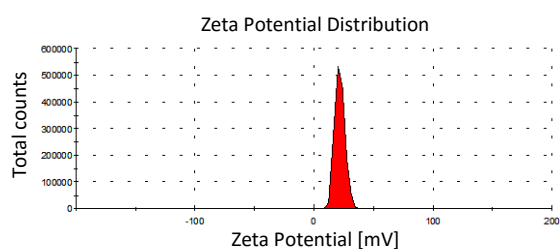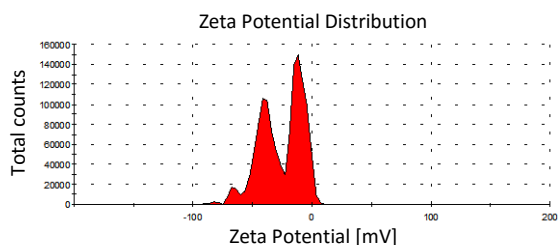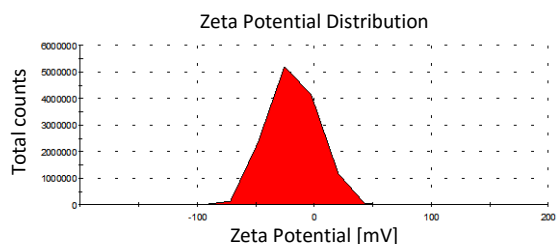

	Zeta potential distribution		
	Max [mV]	Ø [mV]	σ [mV]
1st peak	20.0	21.8	4.05
2nd peak	-----	-----	-----
3rd peak	-----	-----	-----

Figure 9.20 Zeta potential of UCNP@SiO$_2$-NH$_2$: Zeta potential distribution and peak data including maximum (Max), average (Ø), and deviation (σ).
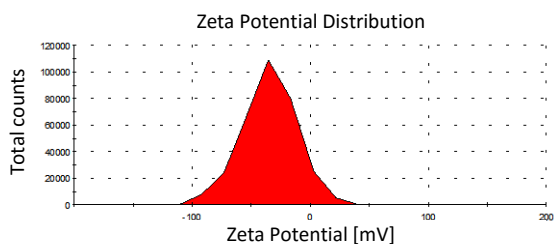
	Zeta potential distribution		
	Max [mV]	Ø [mV]	σ [mV]
1st peak	-35.3	-34.8	22.8
2nd peak	-----	-----	-----
3rd peak	-----	-----	-----

Figure 9.21 Zeta potential of UCNP@SiO$_2$-COOH at pH 9: Zeta potential distribution and peak data including maximum (Max), average (Ø), and deviation (σ).
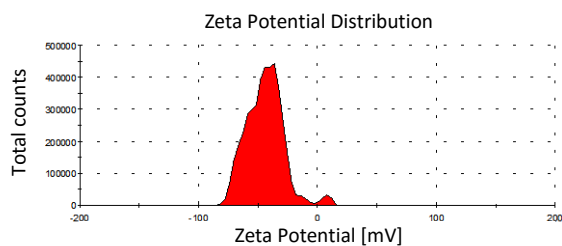

	Zeta potential distribution		
	Max [mV]	Ø [mV]	σ [mV]
1st peak	-67.4	-65.4	3.57
2nd peak	-41.3	-39.1	8.43
3rd peak	-11.5	-10.7	6.10

Figure 9.22 Zeta potential of UCNP@SiO$_2$-COOH at pH 7: Zeta potential distribution and peak data including maximum (Max), average (Ø), and deviation (σ).
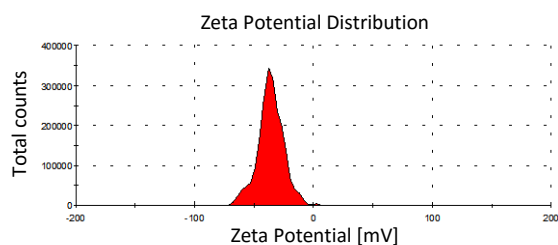

	Zeta potential distribution		
	Max [mV]	Ø [mV]	σ [mV]
1st peak	-25.6	-18.6	20.8
2nd peak	-----	-----	-----
3rd peak	-----	-----	-----

Figure 9.23 Zeta potential of UCNP@SiO$_2$-COOH after optimization: Zeta potential distribution and peak data including maximum (Max), average (Ø), and deviation (σ).

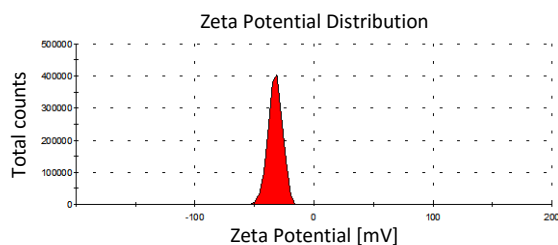|	Zeta potential distribution		
	Max [mV]	Ø [mV]	σ [mV]
1st peak	-55.0	-52.8	9.84
2nd peak	-36.4	-32.6	7.10
3rd peak	8.33	6.59	4.24

Figure 9.24 Zeta potential of UCNP@PAA(2100): Zeta potential distribution and peak data including maximum (Max), average (Ø), and deviation (σ).

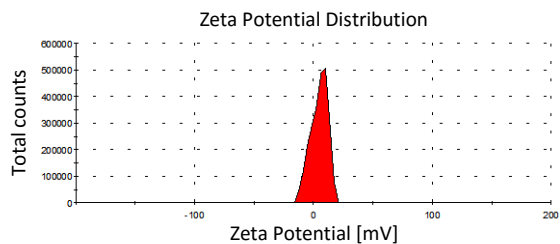|	Zeta potential distribution		
	Max [mV]	Ø [mV]	σ [mV]
1st peak	-38.0	-36.0	10.7
2nd peak	-0.749	-0.212	3.10
3rd peak	-----	-----	-----

Figure 9.25 Zeta potential of UCNP@PAA(5100): Zeta potential distribution and peak data including maximum (Max), average (Ø), and deviation (σ).
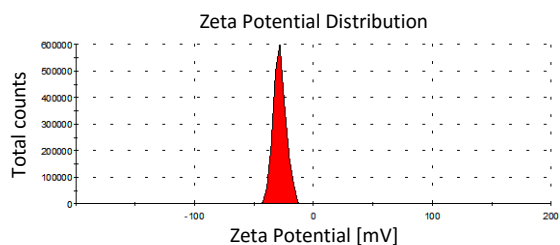

	Zeta potential distribution		
	Max [mV]	Ø [mV]	σ [mV]
1st peak	-31.0	-32.6	5.67
2nd peak	-----	-----	-----
3rd peak	-----	-----	-----

Figure 9.26 Zeta potential of UCNP@SiO$_2$-Ph: Zeta potential distribution and peak data including maximum (Max), average (Ø), and deviation (σ).

	Zeta potential distribution		
	Max [mV]	Ø [mV]	σ [mV]
1st peak	9.99	4.81	7.05
2nd peak	-----	-----	-----
3rd peak	-----	-----	-----

Figure 9.27 Zeta potential of UCNP@ SiO$_2$-Alk: Zeta potential distribution and peak data including maximum (Max), average (Ø), and deviation (σ).
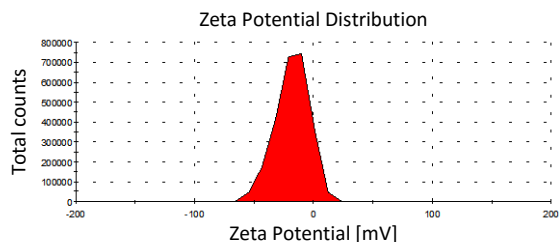

	Zeta potential distribution		
	Max [mV]	Ø [mV]	σ [mV]
1st peak	-28.1	-28.4	5.11
2nd peak	-----	-----	-----
3rd peak	-----	-----	-----

Figure 9.28 Zeta potential of UCNP@SiO$_2$-Az: Zeta potential distribution and peak data including maximum (Max), average (Ø), and deviation (σ).

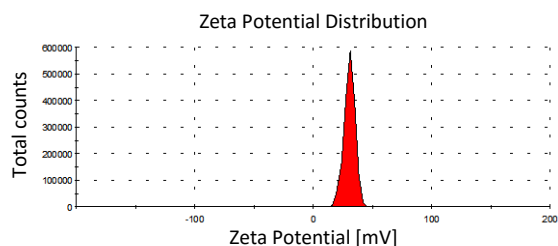|	Zeta potential distribution		
	Max [mV]	Ø [mV]	σ [mV]
1st peak	-9.78	-17.9	14.0
2nd peak	-----	-----	-----
3rd peak	-----	-----	-----

Figure 9.29 Zeta potential of UCNP@SiO$_2$-COOH/Az: Zeta potential distribution and peak data including maximum (Max), average (Ø), and deviation (σ).
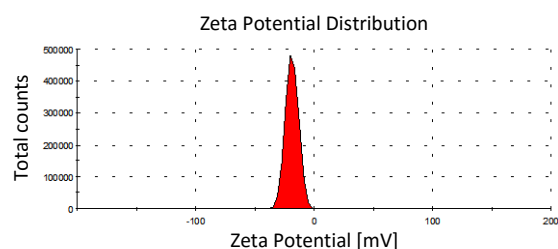
	Zeta potential distribution		
	Max [mV]	Ø [mV]	σ [mV]
1st peak	31.0	30.5	4.54
2nd peak	-----	-----	-----
3rd peak	-----	-----	-----

Figure 9.30 Zeta potential of UCNP@SiO$_2$-Az-NH$_2$: Zeta potential distribution and peak data including maximum (Max), average (Ø), and deviation (σ).

	Zeta potential distribution		
	Max [mV]	Ø [mV]	σ [mV]
1st peak	-20.1	-19.0	5.40
2nd peak	-----	-----	-----
3rd peak	-----	-----	-----

Figure 9.31 Zeta potential of UCNP@SiO$_2$-Az-COOH: Zeta potential distribution and peak data including maximum (Max), average (Ø), and deviation (σ).
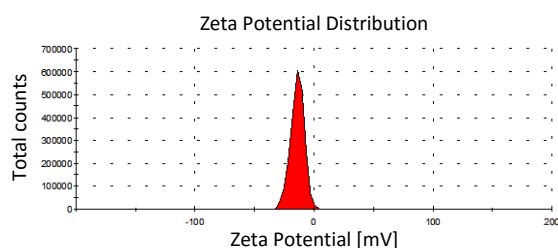

	Zeta potential distribution		
	Max [mV]	Ø [mV]	σ [mV]
1st peak	-14.0	-13.8	5.57
2nd peak	-----	-----	-----
3rd peak	-----	-----	-----

Figure 9.32 Zeta potential of UCNP@SiO$_2$-Az-Ph: Zeta potential distribution and peak data including maximum (Max), average (Ø), and deviation (σ).

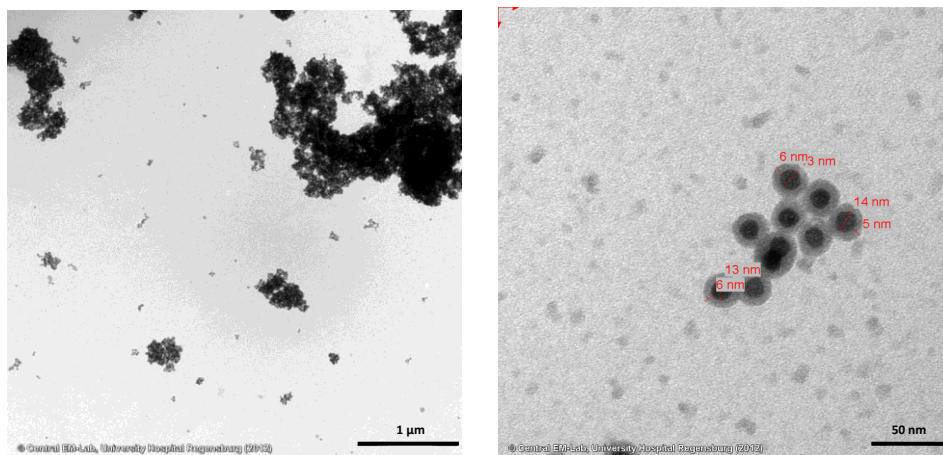## 9.3   Transmission electron microscopy images

Figure 9.33 TEM image of UCNP@SiO$_2$-10 (*left*: 10.000x magnification, scale bar: 200 nm; *right*: 160.000x magnification, scale bar: 10 nm).
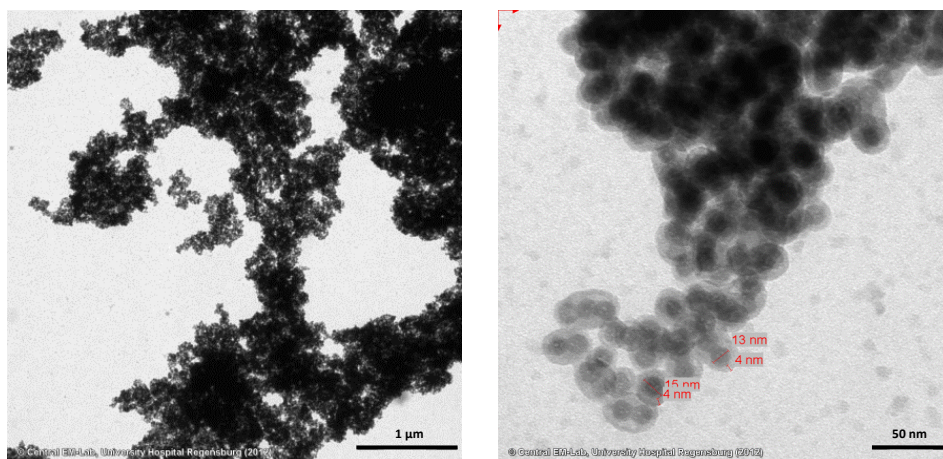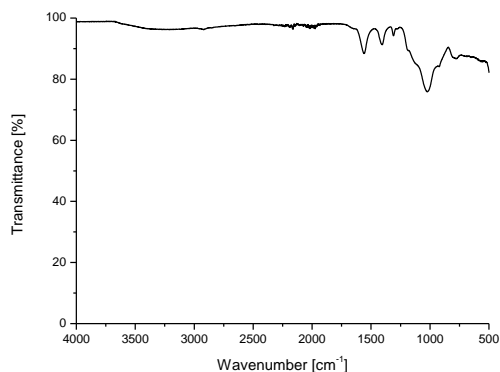

Figure 9.34 TEM image of UCNP@SiO$_2$-5 (*left*: 10.000x magnification, scale bar: 200 nm; *right*: 160.000x magnification, scale bar: 10 nm).

9.4   Infrared Spectra

Wavenumber / cm^{-1}	Band assignment
925.67	(O-H)-deformation vibration in hydrogen bonds
1024.03	(C-O) vibration
1120.45	(C-O) vibration
1309.44	Symmetric stretching vibration (carboxylate)
1405.87	Symmetric stretching vibration (carboxylate)
1558.22	Asymmetric stretching vibration (carboxylate)
2920.70	(O-H) stretching vibration in hydrogen bonds

Figure 9.35 Infrared spectrum of UCNP@SiO$_2$-COOH as dried powder with band assignment.
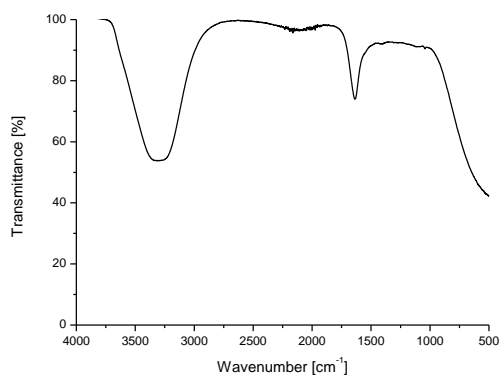
Wavenumber / cm^{-1}	Band assignment
1636.32	Asymmetric stretching vibration (carboxylate)
3321.82	(O-H) stretching vibration

Figure 9.36 Infrared spectrum of UCNP@SiO$_2$-COOH in dispersion with band assignment.

9.5   Calculations for Synthesis Adjustments of UCNP@SiO$_2$-COOH

The different surface areas of a single UCNP utilized in this thesis and literature[248] were determined with the assumption of a quasi-spherical shape of the UCNPs (Eq. 5). The calculation results are given in Table 9.1.

$$S_{NP} = 4 \cdot r_{NP}{}^2 \pi \qquad\qquad \textbf{Eq. 5}$$

with the surface area S$_{NP}$ of the respective UCNP and the radius r$_{NP}$ of the respective UCNP.

Table 9.1 Surface area calculations of a single UCNP with different radii

	r$_x$ [nm]	S$_{NP}$ [nm^2]
UCNP (Literature)	11.5	1661.9
UCNP (Thesis)	6.5	530.9

The absolute number of UCNP had to be considered for the calculation of the overall surface of all UCNPs. This number was derived from the mass concentration in a specific volume. Both the volume and the density of the host material had to be known. Since both nanoparticles were made of NaYF$_4$ with a density of 4 g/mL and again assuming a spherical shape for the volume determination (Eq. 6), the necessary numbers of UCNPs for each synthesis route were calculated by means of the mass of UCNPs utilized for synthesis in 1 mL (Table 9.2).

$$V_{NP} = \frac{4}{3} r_{NP}{}^3 \pi \qquad\qquad \textbf{Eq. 6}$$

with the volume V$_{NP}$ of the respective UCNP and the radius r$_{NP}$ of the respective UCNP.

Table 9.2 Volume and number calculations of UCNPs of different synthesis routes

	r$_x$ [nm]	V$_{NP}$ [nm^3]	V$_{NP}$ [cm^3]	m$_{NP}$ [mg]	m$_{UCNP}$ [mg]	N$_{UCNP}$
UCNP (23 nm)	11.5	6370.6	6.37×10^{-18}	2.5×10^{-14}	0.86	3.4×10^{14}
UCNP (13 nm)	6.5	1150.3	1.15×10^{-18}	0.5×10^{-14}	1.00	2.2×10^{14}

The overall surface area of all UCNPs in the respective synthesis batch was calculated by a simple multiplication of the surface area of a single nanoparticle and the absolute number of UCNPs.

Table 9.3 Calculations of the overall surface area of UCNPs of different synthesis routes

	S$_{NP}$ [nm^2]	N$_{UCNP}$	S$_{overall}$ [nm^2]
UCNP (23 nm)	1661.9	3.4×10^{14}	5.6×10^{16}
UCNP (13 nm)	530.9	2.2×10^{14}	11.5×10^{16}

The correction factor for the silane volumes added during synthesis was determined by calculating the ratio between these two overall surface areas (Eq. 7).

$$R = \frac{S_{NP(25nm)}}{S_{NP(13nm)}} \qquad\qquad \textbf{Eq. 7}$$

Finally, the necessary volumes of TEOS and CEST for an adjusted synthesis providing a good conformity were derived with a correction factor of 2.06 (Table 9.4).

Table 9.4 TEOS and CEST volumes needed for adapted synthesis from literature with a correction factor of 2.06

	V_{TEOS} [μL]	V_{CEST} [μL]
Literature	20	20
Adaption	41	41
Actual used	46	46

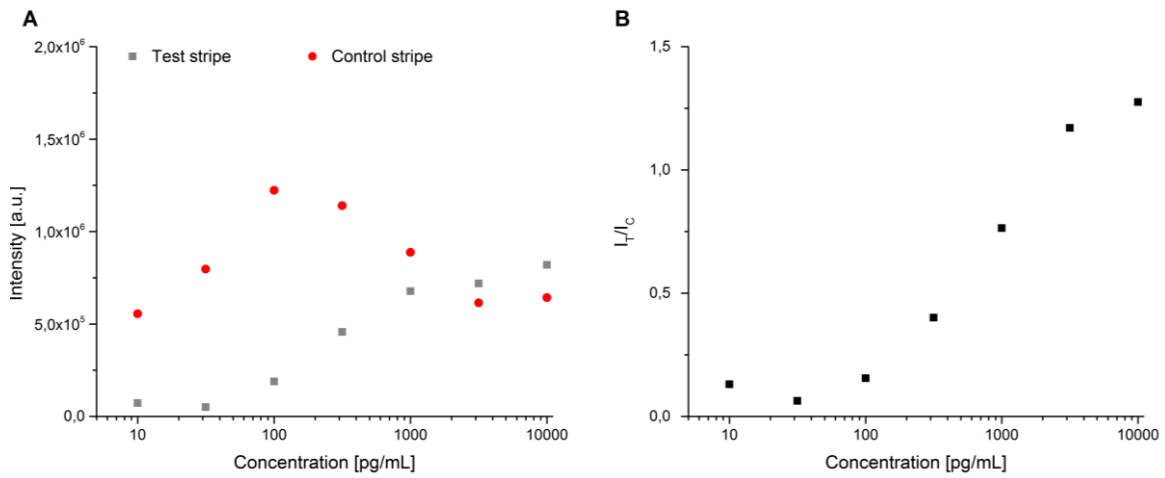## 9.6   Evaluation of Lateral Flow Assays

Figure 9.37 Intensities (A) or intensity ratio (B) of the test and control stripe for different antigen concentrations utilizing the green emission as the detection signal.
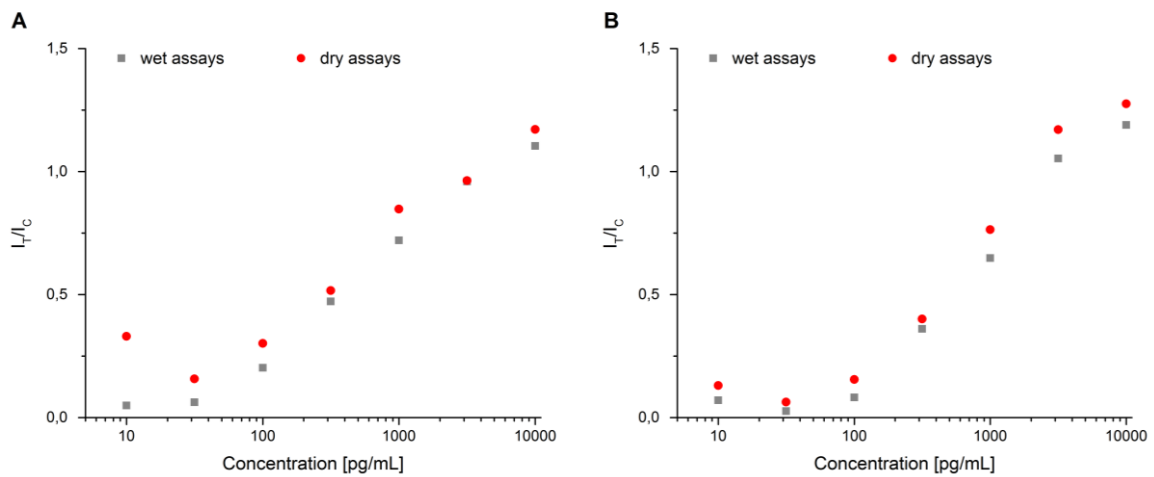

Figure 9.38 Comparison of the intensity ratio for the dry or wet condition of the lateral flow assays utilizing the overall (A) or the green (B) emission as the detection signal
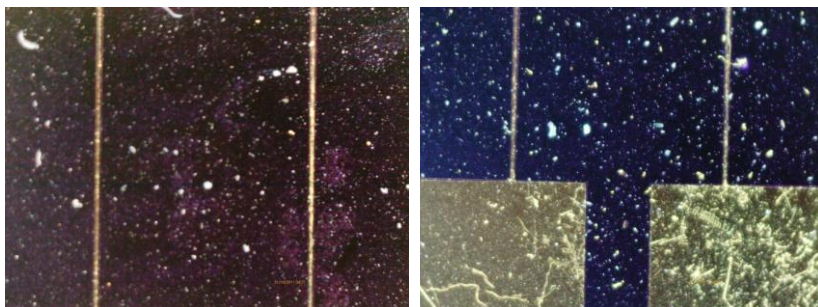
9.7 Wafer Images

Figure 9.39 Real images of non-functionalized microelectrodes illustrating the large silica surface (left) and the two gold electrodes (right)
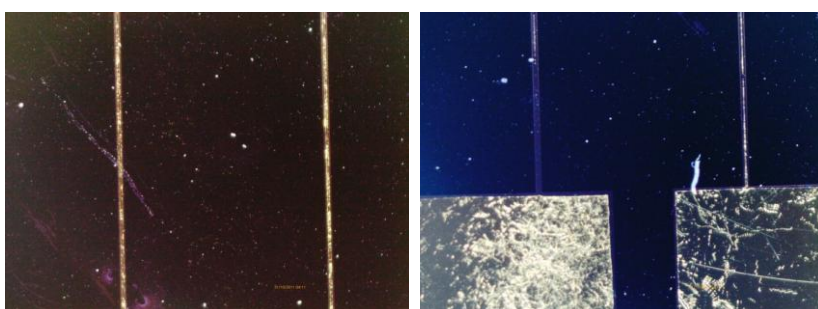

Figure 9.40 Real images of microelectrodes modified with octanyl groups illustrating the large silica surface (left) and the two gold electrodes (right)

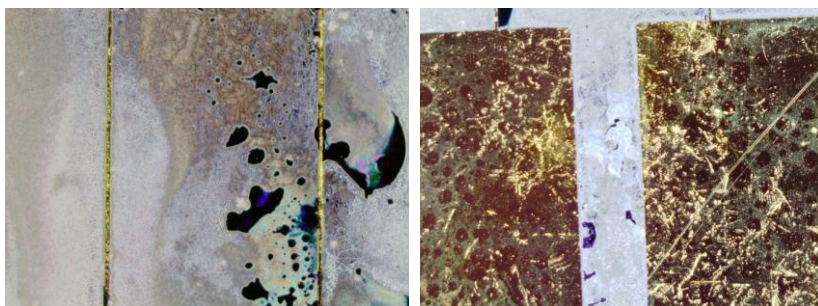**Figure 9.41** Real images of microelectrodes modified with carboxyl groups illustrating the original silica surface (left) and the two gold electrodes (right) confirming the strong contamination of the silica areas and slight tarnishing effect on gold.
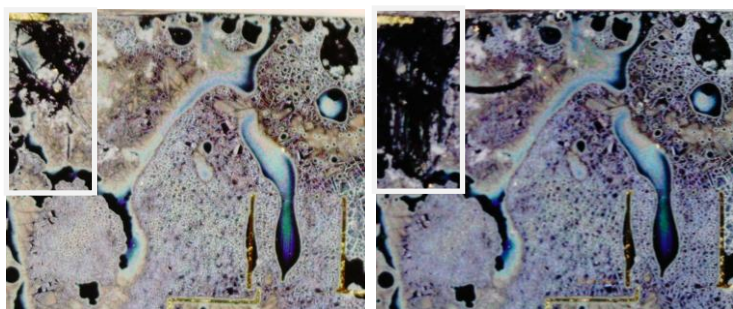

Figure 9.42 Real images of the same microelectrode area modified with carboxyl groups before (left) and after (right) scratching test in the framed area.

9.8   Abbreviations

α-NaYF$_4$	cubic modification of NaYF$_4$
APTES	3-(Aminopropyl)triethoxysilan
β-NaYF$_4$	hexagonal modification of NaYF$_4$
BMV	brome mosaic virus
BSA	bovine serum albumin
CAA	circulating anodic antigen
CCMV	cowpea chlorotic mottle virus
CEST	carboxyethylsilanetriol
CT	computed tomography
CuAAC	copper-catalyzed azide-alkyne cycloaddition
CWL	central wavelength
Da	Dalton (unit)
DMF	dimethylformamide
DNA	deoxyribonucleic acid
ds	double-stranded
EDC	1-ethyl-3-(3-dimethylaminopropyl) carbodiimide
Er	erbium
ESA	excited state absorption
ETU	energy transfer upconversion
FWHM	full width at half maximum
GAM	goat-anti-mouse
GAR	goat-anti-rabbit
Gd	gadolinium
HEPES	4-(2-hydroxyethyl)-1-piperazineethanesulfonic acid
MACAA	mouse-anti-CAA antibody
MRI	magnetic resonance imaging
NADH	nicotinamide adenine dinucleotide (reduced form)
NHS	N-hydroxysuccinimide
NIR	near infrared

PA	photon avalanche
PAA	polyacrylic acid
PBS	phosphate-buffered saline
PdI	polydispersity index
PEG	polyethylene glycol
PET	positron emission tomography
PTA	phosphotungstic acid
rcf	relative centrifugal force (unit)
RNA	ribonucleic acid
rpm	revolutions per minute (unit)
SHG	second harmonic generation
SPECT	single photon emission computed tomography
ss	single-stranded
STPA	simultaneous two-photon absorption
TEM	transmission electron microscopy
TEOS	tetraethyl orthosilicate
TPMS	3-(trihydroxysilyl)propyl-methylphosphonate
Tm	thulium
UC	upconversion
UCNP	upconverting nanoparticle
US	ultrasound
UV	ultraviolet
VIS	visible
VLP	virus-like particle
v/v	volume per volume
Yb	ytterbium

10.   Curriculum Vitae

Andreas Sedlmeier

born on November 22, 1986 in Regensburg, Germany

Education

11.2011 – 12.2015	**PhD thesis** at the Institute of Analytical Chemistry, Chemo- and Biosensors: Prof. Dr. Antje J. Bäumner (University of Regensburg) "Surface modification and Scan imaging of Upconverting nanoparticles"
10.2009 – 11.2011	**Master of Science** Chemistry (University of Regensburg) Master Thesis: "Effect of temperature on the luminescence of upconverting luminescent nanoparticles" Institute of Analytical Chemistry, Chemo- and Biosensors: Prof. Otto S. Wolfbeis (Regensburg)
10.2006 – 09.2009	**Bachelor of Science** Chemistry (University of Regensburg) Bachelor Thesis: "Photokatalytischer Abbau von Ligninmodellverbindungen mit Flavin" Institute of Organic Chemistry: Prof. Dr. Burkhard König (Regensburg)
09.1997 – 06.2006	**University Entrance Diploma** (Gymnasium Neutraubling)

Work Experience

05.2011 – 06.2015	Regular Tasks as Student and Graduate Assistant Supervision of laboratory courses for medical, dentistry and chemistry students, experiment optimization of graduate laboratory coursers
11.2011 – 03.2015	Private Lessons in Inorganic, Physical and Organic Chemistry for Medical and Dentistry Students

Language Skills

German (native), English (fluent), French (basic)

11. List of Publications and Presentations

11.1 Master Thesis

Sedlmeier, A. **Effect of temperature on the luminescence of upconverting luminescent nanoparticles** (2011) Institute for Analytical Chemistry, Chemo– and Biosensors, University of Regensburg.

11.2 Paper

Sedlmeier A, Hlaváček A, Birner L, Mickert MJ, Muhr V, Hirsch T, Corstjens PLAM, Tanke HJ, Soukka T, Gorris HH. **Highly sensitive laser scanning of photon-upconverting nanoparticles on a macroscopic scale** (2015), Analytical Chemistry (doi: 10.1021/acs.analchem.5b04147)

Sedlmeier A, Gorris HH. **Surface modification and characterization of photon-upconverting nanoparticles for bioanalytical applications** (2015) Chemical Society Reviews, *44*, 1526-1560 (doi: 10.1039/c4cs00186a)

Hlaváček A, Sedlmeier A, Skládal P, Gorris HH. **Electrophoretic Characterization and Purification of Silica-Coated Photon-Upconverting Nanoparticles and Their Bioconjugation** (2014) ACS Applied Materials & Interfaces, *6*, 6930-6935 (doi: 10.1021/am500732y)

Sedlmeier A, Gorris, HH. **UCNPs: Aus zwei Photonen mach eins** (2013) GIT Labor-Fachzeitschrift, *9*, 576-580

Sedlmeier A, Achatz DE., Fischer LH, Gorris HH, Wolfbeis OS. **Photon upconverting nanoparticles for luminescent sensing of temperature** (2012) Nanoscale, *4*, 7090-7096 (doi: 10.1039/C2NR32314A)

11.3 Abstracts of Posters and Talks

Sedlmeier A, Gorris, HH, **Surface Modification of Upconverting Nanoparticles by Click chemistry**, 13th Conference on Methods and Applications of Fluorescence (MAF), Genoa, Italy, 2013 (Poster)

Sedlmeier A, Wilhelm S, Gorris HH, **Surface modification of Upconverting Luminescent Nanoparticles for Bioconjugation**, 20 Years Anniversary Symposium, Division of Biotechnology, University of Turku, Turku, Finland, 2012 (Poster)

Sedlmeier A, **Encapsulation of UCLNPs in viral capsids**, *8th ISC Modern Analytical Chemistry*, Prague, Czech Republic, 2012 (Talk)

Eidesstattliche Erklärung

Ich erkläre hiermit an Eides statt, dass ich die vorliegende Arbeit ohne unzulässige Hilfe Dritter und ohne Benutzung anderer als der angegebenen Hilfsmittel angefertigt habe; die aus anderen Quellen direkt oder indirekt übernommenen Daten und Konzepte sind unter Angabe des Literaturzitats gekennzeichnet.

Weitere Personen waren an der inhaltlich-materiellen Herstellung der vorliegenden Arbeit nicht beteiligt. Insbesondere habe ich hierfür nicht die entgeltliche Hilfe eines Promotionsberaters oder anderer Personen in Anspruch genommen. Niemand hat von mir weder unmittelbar noch mittelbar geldwerte Leistungen für Arbeiten erhalten, die im Zusammenhang mit dem Inhalt der vorgelegten Dissertation stehen

Die Arbeit wurde bisher weder im In- noch im Ausland in gleicher oder ähnlicher Form einer anderen Prüfungsbehörde vorgelegt.

_____   _____

Ort, Datum   Unterschrift